Transposition à l'environnement turbiditique chenalisé d'un modèle de systèmes fluviatiles méandriformes pour la modélisation de réservoirs

Martin Lemay

PSL UNIVERSITÉ PARIS

THÈSE DE DOCTORAT
DE L'UNIVERSITÉ PSL

Préparée à MINES ParisTech

Transposition à l'environnement turbiditique chenalisé d'un modèle de systèmes fluviatiles méandriformes pour la modélisation de réservoirs

Soutenue par
Martin LEMAY
Le 19 décembre 2018

Ecole doctorale n° 398
Géosciences, Ressources Naturelles et Environnement

Spécialité
Géosciences et géo-ingénierie

Composition du jury :

Christian, GORINI Professeur, Sorbonne Université	*Président*
Andrea, MOSCARIELLO Professeur, Université de Genève	*Rapporteur*
Thierry, MULDER Professeur, Université de Bordeaux	*Rapporteur*
Pauline, COLLON Maitre de conférences, Université de Lorraine	*Examinateur*
Mickaële, LE RAVALEC Chef de Département, IFP Energies Nouvelles	*Examinateur*
Marco, PONTIGGIA Senior Reservoir Geologist, ENI spa	*Examinateur*
Isabelle, COJAN Directeur de Recherche, MINES ParisTech	*Directeur de thèse*
Jacques, RIVOIRARD Directeur de Recherche, MINES ParisTech	*Directeur de thèse*

MINES ParisTech | PSL

"I choose to listen to the river for a while, thinking river thoughts,
before joining the night and the stars."

Edward Abbey, *Desert solitaire*, 1968

Remerciements

Avant de plonger dans un monde trépident
Sculpté par l'eau et le transport de sédiments,
Assoyons-nous là et prenons quelques instants,
Pour la lecture de sémillants remerciements.

Je voudrais commencer cette partie par remercier chaleureusement *Isabelle Cojan* et *Jacques Rivoirard* pour m'avoir fait entièrement confiance pour ce projet, et pour la grande autonomie que vous m'avez accordée, votre soutien, ainsi que les relectures et corrections apportées tout au long de cette thèse.

Je souhaite également remercier l'ensemble des membres de mon jury, Monsieur le président *Christian Gorini*, Messieurs les rapporteurs *Andrea Moscariello* et *Thierry Mulder*, Mesdames *Pauline Collon* et *Mickaële Le Ravalec*, et Monsieur *Marco Pontiggia*, d'avoir accepté d'évaluer mon travail et pour tous les commentaires élogieux dont vous m'avez fait part.

Je voudrais continuer par dire un grand merci à *Fabien Ors*, papa adoptif de Flumy, pour ta bonne humeur, ton enthousiasme débordant, le temps que tu as pris dès que j'en avais besoin, pour m'avoir dépatouillé des écueils du C++, et avoir rattrapé mes quelques erreurs de code ou de manipulation du SVN (merci d'avoir fusionné les différents moi). J'ai quelque peu « abîmé » ton bébé, mais je suis sûr que tu sauras lui faire recouvrer ses pleines capacités. Pour continuer avec la team Flumy, je dois également beaucoup à *Jean-Louis Grimaud* pour les nombreuses discussions que nous avons eu sur les rivières et les turbidites, les questions que tu as soulevées et qui m'ont guidé, et ton aide dans quelques moments cruciaux. C'est également à toi que je dois mon séjour aux US, et je t'en suis très reconnaissant. Pour tout cela je te dis merci, ça valait bien quelques bouchons de champagne perdus entre Paris et Fontainebleau…

Je tiens aussi à remercier toutes ces personnes croisées au cours de ces trois années de thèse, notamment les membres de l'équipe géologie *Sylvie, Christine*, *Caroline* et *Thomas* pour la bonne humeur régnant au labo en particulier lors des pauses cafés. Je remercie *Bruno* dont l'œil aguerri ne rate pas les incohérences géologiques cachées dans le paysage, pour les agréables moments passés avec *Christine* sur le terrain, que ce soit sur les chemins, aux Terrasses, ou encore au bien mal nommé « Le quartz ». Je remercie également *Didier* pour m'avoir permis de continuer quelques semaines supplémentaires et le projet très intéressant auquel j'ai pu participer (j'espère que mes dessins ont été suffisamment clairs pour expliquer la géologie au géostatisticien que tu es). Je suis enfin grandement reconnaissant à *Sylvie* et *Véronique* pour tout le travail de l'ombre effectué pour nous décharger des tâches administratives, à *Hugues* qui a réussi à me trouver un bureau debout qui a sans aucun doute contribué à une rédaction efficace du mémoire, ainsi qu'à l'ensemble des personnes œuvrant sur le site de Fontainebleau pour le travail effectué afin de nous permettre d'évoluer dans ce cadre très agréable.

A l'image de ce mémoire, je vais maintenant passer à l'anglais pour remercier l'équipe du *Saint Anthony Falls Laboratory* (SAFL) qui m'a accueilli lors de mon séjour à Minneapolis, qui fut possible notamment grâce à la bourse accordée par la Fondation MINES ParisTech que je remercie.

I am very grateful to *Chris Paola*, his team (particularly *Ajay* and *Linn-Elisabeth*), and all the SAFL's staff for having welcomed me, and helped me to set up my experiments and when I needed. I discovered new ways to work and teach, and I learned a lot, particularly about fluvial processes, thanks to the numerous discussions we had. I also have to thank the students: *Zach* for having helped me to get familiar with the lab and to build the experiments, as well as *Avi* and *Blaise* for their great work they did and the results they sent to me after my leaving. I finally want to say a big thank to *Andrea* who very joyfully welcomed me with few words of French, my housemates (including the little *Alexa*) for the short but good time we spent together.

Retour en français pour maintenant m'adresser à la Dopa'team au sens large, désignant tous les doctorants, stagiaires, post-docs, étudiants, etc. croisés à Fontainebleau ou Paris pour vous remercier pour tous ces moments de détente passés ensemble, ces soirées jeux où tous les coups sont permis, ces parties de tarot endiablées, au pas de course dans la forêt, sur les pistes de ski (*#Sarenne*), ou encore les diverses sorties organisées par nos chers présidents pour lesquelles on ne les remercie jamais assez, pas même en payant notre cotiz', alors MERCI à vous *Seb*, *Marine*, *Aurélien*, *Bob, les organisateurs du ski*. Je pense à toutes ces personnes, qu'elles soient françaises, italiennes, grecques, chiliennes, mexicaines, ou d'autres horizons (d'où ces quelques vers belges), rencontrées au cours de mes trois dernières années, bien que je ne me lancerai pas dans le périlleux exercice de tous les citer au risque d'en oublier. Je vais me contenter de remercier les géologues *Fred*, *Benoît* et *Dariouche* qui m'ont accueilli dans l'équipe à mon arrivée, *Benjamin* mon prédécesseur sur Flumy pour ces quelques discussions que nous avons pu avoir, *Kiki* le chaud bouillant nouveau roi du Python, de R et des géostats qui a fini par faire le tour de von Mises malgré les nombreuses fois où tu étais au « fond du gouffre », *Léo* dont les dinosaures ne cessent de remplir les chenaux, et enfin *Alexandre* à qui je souhaite de ne pas flancher sous la pression (des sédiments).

Mes pensées vont également à l'ensemble des personnes rencontrées tout au long de ces années, que ce soit au lycée (*#Heroes*), en prépa (*#Marguerite* ; en particulier *Adeline, Alexia, Laureen, Léa, Maëlan, Marie, Typhaine, Hubert, David* avec une pensée pour notre TIPE sur le Gulf Stream), ou en école (*#Géoliens*), qui ont contribué de par leur instruction, leurs encouragements, et les moments moins sérieux, à mon parcours jusqu'à l'obtention de cette thèse.

Enfin, je voudrais terminer ces remerciements par ma famille qui m'a toujours suivi.

Merci à tous, et bonne lecture !

Résumé

Les systèmes turbiditiques chenalisés permettent le transfert de sédiments depuis le plateau continental vers le domaine marin profond de la même façon que les cours d'eau sur les continents. Les dépôts sédimentaires turbiditiques forment parmi les plus grands réservoirs d'hydrocarbures actuellement exploités (par exemple marges sud Atlantique, golfe du Mexique, delta du Nil). MINES ParisTech développe depuis une vingtaine d'années Flumy, un modèle numérique simulant l'évolution d'un système fluviatile méandriforme pour la simulation de réservoirs. L'approche proposée dans ce travail est de transposer Flumy aux systèmes sous-marins profitant de l'analogie entre ces systèmes.

Une comparaison géomorphologique s'appuyant sur des données naturelles permet d'identifier les systèmes chenaux-levées sous-marins (appelés ci-après chenaux turbiditiques) comme étant les plus analogues aux rivières alluviales méandriformes que se propose de simuler Flumy. Ce résultat s'appuie sur une nouvelle classification géomorphologique des conduits sous-marins, ainsi qu'une méthodologie de mesure adaptée aux conduits actifs et fossiles, et compatible avec celle des rivières. Ainsi, les chenaux turbiditiques se développent de façon confinée au sein d'une vallée ou libre dans les bassins de faible pente (< 1%), et sont particulièrement bien représentés dans des systèmes argileux nourris par de larges fleuves. Par rapport à leurs homologues continentaux, les chenaux turbiditiques présentent des dimensions un ordre de grandeur plus grandes (800 m de large et 25 m de profondeur), un rapport d'aspect (largeur sur profondeur moyenne) trois fois plus grand (moyenne de 30), et des ratios amplitude et longueur d'onde de méandre sur la largeur du chenal trois fois plus faibles (en moyenne 2.5 et 7.5 respectivement). Les rivières alluviales et les chenaux turbiditiques montrent tous deux une augmentation de leur largeur et de leur section en parallèle d'une diminution de la pente du chenal. La profondeur des rivières augmente proportionnellement à leur largeur lorsque la pente diminue, tandis qu'elle est quasiment stable pour les chenaux sous-marins.

La physique des écoulements fluviatiles et sous-marins contrôlant le mode de formation et la morphologie des chenaux diffère fortement. Des expériences analogiques d'écoulements aériens et sous-aquatiques au sein d'une même morphologie sinueuse de chenal montrent une adaptation plus rapide du profil de vitesse de ce dernier par rapport à l'écoulement aérien en réponse à cette morphologie. Ceci explique les dimensions réduites des méandres sous-marins pour une même largeur de chenal.

Tous ces résultats sont intégrés pour la transposition de Flumy aux systèmes turbiditiques chenalisés. Les simulations effectuées avec Flumy reproduisent les dimensions et l'architecture des bandes actives des chenaux turbiditiques en 10000 ans, via un taux de migration latérale similaire aux rivières (environ 0.05 m/an) et un taux d'aggradation 10 fois supérieur (environ 9 m/10^3 an). Enfin, elles soulignent que la trajectoire concave du chenal classiquement observée sur des sections 2D transverses aux méandres, est en partie créée par des changements d'orientation de la migration des méandres par rapport à l'orientation des sections.

Finalement, le cas bien documenté de la vallée incisée du Bénin-major permet d'évaluer la qualité des simulations Flumy en contexte turbiditique. L'incision de la vallée est très bien reproduite, incluant les principaux éléments géomorphologiques tels les méandres abandonnés perchés sur des terrasses ou les levées internes et externes. Les différentes architectures de remplissage observées dans cette vallée sont également reproduites par Flumy, et il apparaît une distribution complexe de la granularité des dépôts qui est en partie indépendante de celle des corps sédimentaires.

Abstract

Channelized turbidite systems act as sediment transfer routes through the submarine realm similarly to rivers on the continents. The turbidite sedimentary deposits create among the biggest hydrocarbon reservoirs currently produced (e.g. South Atlantic margins, gulf of Mexico, Nil delta). MINES ParisTech has developed in the last twenty years Flumy, a numerical model that simulates the evolution of a meandering fluvial system to simulate reservoirs. In this work, we propose to transpose Flumy to submarine systems taking advantage of the analogy between these environments.

A geomorphic comparison of natural data allows us to identify submarine leveed channels (hereafter called turbidite channels) as the most analogous to meandering alluvial rivers that Flumy proposes to simulate. This result relies on a new geomorphic classification of submarine flow pathways and a methodology of survey adapted to both modern and fossil pathways, and compatible with that used for rivers. Turbidite channels can be either confined in a valley or free in gentle basins (<1%), and are mostly part of mud-rich systems fed by large rivers. Compared to fluvial channels, turbidite channels are one order of magnitude larger (means: 800 m wide and 25 m deep), show an aspect ratio (width on mean depth) three times higher (mean 30) and ratios of meander amplitude and wavelength to channel width three times lower (mean 2.5 and 7.5 respectively). Both alluvial rivers and turbidite channels show increasing width and cross-sectional area when channel slope decreases. However, fluvial channel depth proportionally increases with channel width whereas turbidite channel depth is nearly constant.

Fluvial and submarine flow physics that control channel development and morphology radically differ. Laboratory experiments of aerial and subaqueous currents flowing into a same channel sinuous morphology show that the subaqueous current adjusts its velocity field faster than the aerial one in response to channel morphology. This explains the lower submarine meander dimensions for a given channel width.

All these results are integrated for the transposition of Flumy to channelized turbidite systems. The Flumy simulations reproduce submarine channel-belts dimensions and architecture using channel lateral migration rates similar to that of rivers (i.e. around 0.05 m/yr) and aggradation rates ten times greater (i.e. around 9 m/kyr). Finally, they highlight that, the concave-up channel trajectory frequently observed on 2D cross-sections transverse to meanders, is partly due to changes of meander migration direction relatively to the orientation of cross-section. Last but not least, the well-documented Benin-major valley allows us to evaluate the quality of Flumy simulations in the turbiditic context. Flumy is able to accurately reproduce the valley incision, including the main features such as terraced meander loops or inner and outer levees. The different filling architectures of this valley are correctly simulated as well, and a complex grain size arrangement that does not necessarily fit the sedimentary body distribution appears.

Sommaire

Table des figures

Liste des tableaux

Nomenclature

Symbole	Dimension	Description	Chapitre
Paramètres physiques			
ρ	$M.L^{-3}$	Masse volumique de l'eau	1
ρ_t	$M.L^{-3}$	Masse volumique de l'écoulement	3
ρ_w	$M.L^{-3}$	Masse volumique de l'eau	3
ρ_s	$M.L^{-3}$	Masse volumique des sédiments	3
g	$L.T^{-2}$	Gravité	1, 3, 4, 5
R	Ø	Densité réduite des sédiments	3, 4, 5
ϑ	$M.L^{-1}.T^{-1}$	Viscosité dynamique	3
C_f	Ø	Coefficient de friction	1, 3, 4, 5
A_{aff}	Ø	Coefficient d'affouillement	1, 4, 5
A_{sec}	Ø	Coefficient de courants secondaires	1, 4, 5
Variables hydrauliques			
$\vec{u}$	$L.T^{-1}$	Vecteur vitesse	1
$U_{mean,\,0}$	$L.T^{-1}$	Vitesse moyenne de l'écoulement dans un chenal rectiligne	4
U U_{mean}	$L.T^{-1}$	Vitesse moyenne de l'écoulement	1, 5 3, 4, 5
U'_b	$L.T^{-1}$	Perturbation de vitesse sur la berge extérieure	1, 4, 5
$H_{mean,\,0}$	L	Profondeur moyenne de l'écoulement dans un chenal rectiligne	4
$\frac{H_{mean}}{H_{flow}}$	L	Profondeur moyenne de l'écoulement	1, 4, 5
H_{max} H_{flow}	L	Profondeur maximale de l'écoulement	4 5
Q	$L^3.T^{-1}$	Débit d'écoulement	3, 5
e	$M.L^{-2}.T^{-2}$	Energie	1
f_{drive}	$M.T^{-2}$	Force motrice par unité de distance	3
C	Ø	Concentration volumique en sédiments	3, 4, 5
Fr F	Ø	Nombre de Froude	3 1, 4, 5
Re	Ø	Nombre de Reynolds	3
λ_s	Ø	Facteur d'échelle des expériences	3
Géométrie			
s	L	Abscisse curviligne	1, 3, 4, 5
n	L	Ordonnée curviligne	1, 3, 4, 5
z	L	Coordonnée verticale	3
z_b	Ø	Coordonnée verticale normalisée par la profondeur du chenal	3
k	L^{-1}	Courbure de la ligne centrale du chenal	1, 4, 5
θ	Ø	Angle entre la ligne centrale et la direction principale du chenal	3
θ_0	Ø	θ maximal	3
d	L	Distance de Von Mises par rapport au chenal	1
P_i	Ø	Point de la ligne centrale au nœud i	1, 4
I_0	Ø	Pente du domaine	1, 4, 5
I_r S	Ø	Pente locale du chenal	1, 4, 5 3
λ_{arc}	L	Longueur d'arc des méandres	3
λ	L	Longueur d'onde du chenal	1, 2, 4, 5
L_{bend}	L	Distance entre deux points d'inflexion consécutifs	2
$A_{meander}$	L	Amplitude d'un méandre	2
A_{bend}	L	Amplitude d'une boucle	2
W W_{bkf}	L	Largeur du chenal	1, 3, 4 2, 5
$H_{channel}$	L	Profondeur du chenal	1, 4, 5

H			3
$H_{bkf,\ mean}$	L	Profondeur de plein bord maximale du chenal	2
$H_{bkf,\ max}$	L	Profondeur de plein bord moyenne du chenal	2
H_{bank}	L	Hauteur de la berge à partir du fond du chenal	1, 4, 5
W_{cb}	L	Largeur de la bande active du chenal	4
H_{cb}	L	Epaisseur de la bande active du chenal	4
M_{sb}	Ø	*Belt-averaged stratigraphic mobility number*	4
M_{sl}	Ø	*Local stratigraphic mobility number*	4
M_{db}	Ø	*Belt-averaged dynamic mobility number*	4
M_{dl}	Ø	*Local dynamic mobility number*	4
L_c	L	Déplacement horizontal du chenal	4
L_a	L	Déplacement vertical du chenal	4
Processus			
$\overrightarrow{Mig_{th}}$	$L.T^{-1}$	Vecteur migration théorique	1, 4, 5
$\overrightarrow{Mig}$	$L.T^{-1}$	Vecteur migration réel	1, 4, 5
Mig	$L.T^{-1}$	Taux de migration latérale du chenal	4
E	Ø	Erodabilité	1, 4, 5
$Aggrad$	$L.T^{-1}$	Taux d'aggradation du chenal	4
T_{ob}	T	Période d'aggradation	1, 4
i_{ob}	L	Intensité d'aggradation	1, 4
th_{ob}	L	Epaisseur des dépôts de levées	1
λ_{ob}	L	Longueur caractéristique de décroissance des levées	1
$H_{overflow}$	L	Epaisseur de l'écoulement qui déborde du chenal	4
th_{dep}	L	Epaisseur des dépôts de débordement	4
f_{dep}	Ø	Facteur de dépôt	4
T_{av}	T	Période d'avulsion	4
T_{avr}	T	Période d'avulsion régionale	1
T_{lvb}	T	Période de rupture des levées	1

Introduction

1. Problématique

Depuis, la découverte dans les années 50 de systèmes chenalisés turbiditiques situés en pied de talus continental (Menard, 1955), l'intérêt pour ces systèmes ne cesse de croitre en raison d'une part des ressources d'hydrocarbures très importantes qu'ils peuvent contenir (Weimer and Slatt, 2004 ; Mayall et al., 2006 ; Sheperd, 2009), et d'autre part des futurs projets d'infrastructures *offshore* et d'exploitation des ressources minérales sous-marines (Baker et al., 2016). En effet, les formations turbiditiques sont notamment très propices à la formation de réservoirs et l'accumulation d'hydrocarbures en raison de la combinaison de dépôts sableux poreux, et de dépôts argileux imperméables et riches en matière organique précurseurs d'hydrocarbures. Les réservoirs turbiditiques chenalisés peuvent être de volume très importants, mais ils présentent également des géométries et des architectures complexes (Weimer and Slatt, 2004 ; Mayall et al., 2006 ; Shepherd, 2009). De plus, ces réservoirs sont généralement situés au large des côtes, à plusieurs centaines de mètres de profondeur d'eau, augmentant ainsi considérablement le coût de l'acquisition de données. L'exploration puis la production de ces réservoirs s'appuient donc sur une quantité très restreinte de données, incluant des données à grande échelle mais de faible résolution comme les données sismiques, ainsi que de rares données ponctuelles de haute résolution issues de forages.

Afin de pallier ce manque de données, l'industrie pétrolière utilise des modèles numériques de réservoirs afin d'évaluer la présence d'hydrocarbures, estimer leur volume, prévoir les plans de développement des champs, et évaluer les risques techniques et financiers des projets (Mayall et al., 2006 ; Baddeley, 2018). La construction des modèles de réservoir se divise en plusieurs étapes (Figure 1a). (1) Un modèle structural est tout d'abord construit permettant de définir la géométrie globale du réservoir et les éventuels compartiments créés par des failles. (2) Une grille en 3 dimensions basée sur le modèle structural et ensuite discrétisée en cellules de dizaines à centaines de mètres de largeur et dizaines de centimètres à quelques mètres d'épaisseur, représente le réservoir. A chaque cellule de cette grille sont attribuées des propriétés pétrophysiques, comprenant en premier lieu (3) le faciès, caractérisant les types de roche en place et dont dépendent les autres propriétés telles (4) la porosité qui est le volume poreux entre les grains, et la perméabilité représentant la capacité de ces fluides à se déplacer au sein du volume poreux. Cette grille ainsi peuplée permet finalement de réaliser des simulations de production des fluides présents dans le réservoir et ainsi d'essayer de la prévoir et de l'optimiser.

Le travail de cette thèse se concentre sur l'aspect de la modélisation de faciès dont dépend la suite du processus de modélisation, et a pour objet l'étude des réservoirs turbiditiques chenalisés.

2. Approche

Plusieurs méthodes de modélisation de faciès sont utilisées par l'industrie, dépendant notamment des données disponibles et de l'environnement sédimentaire ayant conduit à la mise en place du réservoir. Parmi celles-ci, les *pixel-based* (Matheron, 1963; Strebelle et al., 2002 ; Caers, 2005 ; Mariethoz et Caers., 2014 ; Tahmasebi, 2018) sont des méthodes géostatistiques permettant l'interpolation des propriétés observées aux puits. Ces méthodes stochastiques sont les plus utilisées puisqu'elles permettent de respecter les observations locales (Figure 1b), et de fournir rapidement différentes simulations équiprobables servant à évaluer les incertitudes associées. Néanmoins, malgré les progrès permanents (Sebacher et al., 2015 ; Tahmasebi, 2018), ces méthodes peuvent avoir pour point faible le manque de réalisme des corps sédimentaires simulés, en particulier dans le cas de réservoirs à l'architecture complexe et hétérogène comme les réservoirs turbiditiques chenalisés. Afin d'améliorer le réalisme des simulations, des méthodes *object-based* (Deutsch et Tran, 2002) peuvent être couplées pour prendre en compte des concepts géologiques tel un environnement de dépôt chenalisé. Les méthodes *object-based* sont également stochastiques et conditionnées par les données (Figure 1b), mais dépendent essentiellement de leurs paramètres géométriques, ne permettant donc pas de reproduire toute la complexité des architectures observées.

Au cours de ces dernières décennies, de nombreux modèles numériques ont été développés afin de reproduire l'évolution dans le temps et l'espace de systèmes chenalisés fluviatiles (Ikeda et al., 1981 ; Howard et Knutson, 1984 ; Sun et al, 1996 ; Lopez et al., 2008 ; Pyrcz et al., 2009 ; Rongier et al., 2017 ; Parquer et al., 2017). Selon le degré de complexité de ces méthodes, elles sont qualifiées de *rule-based* lorsqu'elles sont davantage basées sur des règles mathématiques, à *process-based* lorsqu'elles s'attèlent à simuler les processus physiques et sédimentaires en jeu dans le système modélisé (Pyrcz et al., 2015 - Figure 1b). Bien que nettement plus réalistes que les méthodes conventionnelles, ces méthodes sont également plus difficilement conditionnables aux données, ce qui en fait un frein majeur quant à leur utilisation pour la modélisation de réservoirs. En revanche, elles peuvent permettent de tester différents scénarios géologiques et de sélectionner les plus probables. MINES ParisTech développe depuis plusieurs années Flumy (Lopez, 2003 ; Grappe, 2014), un modèle de réservoirs associés aux systèmes chenalisés fluviatiles méandriformes dit *process-based* (Figure 1b). Flumy simule l'évolution dans le temps de systèmes fluviatiles méandriformes (Lopez et al., 2008). Flumy reproduit les principaux processus en jeu dans ces systèmes, incluant la

migration du chenal, les recoupements de méandre, les avulsions, et l'aggradation (Bridge, 2003). Ainsi, les corps sédimentaires simulés correspondent à des barres d'accrétion latérale (*point bar* an anglais) créant l'essentiel des réservoirs, ainsi que des dépôts de levées et de plaine d'inondation, de lobes de crevasse, et de remplissage de chenaux abandonnés.

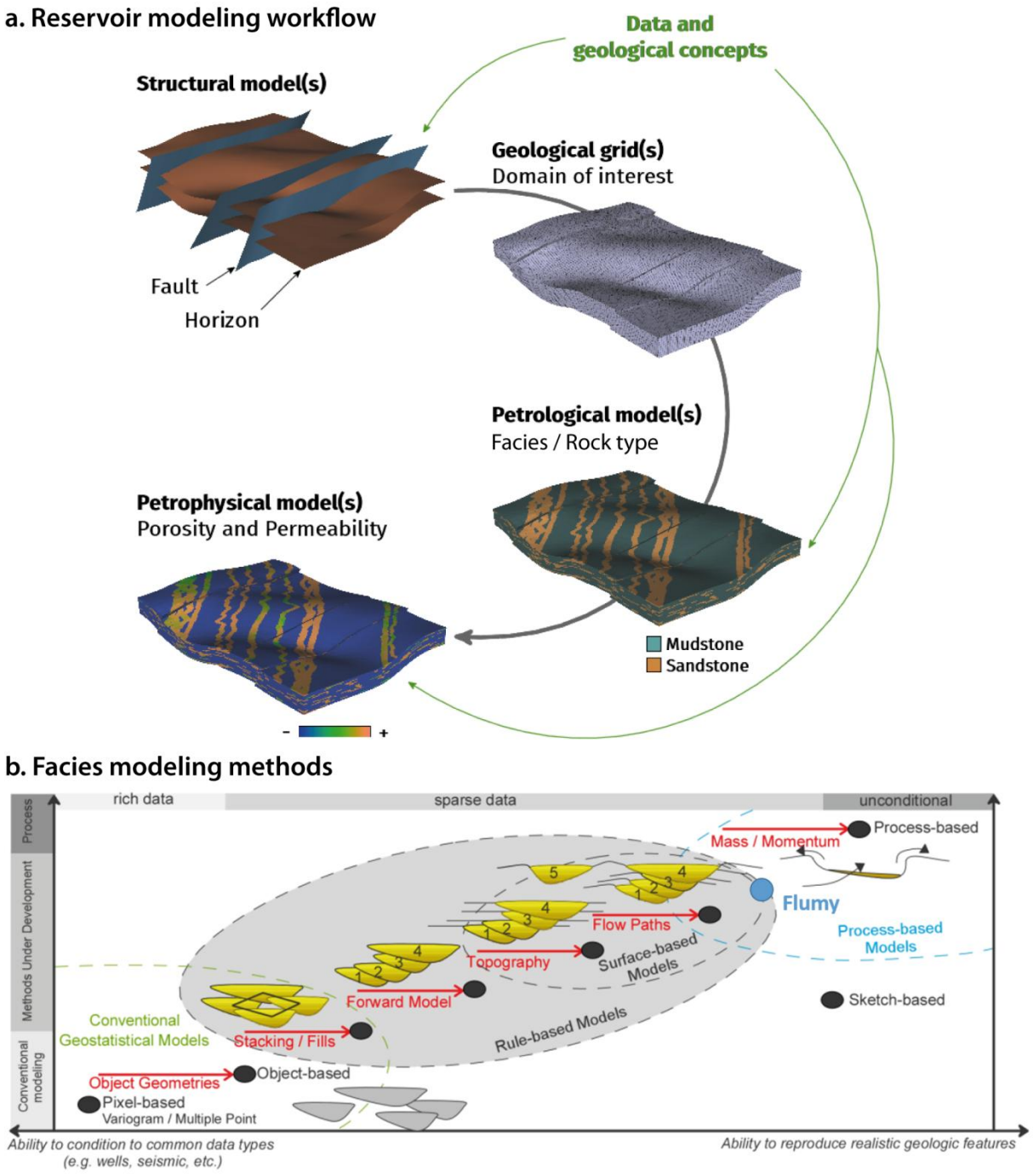

Figure 1 : Processus de modélisation de réservoirs (modifié d'après Rongier, 2016) (a), et classification des méthodes de modélisation de faciès (d'après Pyrcz et al., 2015) incluant le positionnement de Flumy (b).

Une très forte analogie géomorphologique entre les systèmes chenalisés continentaux et sous-marins a été constatée puis décrite depuis plusieurs décennies (Menard, 1955; Flood and Damuth, 1987; Clark and Pickering, 1996 ; Wynn et al 2007 – Figure 2). Cette analogie concerne également les processus en jeu tels la migration latérale du chenal (Abreu et al., 2003 ; Arnott, 2007 ; Maier et al., 2013; Jobe et al., 2016), les recoupements de méandre (Lonsdale and Hollister, 1979 ; Deptuck et al., 2003, 2007 ; Babonneau et al., 2004), l'aggradation (Wynn et al., 2007 ; Jobe et al., 2015) ou les avulsions (Kolla, 2007). En revanche, la physique des écoulements fluviatiles diffère de celle des écoulements sous-marins, notamment dans le cas sous-aquatique en raison du rôle moteur des sédiments (Konsoer et al., 2013), de la stratification de ces derniers (Dorrell et al., 2014; Azpiroz-Zabala et al., 2017b; Luchi et al., 2018; Paull et al., 2018), ou encore des débordements continus de ces écoulements par delà le chenal principal (Peakall et al., 2000 ; Traer et al., 2018). Ces différences de processus conduisent notamment à des dissemblances dans la dynamique des chenaux fluviatiles et turbiditiques telle la stabilisation de la morphologie planaire de ces derniers (Peakall et al., 2000 ; Jobe et al., 2015), ainsi qu'à des différences dans la géométrie et l'architecture des réservoirs fluviatiles et turbiditiques (Sheperd, 2009). De plus, la compréhension des processus en jeu dans les systèmes sous-marins est nettement en retard par rapport à celle des cours d'eau, notamment en raison des difficultés d'observation des chenaux et des écoulements associés.

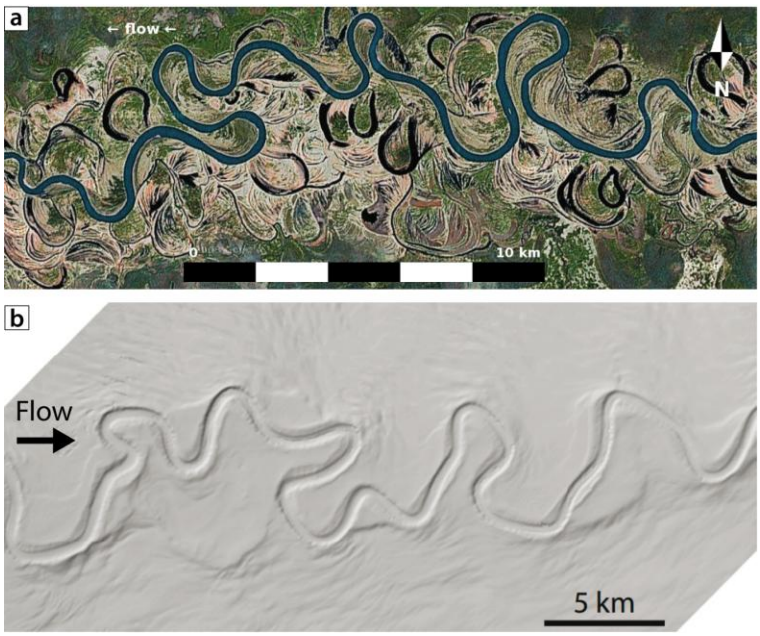

Figure 2 : Systèmes méandriformes (a) fluviatile (rivière Chulym, Russie – Google Earth) ; (b) sous-marin (Joshua Channel, Golf du Mexique – d'après Shumaker et al., 2018).

Ce travail de thèse vise ainsi à transposer Flumy aux systèmes sous-marins afin de simuler les réservoirs turbiditiques chenalisés tout en introduisant une meilleure description des hétérogénéités granulométriques, et passe notamment par une meilleure compréhension des processus eu jeu.

Suivant la citation de Edward Abbey (1968) présentée en préambule, ce travail s'inspire des théories développées pour les systèmes fluviatiles afin d'éclairer les processus en jeu dans les systèmes chenalisés sous-marins.

Ce mémoire est constitué de six chapitres :

- Le premier chapitre présente l'architecture des réservoirs fluviatiles méandriformes et chenalisés turbiditiques, ainsi que le modèle fluviatile Flumy tel qu'il était au début de cette thèse. Une dernière partie s'intéresse aux modèles existants de modélisation des écoulements turbiditiques et d'évolution des chenaux sous-marins.
- Le deuxième chapitre, correspondant à un article soumis à *Marine and Petroleum Geology*, porte sur la comparaison géomorphologique des systèmes chenalisés alluviaux et sous-marins en appliquant les méthodes de mesure des conduits d'écoulements développées pour les systèmes fluviatiles, afin de définir précisément le chenal turbiditique qui sera simulé par Flumy.
- Le troisième chapitre présente la réalisation d'expériences comparatives à échelle réduite d'écoulements fluviatiles et sous-marins. L'objectif de ces expériences est de comparer les champs de vitesse de ces deux types d'écoulements dans un même chenal de morphologie fixée.
- Le quatrième chapitre est un projet d'article qui présente l'application de Flumy aux systèmes chenalisés sous-marins non confinés et explore les mécanismes qui conduisent à la stabilisation de la morphologie planaire du chenal.
- Le cinquième chapitre expose l'utilisation de Flumy au cas d'étude de la vallée du Bénin-major, de son incision à la reproduction de la complexité de son remplissage, et reprend l'article publié dans les *proceedings* du *RING meeting 2018*.
- Enfin, un dernier chapitre synthétise les résultats exposés au cours de cette thèse et évoque les perspectives.

Chapitre 1.

Réservoirs chenalisés fluviatiles et turbiditiques : architecture et modélisation

1.1. Introduction

Les réservoirs issus de systèmes chenalisés fluviatiles ou turbiditiques présentent des géométries et architectures internes très complexes en raison de l'agencement des différents corps sédimentaires les uns par rapport aux autres, et aux variations d'écoulement contrôlant la granularité des dépôts (Shepherd, 2009). Ainsi, bien que les corps sableux formant l'essentiel du volume réservoir soient de taille importante, l'intercalation de corps argileux imperméables est responsable de fortes hétérogénéités voire de la compartimentation des réservoirs, complexifiant par conséquent la connectivité entre les corps sableux et donc les chemins d'écoulement des fluides qui s'y sont accumulés (e.g. Mayall et al., 2006 ; Gainsiki et al., 2013 ; Issautier et al., 2016 ; Willems et al., 2017). La **première partie** de ce chapitre présente une **comparaison de l'architecture des réservoirs fluviatiles méandriformes et turbiditiques chenalisés**. En effet, en dépit de la forte analogie de morphologie entre les systèmes chenalisés fluviatiles et sous-marins (Menard, 1955; Shepard, 1965 ; Lonsdale et Hollister, 1979; Flood et Damuth, 1987; Miall, 1989; Clark et Pickering, 1996 ; Leeder, 1999; Wynn et al 2007 ; Konsoer et al., 2013), le type, la géométrie et l'architecture des réservoirs associés à chacun de ces systèmes sédimentaires diffèrent fortement (Shepherd, 2009).

Afin de prendre en compte la complexité des réservoirs, l'industrie s'appuie sur des modèles numériques permettant d'estimer les volumes de fluides (eau, hydrocarbures) en place, proposer des plans de développement des champs, prévoir la production, et évaluer les risques techniques et financiers des projets (Mayall et al., 2006 ; Baddeley, 2018). Outre les approches de modélisation *pixel-based* (Matheron, 1963; Strebelle et al., 2002 ; Caers, 2005 ; Mariethoz et Caers., 2014 ; Tahmasebi, 2018) et *object-based* (Deutch et Tran, 2002) classiquement utilisés par l'industrie, de nombreuses approches *rule* ou *process-based* (Pyrcz et al., 2015) dédiées aux réservoirs fluviatiles méandriformes voient le jour depuis plusieurs années (Lopez et al., 2008 ; Pyrcz et al., 2009 ; Parquer et al., 2017 ; Rongier et al., 2017 **;** Yan et al., 2017). La **deuxième partie** de ce chapitre présente **Flumy au début de cette étude**, le modèle *process-based* développé par MINES ParisTech pour la simulation des réservoirs chenalisés méandriformes fluviatiles.

La **dernière partie** présente une synthèse de ces différentes méthodes utilisées dans les **modèles *rule* ou *process-based*** de simulation de **systèmes et réservoirs turbiditiques chenalisés** qui sont davantage au stade de développement que leurs homologues fluviatiles. Ainsi, plusieurs approches existent pour simuler l'évolution des chenaux et/ou les écoulements turbiditiques.

1.2. Architecture des réservoirs fluviatiles méandriformes et turbiditiques chenalisés

Les réservoirs fluviatiles méandriformes sont essentiellement formés par l'amalgamation horizontale et/ou verticale des barres de méandre (Figure 1.1a – Shepherd, 2009 ; Miall, 2014). Ces réservoirs se situent donc dans des grès grossiers à moyens, de forte porosité et perméabilité. La complexité de ces réservoirs réside principalement dans la géométrie les barres d'accrétion latérale et leur connectivité latérale et verticale qui dépendent des paramètres cinématiques des chenaux (i.e. taux de migration, d'aggradation, et d'avulsion – Koneshloo et al., 2017). Par exemple, une fréquence d'avulsion élevée favorise la formation de corps sableux isolés dans les faciès fins de plaine d'inondation (i.e. réservoir de type *ribbon*), tandis qu'un fort taux de migration permet le développement de larges barres de méandre (i.e. réservoir de type *sheet*). De plus, des barrières créées par les chenaux abandonnés ou la présence de fines couches argileuses au sein des barres de méandre peuvent compartimenter le réservoir (Figure 1.1a). Enfin, les lobes de crevasse et les levées peuvent également contribuer au volume poreux du réservoir mais ne suffisent pas à créer de réservoirs à part entière.

Les réservoirs dans les systèmes turbiditiques (Figures 1.1b, 1.1c) sont constitués par les corps chenalisés, les levées et les lobes de crevasse, ou encore les lobes frontaux (Shepherd, 2009). Ceux situés dans des corps chenalisés sont créés lors du remplissage d'une vallée incisée par l'amalgamation de remplissages de chenaux et de LADs (*Lateral Accretion Deposits*) (Figure 1.1b – Mayall et al., 2006 ; Arnott, 2007). Leur architecture peut être très complexe en fonction des composantes respectives de la mobilité latérale et verticale des chenaux, qui génèrent des proportions de corps sableux très variables et des connectivités plus ou moins développées (Clark et Pickering, 1996). Les réservoirs situés au sein des levées et des lobes de crevasse sont formés par l'empilement de fins bancs silto-sableux de très grande extension latérale en alternance avec des argiles (Figure 1.1c – Clemenceau et al., 2000 ; Shepherd, 2009). Les corps chenalisés sableux peuvent également contribuer au réservoir si des connexions avec les dépôts grossiers des levées existent. Ces réservoirs sont principalement exploités pour du gaz en raison de leur faible perméabilité. Enfin, le dernier type de réservoir turbiditique correspond aux lobes frontaux (Shepherd, 2009) dont la géométrie et la présence de niveaux argileux constituent des défis pour leur exploitation.

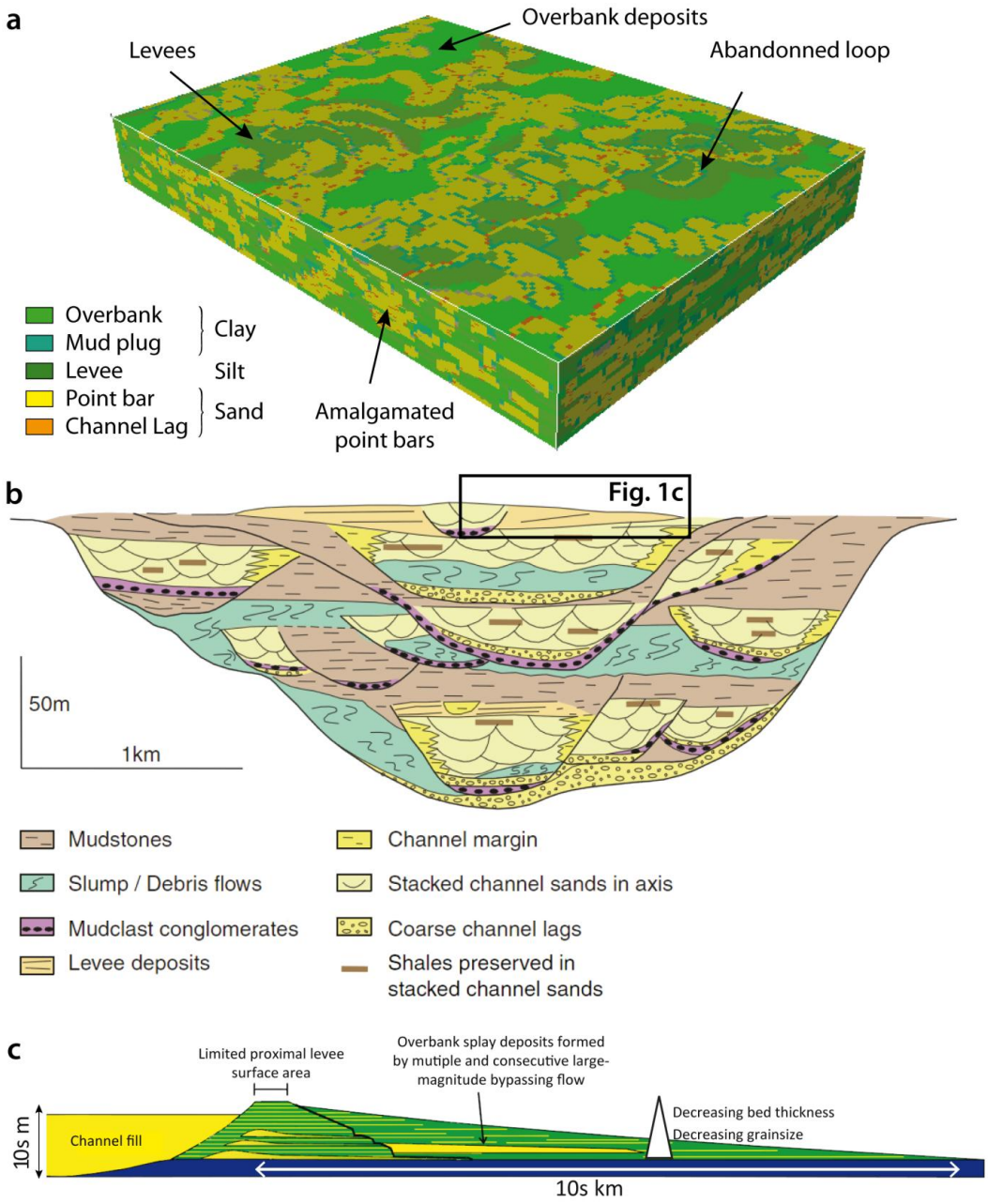

Figure 1.1 : Architecture des réservoirs (a) fluviatiles (bloc 3D de faciès issu d'une simulation Flumy), (b) turbiditiques confinés (Mayall et al., 2006), et (c) turbiditiques non confinés (Khan et al., 2011).

1.3. Modélisation des réservoirs fluviatiles méandriformes avec Flumy

Flumy simule les principaux processus en jeu dans les systèmes fluviatiles méandriformes (migration, aggradation et avulsions) ainsi que les corps sédimentaires qui en résultent (Lopez, 2003 ; Lopez et al., 2008 ; Grappe, 2014). La migration de la ligne centrale du chenal conduit à la formation de méandres et le dépôt de barres d'accrétion latérale (*point bars*), pouvant évoluer jusqu'à leur recoupement donnant ainsi naissance à des bras morts comblés par des bouchons sableux et argileux. L'aggradation du chenal au cours des crues de débordement contribue à la construction de la plaine d'inondation associée au chenal. Le phénomène d'avulsion conduit dans un premier temps

à la formation de lobes de crevasse, puis en cas d'avulsion réussie à l'abandon par remplissage progressif de la portion du chenal située à l'aval du nœud d'avulsion, et à la construction de nouveaux tracés assurant ainsi le balayage du domaine simulé (Figure 1.2). Flumy est donc un modèle hybride, comprenant trois modules dédiés à chacun des trois processus simulés (en violet - Figure 1.3) :

- Module de migration latérale du chenal
- Module d'incision et d'aggradation du chenal associé à l'érosion ou la construction de la plaine d'inondation
- Module de gestion des avulsions

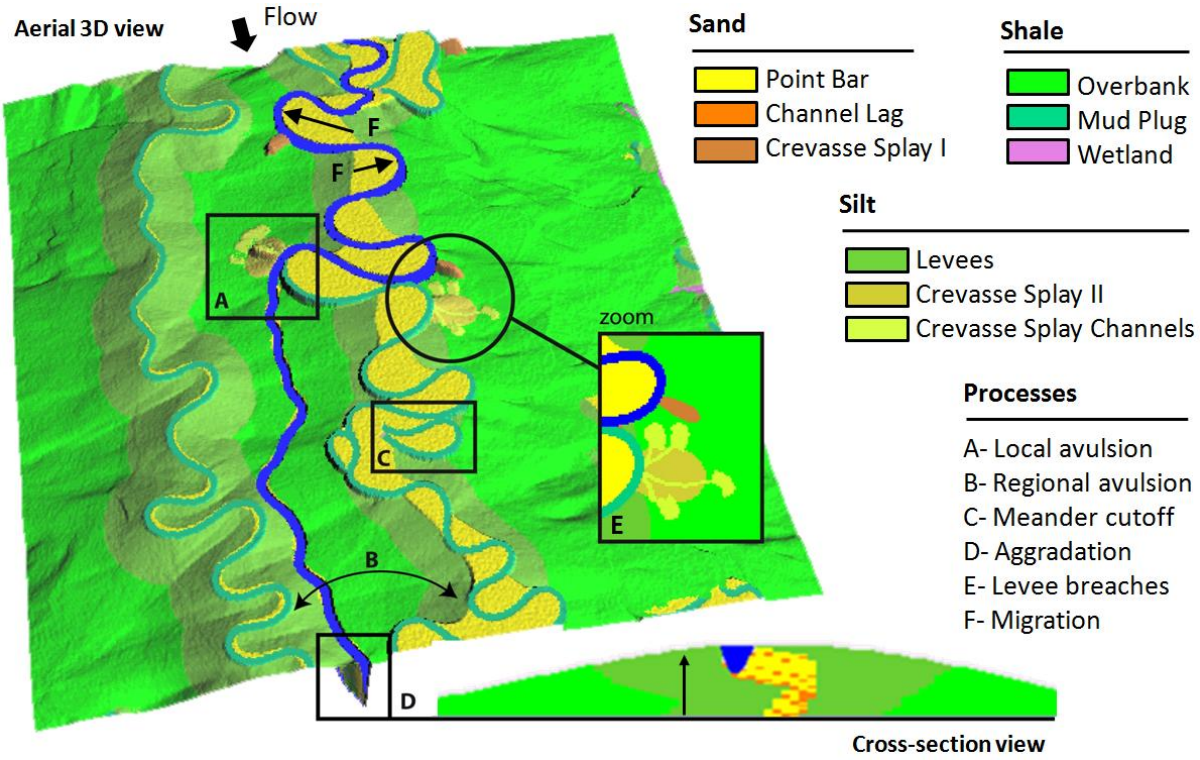

Figure 1.2: Processus et faciès simulés avec Flumy dans le cadre d'un système fluviatile méandriforme.

En complément, deux autres modules permettent d'une part de gérer les dépôts associés aux différents processus (en vert – Figure 1.3), et d'autre part de conditionner les simulations aux données (en rouge – Figure 1.3). Cette construction modulaire de Flumy lui apporte une grande souplesse puisque chaque processus est géré localement dans l'algorithme et de nouveaux processus peuvent être ajoutés relativement facilement. Néanmoins, la difficulté liée à cette organisation est de faire interagir ces différents modules. Ainsi, dans le modèle initial l'essentiel des interactions entre les processus se font via la modification de la morphologie du chenal et de la topographie issue du bloc 3D de dépôts (Figure 1.3).

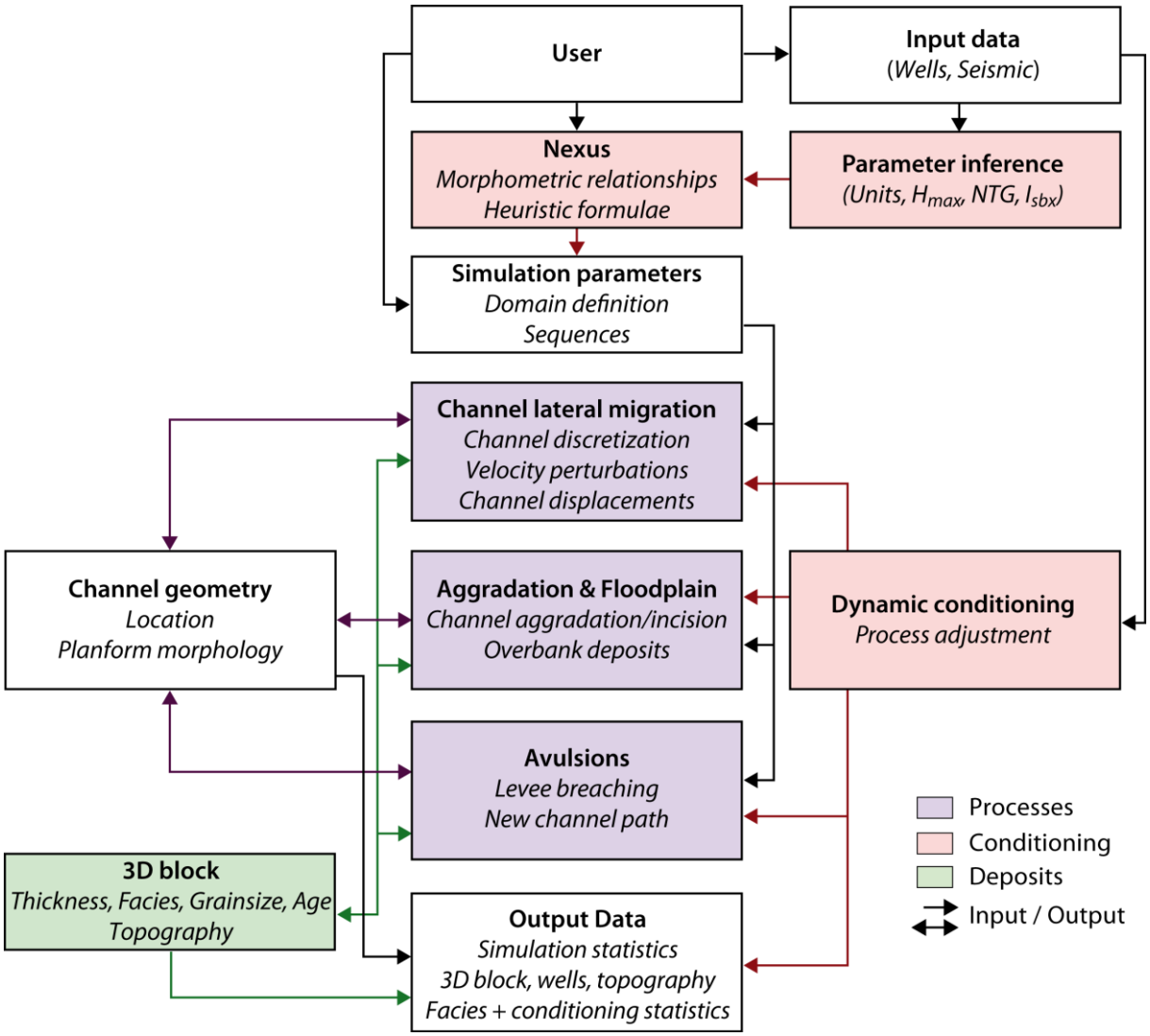

Figure 1.3 : Schéma de l'organisation modulaire de Flumy et des interactions entre chaque module. Nexus : Non-Expert User calculator, H_{max} : profondeur maximale du chenal, NTG : Net-to-Gross, I_{sbx}: indice d'extension des corps sableux.

1.3.1. Module de migration latérale du chenal

Le module de migration latérale du chenal est basé sur le modèle d'Ikeda et al. (1981) qui considère que le vecteur de taux de migration latérale ($\overrightarrow{Mig_{th}}$) est proportionnel à la perturbation de vitesse longitudinale sur la berge extérieure (U'_b) et orientée selon la normale au chenal en direction de la berge extérieure ($\vec{n}$) (Figure 1.4). Cette perturbation de vitesse correspond à la différence entre la vitesse de l'écoulement et sa moyenne (U_{mean}). Le coefficient *E* est appelé érodabilité et représente la résistance de la berge à l'érosion (i.e. plus *E* est petit, moins la berge est érodable) intégrant de nombreux phénomènes tels la composition de la berge et son degré de cohésion (Ferguson, 1987 ; Howard, 1996 ; Sun et al., 1996), ou encore la présence de végétation (Perucca et al., 2006 ; van Oorschot et al., 2016).

$$\overrightarrow{Mig_{th}} = E.U'_b.\vec{n} \quad (1.1)$$

Tandis que l'érodabilité est un paramètre défini par l'utilisateur, la perturbation de vitesse est calculée via le modèle d'écoulement de Saint-Venant en deux dimensions. Le modèle de Saint-Venant est basé sur les équations de Navier-Stockes (équations 1.2-1.4) où les grandeurs sont moyennées selon la profondeur de l'écoulement.

$$\frac{\partial \rho}{\partial t} + div(\rho.\vec{u}) = S_{(\rho)} \quad \text{(conservation de la masse)} \quad (1.2)$$

$$\frac{\partial \rho.\vec{u}}{\partial t} + div(\rho.\vec{u} \otimes \vec{u}) = \vec{S}_{(\rho.\vec{u})} \quad \text{(conservation de la quantité de mouvement)} \quad (1.3)$$

$$\frac{\partial \rho.e}{\partial t} + div(\rho.e.\vec{u}) = S_{(\rho.e)} \quad \text{(conservation de l'énergie)} \quad (1.4)$$

où ρ est la masse volumique du fluide qui s'écoule, $\vec{u}$ son vecteur vitesse, e l'énergie, et S désigne le terme source de chaque grandeur.

Le chenal est représenté par sa ligne centrale et plusieurs hypothèses concernant le fluide et l'écoulement sont inhérentes à ce modèle mais couramment admise pour les écoulements fluviatiles (Ikeda et al., 1981) :

- Fluide incompressible et newtonien
- Ecoulement permanent
- Largeur de l'écoulement constante et grande par rapport à sa profondeur
- Profil linéaire de vitesse selon la direction transverse au chenal

1.3.1.1. Calcul des perturbations de vitesse sur la berge extérieure

Les perturbations de vitesse sur la berge extérieure sont calculées le long de l'abscisse curviligne (s) du chenal selon l'équation différentielle (1.5) et dépendent de la largeur (W), de la profondeur moyenne (H_{mean}), de la vitesse moyenne (U_{mean}) de l'écoulement, ainsi que des courbures (k) de cette ligne centrale.

$$\frac{\partial U'_b}{\partial s} + 2.\frac{C_f}{H_{mean}}.U'_b = \frac{1}{2}W.U.\left(\frac{\partial k}{\partial s} - k\frac{C_f}{H_{mean}}.(F^2 + A - 1)\right) \quad (1.5)$$

où F est le nombre de Froude tel que $F^2 = \frac{U_{mean}^2}{g.H_{mean}}$, $A = A_{aff} + A_{sec}$ avec A_{aff} (= 4) le coefficient d'affouillement provenant de l'équation d'Exner (Ikeda et al, 1981) décrivant la géométrie du fond du chenal, A_{sec} (= 3) le coefficient d'écoulements secondaires introduit par Johannesson et Parker

(1989), et C_f le coefficient de friction sur le fond du chenal calculé selon l'équation suivante $C_f = \frac{2.\pi.H_{mean}}{4.\lambda.\left(\sqrt{1+0.5(A+F^2)}-1\right)}$ avec λ la longueur d'onde des méandres (Ikeda et al, 1981).

Dans le modèle initial, la pente du chenal (I_r) est considérée constante tout le long du tracé et pendant toute la simulation. Ceci a pour conséquence que la vitesse moyenne et la profondeur moyenne de l'écoulement sont également constantes tout le long du chenal et calculées comme suit :

$$U_{mean} = \sqrt{\frac{g.H_{mean}.I_r}{Cf}} \tag{1.6}$$

avec g la gravité terrestre, $H_{mean} = H_{channel}/1.5$ où $H_{channel}$ est la profondeur maximale du chenal avec le coefficient 1.5 correspondant à une section parabolique, et $I_r = I_0/2$ avec I_0 la pente de la plaine alluviale définie par l'utilisateur où 2 correspond à la sinuosité moyenne observée dans les systèmes fluviatiles méandriformes (Bridge, 2003).

1.3.1.2. Discrétisation de la ligne centrale et calcul des courbures

La ligne centrale du chenal est discrétisée en un ensemble de points, dont la distance entre chacun est maintenue comprise entre un quart et trois quarts de la largeur du chenal afin de garantir la stabilité de l'algorithme (Crosato, 2007; Schwenk et al., 2015). Cet espacement constitue l'espacement optimal d'après Crosato (2007). Au fur et à mesure que le chenal migre latéralement, sa longueur augmente, nécessitant d'ajouter des points dès lors que la distance entre ces derniers dépasse trois quarts de la largeur du chenal. Chaque nouveau point (P_{new}) est ajouté entre deux points (P_i et P_{i+1}) tel que $\overrightarrow{P_iP_{new}} = \frac{0.5W}{2}\left(\frac{\overrightarrow{P_iP_{i+1}}}{\|\overrightarrow{P_iP_{i+1}}\|} + \frac{\overrightarrow{P_iP_{i-1}}}{\|\overrightarrow{P_iP_{i-1}}\|}\right)$ (Figure 1.4) où P_{i-1} et P_{i+1} sont les points amont et aval à P_i respectivement. Au contraire, lorsque la distance entre deux points consécutifs devient inférieure à un quart de la largeur du chenal, le point aval P_i est supprimé ou remplacer par un point mieux positionné si la distance $P_{i-1}P_{i+1}$ est supérieure au seuil maximal.

L'équation différentielle (1.5) est résolue en chaque point de la ligne centrale via un schéma de différences finies décentrées amont. Le calcul de ces perturbations de vitesse dépend des courbures de la ligne centrale. Ces courbures sont calculées à partir de trois points via l'équation $k = \frac{1}{Radius}$ où *Radius* est le rayon de courbure défini selon l'équation suivante :

$$Radius = \frac{\sqrt{\overrightarrow{P_{i-1}P_i}^2.\overrightarrow{P_iP_{i+1}}^2.\overrightarrow{P_{i-1}P_{i+1}}^2}}{2.det\left(\overrightarrow{P_{i-1}P_i}\ ,\ \overrightarrow{P_{i-1}P_{i+1}}\right)} \tag{1.7}$$

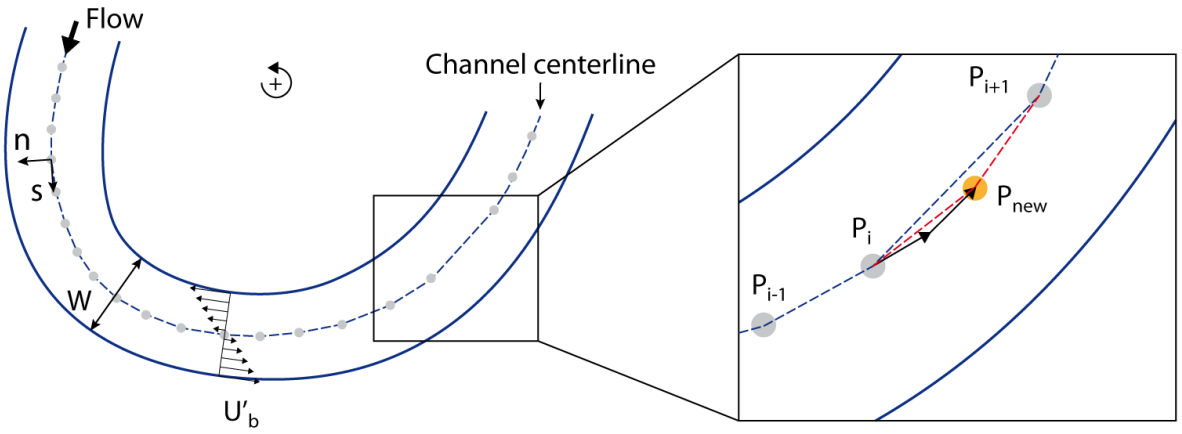

Figure 1.4: Perturbation de vitesse (U') et discrétisation de la ligne centrale. U'$_b$ est la perturbation de vitesse le long de la berge.

1.3.1.3. Autres phénomènes liés à la migration du chenal

Contrairement au modèle de base où la migration se déroule sur un plan 2D, la migration se produit ici sur une topographie 3D. Le chenal est donc régulièrement amené à migrer contre des berges plus hautes que la surface libre de l'écoulement, ce qui a pour conséquence de ralentir sa migration en raison d'une plus grande hauteur de berge à éroder. Considérant un volume à éroder constant pour un écoulement donné, ce phénomène est pris en compte dans Flumy via la correction du taux de migration latérale par le ratio entre la hauteur de la berge à éroder et la profondeur du chenal (équation 1.8, Figure 1.5).

$$\overrightarrow{Mig} = \overrightarrow{Mig_{th}} . \frac{H_{channel}}{H_{bank}} \quad (1.8)$$

Enfin, les boucles de méandre les plus développées finissent par se recouper formant un recoupement de méandre détecté par l'algorithme.

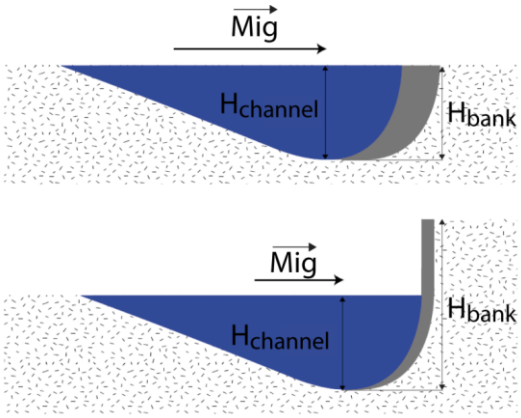

Figure 1.5 : Correction du vecteur migration ($\overrightarrow{Mig}$) par la hauteur de la berge (H_{bank}) par rapport à la hauteur de l'écoulement ($H_{channel}$). Modifié d'après Lopez (2003).

1.3.2. Module d'incision et d'aggradation du chenal et de construction de la plaine d'inondation

L'aggradation ou l'incision du chenal dans Flumy est paramétrée par une période d'occurrence des crues de débordements (T_{ob}) ainsi que de leur intensité (ou épaisseur) (i_{ob}) d'aggradation (si i_{ob}>0) ou d'incision (si i_{ob}<0). Lorsque l'incision ou l'aggradation se produit, le chenal est déplacé en moyenne d'une hauteur correspondante à i_{ob}. Dans le cas de l'aggradation, une épaisseur de dépôt (th_{ob}) égale à i_{ob} est également ajoutée aux cellules de la grille adjacentes au chenal, correspondant à la crête des levées, puis diffusée aux cellules de la grille de proche en proche en s'éloignant du chenal selon une loi exponentielle décroissante (équation 1.9) dont le paramètre de décroissance (λ_{ob}) est défini par l'utilisateur :

$$th_{ob} = i_{ob}.e^{-d/\lambda_{ob}} \quad (1.9)$$

où d est la distance entre la cellule considérée et le point du chenal le plus proche. L'épaisseur des dépôts est cependant pondérée par la topographie existante de telle sorte que les zones surélevées ne puissent pas être recouvertes de dépôts.

De plus, Flumy reproduit la formation de zones humides, correspondant aux zones d'affleurement de la nappe phréatique. Sont considérées comme zones humides les cellules dont l'altitude est inférieure à une altitude de référence. Cette altitude de référence est fixée de telle manière que la surface des zones humides représente un pourcentage du domaine simulé, ce pourcentage étant un paramètre fourni par l'utilisateur. Ces zones sont progressivement comblées par des dépôts de type lacustre, par exemple riche en matière organique.

1.3.3. Module de gestion des avulsions

Flumy simule à la fois des avulsions se produisant à l'amont du domaine de simulation, appelées avulsions régionales, et des avulsions se produisant à l'intérieur du domaine, appelées avulsions locales (Figure 1.2). Pour chacune des avulsions l'utilisateur défini une période d'occurrence (T_{avr} et T_{lvb} pour les avulsions régionales et locales respectivement) ainsi qu'une probabilité de réussite pour les avulsions locales. Les avulsions locales sont associées à des ruptures de levée conduisant au dépôt de lobes de crevasse de différents degrés d'évolution (*CSI* et *CSII*), puis, si l'avulsion réussit, à un nouveau tracé du chenal. Ces ruptures de levées se produisent préférentiellement au niveau des points du chenal de plus forte courbure et la probabilité de réussite d'une avulsion augmente dans les zones de plus fort contraste topographique entre l'altitude du chenal et celle de la plaine inondée. Dans le cas des avulsions régionales, le point d'avulsion se situe à l'amont du domaine simulé, le point d'entrée du nouveau chenal est choisi parmi les points

topographiques les plus bas. Ensuite, à partir de ce point d'entrée ou du nœud d'avulsion, le nouveau tracé du chenal est déterminé selon un algorithme de marche aléatoire dans la direction de plus grande pente (Figure 1.6). Par défaut, un quart des ruptures de levée conduisent à une avulsion locale réussie, et la répartition entre avulsions locales réussies et régionales est de 30% / 70%. La construction des lobes de crevasse et les avulsions sont considérées ici comme des événements instantanés alors qu'en réalité elles peuvent durer plusieurs années (Bridge, 2003).

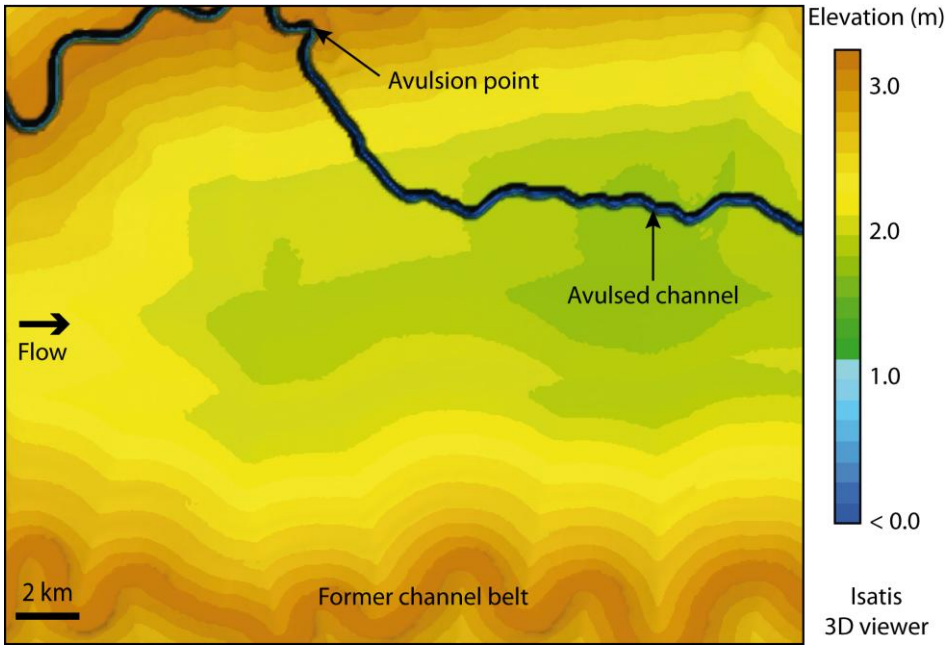

Figure 1.6 : Topographie après une avulsion locale au cours d'une simulation Flumy.

1.3.4. Module de gestion des dépôts

L'ensemble des processus sont enregistrés (Figure 1.3) sous forme de dépôts sédimentaires ou d'érosion via une *pillar grid* 2D de la taille du domaine de simulation. Les dépôts sont empilés dans chaque cellule de la grille, modifiant ainsi la topographie utilisée pour la suite des simulations (Figure 1.3). En plus de l'épaisseur des dépôts, sont répertoriés le faciès, la granularité et l'âge des dépôts. Au total 13 faciès et 16 classes granulométriques sont simulés. Les faciès sont présentés ci-après par processus et granularité décroissante (Figure 1.7).

Le faciès *Channel Lag* (*CL*), de granularité correspondant à des graviers, nappe le fond du chenal lors de son aggradation. Le facies *Point Bar* (*PB*) composé de sables moyens (Figure 1.7) est déposé en lieu et place du chenal à l'intérieur des méandres lors de sa migration latérale. Lors du processus d'avulsion, l'ancien chenal est rempli par des faciès de *Sand Plug* (SP) de la granularité des sables fins selon une épaisseur suivant une loi exponentielle décroissante en s'éloignant du point d'avulsion, et de *Mud Plug* (*MP*) (granularité des argiles) dans le reste du chenal. Les faciès de lobes

de crevasse (*CS1, CS2*) correspondent à des degrés de maturité différents de ces lobes. Leur géométrie est une ellipse dont la taille dépend de la topographie. Les lobes de type 2 (*CS2*) peuvent également voir le développement de chenaux de lobes (faciès *CCH*). La granularité de ces faciès varie des sables fins aux silts grossiers (Figure 1.7). Les dépôts de crue sont divisés sur la base de la granularité entre les faciès silteux de *Levee* (*LV*) et argileux d'*Overbank* (*OB*). La granularité de ces dépôts décroit exponentiellement en s'éloignant du chenal, tel que la limite entre les faciès LV et OB se situe à une distance du chenal donnée par l'utilisateur (en multiple de la largeur du chenal). Les faciès LV et OB sont ainsi les seuls faciès dont la granularité varie sur plusieurs classes, les autres facies ont une granularité constante (Figure 1.7). Finalement, les dépôts de zones humides correspondent au faciès *WetLand* (*WL*), et le faciès *Draping* (*DR*) permet de représenter des dépôts issus d'environnements sédimentaires différents (par exemple dans le cas d'une incursion marine).

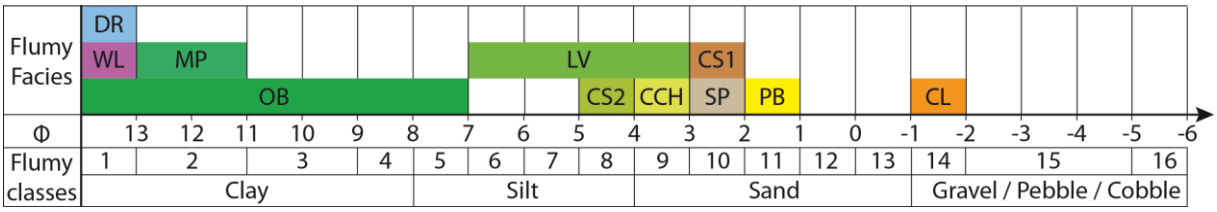

Figure 1.7 : Classes granulométriques incluses dans Flumy et distribution de la granularité pour chaque facies. CL : Channel Lag, PB : Point Bar, SP : Sand Plug, CS1 : Crevasse Splay de type 1, CCH : chenaux de lobes de crevasse, CS2 : Crevasse Splay de type 2, LV : Levees, OB : Overbank, MP : Mud Plug, WL : WetLand, DR : Draping. $\Phi = -log\ (d)$ *with d the grain siameter.*

1.3.5. Module de conditionnement

Flumy inclut un module de conditionnement aux données (Figure 1.3), permettant d'une part de déduire l'ensemble des paramètres du modèle à partir de données de puits ou d'un nombre restreint de paramètres (3 au minimum) via le *Non-Expert User calculator* (Nexus), et d'autre part de réaliser un conditionnement dynamique en cours de simulation.

1.3.5.1. Module d'inférence des paramètres et Nexus

Le Nexus permet à partir des trois paramètres seulement que sont la profondeur maximale du chenal (H_{max}), la proportion de sable (*NTG, Net-To-Gross*), et l'indice d'extension des corps sableux (I_{sbx}), de proposer un jeu complet de paramètres cohérents (Figure 1.8). Ces trois paramètres clés sont fournis par l'utilisateur en fonction des caractéristiques qu'il souhaite obtenir dans le bloc simulé, ou bien ils peuvent également être déduits directement à partir des données de puits qui sont chargées dans Flumy (Cojan et al., 2012). Ensuite, de la profondeur du chenal sont déduits notamment sa largeur et sa longueur d'onde à l'aide de relations géomorphologiques dérivées de systèmes naturels (Held, 2011) ainsi que les paramètres de migration (érodabilité). La proportion de sable permet de déterminer les paramètres d'aggradation, tandis que les paramètres d'avulsion

dépendent de l'indice d'extension des corps sableux. Le Nexus est calibré autour d'un scénario par défaut correspondant aux dimensions médianes observées dans les systèmes fluviatiles méandriformes. De plus, il existe depuis peu un outil de détection semi-automatique d'unités stratigraphiques à partir des données de puits, permettant de définir un jeu de paramètres spécifique à chacune (Bubnova et al., soumis).

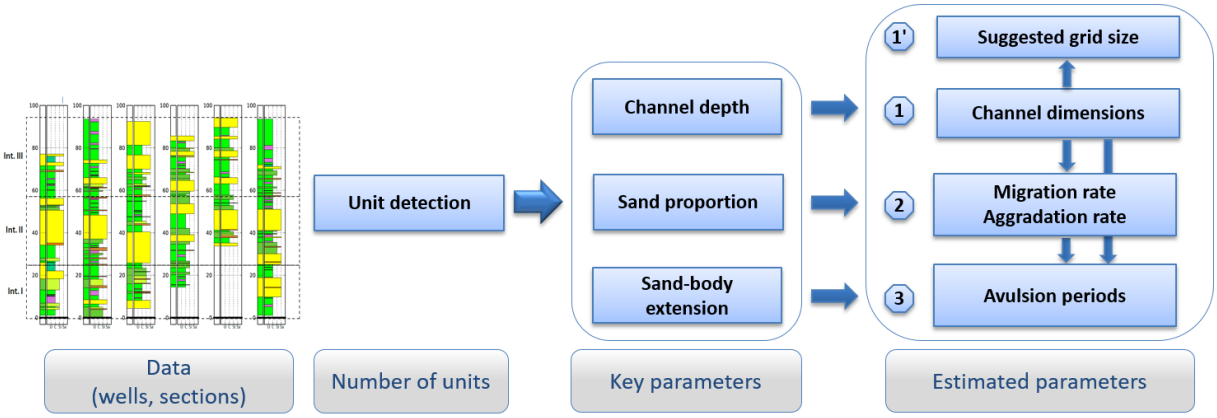

Figure 1.8 : Schéma de fonctionnement du Nexus et de l'inférence de l'ensemble des paramètres de Flumy à partir des données de puits.

1.3.5.2. Conditionnement dynamique

Le conditionnement dynamique permet d'agir sur les processus en cours de simulation afin que le bloc de faciès final respecte les données disponibles. Deux mécanismes de conditionnement existent : l'attraction / répulsion du chenal par chaque puits et l'utilisation d'une carte d'érodabilité (Emap).

Les faciès ou les variables continues décrits dans les logs de forage sont dans un premier temps convertis en faciès Flumy. Les faciès CL et PB indiquent le passage du chenal au niveau du puits, les faciès LV ou CS1/2 témoignent de la proximité immédiate du chenal, tandis que le faciès OB ou WL indique au contraire l'éloignement du chenal. En fonction des faciès voulus dans les différents puits au niveau de la topographie des dépôts simulés et dans un environnement proche du puits, la migration du chenal est maintenue telle quelle, accélérée ou ralentie via une légère pondération de ses vecteurs de migration (Bubnova, 2018). De plus, l'aggradation du chenal peut également être retardée afin d'attendre que le chenal atteigne ou s'éloigne d'un puits donné. Enfin, lors du tirage des avulsions, la topographie est virtuellement modifiée autour des puits afin de favoriser ou éloigner le tracé du nouveau chenal en fonction des faciès des puits tout en conservant l'algorithme du tracé du chenal selon une marche aléatoire dans la direction de plus forte pente (Bubnova, 2018).

L'Emap 2D ou 3D permet de définir une érodabilité variable au sein du domaine de simulation, augmentant ou diminuant localement la migration latérale du chenal et donc l'extension

des barres d'accrétion latérale sableuses. L'Emap intervient également lors du tirage des avulsions en favorisant (ou défavorisant) le passage du chenal dans les zones de fortes (ou faibles) érodabilités selon le même mécanisme de déformation virtuelle de la topographie qu'autour des puits (Rivoirard et al., 2007).

1.3.6. Conclusions

Tandis que la migration latérale du chenal qui est le principal module de Flumy, s'appuie sur une approche *process-based*, l'aggradation et l'avulsion sont modélisées via une approche *rule-based* (Pyrcz et al., 2015). Lla géométrie du chenal ainsi que celle de certains corps sédimentaires (levées, lobes de crevasse) sont régies par une approche *object-based*. De plus, de la stochasticité est incorporée dans plusieurs algorithmes tels que l'initiation de la méandrisation, le choix du nœud d'avulsion, la recherche du chemin de plus grande pente pendant les avulsions, le calcul des occurrences d'avulsion et d'aggradation selon une loi de Poisson, ou encore l'épaisseur de certains dépôts selon des lois de distribution uniformes ou normales.

De nombreux autres modèles de migration latérale du chenal ont été proposés, parfois basés uniquement sur la géométrie du chenal sans simulation de l'écoulement (Howard et Knutson, 1984), ou bien plus complexes incluant le transport de sédiments (Johannesson et Parker, 1989 ; Zolezzi et Seminara, 2001 ; Eke et al., 2014). Ces modèles aboutissent tous à des géométries de méandre statistiquement semblables à long terme notamment en raison des avulsions et recoupements de méandre réinitialisant la géométrie du chenal (Camporeale et al. 2007).

Le modèle inclus dans Flumy résulte d'un compromis entre simplification et rapidité des simulations d'une part, et complexité et reproduction de phénomènes locaux d'autre part. Les simulations montrent une bonne reproduction de l'architecture des réservoirs fluviatiles méandriformes (Lopez et al., 2008).

1.4. Modèles de systèmes turbiditiques et application à la simulation de réservoirs

Les réservoirs chenalisés turbiditiques sont classiquement modélisés via des méthodes *pixel* ou *object-based* (e.g. Strebelle et Journel, 2001 ; Duvbiama et Ikomi, 2017). Néanmoins, les simulations d'écoulement réalisées à partir de ces modèles de faciès présentent des limites en ce qui concerne leur prévision de la production, notamment en raison du manque de réalisme du modèle de faciès. Plusieurs approches *rule-based* ont ainsi été développées afin de simuler les positions successives d'un chenal turbiditique. Parmi ces approches peuvent être distinguées les approches dites *forward* (McHargue et al., 2011 ; Sylvester et al., 2016 ; Rongier et al., 2017) et celles dites

backward (Labourdette, 2008 ; Rongier et al., 2017). Les modèles *backward* simulent l'évolution d'un chenal à rebours dans le temps (Figure 1.9a), en partant de la dernière position du chenal observée par exemple à partir de données sismiques. Ces modèles sont ainsi parfaitement conditionnés à cette dernière position. Une des principales difficultés est la paramétrisation des paramètres cinématiques des chenaux. Ces modèles tendent à diminuer la sinuosité du chenal et à aboutir à un chenal rectiligne. Or l'évolution des chenaux naturels s'accompagne d'avulsions (Kolla, 2007) et de recoupements de méandres (Lonsdale et Hollister, 1979; Flood et Damuth, 1987 ; Deptuck et al., 2003 ; Babonneau et al., 2004). Les approches *backward* présentent des difficultés pour prendre en compte ces processus bien que Parquer et al. (2017) (voir aussi Parquer, 2018) aient développé une méthode afin d'incorporer de façon stochastique les boucles de méandre abandonnées (Figure 1.9a). Les modèles *forward* (McHargue et al., 2011 ; Sylvester et al., 2016 ; Rongier et al., 2017) simulent quant à eux les positions successives d'un chenal en partant d'une position et d'une géométrie hypothétique du chenal lorsque cette dernière n'est pas visible. Qu'ils soient *forward* ou *backward*, ces modèles permettent de reproduire la géométrie de corps chenalisés et leurs positions successives de façon cohérente. Néanmoins, ils sont entièrement dépendant des paramètres géométriques et l'apparition de géométries émergentes provenant d'interactions entre les règles imposées reste limitée (Hassanpour et al., 2013 ; Pyrcz et al., 2015).

Une dernière approche consiste à simuler les écoulements turbiditiques responsables de la mise en place et de l'évolution des chenaux. De nombreux modèles plus ou moins complexes en une, deux ou trois dimensions ont ainsi été proposés, tous s'appuyant sur les équations de Navier-Stokes, et pouvant inclure le transport de sédiments. Les modèles 1D ou 2D selon les directions longitudinale et verticale simulent la propagation de l'écoulement le long de la ligne centrale du chenal et leur évolution vers l'aval (Komar, 1973 ; Parker et al., 1986 ; Pirmez et Imran, 2003 ; Bolla Pittaluga et al., 2014, 2018 ; Luchi et al., 2018 ; Traer et al., 2018a). Ces modèles permettent l'étude de l'évolution de ces écoulements (profil de vitesse, hauteur) et leur caractère érosif ou constructif, par exemple en réponse à différentes conditions initiales, des variations de pente ou de lithologie du substratum. Traer et al. (2018a, b) ont notamment mis en évidence l'importance du débordement des écoulements dans le maintien d'un débit constant malgré l'entrainement d'eau ambiante et de sédiments. Luchi et al. (2018) ont montré que sous des conditions de flux nets de sédiments nuls entre l'écoulement turbiditique et le substratum, la stratification de l'écoulement conduit à la formation d'une couche basale concentrée motrice et d'une couche supérieure diluée entraînée par la première. De plus, des modèles 2D dans les directions longitudinale et transverse au chenal, permettent notamment de calculer les taux de migration latérale du chenal (Imran et al., 1999 ; Sylvester et al., 2011 ; Das et al., 2004). Ces modèles peuvent inclure un profil transverse de vitesse

simplifié (Imran et al., 1999 ; Sylvester et al., 2011), ou bien résoudre les équations de Navier-Stokes directement en 2D, en moyennant l'écoulement sur la verticale (Das et al., 2004). Ces derniers permettent ainsi de capturer davantage la complexité des écoulements en réponse à la morphologie du chenal. De plus, via l'ajout des équations de transport des sédiments, ces modèles calculent la position des dépôts dans le chenal ainsi que leur architecture interne (Figure 1.9b). Enfin, la dimension verticale des écoulements peut être prise en compte soit via l'ajout d'un profil vertical (Dorrell et al., 2014; 2017), soit via la résolution en 3D des équations de Navier-stokes. Ces modèles 3D permettent de simuler l'ensemble des processus contrôlant l'évolution des écoulements vers l'aval (Kassem et Imran, 2004 ; Imran et al., 2004 ; Meiburg et Kneller, 2010 ; Giorgio Serchi et al., 2011 ; Huang et al., 2005 ; Cantero et al., 2007 ; Abd El-Gawad et al., 2012 ; Ezz et Imran 2014 ; Meiburg et Nasr-Azadani, 2018) et d'étudier leur structure 3D (Figure 1.9c) et notamment l'orientation des écoulements secondaires (Corney et Peakall, 2006 ; Giorgio Serchi et al., 2011 ; Ezz et Imran 2014 ; Dorrell et al., 2017), ou encore leur propagation sur tous types de topographie et non plus seulement au sein de chenaux (Meiburg et Nasr-Azadani, 2018).

Plus ces modèles sont complexes, plus ils demandent des ressources informatiques importantes (Janocko et al., 2013). Les modèles résolvant les équations de Navier-Stokes en 2D ou 3D ne conviennent donc pas à la simulation de réservoirs turbiditiques de plusieurs dizaines de mètres d'épaisseur. Cependant, une approche intéressante vise à simuler la propagation des écoulements via le principe de conservation des énergies (Salles et al., 2007 ; Albertao et al., 2015 ; Teles et al., 2016), permettant de simuler en quelques minutes des dépôts de quelques mètres d'épaisseur et donc rendant leur application à la simulation de réservoirs envisageable (Figure 1.9d). En revanche, aucun modèle précédemment cité ne reproduit simultanément en 3D les principaux processus en jeu dans les systèmes turbiditiques que sont la migration latérale du chenal, son aggradation, ou les avulsions associées à la formation de lobes de crevasse.

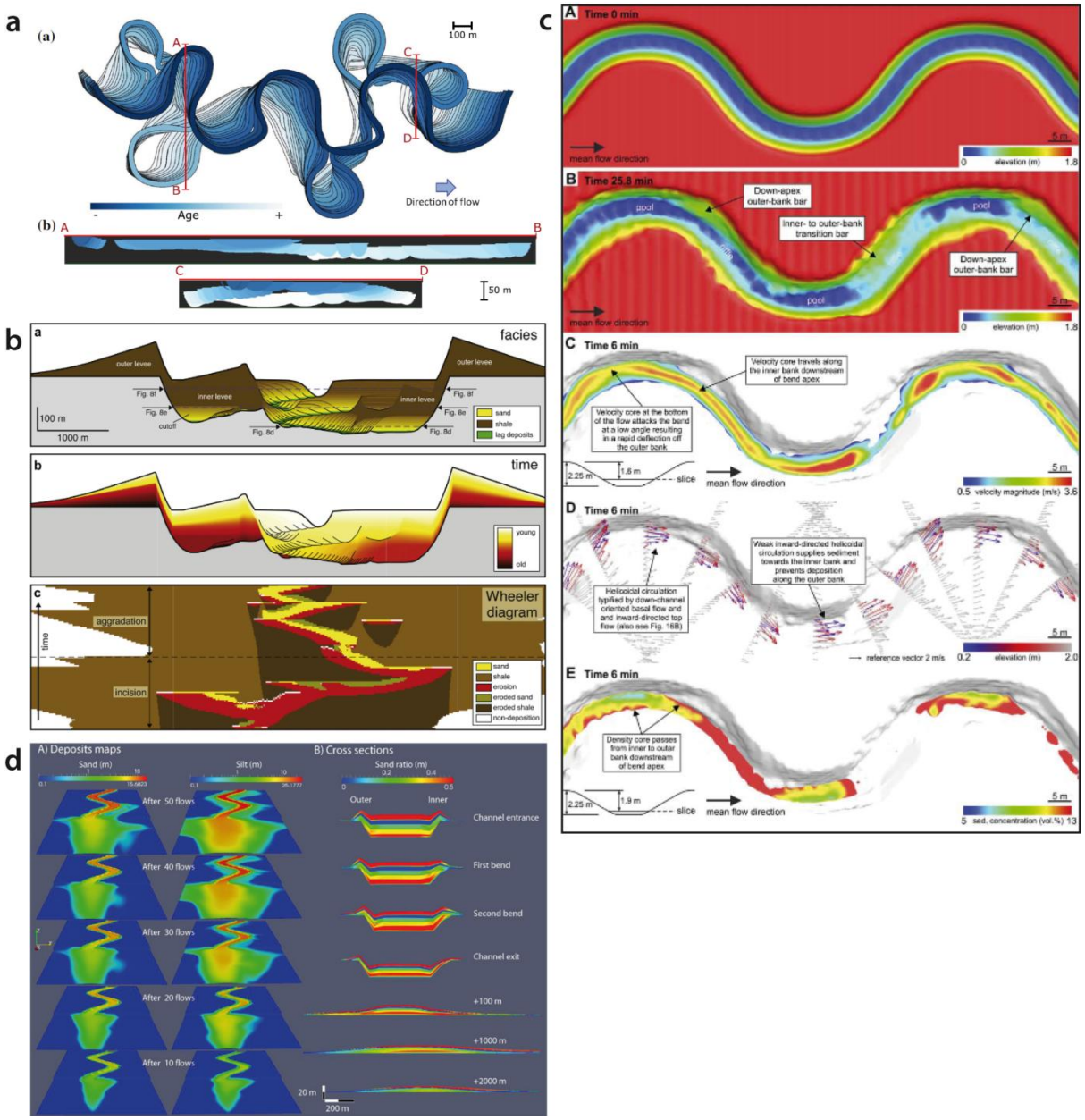

Figure 1.9 : Modèles de réservoirs turbiditiques (a) backward et rule-based (Parquer et al., 2017), et forward et process-based : (b) incluant les déplacements latéraux et verticaux du chenal (Sylvester et al., 2011), (c) simulation CFD (Computation Fluid Dynamic) dans un chenal à petite échelle (Janocko et al., 2013), (d) modèle CATS (Teles et al., 2016).

1.5. Conclusions

Le type et la géométrie des réservoirs fluviatiles méandriformes et chenalisés turbiditiques diffèrent fortement. Les réservoirs fluviatiles sont formés par l'amalgamation des barres de méandre et les barrières d'écoulement sont créés par des drapages argileux internes et les méandres abandonnés. Les réservoirs turbiditiques sont quant à eux formés par l'amalgamation des corps chenalisés au sein de systèmes confinés, et/ou par les dépôts silto-sableux au sein des levées, avec de fortes hétérogénéités internes. L'élaboration d'un modèle opérationnel de réservoir turbiditique

passe donc par sa capacité à simuler l'incision puis le remplissage de vallées d'une part, et d'autre part la géométrie et l'architecture des levées. Une description précise de la granularité des dépôts responsable des hétérogénéités internes aux réservoirs est également nécessaire pour les réservoirs turbiditiques.

Flumy est un modèle de réservoir qui répond aux attentes de l'industrie quant son utilisation dans un cadre opérationnel que sont notamment une paramétrisation dépendante de données disponibles tels les puits ou les données sismiques, un conditionnement à ces dernières, un temps de calcul réduit, et la stochasticité des simulations. Le modèle fluviatile de Flumy constitue donc un point de départ intéressant pour la simulation des systèmes turbiditiques en raison de l'analogie géomorphologique entre ces systèmes, bien que des différences notables quant aux dimensions des chenaux et les relations entre les paramètres morphométriques aient été constatées. En outre, tous les modèles d'écoulements turbiditiques montrent l'importance de prendre en compte la structure 3D de ces écoulements ainsi que le transport des sédiments, afin de capturer les processus influant sur la migration du chenal et l'aggradation du système. Ces processus incluent notamment la super-élévation de l'écoulement à l'extérieur des méandres impactant la géométrie des levées, ou le transport des sédiments contrôlant la granularité des dépôts. Ainsi, l'étude précise des similitudes et différences est nécessaire afin de réaliser la transposition de Flumy aux systèmes turbiditiques.

Chapitre 2.

Geomorphic variability of submarine flow pathways along continental margins: comparison with fluvial meandering channels

Abstract

Understanding submarine flow pathways (FP) is a challenging task given its applications in offshore industries and source-to-sink studies. Despite flow structure dissimilarities, sinuous submarine threads display morphologies similar to alluvial meandering rivers. An extensive quantification of degrees of (dis)similarity is however lacking. This study combines (a) a new geomorphic classification of FP with (b) measurements of planform (sinuosity, wavelength, amplitude) and cross-sectional (width, area, depth) parameters to compare alluvial meandering and submarine systems. We apply the methods to a worldwide dataset of 341 measurements in both modern and fossil settings. We identify six types of FP including composite (i.e., canyon and valley) and unit (i.e., channel – whether incised or leveed and confined or unconfined) types. We find that (i) FP geomorphology is strongly controlled by their location along the continental margin, composite FP being located on the continental slope and unit channels extending down to the basin floor. (ii) Submarine unit leveed channels (LC) form a consistent group of smaller-size and more laterally mobile FP. (iii) These are the most analogous to alluvial meandering rivers. (iv) Without discharge contribution from tributaries, long-running submarine flows width and area increase as they migrate towards the abyssal plains. Such behavior is similar to rivers, although it is better explained for submarine FP by progressive flow deconfinement and loss of bank cohesion.

2.1. Introduction

Submarine channelized systems are the final links of the source-to-sink sediment transfer chain (Allen, 2017). They extend over the entire submarine environment from the shelf to the abyssal plain and act as the main sediment pathways from continent to deep-sea basins (Figure 2.1 – Shepard, 1963; Mutti and Normark, 1991; Stow and Mayall, 2000; Deptuck et al., 2007; Wynn et al., 2007). The interest in these channelized systems is constantly growing because they create large hydrocarbon fields (Weimer and Slatt, 2004) and may impact offshore facilities such as hydrocarbon production platforms, pipelines, telecommunication cables, wind power plants, or –in the near future – deep water mining apparatus (Baker et al., 2016). One aim is therefore to constrain the evolution of these systems to improve their modeling.

Despite recent progresses on in-situ flow measurements (Azpiroz-Zabala et al., 2017a; Paull et al., 2018), our understanding of the long-term (10^{2-4} yr) evolution of submarine density flows and associated deposits is still incomplete (Mulder and Alexander, 2001; Peakall and Sumner, 2015; Jobe et al., 2017; Leeuw et al, 2017; Ono and Plink-Björklund, 2018). Due to limited monitoring of submarine flow pathways (FP) evolution, a common approach is the adaptation of the better-constrained fluvial processes. Physical processes at play at the scale of the full turbidity current profile are incontestably different from that of rivers (Wynn et al., 2007 and references therein) – e.g., due to the role of sediments as flow driver (Parker et al. 1986; Konsoer et al., 2013; Traer et al., 2018a), flow stratification (Dorrell et al., 2014; Azpiroz-Zabala et al., 2017a; Luchi et al., 2018), friction at flow upper interface (Konsoer et al., 2013), water entrainment (Ellison and Turner, 1959; Pirmez and Imran, 2003; Traer et al., 2018b), flow overspill and stripping (Peakall et al., 2000; Traer et al., 2018a, 2018b), or variations in secondary currents (Azpiroz-Zabala et al., 2017b; Dorrell et al., 2018). However, similarities of planform morphology and geomorphic features suggest that a transposition of fluvial processes to submarine flows may be envisioned – especially to features associated with the deeper part of flow (Lonsdale and Hollister, 1979; Flood and Damuth, 1987; Miall, 1989; Leeder, 1999; Wynn et al 2007). Indeed, both fluvial and submarine FP display braid bars (Hesse et al., 2001; O'Cofaigh et al., 2006; Foreman et al., 2015), lateral accretion deposits (Abreu et al., 2003; Arnott, 2007), bend cutoffs, levees or crevasse splays (Figure 2.1 – Posamentier, 2003; Wynn et al., 2007), which suggest comparable origins. This is especially true at the large scale, where process-based theory may be used in both environments for comparison – e.g., the braiding-sinuous threshold (Foreman et al., 2015) or the channel mobility number (Jobe et al., 2016).

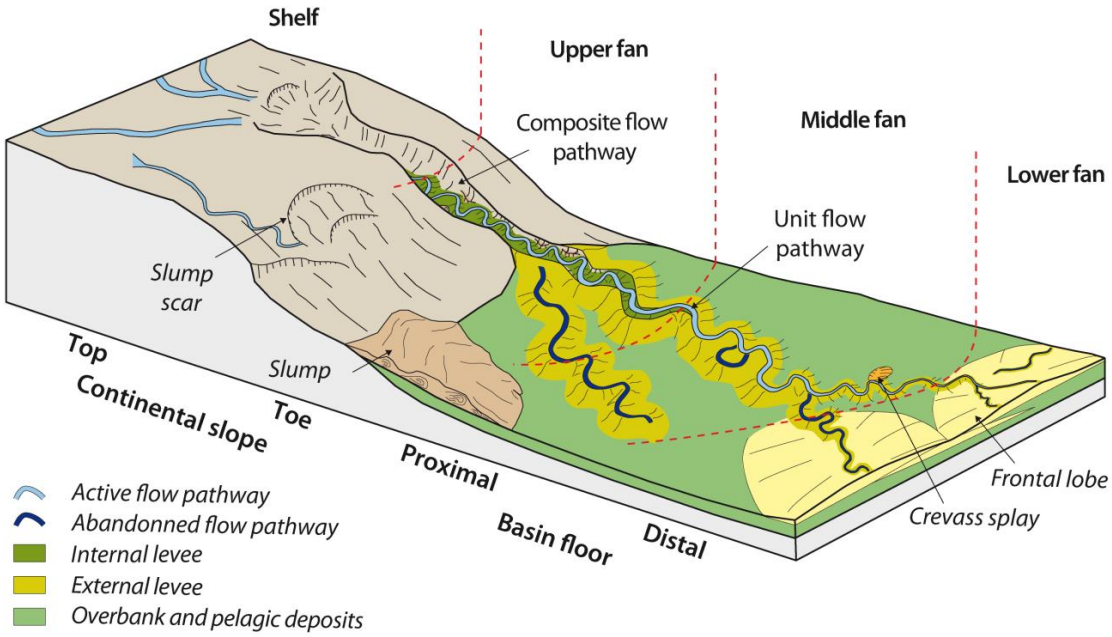

Figure 2.1: Channelized submarine systems with the submarine environment subdivision used in this study.

Geomorphic parameters are useful markers of fluvial channel pattern and behavior (Bridge 2003 and references therein; Gleason, 2015; Blom et al., 2017; Métivier et al., 2017). It has indeed be proposed that channel planform morphology (sinuosity, wavelength, amplitude) (e.g. Jefferson, 1902; Friedkin, 1945; Leopold and Wolman, 1960) or cross-sectional morphology (bankfull width, depth) (Leopold and Wolman, 1960; Williams, 1986; Bridge and Mackey, 1993) may be related to river dynamics (e.g., slope, flow or sediment discharge; Leopold and Wolman 1957). Such approach would have promising applications in submarine systems. For example, the larger size of submarine FP compared to river channels may be explained theoretically, by the lower density contrast between the current and the ambient fluid (Flood and Damuth, 1987; Clark and Pickering, 1996; Pirmez and Imran, 2003; Limaye et al, 2018; Shumaker et al., 2018). Accurately assessing the scale of submarine FP is however still a challenge because, contrarily to fluvial systems where survey methodology is well defined (USGS methodology, see Sauer and Turnipseed, 2010), there is no standard procedure. This results in estimations that vary by factor of 2-3 depending on available data and authors (Pirmez and Imran, 2003). For example, flow super-elevation at outer bends that can reach 80% of the flow mean height (Imran et al., 1999) is responsible for submarine levee asymmetry (Peakall et al., 2000; Jobe et al., 2016), and then FP depth can dramatically change depending on measurement procedure. The lack of accuracy of current nomenclatures (Wynn et al., 2007) as well as the scarcity of data – which mostly come from indirect observations using incomplete outcrops, multibeam bathymetry, sonar and seismic data of multiple resolution – brings further variability and uncertainties to submarine datasets.

In this study, we compare modern and fossil submarine FP to free migrating alluvial rivers, by developing (i) a classification based on geomorphic elements and (ii) a survey methodology comparable with the fluvial one. This methodology is applied to a set of ancient and modern submarine systems based on published data. This allows us to compare the variability of FP dimensions and morphology in between the different classes and discuss analogies with fluvial meandering channels.

2.2. Quantitative parameters for alluvial meandering systems

In the following, we describe the existing hydraulic relationships for rivers, which represent powerful tools that can be applied to different purposes. In hydraulic engineering and restoration projects, engineers are able to adjust channel geometry by monitoring flow and sediment discharges (e.g. Kondolf, 2016 and references therein). In paleo-hydrologic studies, a full description of the geometry of the paleo-channel and the formative hydraulic conditions can be inferred from observed relicts of this channel (William, 1978, 1986; Brigde, 2003 and references therein; Held, 2011; Ghinassi et al., 2014). Changes in channel morphology are used to retrieve climate or physiographic condition variations (Rotnicki, 1991; Leigh and Feeney, 1995; Sidorchuk et al., 2001). Last but not least, geometrical relationships are input parameters for reservoir object-based models (Tye, 2004; Pyrcz et al., 2015; Rongier et al., 2017) or process-based models (Bridge and Mackey, 1993; Heller and Paola, 1996; Lopez et al., 2008).

Relationships between geometrical parameters depend on physiographic conditions and climate (Bridge 2003). Several studies showed that all river geometric parameters are correlated to the flow discharge (Leopold and Maddock, 1953; Dury, 1976; Williams, 1978; Métivier et al., 2017). As a result, Leopold and Maddock (1953) introduced the concept of *bankfull hydraulic geometry*, which is considered to be the result of the “dominant discharge” – often named the channel forming discharge (Wolman and Miller, 1960; Copeland et al., 2000). This simplification of the effects of a succession of varying natural flows by a series of steady events is still criticized but explains most of the processes acting on channel-equilibrium geometry even for rivers under variable regimes (Blom et al., 2017; Billi et al., 2018). This concept thus particularly applies to rivers of relatively steady flow regimes such as those of humid climatic regions, where a temporary geometry of the channel resulting from extreme events is rapidly reshaped due to the effectiveness of the short to medium return period events (Wolman and Miller 1960; Johnson and Fecko 2008; Held, 2011; Blom et al., 2017).

How to measure river geometry has been extensively discussed until a robust methodology was defined. The river path is often described by its centerline. A meander corresponds to two consecutive bends (Figure 2.2; Leopold and Wolman, 1960). Planform morphology is usually characterized at the scale of the stream reach (sinuosity) or meander/bend (wavelength, amplitude) (Leopold and Wolman, 1960; Schwenk et al., 2015). At the scale of the stream, sinuosity is defined as the ratio between the length of the centerline and the sum of the distances between the inflexion points between the two ends points of the studied reach (blue curve in Figure 2.2a) (Allen, 1984). Stream slope or gradient corresponds to the difference in elevation between the two end points of the studied reach divided by the length of the centerline. At the scale of the meander, meander wavelength λ is the Euclidian distance between the upstream and downstream inflexion points of the meander (Figure 2.2b). The meander amplitude $A_{meander}$ is taken as the distance between the apex of the meander and the middle of the segment that links the upstream and downstream bend apexes (Figure 2.2b). Bend apex corresponds to the maximal absolute curvature. At the scale of the bend, metrics are the bend length L_{bend}, defined as the distance between the two inflexion points of the bend, and the bend amplitude A_{bend} defined as the distance between the bend apex and the middle of the segment that links the inflexion points of the bend. On average, bend metrics are half the meander ones.

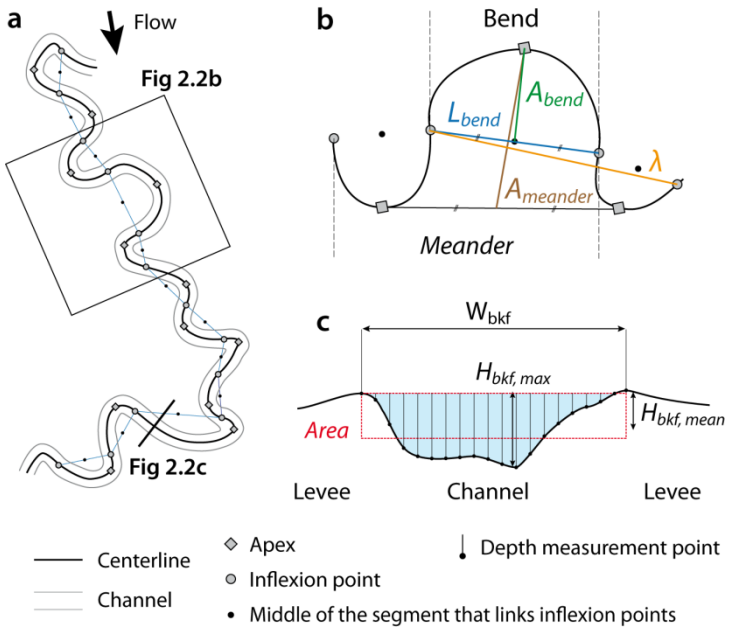

Figure 2.2: River planform morphology definition and methodology of measurement at the scale of the stream reach (a), at the scale of meander and bend (b) and at the scale of a cross-section (c). λ: wavelength, L_{bend}: bend length, $A_{meander}$: meander amplitude, A_{bend}: bend amplitude, W_{bkf} bankfull width, $H_{bkf,\ mean}$: mean bankfull depth, $H_{bkf,\ max}$: maximal bankfull depth. River path inspired by Red River from Google Earth.

River cross-sectional parameters (bankfull width, mean and maximal bankfull depths, cross-sectional area) are measured at gauging stations or ungauged reaches along relatively straight and uniform reaches generally devoid of unusual riffles or bars (USGS methodology, see Sauer and Turnipseed, 2010). Channel cross-sectional parameters are measured at the bankfull stage which corresponds to the maximal discharge that a channel can contain before overbank flooding (Leopold and Wolman, 1957; Bridge, 2003). The channel bankfull width W_{bkf} is taken as the distance between the top of the point bar and/or the levee crests (Figure 2.2c; Williams, 1978; Sweet and Geratz 2003). The channel maximal bankfull depth $H_{bkf,max}$ is the difference in elevation between the deepest channel point and the elevation of the bankfull water surface in the surveyed section (Figure 2.2c). It is dependent of the channel curvature and the occurrence of riffles and pools. The channel mean bankfull depth $H_{bkf,mean}$ is calculated by dividing the cross-sectional area by the bankfull width (Figure 2.2c). It corresponds to the height of a rectangular section of the same width and area as the channel section.

Table 2.1: Example of fluvial geometric relationships.

Parameter	Power law	R^2	Sinuosity
Meander wavelength (λ) to meander amplitude ($A_{meander}$)			
Leopold and Wolman (1960)	$\lambda = 4.04\ A_{meander}^{1.0}$	NA	NA
Williams (1986)*	$\lambda = 2.23\ A_{meander}^{1.0}$	0.98	> 1.3
Meander wavelength (λ) to bankfull width (W_{bkf})			
Leopold and Wolman (1960)	$\lambda = 10.9\ W_{bkf}^{1.01}$	NA	NA
Williams (1986)*	$\lambda = 7.5\ W_{bkf}^{1.12}$	0.92	> 1.3
Meander wavelength (λ) to mean bankfull depth ($H_{bkf,\ mean}$)			
Williams (1986)	$\lambda = 240\ H_{bkf,\ mean}^{1.52}$	0.74	> 1.3
Meander amplitude ($A_{meander}$) to bankfull width (W_{bkf})			
Leopold and Wolman (1960)	$A_{meander} = 2.7\ W_{bkf}^{1.1}$	NA	NA
Williams (1986)*	$A_{meander} = 3.14\ W_{bkf}^{1.10}$	0.92	> 1.3
Meander amplitude ($A_{meander}$) to mean bankfull depth ($H_{bkf,\ mean}$)			
Bridge Mackay (1993)	$A_{meander} = 192\ H_{bkf,\ mean}^{1.37}$	0.65	> 1.0
Channel bankfull width (W_{bkf}) to mean bankfull depth ($H_{bkf,\ mean}$)			
Williams (1986)	$W_{bkf} = 21.3\ H_{bkf,\ mean}^{1.45}$	0.66	> 1.3
Williams (1986)	$W_{bkf} = 15.5\ H_{bkf,\ mean}^{1.4}$	0.60	> 1.7
Bridge and Mackey (1993)	$W_{bkf} = 8.9\ H_{bkf,\ mean}^{1.82}$	0.60	> 1.0
Held (2011)	$W_{bkf} = 10.9\ H_{bkf,\ mean}^{0.93}$	0.73	> 1.5

* Derived from combined equations.

Many studies on meandering fluvial systems have identified relationships – mostly power laws – between the geometrical (Table 2.1) and hydraulic parameters of rivers (Leopold and Wolman, 1960; Williams, 1986; Bridge and Mackey, 1993; Held, 2011). Relationships are more robust when expressed as a function of the meander amplitude or channel bankfull width rather than using mean bankfull depth – as highlighted by the correlation coefficients (Table 2.1). The variability observed in the proposed relationships is in part related to differences of databases and fitting methods (discussion in Williams, 1986) (Table 2.1).

2.3. Material and methods

2.3.1. A worldwide dataset of modern and fossil submarine systems

In order to build an extensive dataset, we compiled data from more than 80 papers, and obtained 341 measurements from both modern (266) and fossil (75) submarine systems (Figure 2.3a, see Annex A). Special attention was paid to collect data from a large range of latitude (from -45° for the Bounty fan to +65° for the Lofoten basin), or tectonic settings (17.3% from active margins and 82.7% from passive margins of different types according to the classification of Wetzel (1993)) (Figure 2.3). Studied systems comprised very large to middle size submarine systems such as the Indus or the Magdalena fans, and small ones like the Golo fan or the Rupert Inlet system. The systems are fed by a wide range of sediment sources with varied mechanisms initiating the flows, i.e., deltas (62%), estuaries (18%; e.g. Congo fan), directly the shelf (13%; e.g., Navy fan), and even glaciers (3.5%; i.e., NAMOC and Surveyor Channel). The sediment load may be muddy (58.7%; e.g., Amazon or Mississippi fans), sandy (20.5%; e.g., La Jolla fan or the Cascadia system) or mixed (19.6%; e.g., Rhone or Nile fans) (Figure 2.3b).

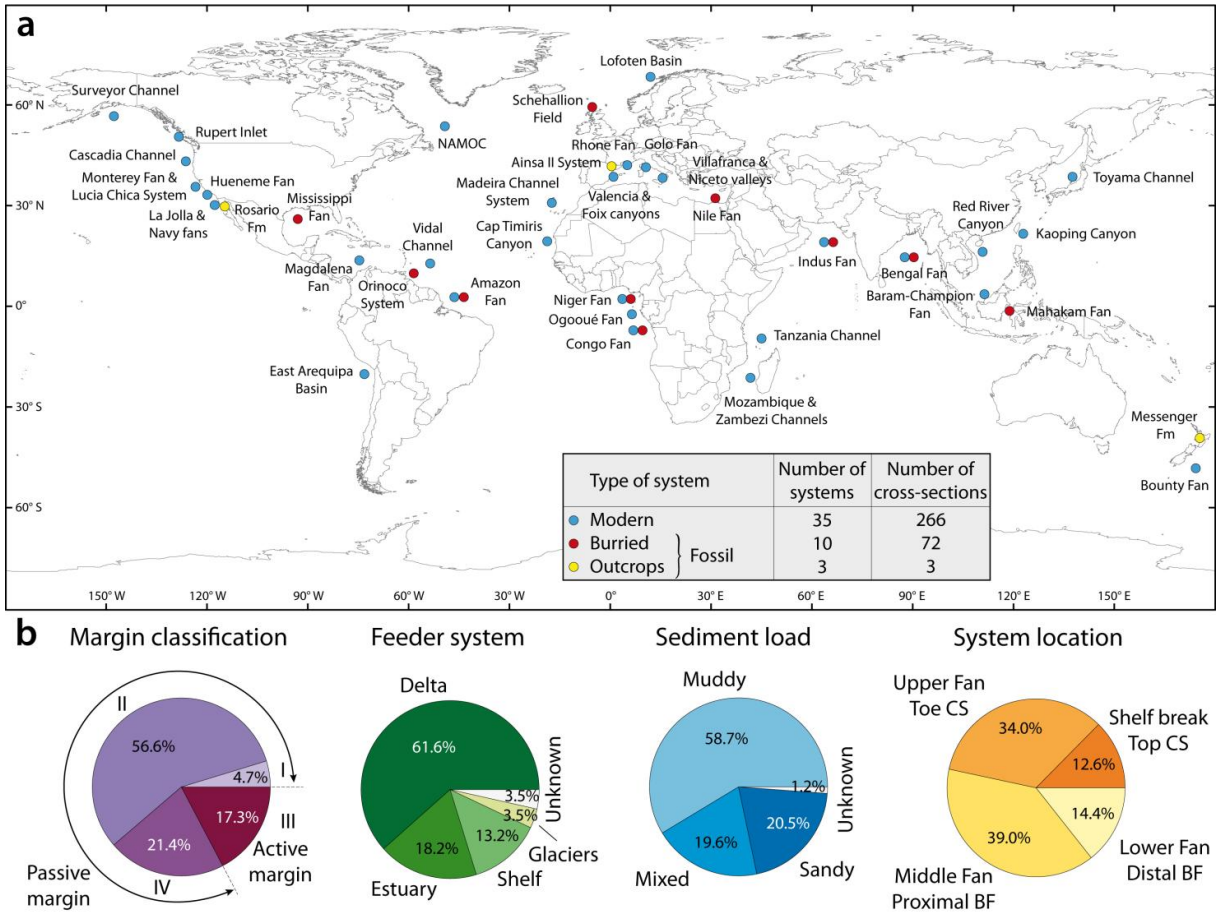

Figure 2.3: Location of sampled submarine systems (a). Repartition of submarine systems according to: margin classification (Wetzel, 1993), feeder system, sediment load grain size and system location

(b). CS: continental slope, BF: basin floor, I: immature passive margin, II: mature passive margin, III: active margin, IV: passive margin with active hinterland.

The majority of the sampled FP comes from submarine fans (59.3%) but 41.7% are from isolated FP such as NAMOC or the Tanzania Channel. Four marine environments are represented, based on the location relatively to the continental slope: (i) the top of the continental slope (or shelf break zone), (ii) the toe of the continental slope (or upper fan), (iii) the proximal basin floor (usually middle fan), and (iv) the distal basin floor (or lower fan) (Figures 2.1, 2.3b and 2.7a). This submarine environment zonation applies for both turbidite fans and isolated FP.

2.3.2. Submarine flow pathway geomorphic classification

Submarine FP from the dataset were sorted out into a classification based on the observed geomorphic features, allowing us to define six types of pathways according to three criteria (Figure 2.4). The first criterion is the occurrence or absence of levees flanking the FP. Absence of levees corresponds to purely erosional confinement (i.e., as shown on seismic or sonar cross sections) (Normark, 1970; Fildani et al., 2013; Weill et al., 2014), while the presence of levees indicates partly or fully constructional FP (Normark, 1970; Wynn et al., 2007; Straub and Mohrig, 2008). The second criterion is the presence of smaller confined FP within the considered FP, which allows distinguishing *composite* from *unit* FP (Figure 2.4). These two criterions enable the identification of two classical composite FP (canyons without flanking levees and valleys bordered with levees) and two unit FP (leveed channels and incised channels) (Figure 2.4). Note that incised channels located on the shelf break are considered as canyons. This is consistent with unconfined incised channels located on the top of the continental slope being classically considered as “canyon” in the literature – where it is shown that they experienced multiphase history (Wynn et al., 2007 and references therein). The last criterion is whether unit FP are confined within a larger FP, which conversely allows distinguishing isolated FP. Note that these three criteria may be applied to rivers, which eases the comparison between fluvial and submarine systems.

Based on these three criteria, two groups comprising six types of FP were identified (Figure 2.4): Leveed FP may be either composite (valleys) or unit (confined (CLC) or unconfined (ULC) channels). Incised FP may be either composite (canyons) or unit (confined (CIC) or unconfined (UIC) channels). Incised channels (IC) may be used to indicate indistinctively CIC or UIC, and leveed channels (LC) for CLC and ULC.

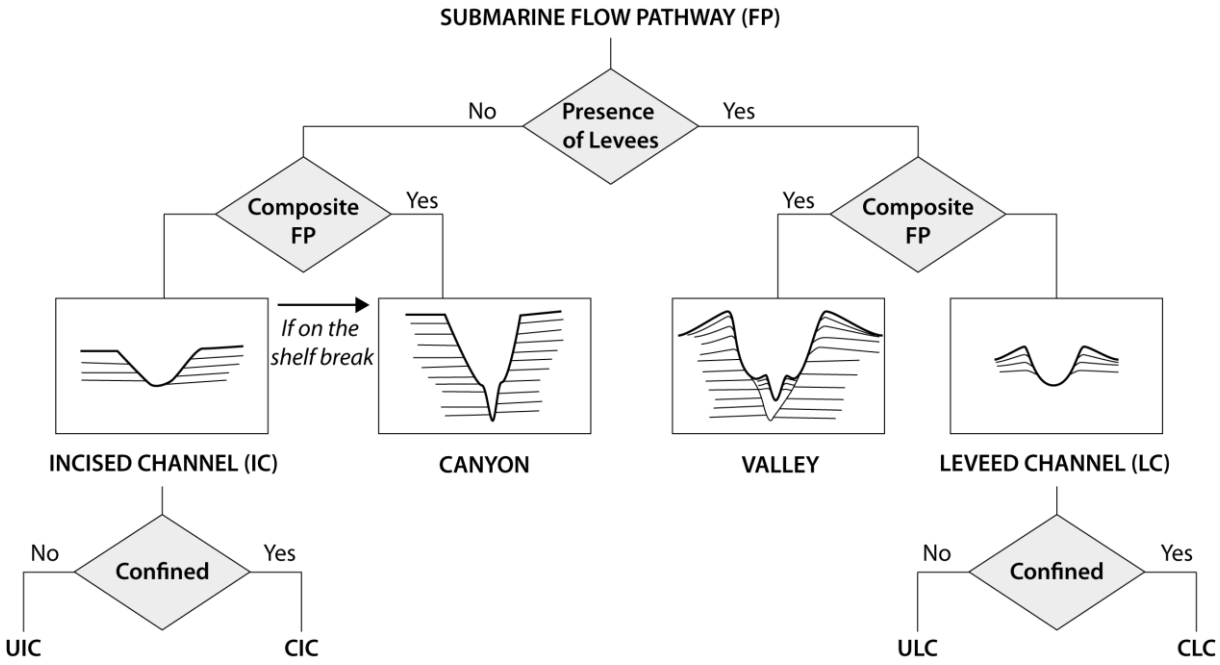

Figure 2.4: Classification of the submarine FP (CIC: Confined Incised Channel, UIC: Unconfined Incised Channel, CLC: Confined Leveed Channel, ULC: Unconfined Leveed Channel).

2.3.3. Measurement of hydraulic parameters of submarine flow pathways

In order to compare our dataset with alluvial meandering systems, we developed a method – adapted from river surveys – that allowed consistent measurements from both modern and fossil submarine FP. We used seafloor, seismic, sonar and outcrop data. Modern bathymetric (sonar or shallow seismic) surveys provide accurate seafloor depth profiles where the vertical resolution is less than one to few meters. Buried fossil submarine systems are imaged by seismic surveys. The seismic vertical resolution (most often more than 10 meters) is far lower than that of sonar surveys, with further uncertainties in the time-to-depth conversion. For each dataset, we applied time-to-depth conversion using seismic velocity given in the publication when needed. Outcrops surveys (Ainsa II, Messenger and Rosario formations) are accurate but laterally and vertically limited. Note that we did not take into account burial and compaction history for fossil systems (30% of our dataset) which may impact vertical dimension measurements. Hence, one should keep in mind that despite our carefulness, data contain uncertainties, but this is inherent to large datasets and does not preclude the identification of major trends.

Digitalization of the centerline was the first step of the characterization of the planform morphology of submarine FP. Centerline was defined as the middle line of the pathway (Figure 2.5a), which were often interpreted in published data. For modern systems, the FP contours were delimited by the slope break observed at the top of levees (when present) or along the substrate. In buried systems, FP is marked by the interruption of flat reflectors on the edges, and is often associated with

a contrast of amplitude with surrounding reflectors (Figure 2.6). During digitalization, centerline point longitudinal spacing was on average equal to one quarter of the FP width. The curvature at a given point was taken as the inverse of the radius of curvature of the circle passing through: the given point, as well as the third point upstream and the third points downstream from the given point. Such spacing enabled stabilizing the curvature value by increasing the arc length. Inflexion points (Figure 2.5a) were defined as changes of sign of the curvature along the digitalized centerline. Centerline spatial parameters were computed using inflexion points and maximum curvature points. At the scale of the bend, the bend length L_{bend} corresponded to the segment length between two consecutive inflexion points (Figure 2.2b). Bend apex was chosen by maximizing the bend amplitude A_{bend} among the 5 points with the highest curvatures in order to avoid some discrepancy due to picking. Bend amplitude was defined as the distance between the apex and the middle of the segment joining inflexion points (Figure 2.2b). Bend amplitudes were discarded when lower than one tenth of the bankfull width.

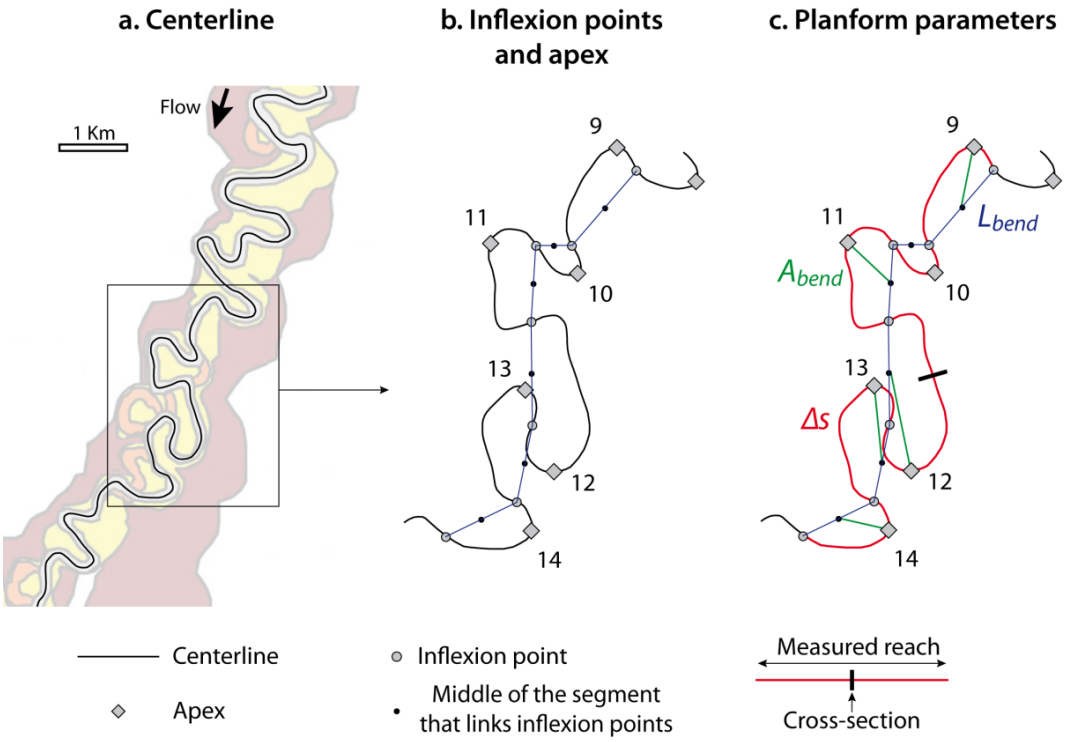

Figure 2.5: Planform geometry measurements. The sinuosity is equal to the ratio of the curvilinear length Δs to the sum of the bend length L_{bend} over the measured reach. A_{bend}: bend amplitude. FP example is from Abreu et al. (2003).

For each studied reach, mean bend length L_{bend}, bend amplitude A_{bend} and *sinuosity* are computed along a centerline length Δs equal to 20 times the FP width (Figure 2.5c) that allows sampling on average eight bends. *Sinuosity* is computed similarly to fluvial systems (see section 2.1; Allen, 1984) as the ratio between the curvilinear distance along the studied reach and the sum of the

associated bend lengths. FP *bed slope* data are available for modern systems only and correspond to the talweg slope. By multiplying the FP bed slope and the sinuosity, we get a *regional slope* corresponding to the slope in the main direction of the FP. In the case of confined FP, the computed regional slope corresponds to the gradient of the confining FP.

FP cross-sectional parameters were also surveyed in a manner as similar as possible to that of fluvial systems (Figure 2.6). We only selected cross-sections located in relatively straight reaches and perpendicular or slightly oblique to the FP of a well defined geometry. This probably resulted in a slight over-estimation of FP widths and areas.

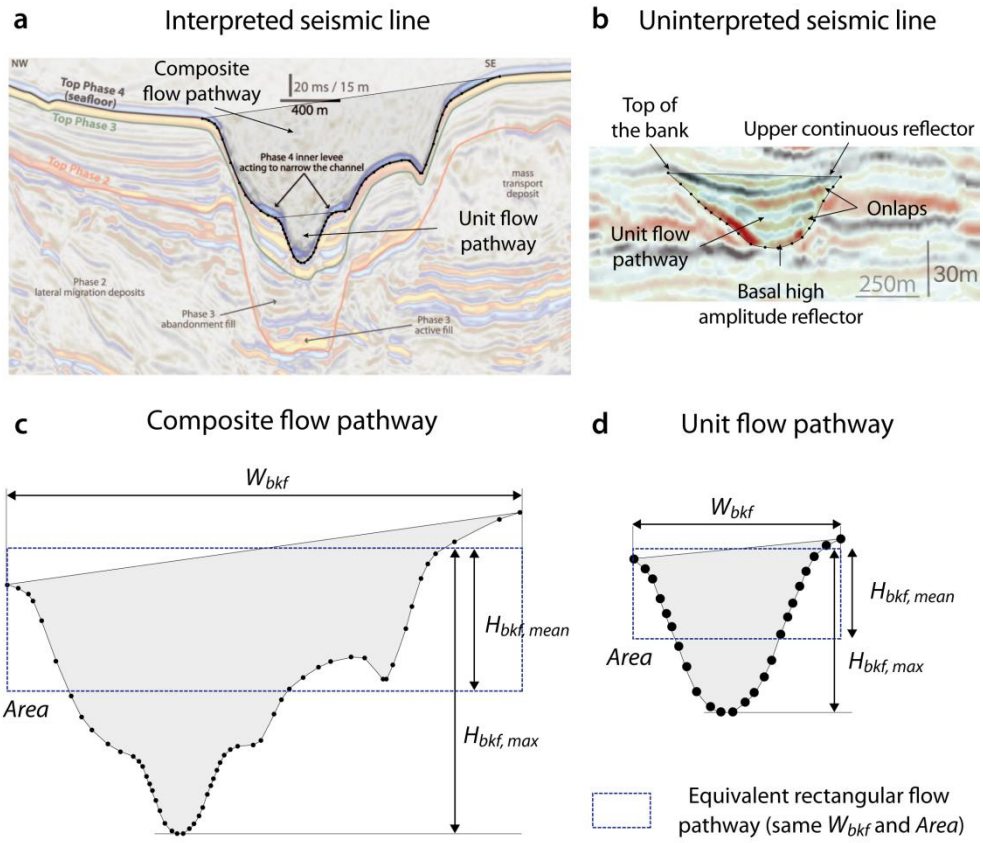

Figure 2.6: Cross-sectional measurement methodology. Interpreted seismic line (from Jobe et al., 2016) showing a large scale FP confining a small scale one (a). Uninterpreted seismic line (from Mayall et al., 2006) showing the contouring of a small scale FP (b). Definition of the bankfull width (W_{bkf}), maximal ($H_{bkf, max}$) and mean ($H_{bkf, mean}$) bankfull depth, and the cross-sectional area for a composite (c) and a unit (d) scale FP.

Contour of the FP section was digitalized accordingly to the interpretation in the publications. When no contour was drawn, we used the method of Jobe et al. (2016): the bed was taken at the bottom of the basal high amplitude reflector, the bank contours followed the location of onlaps, until the bottom of the first continuous reflector above the gully shape (Figure 2.6a and 2.6b). The number of picked points depended on the complexity of the FP shape as illustrated in Figure 2.6. The

horizontal distance between the two upper points of the bank was taken as the FP *bankfull width* W_{bkf}, based on the similarity with the bankfull width in fluvial systems (Figure 2.6c and 2.6d). Due to levee asymmetry (Peakall et al., 2000; Straub et al., 2008), the *maximal bankfull depth* $H_{bkf,max}$ of the FP was defined as the vertical distance between the lower point of the contour and the mean elevation of the upper banks (Konsoer et al., 2013). The FP cross-sectional area was defined as the area comprised within the contour of the FP and the line that tied the upper points of the banks. Finally, the FP *mean bankfull depth* $H_{bkf,mean}$ was computed as the ratio of the cross-sectional area to the bankfull width, similarly to fluvial surveys.

To summarize, every FP measurement sets comprise – when available – the planform parameters (bed slope, regional slope, sinuosity, wavelength and amplitude) as well as the cross-sectional geometry parameters (bankfull width, cross-sectional area, maximal bankfull depth, and mean bankfull depth). Additionally, five ratios were computed from these parameters: the wavelength-to-width and amplitude-to-width ratios, the ratio of wavelength to amplitude, the aspect ratio (bankfull width to mean bankfull depth ratio), and the depth ratio (maximal to mean bankfull depth ratio).

2.3.4. Comparison with a fluvial dataset

We compared our submarine data to a fluvial dataset built by Held (2011). These data were gathered from hydrologic studies in regions of comparable hydrophysiographic settings: alluvial rivers and humid climate in both the United States and Australia. Selected fluvial data corresponds to streams with steady flow regimes, i.e., where the concept of channel-forming discharge applies (Wolman and Miller, 1960; Copeland et al,. 2000). All selected rivers display a constructional behavior attested by the presence of levees. In addition to channel cross-sectional data, planform morphology was measured (bend amplitude and wavelength) to obtain a comprehensive dataset, comparable to that of the submarine FP.

The morphometry of meandering alluvial rivers were compared with submarine FP as a whole, and then with submarine leveed channels alone (see section 4). Submarine (and alluvial meandering) FP relationships are derived from least-square linear regressions on log-transform data, resulting in power-law equations. To ensure the quality of the regressions, they are performed on data within the interval $\mu \pm 2\sigma$, where μ is the average ratio between the two parameters, and σ the associated standard deviation. These parameters are computed from the normal distribution function fitted on the distribution of the logarithm of the ratios between the parameters (Figures 2.11 and 2.12). The regression curves and equations are displayed only when the *p-value*, which tests the non-correlation hypothesis, is lower than 0.01 and/or R^2 higher than 0.1.

2.4. Results

2.4.1. Geomorphic control on the distribution of flow pathway data

The obtained dataset (n=341) encompasses a wide range of geological and geomorphic settings over four submarine domains (Figures 2.1, 2.3 and 2.7a). The sampling further accounts for variable regional slopes with the average decreasing from 2.0% (top of continental slope) to 0.5% (distal basin floor). Most features are unit FP (80.7%), which include 59% leveed channels (n=200) and 20% incised channels (n=70). Composite FP (n=66) are distributed between canyons (24%) and valleys (76%). Unconfined channels represent 75% of their respective datasets. FP are mainly located at the toe of continental slope (34%) and within proximal basin floor (39%). The remaining FP (29%) are evenly distributed between the top of the continental slope (13%) and the distal basin floor (14%).

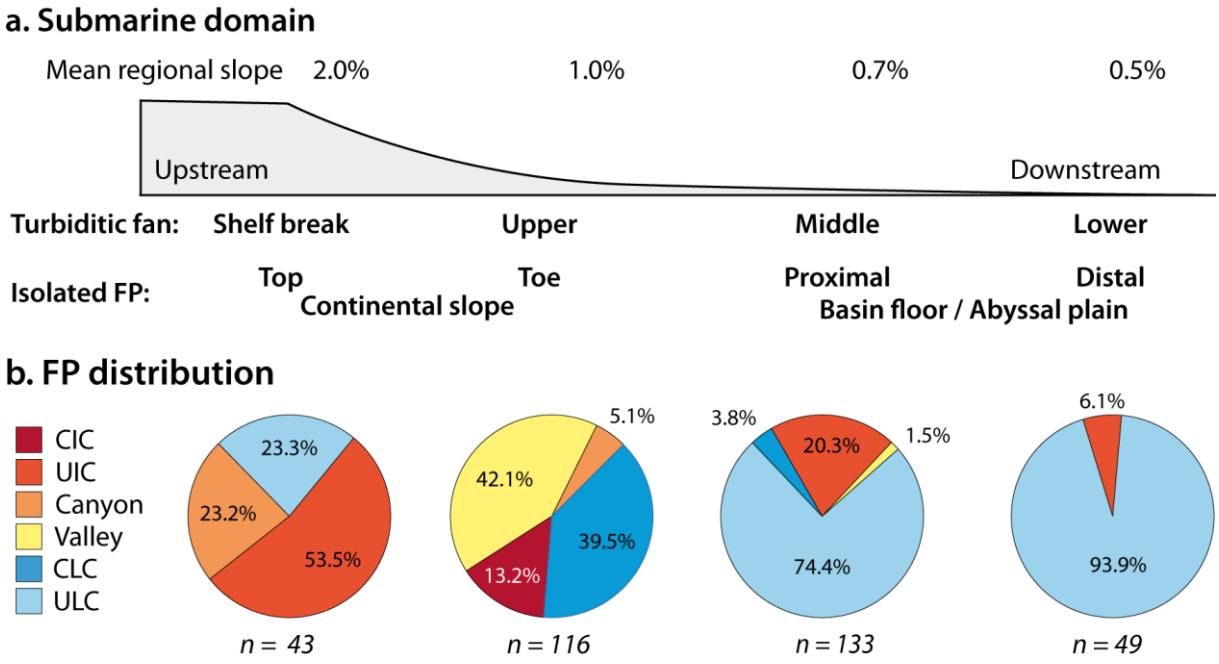

Figure 2.7: Distribution of FP types in the submarine environment. Slope evolution along submarine domains (a) and associated FP distribution (b; n: number of FP in each domain). See Figure 2.4 for FP type abbreviations.

We observe a strong control of the submarine slope on the distribution of the FP types (Figure 2.7). The upstream part of the continental slope is dominated by UIC (53.5%), then ULC (23.3%) and canyon (23.2%). The toe of the continental slope is dominated by two FP types: valleys (42.1%) and confined leveed channels (CLC – 39.5%) that represent more than 80% of the data. The remaining FP correspond to confined incised channels (CIC – 13.2%) and canyons (5.1%). Going downslope, ULC become increasingly dominant (i.e., 74.4% of the proximal and 93.9% of the distal plain). UIC represents the second most abundant FP type of the basin floor (20.3% proximal and 6.1%

distal). In the proximal basin floor zone, some CLC (3.8%) and valleys (1.5%) are present. Hence, canyons and valleys as well as confined channels (CLC and CIC) are respectively limited to the top and the toe of the continental slope. On the contrary, unconfined channels (ULC and UIC) dominate the basin floor areas, although they are present at the top of the continental slope.

2.4.2. Dimensions of submarine flow pathways

In the following, the distributions of the morphometric parameters (Figure 2.8 and 2.9) are presented following the classification scheme (Figure 2.4). UIC and CIC are gathered as IC due to the low number of CIC in our database (15). IC and canyon are highlighted in red, valley in yellow and LC in blue (Figures 2.8 to 2.11).

2.4.2.1. Slope and planform morphology

Consistently with their distribution into geomorphic domains, the different submarine FP types (i.e., IC, canyon, valley, CLC and ULC) can be roughly distinguished according to their large-scale geometry (Figures 2.8 and 2.9). Mean along-FP slope values range from 0.4 to 1.3%, with canyon and ULC having the largest variability and CLC having the lowest variability (Figure 2.8a). Canyons are the steepest (1.3%) and IC are the less steep (0.4%), while valleys, ULC and CLC have very similar, intermediate slopes (0.7 to 0.9%).

Overall, LC are more sinuous than other FP types (Figure 2.8b). Mean sinuosity is the highest for CLC (1.48), with an important dispersion. Valleys are the less sinuous (1.14) (Figure 2.8b), while IC, canyons and ULC show intermediate mean sinuosities (1.18, 1.19 and 1.23, respectively – the latter having more dispersion). Mean wavelengths are highly variable, i.e., one order of magnitude between IC-ULC (39.8-50.7 km) and CLC (5.14 km) (Figure 2.8c). Canyon and valley show intermediate mean values, respectively 7.58 and 18.2 km. The pattern and values of bend amplitude are very similar to that of wavelengths – although bend amplitude is one order of magnitude lower (Figure 2.8d).

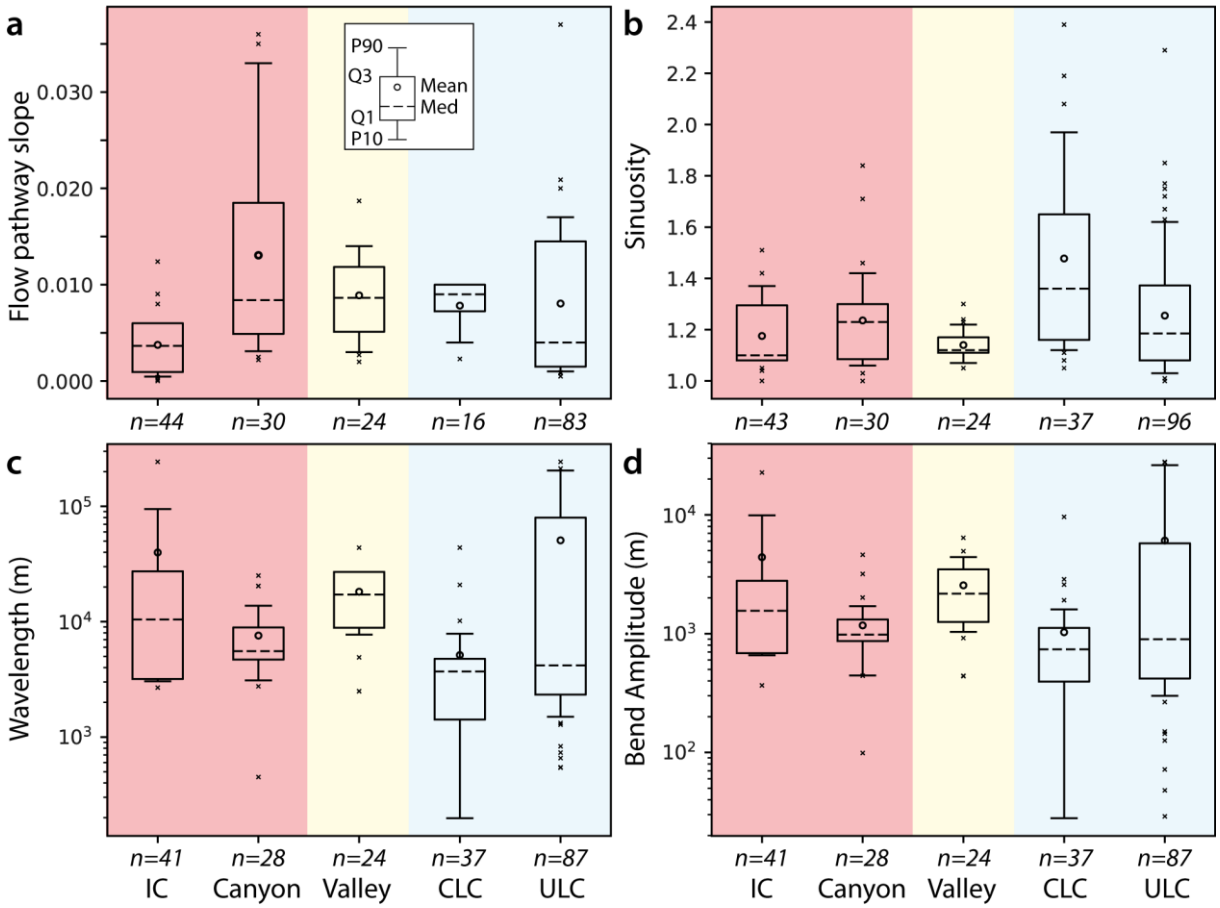

Figure 2.8: Submarine FP planform morphology: slope (a), sinuosity (b), meander wavelength (c) and bend amplitude (d). Red stripe corresponds to incised FP, yellow stripe to valleys and blue stripe to leveed channels (P10: tenth percentile, Q1: first quartile, Med: median, Q3: third quartile, P90: ninetieth percentile). See Figure 2.4 for FP type abbreviations.

2.4.2.2. Cross-sectional geometry

When looking at cross-sectional geometrical parameters (Figure 2.9), two groups of FP can clearly be identified: the large ones (IC, canyons and valleys) and the small ones (CLC and ULC). The former have indeed cross-sectional areas one order of magnitude larger than the latter (Figure 2.9a). Mean bankfull width, mean and maximal bankfull depths follow trends similar to cross-sectional area (Figures 2.9b, 2.9c and 2.9d). Within the small ones group, CLC are usually two times smaller than ULC. Within the large ones group, canyons are the largest FP according to every cross-sectional metrics.

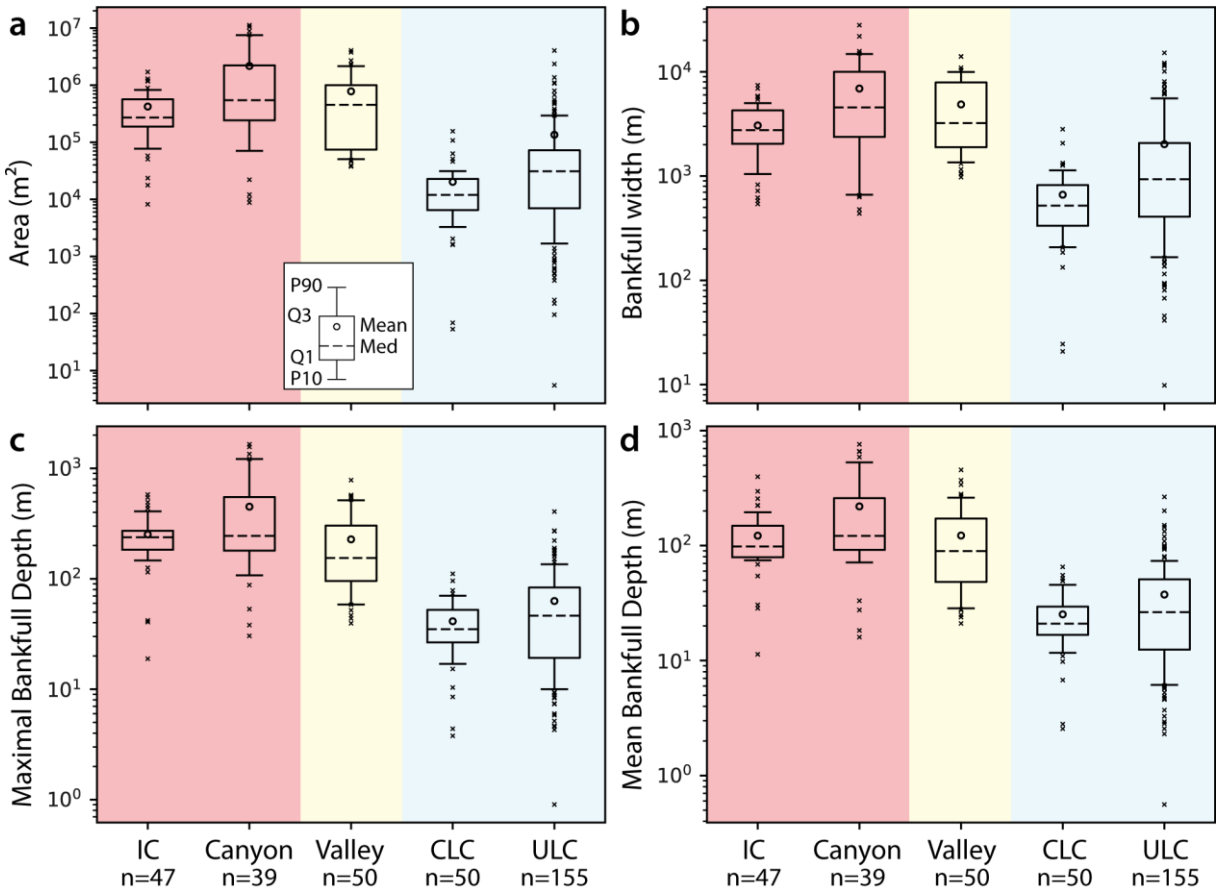

Figure 2.9: Cross-sectional dimensions of submarine FP: cross-sectional area (a), bankfull width (b), maximal bankfull depth (c) and mean bankfull depth (d). See Figures 2.4 and 2.8 for abbreviations and stripes.

2.4.3. Flow pathway geomorphic relationships

2.4.3.1. FP planform morphologies related to width

In the following, submarine FP metrics are combined into relationships comparable to the fluvial literature ones. Pairs of planform morphologies are shown either as ratios in each FP type or as a plot including the whole dataset (Figure 2.10). The ratio of wavelength to bend amplitude (Figure 2.10a) is very similar in every FP types (i.e., mean value around 7 and interquartile range between 5 and 10). This is consistent with bend amplitude being about one order of magnitude lower than bend wavelength (Figures 2.8c and 2.8d). As the result, there is an excellent relationship between the two parameters (R^2=0.95; Figure 2.10 a2).

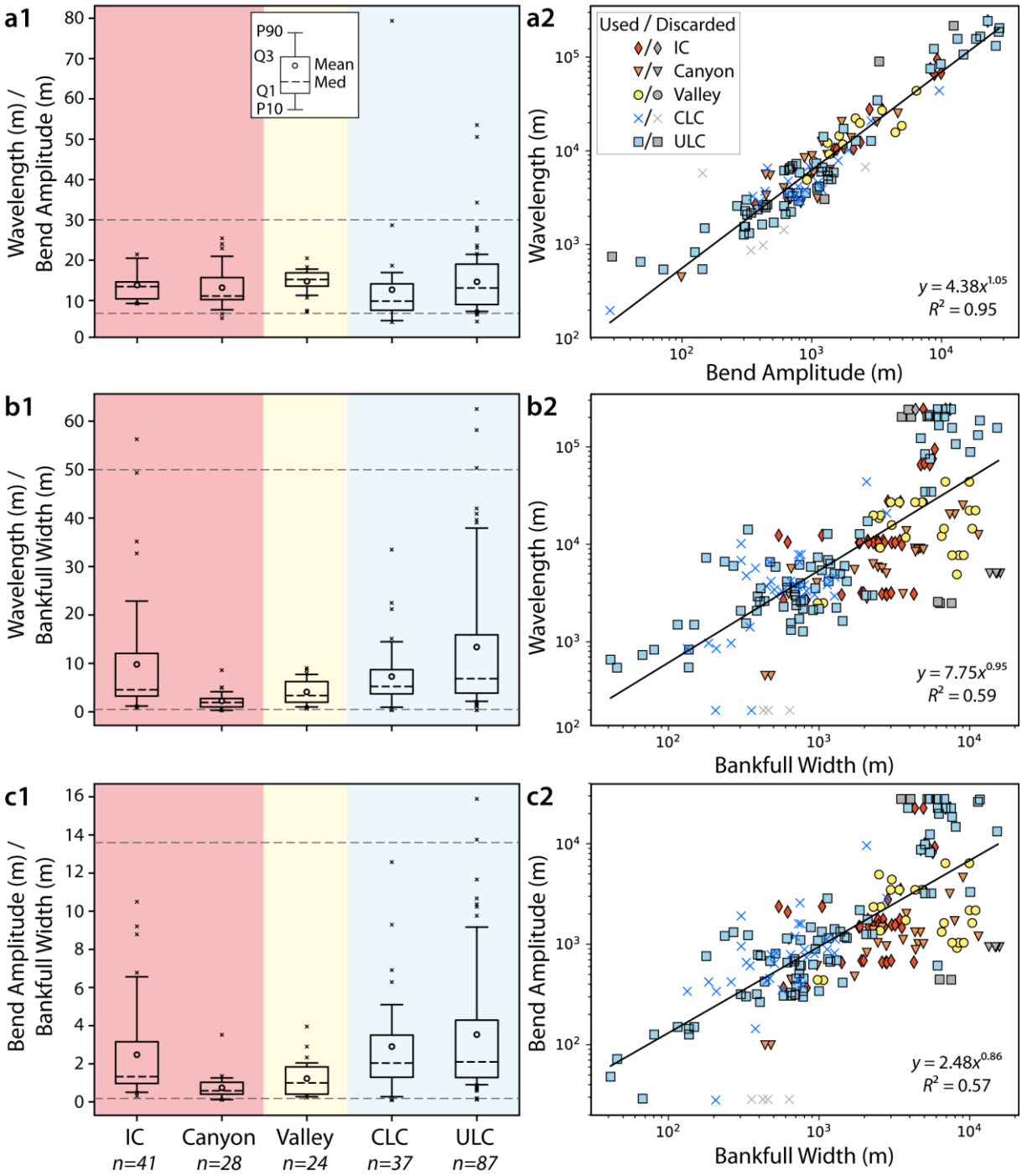

Figure 2.10: Relationships between planform morphology parameters: wavelength versus bend amplitude (a), wavelength versus bankfull width (b), bend amplitude versus bankfull width (c). Left: Box plots of the ratios according to the FP classification; right: scatter plots and regression curves. Grey dash-lines in box plots correspond to p5-p95 cutoffs for the associated regressions. The associated discarded data are in grey. See Figures 2.4 and 2.8 for abbreviations and stripes.

On the contrary, the ratios of wavelength or amplitude to bankfull width are dissimilar from one FP type to another one (Figures 2.10b and 2.10c). Overall, data have a greater dispersion, which results in weaker correlations between bankfull width and the wave numbers (R^2=0.59 and 0.57). Nevertheless, these normalized wave numbers allow distinguishing between two main groups: unit

FP (IC, CLC and ULC) and composite FP (canyons and valleys) (Figures 2.10 b1 and 2.10 c1). Indeed, ULC, CLC and IC have the highest normalized bend amplitude (mean values 1.8, 1.5 and 1.2, respectively) – with ULC having the highest dispersion – compared to canyons and valleys (mean values 0.5 and 0.4 respectively).

2.4.3.2. Cross-sectional geometric relationships

Cross-section geometries are shown either as ratios in each FP type or as a plot including the whole dataset (Figure 2.11). Overall, the depth ratio (maximal to mean bankfull depths) is decreasing from IC to CLC-ULC (i.e., mean from 2.2 to 1.6-1.7) (Figure 2.11 a1). Two main groups, i.e., the large ones (IC, canyons and valleys) and the small ones (CLC and ULC), may be identified based on FP size (Figure 2.11). When plotting maximum versus mean bankfull depths, a good linear relationship is found (R^2=0.96) (Figure 2.11 a2) but with a factor (1.5) that is lower than ratios found separately in each FP type.

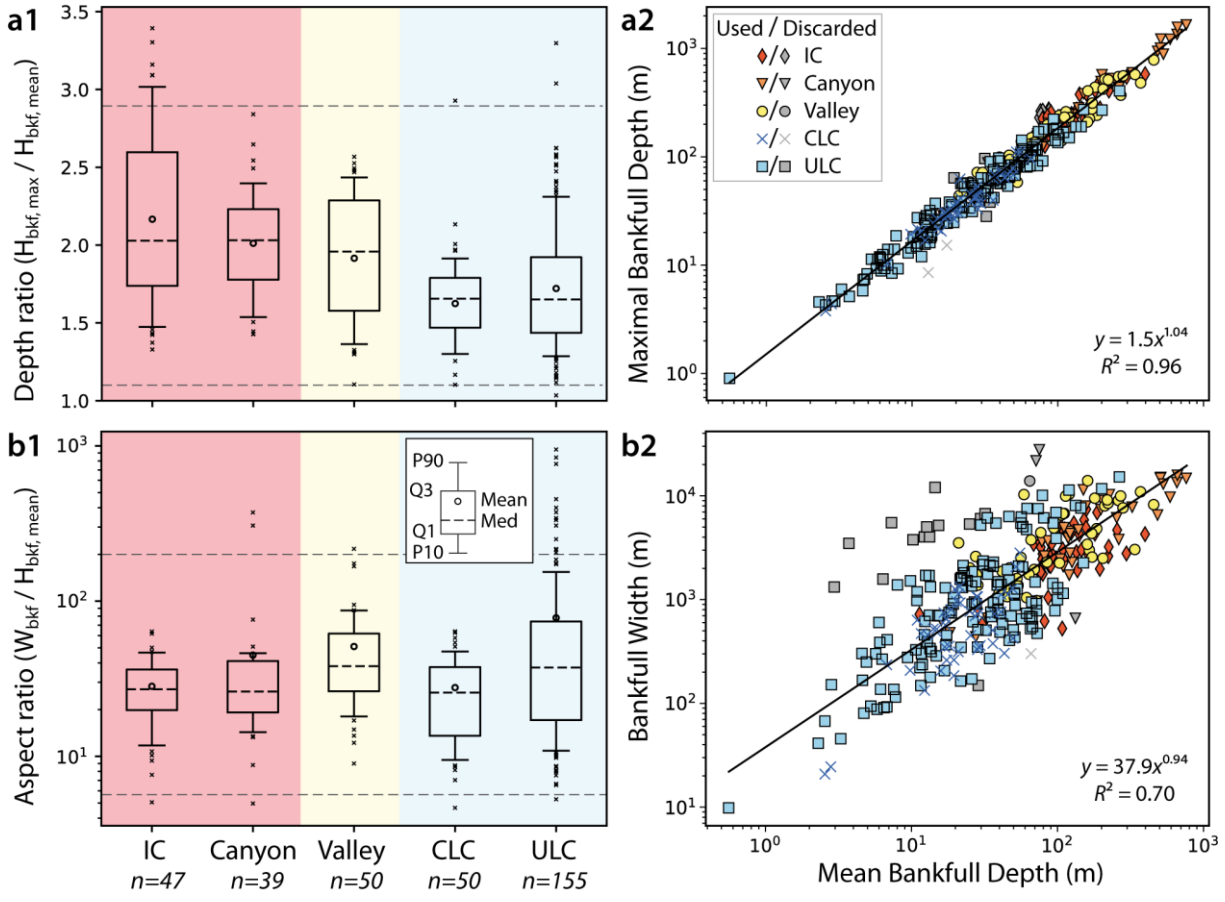

Figure 2.11: Relationships of cross-sectional geometric parameters: maximal bankfull depth versus mean bankfull depth (a) and bankfull width versus mean bankfull depth (b). Left: ratios according to the FP classification; right: scatter plots and regression curves. See Figures 2.4, 2.8 and 2.10 for abbreviations, stripes, and grey dashed-lines.

Mean aspect ratio (bankfull width / mean bankfull depth) is more irregularly distributed (Figure 2.11 b1). It is high for ULC (78) with a large dispersion of the data. Mean aspect ratios are low for IC and CLC (28), while they are quite similar for canyons and valleys (45 and 51 respectively). It results in a relationship between mean bankfull depth and width with a fairly low R^2 (0.70) (Figure 2.11 b2). Similarly to the depth ratio relationship, ULC and CLC represent more than two third of the data.

2.4.4. Comparison between submarine flow pathways and alluvial meandering rivers

In the following, the geomorphic relationships obtained from all types of submarine FP and those specific to submarine LC are compared to the river ones (Figures 2.12 and 2.13).

2.4.4.1. Aspect ratios

Despite differences in width-to-depth correlation coefficients, the exponents of the power law relationships for the aspect ratio (width to depth) are close to one (Figure 2.12; i.e., 0.94 for submarine FP, 0.95 for submarine LC, and 0.93 for rivers), indicating that widths of submarine FP and rivers are nearly proportional to their mean bankfull depth. However, even though the coefficients of submarine FP and LC regression lines are very close (37.9 and 36.3 respectively), they are around 3.3 times higher than that of fluvial regression (10.9), highlighting that submarine FP are three times larger than fluvial channels for a given mean bankfull depth (Figure 2.12).

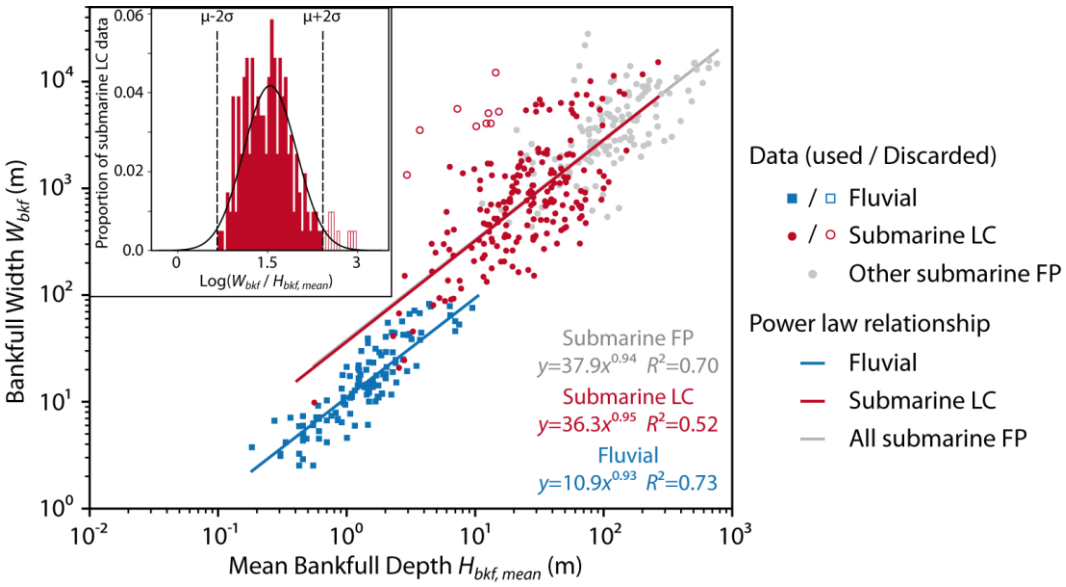

Figure 2.12: Cross-plot of bankfull width to the mean bankfull depth for fluvial and submarine flow pathways, and histogram of the logarithm of the aspect ratio of submarine LC. Fluvial data are from Held (2011). μ is the mean, σ the standard deviation.

2.4.4.2. Meander dimensions

The relationships between wavelength and bend amplitude are very similar between submarine FP, submarine LC, and fluvial systems, with exponents around one and coefficients around 4.4 (Figure 2.13a). In contrast, the relationships between wavelength or bend amplitude to bankfull width are much comparable to the fluvial ones for LC than for the full set of submarine FP. Wavelength to bankfull width relationship coefficient (Figure 2.13b) is about four times greater when looking at all submarine FP (7.75) than for submarine LC only (1.87); while the bend amplitude to bankfull width relation coefficient (Figure 2.13c) is 4.4 times higher for the whole dataset compared to LC only. Overall, there is a better R^2 for regressions of submarine LC (0.74 and 0.78, respectively) than for the whole submarine FP dataset (0.59 and 0.57, respectively). The associated regression exponents are furthermore closer to fluvial ones (1.1) for LC (respectively 1.21 and 1.12) than for the full submarine dataset (0.95 and 0.86).

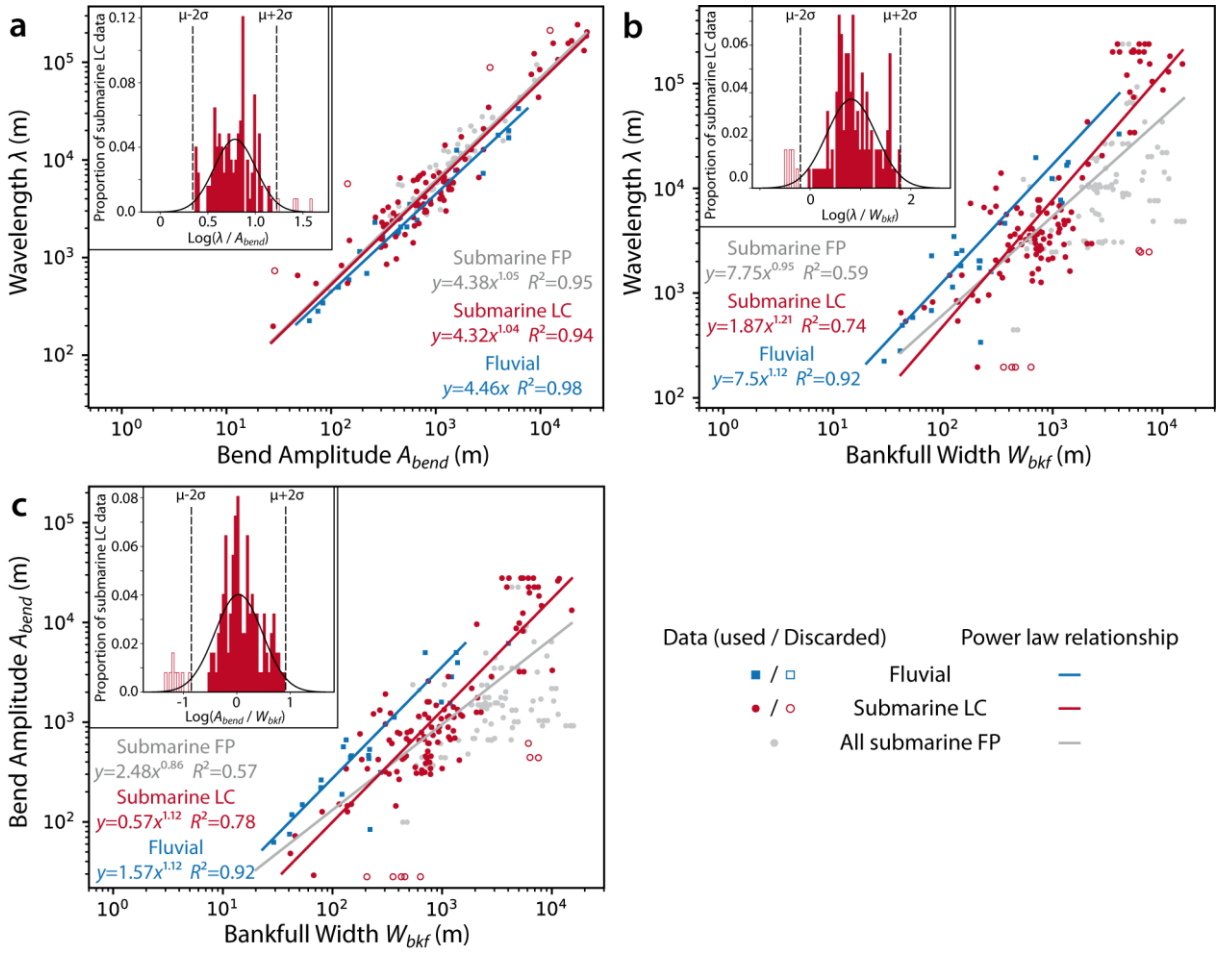

Figure 2.13: Submarine LC and meandering river planform morphology relationships: wavelength versus bend amplitude (a), wavelength versus channel bankfull width (b), bend amplitude versus channel bankfull width (c), and associated histograms of the logarithm of the ratio between the parameters. Fluvial relationships are from Williams (1986). μ is the mean, σ the standard deviation.

Therefore, submarine LC show morphometric relationships comparable to rivers although wave numbers are smaller than fluvial ones for a given channel width. The main differences between LC and fluvial meandering systems are found in the regression coefficients: for a given bankfull width, LC wavelength is half that of the fluvial one and LC bend amplitude is about a third of the fluvial one (Figures 2.13b and 2.13c).

2.4.4.3. Channel morphometric parameters related to slope

Similarly to Figures 2.8a and 2.9, Figure 2.14 illustrates that submarine LC are smaller and less steep than the other submarine FP, although they remain few order of magnitude larger than rivers (around 100 times wider and 10 times deeper). The slope of submarine FP, and particularly LC, globally decreases from the top of the continental slope to the distal basin floor.

Bankfull width is negatively correlated to the slope for submarine FP, submarine LC, and fluvial channels, although it should be considered with caution as the determination coefficient R^2 are very low (respectively 0.11, 0.44, and 0.30). There is no correlation between mean bankfull depth and slope for submarine FP and LC whereas it is weakly correlated for fluvial channels (R^2 = 0.38, Figure 2.14b). There is no correlation between cross-sectional area (i.e., the product of the bankfull width and mean bankfull depth) and slope for submarine FP. In contrast, a weak inverse correlation exists for submarine LC and fluvial channels (regression coefficients of 93.7 and 0.02, respectively; Figure 2.14c). Finally, the relationship between aspect ratio (i.e., mean bankfull width divided by mean bankfull depth) and slope is weakly significant for submarine LC (R^2 = 0.31) (Figure 2.14d), while no correlation appears for submarine FP and fluvial data. This indicates that submarine LC are wider and deeper downstream, with their width increasing faster than their depth.

Overall, the relationships found support that submarine LC, which may be found in many submarine geomorphic settings, are more similar to meandering alluvial rivers than all submarine FP together (Figure 2.14).

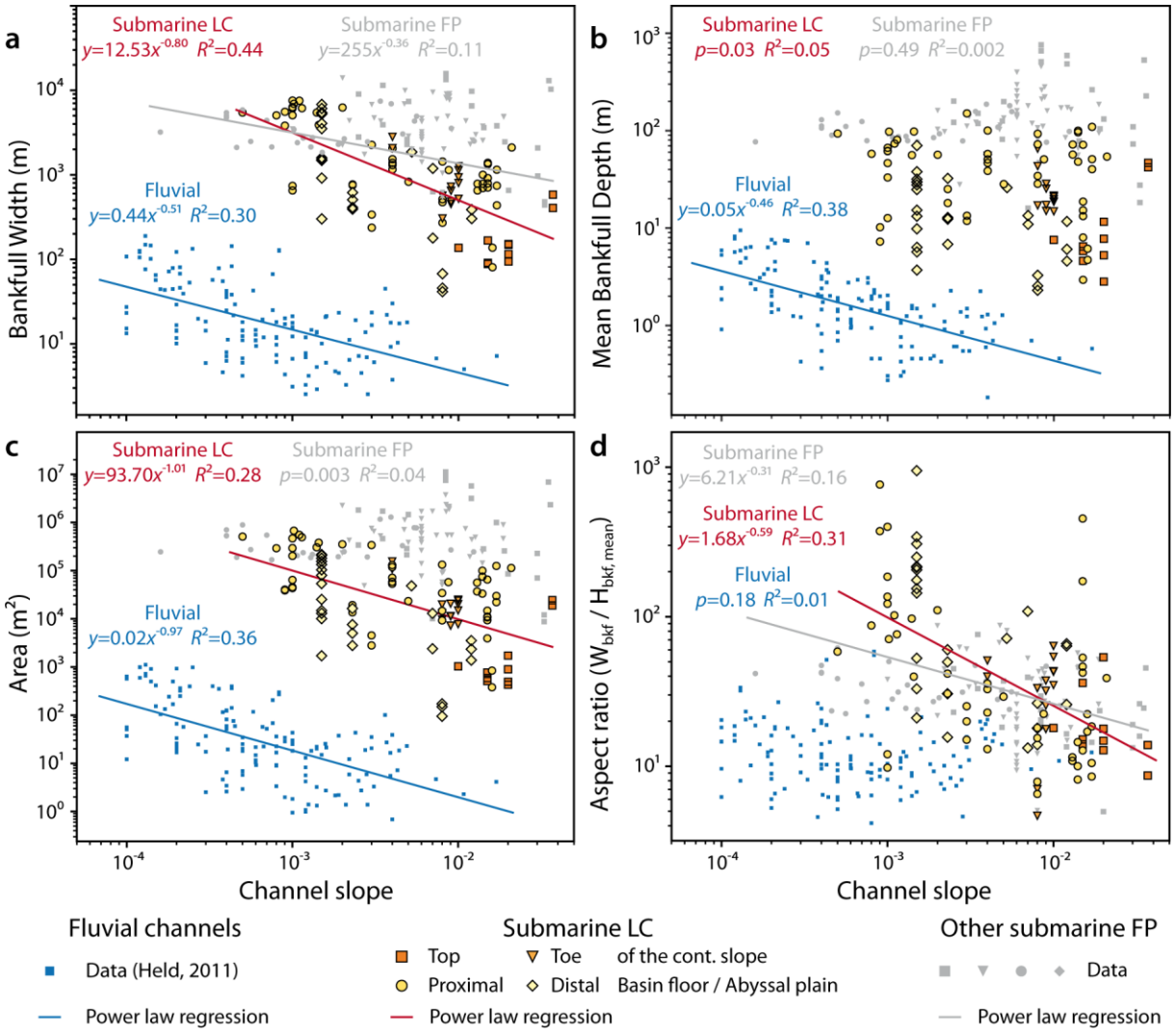

Figure 2.14: Cross-plots of bankfull width (a), mean bankfull depth (b), cross-sectional area (c), and aspect ratio (d) versus channel slope for rivers, submarine LC, and all submarine FP. Regression curves are not represented for p (p-value) > 0.001.

2.5. Discussion

To our knowledge, the present database is the most exhaustive compilation of submarine FP data from academic research publications. Sampled submarine FP extend over diverse geological settings, comprise varied sediment feeding systems, and include measurements in varied geomorphic locations from the top of continental slopes to abyssal plains (Figure 2.3). Such compilation is of use to both field- and modeling-oriented geologists. Indeed, despite the variability inherent to large datasets, first-order trends between geomorphic parameters may be identified (i.e., similarly to rivers), together with their implications on the understanding of submarine FP dynamics. In the following, we discuss in turn the relevance of the new geomorphic classification and its applications, as well as the distribution of submarine FP (particularly LC) and their analogy with alluvial meandering streams.

2.5.1. Submarine flow pathways classification

2.5.1.1. Relevance of the classification

The submarine FP classification developed in this work is based on three simple geomorphic criteria: presence/absence of levees, composite nature of the studied FP, and confinement within a larger-scale FP (Figure 2.4). These geomorphic criteria can be inferred from 2D cross-sections, and do not need any spatial information such as FP location in the submarine system (Shepard, 1965), or FP planform morphology (e.g. braiding versus sinuous pattern, see Foreman et al., 2015 and references therein). This classification can be easily applied to both modern and fossil systems. It is furthermore compatible with existing classifications such as that of Normark (1970) based on erosive, aggradational or mixed FP.

The classification may be used in fossil submarine FP studies to infer paleo-environment, paleo-geographic location and dimension of the related system from observed geomorphic features and dimensions (e.g., Harishidayat et al., 2018). Identification of varied submarine FP types within a system may also contribute to paleo-hydrologic (Konsoer et al., 2013) and paleo-climate (Castelino et al., 2017) reconstructions. For example, incised FP result from erosive or by-passing energetic flows (Normark, 1970; Fildani et al., 2013; Weill et al., 2014) while leveed FP come from depositional ones (Normark, 1970; Wynn et al., 2007; Straub and Mohrig, 2008). In this sense, our classification is comparable to meandering fluvial systems since continental pathways may be either unit or composite, levees-flanked or not, and confined or not (i.e. within a fluvial or glacial valleys). Hence, similarly to the meandering streams being classically split into bedrock and alluvial rivers based on local sediment transport conditions (i.e., Montgomery et al., 1996 and references therein), our classification may be used to infer local flow dynamics, without any *a priori* consideration, e.g., location along the continental margin.

Finally, the proposed hierarchical basis between FP, common to numerous terminologies (Mayall et al., 2006 and references therein), reflects either single or multi phase FP evolutions (Clark and Pickering, 1996; Deptuck et al., 2007; Babonneau et al., 2004; Bain and Hubbard, 2016). Such distinction is useful because the sedimentary architectures of composite FP results from a multi-phase evolution and the interaction of different processes (Mayall et al., 2006; Deptuck et al., 2007). Fluctuations in flow characteristics through time are indeed recorded by changes in sedimentary body arrangement and grain size distribution that impact the location, architecture, and petrophysical properties of hydrocarbon reservoirs (Wynn et al., 2007).

2.5.1.2. Dimensions of the sampled submarine flow pathways

At first order, the different FP types within the classification have contrasted dimensions. Surveyed submarine FP size spans several orders of magnitude, with for example their width ranging from 10 m to 30,000 m. Canyons, valleys, and IC are one order of magnitude wider and deeper than LC (Figure 2.9). Unit channels are more sinuous than composite FP (Figure 2.8b), which reflects higher wavelength-to-width and amplitude-to-width ratios (Figures 2.13b, 2.13c), and indicates that they are more laterally mobile. As highlighted before, the smallest FP are therefore key elements to understand sedimentary fills of larger FP.

In studies on submarine FP geometry, small FP are rarely reported. As shown in the database, only 3.2% of submarine FP are less than 100 m wide, and 9.4% are less than 10 m deep. One may question to what extent it is related to their actual rarity or due to the low resolution of submarine digital elevation models and seismic surveys (e.g., Konsoer et al., 2013; Shumaker et al., 2018). Locally, small FP are reported in 3D seismic surveys, for instance in frontal lobes (Doughty-Jones et al., 2017), but data vertical resolution is too low to accurately measure channel cross-sectional parameters. From outcrops, McHargue et al. (2011) developed the concept of “channel elements” up to four times narrower and shallower than the unit channels identified in this study, suggesting reinterpretation of some seismic data into smaller unit channels.

Hence, although very large channels (> 5000 m) are observed on modern ocean floors (e.g. Zambezi channel – Wiles et al., 2017), some of the largest channels we identified (particularly from old data) may correspond to composite FP (see Annex A). However, owing to the fact that majority of our data comes from high resolution bathymetric, sonar or shallow seismic surveys, we assume that the attribution of these FP to unit systems is correct. We therefore acknowledge that, without access to higher resolution data (e.g., from the industry), the present dataset may be truncated for very small submarine FP (< 100 m wide or 10 m deep); but we emphasize that it nevertheless covers 3 orders of magnitude, which highlights the large size of submarine channels compared to rivers.

2.5.2. Distribution of submarine flow pathways and analogies with fluvial channels

Locations of the submarine FP types within the submarine environment show predominance of composite FP on the continental slope and unit channels in the basin floor (Figure 2.7). Moreover, deep incised FP are mostly located on the top of the continental slope while shallower leveed FP are dominant in the distal part of submarine systems (Figures 2.7, 2.9c and 2.14). This distribution reflects major process changes along the continental margin (Figures 2.1 and 2.5) that are likely related to geomorphic adjustment to flow conditions similarly to rivers (Pirmez et al., 2000; Kneller, 2003; Samuel et al., 2003; Hodgson et al., 2011). The upstream part is therefore dominated by high

transport capacity flows resulting in erosive unit FP, which are confined within larger long-lived FP. These composite FP have experienced multi-phase evolution under varying discharge. On the contrary, the downstream part of continental margins is dominated by lower transport capacity FP, which are unconfined. These short-lived FP are laterally mobile, whether in the form of lateral migration or avulsion (Figure 2.1).

As observed in other studies (Clark and Pickering, 1996; Pirmez and Imran, 2003; Konsoer et al., 2013), surveyed submarine FP are one to two orders of magnitude wider and deeper than alluvial meandering channels (Figures 2.12 and 2.15a). Nevertheless, bend geometry of sinuous fluvial and submarine FP are very similar, as highlighted by the meander wavelength-to-amplitude relationship (Figure 2.13a and 2.15a). More generally, wavelength-to-amplitude and wavelength-to-bend-radius relationships are close in all systems where fluid motion occurs, i.e., perennial rivers (Leopold and Wolman, 1960; Williams, 1986), ephemeral streams (Billi et al., 2018), submarine channels, Mars channels, and ocean currents such as the Gulf Stream (Pirmez and Imran, 2003 and references therein), or even supra-glacier rivers (Karlstrom et al., 2013; Yang et al., 2016). This suggests that meander geometry is independent of the environment (in particular aerial or subaqueous) and flow dimensions (from decimeter to hundreds of meters thick), and that similarities of planform development of meanders should be observed in all cases. Hooke (1975) suggested that these ratios are related to intrinsic properties of fluids in motion but no studies have further explored the controlling parameters; generalized equations explaining such behavior have yet to be proposed.

Results of this study suggest that submarine LC are the most analogous to meandering alluvial rivers. Submarine LC indeed form a consistent group of smaller submarine FP that are the most sinuous (Figure 2.8b) and have the largest meanders relatively to their size (Figures 2.10b and 2.10c). Submarine LC display wavelength-to-width and amplitude-to-width relationships more similar to meandering alluvial rivers than when considering all submarine FP together (Figures 2.13b and 2.13c). Submarine LC also show downstream increases of both channel width and cross-sectional area similar to rivers (Figures 2.14a, 2.14c, and 2.15b), although the associated channel depth increase is less rapid than for rivers (Figure 2.14b). Consequently, we focus on LC in the rest of the discussion.

2.5.3. Submarine leveed channel flow processes in the light of fluvial meandering ones

2.5.3.1. Channel morphometric parameter scaling

Although they are the smallest FP type, submarine LC remain one order of magnitude wider and deeper than fluvial meandering channels (i.e., Figures 2.12 and 2.15a). 90% of the sampled

submarine LC are between 100 and 2000 m wide and between 10 and 100 m deep (maximal bankfull depth). Submarine LC are also three times wider than rivers for a given mean depth (Figures 2.11 and 2.15a). This value is two times lower than proposed by Konsoer et al. (2013). This result likely reflects the influence of the large proportion of submarine FP narrower than 1000 m in our study (40%) compared to Konsoer et al. (5%) since small size FP have the lowest aspect ratios (Figure 2.12). In addition, we discarded LC data with very high aspect ratios (i.e., greater than 260), which are more likely to be braided turbidites (Foreman et al., 2015) and are not relevant for the present comparison. The LC data presented in this study are therefore relatively small elements in the hierarchy of the submarine realm but they are close to the unit FP building larger sedimentary bodies, similarly to individual meandering streams in alluvial plains.

The relationships derived from LC (Figure 2.15a) provide the first order trends in terms of geomorphic parameter scaling. The database established here, which may be completed with further investigations using the same methodology of measurement, may be used in submarine LC models to calibrate parameter distributions, and in natural system to highlight field (dis)similarities of channel morphometric relationships depending on geological settings (latitude, margin type, feeder system, sediment load). This study is thus a first step to understand the relationships between channel morphology and channel forming flows.

The relationships show that amplitude and wavelength of submarine LC bends are three times smaller than those of fluvial bends with respect to channel width (Figures 2.13 and 2.15) as shown in the Amazon fan (Pirmez and Imran, 2003). This reflects a reduced growth of bend interpreted as a stabilization of the flow path that is much less pronounced in fluvial channels (Peakall et al., 2000; Jobe et al., 2016). Several processes are invoked to explain submarine channel stabilization such as clay hysteresis that decreases lateral migration rates (Peakall et al., 2000), change of flow properties due to climate or base-level change, flow super-elevation responsible for levee asymmetry (Imran et al., 1999; Jobe et al., 2016), or reverse secondary flow cells that modify shear stress on banks and net sediment transport (Peakall et al., 2000; Azpiroz-Zabala et al., 2017b; Dorrell et al., 2018). Hence, in addition to natural system studies, complementary approaches such as numerical modeling based on CFD (computational fluid dynamics) simulations or small-scale experiments may also bring valuable information to this end.

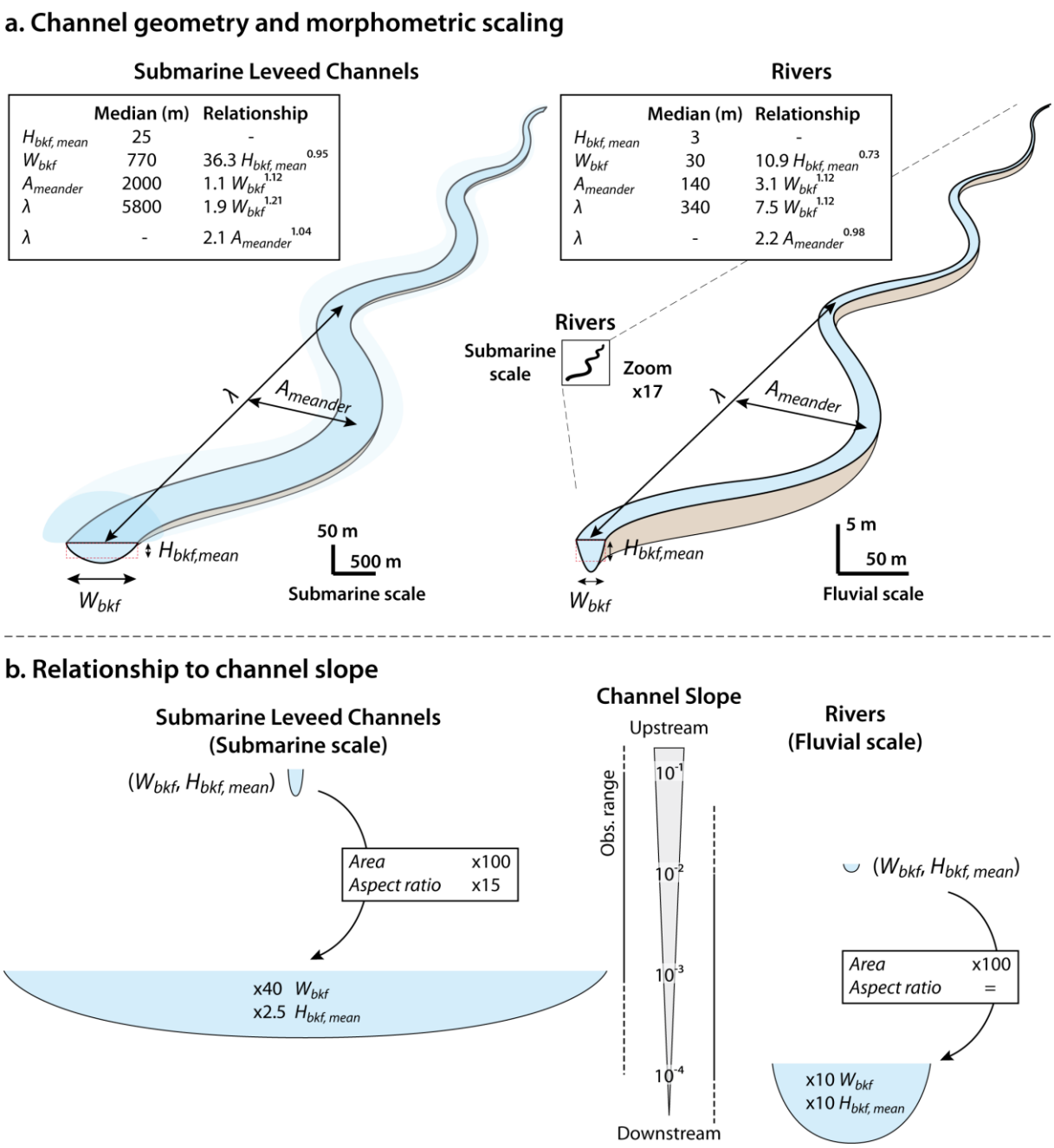

Figure 2.15: Comparative sketches between meandering fluvial and submarine leveed channel. Median geometry and morphometric scaling (a). Relationships between cross-sectional geometry and channel slope (b). See Figure 2.2 for abbreviations. Vertical exaggeration is x7.

2.5.3.2. Downstream evolution of submarine leveed channel geometry

Similarly to alluvial meandering rivers, submarine LC width and cross-sectional area show a small negative correlation with channel slope (Figures 2.14a, 2.14c, and 2.15b) as hypothesized by Konsoer et al. (2013). Note that this applies to modern systems only (see section 2.3.3). Overall, this suggests that the size of LC sections increases downstream. There is however little correlation between channel depth and slope (Figure 2.14b). This reflects complexity of the submarine LC geometry (Shumaker et al., 2018) that the present compilation may miss because it is a worldwide

set, which does not capture slope variations along a given system. Other phenomena may be at play such as the downstream decrease of levee thickness as pointed by Skene et al. (2002) on six submarine systems and by Shumaker et al. (2018) on the Bengal system. Finally, channel aspect ratio slightly increases downstream (Figure 2.14c) as observed by Shumaker et al. (2018), when it remains roughly constant in the case of rivers.

Perennial alluvial rivers used in the fluvial database are tributary systems, in which discharge increases downstream while slope decreases (Held, 2011 and references therein) and channel dimensions proportionally increase (Leopold and Maddock, 1953; Dury, 1976; Williams, 1978). On the contrary, most submarine LC in our database belongs to distributary systems. Similarly to the fluvial systems, submarine channel slope decreases downstream (Figures 2.14 and 2.15b), but conversely submarine flow discharge is most likely to decrease due to flow overspill and sediment deposition (Hiscott et al., 1997; Konsoer et al., 2013; Traer et al., 2018b). Hence, without discharge contribution from tributaries, long-running submarine flows increase their width and area as they migrate towards the abyssal plains (Figure 2.14a, 2.14c), a behavior that does not follow the fluvial scheme.

Since fluvial processes fail to explain the downstream evolution of LC geometry, flow stratification (Dorrell et al., 2014; Azpiroz-Zabala et al., 2017b; Luchi et al., 2018; Paull et al., 2018) and flow overspill and stripping (Peakall et al., 2000; Traer et al., 2018a, 2018b) become better candidates. Indeed, numerical simulations (Luchi et al., 2018) – confirmed by natural observations (Paull et al., 2018) – invoked the role of flow stratification to create a steady coarse-grained basal driving layer overlaid by a dilute fine-grained driven layer. Consequently, a roughly constant or slowly decreasing discharge – corresponding to the submarine flow forming discharge in the sense of Wolman and Miller (1960, see also Copeland et al., 2000) – may be conserved for long distances inside the channel, while the upper layer progressively vanishes due to flow overspill (Hiscott et al., 1997; Konsoer et al., 2013; Traer et al., 2018b), resulting in downstream decreasing levee height (Skene et al., 2002), and then loss of confinement (Shumaker et al., 2018). Flow overspill is also responsible for the loss of the finest sediments, which contributes to reduce flow cohesion and bank cohesion. Hence, we propose that both effects result in down-slope channel widening (Figures 2.14a, 2.14d), which increases aspect ratio and may lead to the development of a braiding pattern (e.g., Foreman et al., 2015) and/or ultimately to the building of terminal lobes in the lower fan.

2.6. Conclusion

This study uses an extensive dataset based on available publications to analyze the geometry and dynamics of modern and fossil submarine flow pathways. We combine (a) a new classification of modern and fossil submarine flow pathways (FP) into six types based on three geomorphic criteria: presence/absence of flanking levees, composite nature of the FP, and confinement by a larger-scale FP with (b) a survey methodology adapted from the fluvial one for measuring geometric parameters.

We find that: (1) the continental margin strongly controls FP geomorphology, composite FP being located on the continental slope and unit channels in the basin floor; (2) submarine unit leveed channels (LC) form a consistent group of smaller-size and higher lateral mobility FP, and are consequently (3) the most analogous to alluvial meandering rivers; (4) without discharge contribution from tributaries, long-running submarine flows can increase their width and area as they migrate towards the abyssal plains similarly to rivers. The latter can be explained by the progressive flow deconfinement and loss of overspill-related bank and flow cohesion. Finally, the relationships derived from LC provide the first order trends in terms of geomorphic parameter scaling, which may be used to calibrate submarine FP models.

Ce chapitre a ainsi permis de définir les systèmes chenaux-levées (*leveed-channel*) comme étant les conduits d'écoulement sous-marins les plus analogues aux cours d'eau méandriformes alluviaux. Flumy visera donc à simuler ce type de chenaux turbiditiques, dont les dimensions sont plus d'un ordre de grandeur plus grandes que les rivières initialement reproduites. Ces dimensions médianes, ainsi que les nouvelles relations morphométriques établies, permettront également de calibrer le Nexus pour le scénario turbiditique. Néanmoins, compte tenu des différences dans la physique des écoulements fluviatiles et turbiditiques, une étude spécifique est nécessaire et fait l'objet du chapitre suivant.

Chapitre 3.

Subaerial- versus subaqueous density-flow dynamics using a same sinuous path: insights on channel migration theories

Abstract

Submarine flows carry on sediments from the continents to the deepest part of the oceans allowing the formation of hydrocarbon reservoirs. Understanding their dynamics would enhance the prediction of the geometry and the architecture of the resulting deposits. Submarine flows create sinuous channels that resemble to rivers, although flow physics highly differ. This study aims at comparing the response of subaerial and subaqueous flows in terms of velocity field to a given channel morphology. The PIV (Particle Image velocimetry) technique is for the first time applied to subaqueous flows using millet grains that are transported within it. Based on the preliminary study of the flow vertical structure and by comparing with the subaerial flow, the results suggest that PIV technique capture the velocity field of the basal high-velocity layer. This study (i) reaches to the development of a new velocity vertical function valid for both fluvial and subaqueous flows – based on the weighted sum of a fluvial-like logarithmic profile and a cosine-based function – and (ii) shows that subaqueous flow stream-wise velocity adjusts faster to the channel morphology than the subaerial flow one, explaining smaller submarine bend dimensions compared to river ones relatively to channel width. (iii) However, cross-stream velocity profiles of subaqueous flows are similar to that of subaerial ones, and the results are discussed in terms of channel lateral migration.

3.1. Introduction

Meandering is an ubiquitous process related to fluid motion (Sahagian et Diplas, 2017), which occurs for instance in fluvial systems (e.g. Leopold and Wolman, 1960; Williams, 1986), on supra-glacier rivers (Karlstrom et al., 2013 ; Fernandez, 2018), in the submarine environment (Stommel, 1965; Clark and Pickering, 1996; Pirmez and Imran., 2003, Chapter 2), or in other planets such as Mars (Weihaupt, 1974 ; Matsubara et al 2015 and references therein). In all these environments, and particularly in the fluvial and submarine ones, meanders have a very similar shape as shown by close ratios of wavelength to amplitude (Pirmez and Imran., 2003; Chapter 2) or wavelength to radius of curvature (Bellaiche et al., 1986; Pirmez and Imran., 2003), which suggests similar mechanisms of bend growth. Meander evolution, in both fluvial and submarine realms, is controlled by channel lateral migration, which is classically assumed to be proportional to the stream-wise flow velocity deviation from its transverse-averaged value along the banks, commonly called the velocity perturbation in the migration model (Figure 3.1 – Ikeda et al., 1981; Johannesson and Parker, 1989; Imran et al., 1999). Hereafter, to avoid any confusion, we will use the term “stream-wise flow velocity deviation” when describing our results, and “stream-wise velocity perturbation” when speaking about the classic migration model. The velocity perturbation is commonly positive at the outer bank and negative at the inner bank, leading to bend growth. This model provides realistic bend geometries and has been widely used for research and industrial purposes (e.g. Frascati and Lanzoni, 2010; Sylvester et al., 2011; Bogoni et al., 2017; Chapter 1). Nevertheless, submarine wavelength and amplitude are three times lower than the fluvial ones for a given channel width (Pirmez ad Imran, 2003; Chapter 2), which might be due to the differences in terms of flow dynamics (Wynn et al., 2007; Konsoer et al., 2013). Extensive studies on the parameters controlling meander geometry is however lacking.

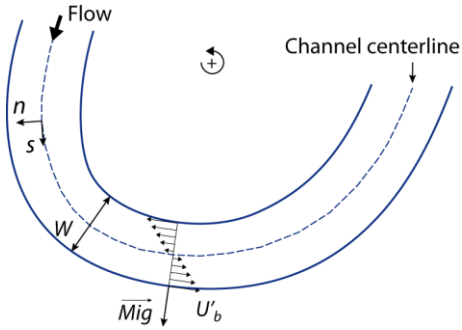

Figure 3.1: Bank migration theory according to Ikeda et al. (1981): the migration vector ($\overrightarrow{Mig}$) is proportional to the velocity perturbation along the bank (U'_b). W channel width; s and n curvilinear abscissa and ordinate.

Direct observations of natural submarine flows are very scarce, and most often in relatively straight canyons (Khripounoff et al., 2003; Sumner et al., 2014; Azpiroz-Zabala et al., 2017a; Paull et al., 2018). Small-scale experiments bring valuable information on flow dynamics, and on the relationships between channel geometry and their formative flows, e.g., submarine channel initiation processes (Straub et al., 2008; Rowland et al., 2010; Weill et al., 2014; de Leeuw et al., 2016). Self-formed sinuous channels are highly difficult to obtain in both subaerial (Paola, 2001; Peakall et al., 2007b; Métivier et al., 2017) and subaqueous (Wynn et al., 2007) conditions – although some examples of weakly sinuous self-formed subaqueous channels exist (Métivier et al., 2005; Yu et al., 2006) – due to the difficulty to adequately calibrate the bank cohesion relatively to the flow in small-scale experiments (Peakall et al., 2007a). Consequently, most of subaqueous experiments studying flow dynamics in a sinuous channel were performed using a static channel form, allowing investigating in-channel and overbank deposit location (Peakall et al., 2007b; Straub et al., 2008; Amos et al., 2010; Ezz et al., 2013; Janocko et al., 2013; Fernandez et al., in press), or flow structure (Keevil et al., 2006; Islam and Imran, 2010; Abad et al., 2011; Farhadi et al., 2018) and for many of them comparing their results with what happens in aerial experiments. However, none of them used the same channel morphology in both conditions, which would greatly ease comparisons of in-channel deposit location or flow velocity field. Only Keevil et al. (2006) ran subaerial and subaqueous flows in a same channel and measured the velocity field at bend apexes and inflexion points using ultrasonic Doppler velocity profiling (UDVP). They observed reverse secondary flow cell orientation in subaqueous experiments. In addition, experimental channels most often exhibit width-to-depth ratios much higher than the natural ones (both submarine and fluvial), which control secondary current strength and may change the flow velocity field (Peakall and Sumner, 2015).

This study aims at comparing subaqueous and subaerial 2D flow fields within the same sinuous channel morphology. Flow field structure is analyzed using Particle Image Velocimetry (PIV) which was for the first time applied to subaqueous experiments. Surveyed flow velocity field is first analyzed based on velocity vertical profiles of subaerial and subaqueous flows. The results of subaqueous and subaerial experiments are then compared and discussed in terms of channel lateral migration.

3.2. Methodology

3.2.1. Experimental setup

Experiments were carried out in the Saint Anthony Falls Laboratory, University of Minnesota, Minneapolis. The tank is 1 m wide, 4 m long and 1 m deep (Figure 3.2a; see Limaye et al., 2018). A

1 m wide, 2.4 m long rigid board was setup within the tank using 2x3 threaded rods allowing us to precisely set the board slope at 0.2 %. Two channels were cut in a 25.4 mm thick Styrofoam sheet and glued on the board (Figure 3.2a): a straight one in the down-slope direction, and a sinuous one (sinuosity 1.14) consisting in five full bends, plus a half-bend at the beginning and another one at the end followed by a 0.4 m long straight reach in the downstream direction. The sinuous shape follows a sine-generated curve (equation 3.1) that is widely used to model sinuous streams (Langbein and Leopold, 1966; Johannesson and Parker, 1989; Imran et al., 1999; Das et al., 2004; Straub et al., 2011; Ezz et al., 2013).

$$\theta = \theta_0 sin\left(\frac{2\pi}{\lambda_{arc}} s\right) \quad (3.1)$$

where θ is the angle between the channel centerline and the down-slope direction, θ_0 is its maximal value, λ_{arc} the arc-wavelength measured along the centerline, and *s* is the curvilinear coordinate.

The experimental channel geometry was chosen such as to respect at best the median proportions observed in natural submarine channels, consisting in a channel around 750 m wide, and 25 m deep (mean depth) (Chapter 2). Taking into account the dimensions of the tank, the angular amplitude of the experimental channel centerline (θ_0) is 40° and the arc-wavelength measured along the centerline (λ_{arc}) is 0.98 m (Figure 3.2b), resulting in bend amplitude of 0.1 m and wavelength of 0.86 m. The channel cross-sectional geometry is rectangular, 0.17 m wide and 0.017 m deep (Figure 3.2b). Based on channel width (W_{model} and W_{nature} for experimental and natural channel widths respectively), it results in a scaling factor λ_s (equation 3.2) 2.2×10^{-4} for subaqueous experiments and 5.7×10^{-3} for subaerial experiments, assuming a 30 m wide river. The experimental sinuous channel is thus equivalent to a fluvial channel with bend wavelength and amplitude of 152 m and 92 m respectively, and a submarine channel with wavelength and amplitude equal to 5800 m and 1000 m respectively.

$$W_{model} = \lambda_s W_{nature} \quad (3.2)$$

The resulting aspect ratio (width-to-depth ratio) of the experimental channel is 10, which is commonly observed in natural rivers, and corresponds to the lower range of observed values for submarine channels (median 30, Clark and Pickering, 1996; Lemay et al. paper). Yet this aspect ratio is higher and more realistic than that of many subaqueous experiments, i.e. 2-5.5 (Keevil et al., 2006; Amos et al., 2010; Ezz et al., 2013; Janocko et al., 2013; Farhadi et al., 2018). The resulting bend wavelength to width ratio (5) and bend amplitude to width ratio (0.6) are frequently observed in modern submarine channels (Clark and Pickering, 1996; Pirmez and Imran, 2003; Lemay et al,

submitted), although they correspond to low values for rivers (>10 and >2 respectively, Leopold and Wolman, 1960; Williams, 1986).

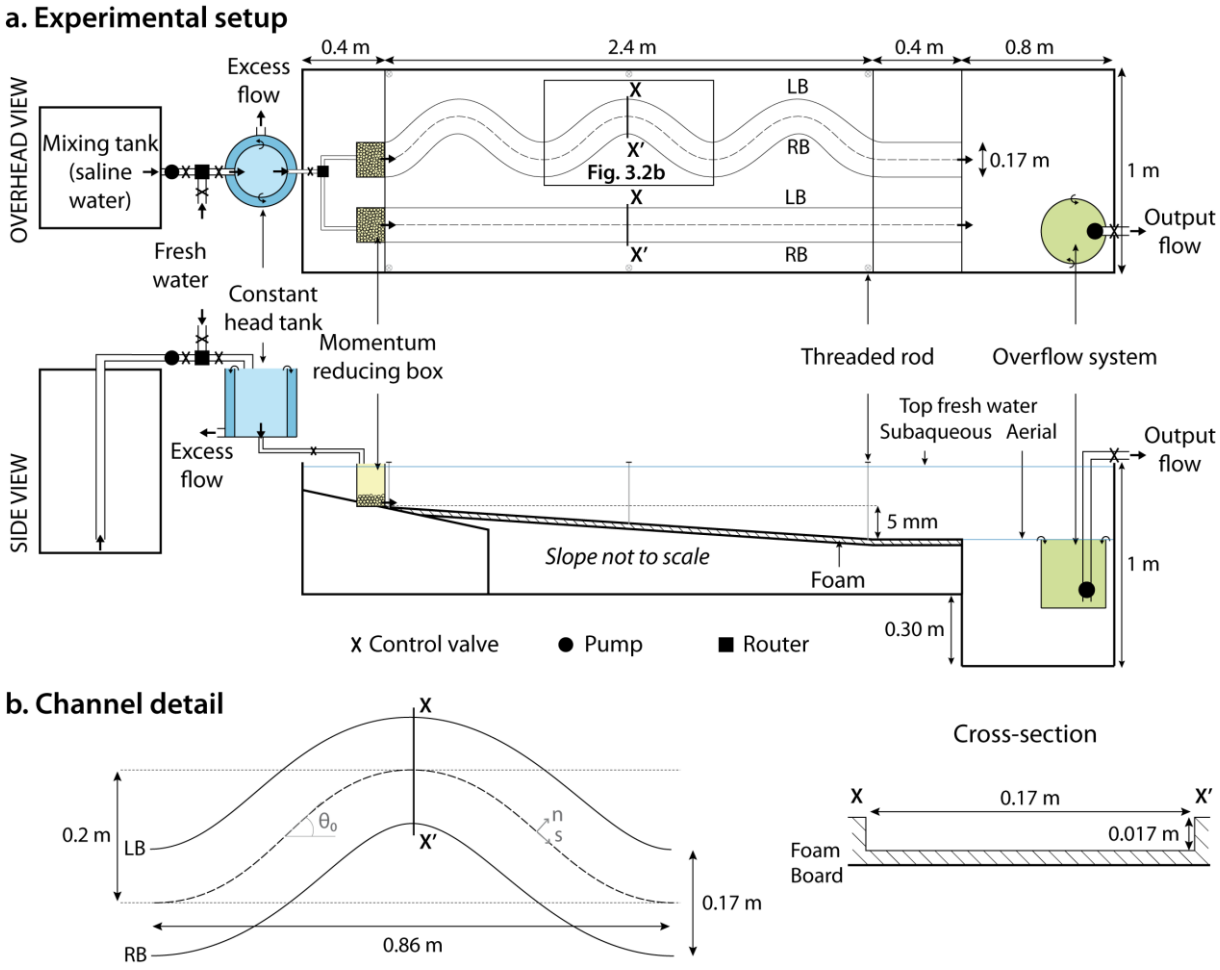

Figure 3.2: Experimental design common to both subaerial and fluvial experiments (a) and detail of the channel geometry (b). LB: left bank, RB: right bank.

Four experiments were carried out in this work: a subaerial and a subaqueous flow in the straight and sinuous channels. An additional experiment was carried out in the sinuous channel where plastic sediments (density 1.25, diameter 125 µm) were added in the flow to observe the location of the deposits (Figure 3.10). For the subaerial experiments, we set the base level at the elevation of the top of the channel at the downstream end (Figure 3.2a). Ambient water level was kept constant using an overflow system adjustable in height. Input fresh water discharge was set at 0.63 ± 0.03 L/s such as the flow was at the bankfull stage in the sinuous channel. For the subaqueous experiments, the tank was filled up with fresh water (Figure 3.2a) and the level kept constant using the same overflow system as for subaerial experiments. Saline water of density 1018 ± 1.5 kg/m^3 (excess density 1.8 ± 0.15%) was prepared in a 2.5 m^3 mixing tank and pumped into the experimental tank. This saline water is equivalent in terms of excess density to a sediment concentration (*C*) of

0.7% in marine water assuming $\rho_t = \rho_w(1 - C) + \rho_s C = \rho_w(1 + RC)$ with R = 1.65, and ρ_t, ρ_w, ρ_s the density of the flow, marine water (1025 kg/m^3), and sediments (quartz 2650 kg/m^3) respectively.

Input water, either fresh or saline, passes through a constant head tank to ensure a constant discharge, then by a momentum reducing box composed of gravels, and finally flows into the channel (either straight or sinuous). Momentum reducing box inlet dimensions are 170 mm wide and 51 mm high. Flow discharge was fixed at 0.080 ± 0.005 l/s such as the subaqueous flow trajectory followed channel morphology with limited overspill near bend apexes. Saline water was pumped at the base of the tank at a higher rate than input discharge in order to slow down the mixing between saline and fresh water (e.g. fresh water density 1000-1005 kg/m^3 in Limaye et al., 2018). The difference was compensated by adding fresh water during the experiments.

3.2.2. Data acquisition

Flow velocity measurements were carried out using two techniques: Particle Image Velocimetry (PIV) for both subaerial and subaqueous experiments, and a single point Acoustic Doppler Velocimetry (ADV) for subaqueous ones only since subaerial flows were too shallow.

3.2.2.1. Acoustic Doppler Velocimetry

The velocity of subaqueous flows in the straight channel was measured by ADV using a single point *Nortek Vectrino* side-looking probe. The probe consists of a central acoustic transmitter surrounded by four receivers. The sampling volume is a cylinder (6 mm of diameter and 4 mm high) centered 5 cm away from the central transmitter (Figure 3.3). The velocity is measured using Doppler effect, which corresponds to a change of the frequency of the transmitted signal due to flow velocity. ADV thus provides a 3D velocity vector of the flow.

In order to capture a representative flow velocity field, measurements were done at several locations along channel cross-sections by installing the probe on a programmable cart. Each measured cross-section was 1.75 m from the inlet and consisted of 10 vertical lines spaced every 17 mm, each of these being sampled by 14 points located every 5 mm for a total height of 75 cm (Figure 3.3). Since measurements were carried out by side, six centimeters are lost along the channel banks. Consequently, the cross-section was build measuring first the left side looking downstream then the right side (Figure 3.3). The flow was stopped between each set of measurement, which may have lead to small variations of flow discharge. The measurement of each point lasted 10 seconds, thus the half cross-section took around 13 minutes. Each measurement point consists of 500 values in the three directions of space since velocity recording lasted 10 s with a frequency of 50 Hz. These

values are relatively constant during the measurement period, and we kept the median values in each direction. ADV measurements unfortunately failed in the sinuous channel.

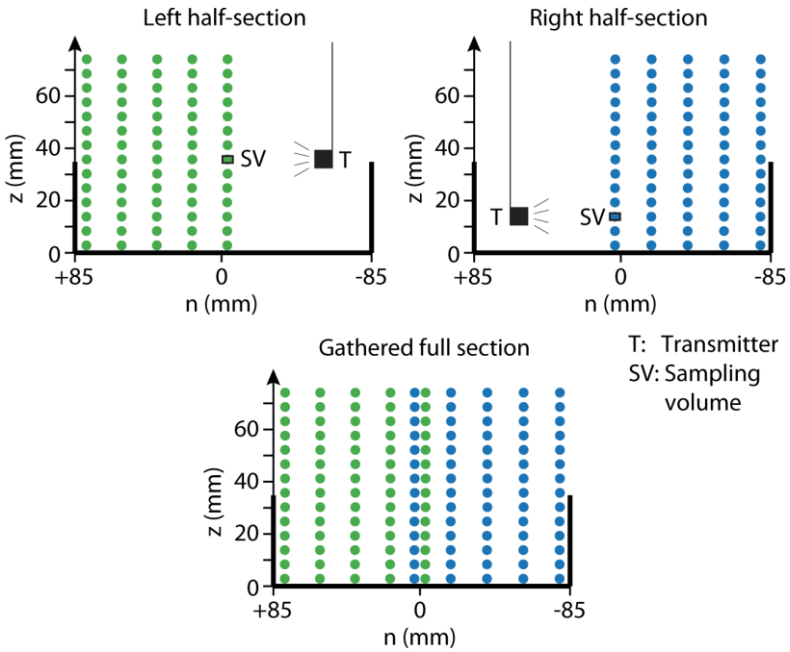

Figure 3.3: ADV measurements points and section reconstruction in the straight channel.

3.2.2.2. Particle Image Velocimetry

PIV consists in tracking patterns of particles that move with the flow in a pair of successive images. It allows computing the displacement of these patterns when picture scales and time lapse (here 24 frames/s) are known. The scale of images was calibrated by drawing a regular 10 cm mesh on the foam (corresponding to the top of the channel). Individual frames were extracted and the background image was subtracted in order to visualize particles only. PIV processing was performed using the openPIV package in Python (http://www.openpiv.net). Image displacements are computed by first defining an interrogation area on both images, and looking for the highest cross-correlation between both areas (Raffel et al., 2018). By simultaneously moving interrogation areas over the entire frames, a velocity vector map is finally obtained.

For subaerial experiments, the camera was placed 2.4 m above the channel such as the straight and last 4 bends of the sinuous channels were captured at once. Particles were few millimeters wide paper dots spread on the water surface. PIV measurements resulted in a regular mesh with a velocity vector every 1.7 cm (10 vectors per channel width – Figures 3.4a, 3.4b).

For subaqueous experiments, PIV was performed only in the sinuous channel. The camera was a *GoPro* (*Hero3*) submerged in the ambient water to avoid refraction at the surface of ambient fluid. Nonetheless, a slight refraction still exists at the interface between fresh water and the saline

flow. The camera was placed 0.3 m above the channel allowing us to survey 0.035 m² with a resolution of 7060 pixels per meter. Particles were millet grains previously soaked with the saline water used for the saline flow. Such particles had nearly the same density as the flow and were maintained in suspension in about 20 mm thick layer above the channel floor. Unfortunately, the exact elevation of each particle cannot be determined precisely, which results in slight errors when computing the displacements and then the velocity due to changes of the distance from the camera (± 3.4%). Moreover, particle velocity vectors depend on their elevation in the flow. Consequently, we measured here the average velocity of the flow inside the basal layer in which particles were transported. The camera was moved along the channel to survey the last four bends (Figure 3.4) and the flow was stopped and restarted between each recording, which might have resulted in small variations of discharge between each surveyed zones. This results in a mesh with a velocity vector 0.7 cm (i.e. 24 vectors per channel width).

Several outlier vectors are often observed after PIV process due to misidentifications of patterns during the cross-correlation procedure, particularly at the edges of the channel. Thus, on each pair of frames PIV results of both subaerial and subaqueous experiments were filtered according to local median vectors with a 100 pixel square neighborhood. Finally, at each mesh node we obtained as many velocity 2D vectors as the number of frames minus one. For each node of the regular Cartesian grid, we kept the median velocity vector.

3.2.2.3. Velocity extraction along the banks

This study focuses on the flow behavior along the banks, responsible for deposition/erosion and thus the modification of natural channels' morphology. Stream-wise and cross-stream velocities along the banks are thus extracted from consecutive cross-sections. Cross-section locations are defined according to the meander wavelength such as 16 sections cover one wavelength (i.e. phase lag of $\pi/8$ between each croos-section – Figure 3.4a). Cross-sections are oriented according to the local curvilinear coordinate system. Because PIV results align along a Cartesian grid, each cross-section consists of 9 and 10 velocity vectors for subaerial and subaqueous experiments respectively. A vector corresponds to the median of all vectors included for subaerial experiments in a 4x1.9 cm² rectangle. Thus, a vector samples between 2 and 5 nodes of the regular mesh (Figure 3.4b). For subaqueous experiments, the rectangle is 4x1.7 cm² and a vector gathers 25 nodes on average (0-30 nodes – Figure 3.4b). For both experiments, each velocity vector defined in the Cartesian coordinate system $(\vec{x}, \vec{y})$ is then projected in the local curvilinear coordinate system $(\vec{s}, \vec{n})$, where the stream-wise velocity U_s is parallel to channel walls and the cross-stream velocity V is positive toward the left bank and negative toward the right bank according to the flow direction (Figures 3.4a, 3.4b).

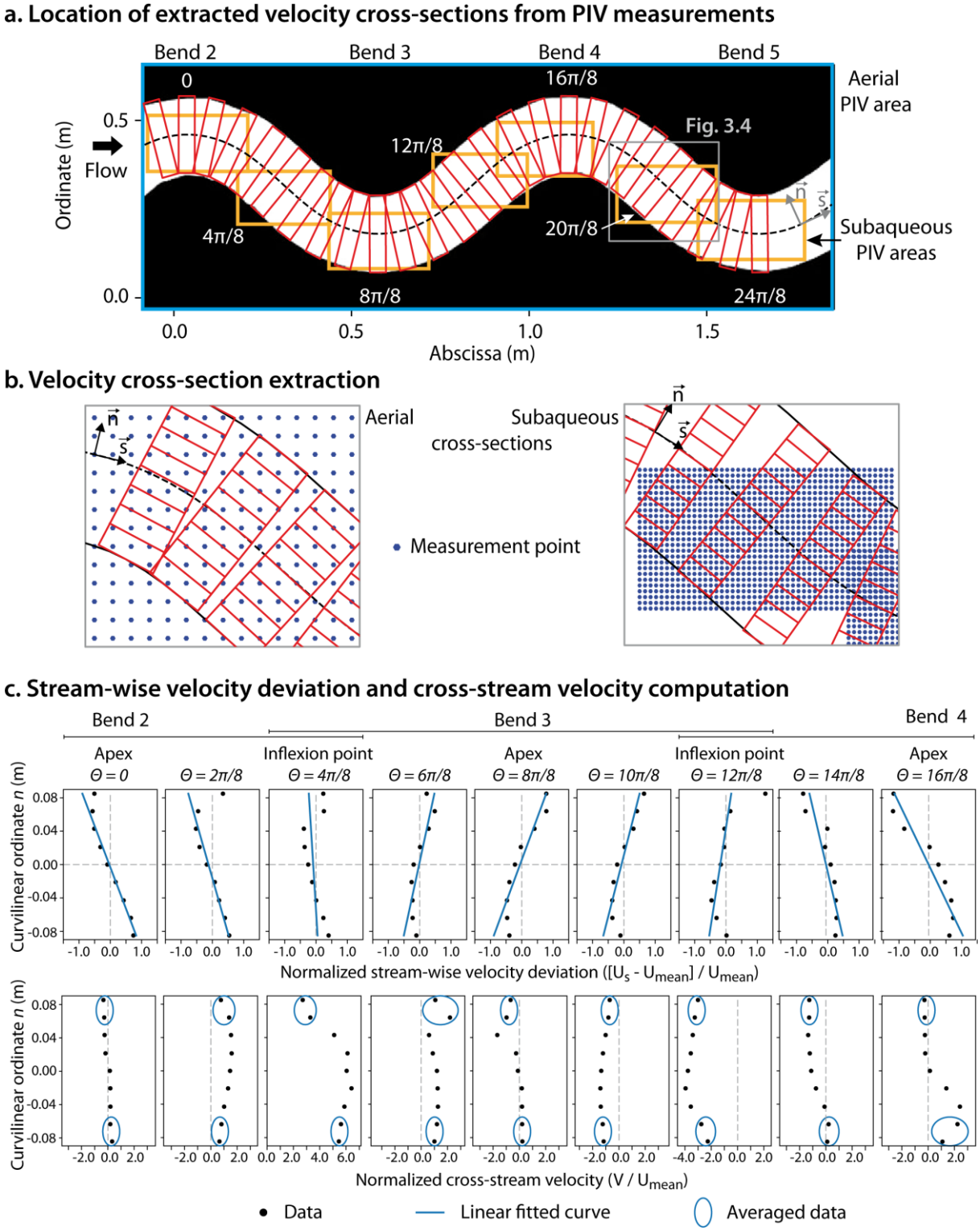

Figure 3.4: Cross-section locations along the channel for PIV analysis (a). A cross-section consists in 9 points averaging 2-5 measurement points for subaerial experiments, and in 10 points averaging 25 (mean) measurement points for subaqueous ones (b). Velocity extraction along the banks using the linear fitted model (blue curve) for the stream-wise component and the mean transverse component of the two last points (blue circle) in the case of subaerial experiments (c). U_{mean}: mean stream-wise velocity, V cross-stream velocity, ϑ: phase lag relatively to meander wavelength.

Since migration numerical models assume that lateral migration is proportional to the stream-wise velocity deviation from its transverse-averaged value along the bank (Ikeda et al., 1981; Johannesson and Parker, 1989; Imran et al., 1999), a linear velocity profile is fitted to the stream-wise velocity (Figure 3.4c), and then the velocity deviation (U'_b) is taken as the difference between the velocity along the bank given by the linear model ($U_{s,b}$), and the section-averaged stream-wise velocity (U_{mean}) such as $U'_b = U_{s,b} - U_{mean}$. The velocity deviation is then normalized by the section-averaged stream-wise velocity. Finally, cross-stream velocity is extracted by averaging the two last data points along each bank (Figure 3.4c) and normalized by the mean stream-wise velocity.

3.2.3. Flow modeling

3.2.3.1. Flow scaling

We computed additional flow parameters from the measurements, allowing us comparing the different flows in-between, and inferring real flow processes using dimensionless numbers. The flow real discharge is computed using the flow height (H), mean velocity (U_{mean}), and width (W) according to $Q_{comp} = H.W.U_{mean}$. The driving force per unit distance (i.e., unit driving force) on a control volume of fluid is the resulting force taking into account the gravity and the fluid buoyancy that acts as the driver of the flow (which is counterbalance by the friction) and is computed according to equation 3.3 (Konsoer et al., 2013):

$$f_{drive} = g\rho_f S \tag{3.3}$$

where g is the gravity, ρ_f the density of the flow, and S the channel slope.

Dimensionless numbers consist of the Froude number (Fr; equation 3.4) that corresponds to the ratio of inertial to gravitational forces (subcritical flow if Fr<1, supercritical flow is Fr>1), and the Reynolds number (Re; equation 3.5) that is the ratio of inertial to viscous forces (laminar flow if Re<1000, turbulent flow if Re>5000).

$$Fr = \frac{U_{mean}^2}{g'H} \tag{3.4}$$

where g' = g for an subaerial flow and $g' = g(\rho_t/\rho_w - 1)$ for a saline flow.

$$Re = \frac{H\,U_{mean}}{\vartheta} \tag{3.5}$$

where ϑ is the dynamic viscosity equal to 1.0e^{-3} kg.m^{-1}.s^{-1} for fresh water and 1.05e^{-3} kg.m^{-1}.s^{-1} for the saline water used in this study.

Laboratory experiments on conservative subaqueous flows may be scaled based on the Froude number similitude (Straub et al., 2008; Ezz et al., 2013; Imran et al., 2016). Considering the same Froude number between the experimental and natural flows, and assuming the same flow excess density and channel slope, natural flow conditions are retrieved using the scaling factor (equation 3.2) according to equations 3.6 (Ezz et al., 2013).

$$L_{model} = \lambda_s \, L_{nature} \qquad U_{model} = \sqrt{\lambda_s} \, U_{nature} \qquad Q_{model} = \lambda_s^{5/2} \, Q_{nature} \tag{3.6a, b, c}$$

where *L* denotes for length-dimensioned parameters (i.e. width, depth, wavelength, amplitude), *U* for velocity, and *Q* for flow discharge.

3.2.3.2. Vertical velocity profile

Open channel subaerial flow vertical velocity profile is usually modeled using the mean velocity (U_{mean}) and a vertical shape function ($T(z_b)$ with $z_b = z/H$; equation 3.7), which is either a logarithmic ($T_{log}(z_b)$; equation 3.8), power or parabolic profile. The integer of the vertical shape function from z_b=0 to z_b=1 yields one, such as the mean flow velocity equals the input one U_{mean}.

$$U(z_b) = U_{mean}.T(z_b) \tag{3.7}$$

$$T_{log}(z_b) = 1 + \frac{\sqrt{C_f}}{k}.\left(1 + ln(z_b)\right) \tag{3.8}$$

where k=0.4 is the von Karman constant, and C_f the friction coefficient (equation 3.9)

$$C_f = \frac{g\prime.H.S}{U_{mean}^2} \tag{3.9}$$

Subaqueous density currents stream-wise velocity vertical profile classically displays a belly-shape, with a maximum velocity located close to the channel floor (Kneller et al., 1999; Hosseini et al., 2006; Islam and Imran, 2010; Sequeiros et al., 2010). The height of the velocity maximum decreases as the channel slope increases and/or the flow stratification becomes stronger (Stacey and Bowen, 1988; Sequeiros et al., 2010; Abad et al., 2011; Giorgio Serchi et al., 2011). Note that flow stratification depends on the Froude number, subcritical flow showing limited stratification (Sequeiros et al., 2010; Cortés et al., 2014; Peakall and Sumner, 2015). Vertical velocity profile models were proposed based either on a piecewise function (Hosseini et al., 2006), a cumulative Gaussian-distribution coupled with a fluvial profile (Kneller et al., 1999), or an even more numerically complex function (Bolla Pittaluga and Imran, 2014). However, all these functions cannot be directly integrated, which may cause some issues for numerical modeling, for instance to easily fit a vertical velocity profile knowing its mean value.

Hence, we propose a new vertical velocity profile model for subaqueous flows that can be relatively easily integrated. This profile is based on equation 3.7, where the subaqueous shape function $T_{subaq}(z)$ relies on a fluvial shape function $T_{log}(z)$ (equation 3.8) plus a corrective function (equation 3.10) derived from a cosine-based equation 3.($T_{corr}(z)$; equation 3.11).

$$T_{subaq}(z_b) = A\,T_{log}(z_b) - B\,T_{corr}(z_b) \tag{3.10}$$

$$T_{corr}(z_b) = \left(1 - cos(\pi\, z_b)\right)^{\alpha} \tag{3.11}$$

In addition to the flow height, the subaqueous shape function is adjusted using 4 parameters. The friction coefficient C_f accounts for friction at the upper interface and the bed, and adjusts the height of the maximal velocity. *A* and *B* control the influence of the fluvial and corrective functions respectively, as well as the maximal and minimal velocities. The parameter α controls the opening of the belly-shape and secondarily the height of the velocity maximum.

The integer over the flow height of the corrective function is given by equation 3.12. Constraints on the four fitting parameters comes from the condition of unity of the integer of T_{subaq} such as α>0.5.

$$\int_0^1 T_{corr}(z_b)\, dz_b = \frac{2^{\alpha}\Gamma\left(\frac{1}{2}+a\right)}{\sqrt{\pi}\,\Gamma(1+a)} \qquad if\ Re[\alpha] > \frac{1}{2} \tag{3.12}$$

where Γ is the Gamma function, and $Re[\alpha]$ is the real part of α.

This profile is able to reproduce a wide spectrum of velocity vertical profiles (Figure 3.5) that correspond to variable flow conditions (i.e. subcritical to supercritical) with varying degree of flow stratification. The parameter α of the vertical velocity function proposed here, which controls the opening of the belly-shape and then reflects the degree of flow stratification, is related to the Froude number such as a threshold of 0.5 may correspond to the transition from supercritical (Fr>1, α<0.5) to subcritical flows (Fr<1, α>0.5).

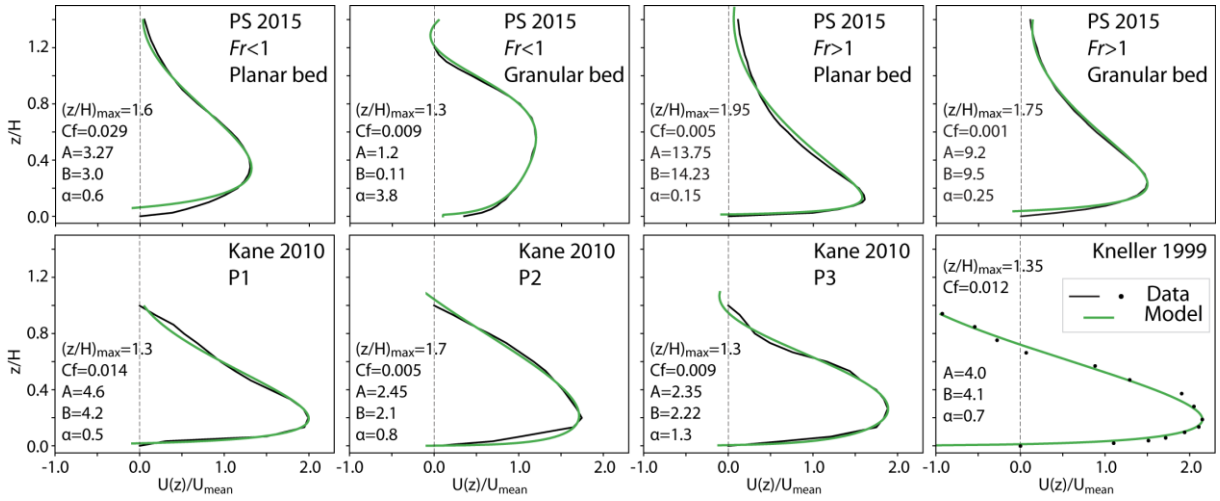

Figure 3.5: Examples of velocity vertical profile models (equations 3.10 and 3.11, in green) fitted to published experimental data (black) from Peakall and Sumner (2015) (PS 2015), profiles P1, P2, P3 in Kane et al. (2010), and Kneller et al. (1999). Fr: Froude Number, C_f: friction coefficient, z: elevation, H: flow thickness, A, B, α: fitting coefficients.

3.3. Results

3.3.1. Flow velocity vertical profile along the straight channel

3.3.1.1. Fluvial experiments

PIV analysis in the straight channel resulted in the velocity vector map given in Figure 3.6a, from which the transverse velocity profile in Figure 3.6b was extracted. The stream-wise velocity transverse profile follows a parabolic shape with the highest velocity (0.65 m/s) in the middle of the channel, and a lower velocity along the banks. The mean measured velocity was 0.56 m/s.

Combining the measured transverse velocity profile with the logarithmic profile (equations 3.7 and 3.8 – Figure 3.6c) we obtained the cross-sectional subaerial flow field in Figure 3.6d, which shows the highest flow velocity at the water surface in the middle of the channel, and the lowest velocities along the banks and right above the channel floor.

The mean velocity computed from this profile reached 0.52 m/s (Table 3.1) which was around 80% of the measured maximal velocity. The flow depth was 1.7 cm and it results in a Froude number around 1.3 (Table 3.1) that corresponds to a slightly supercritical flow and which agrees with the observation of waves near the inlet. The flow was fully turbulent as shown by the Reynolds number around 9000 (Table 3.1). The resulting upscaled flow would be a 3 m deep (mean depth) and 30 m wide river, with a flow velocity of 6.9 m/s and a discharge of 622 m^3/s.

Table 3.1: Flow parameter comparison of subaerial and subaqueous experiments in the straight channel

		H (m)	U_{mean} (m/s)	Q_{comp} (L/s)	f_{drive} (N/m)	Fr	Re
Subaerial		0.017	0.52	1.52	19.62	1.3	9010
Subaqueous	Whole flow	0.04	0.016	0.11	0.35	0.19	620
	Confined flow	0.017	0.069	0.20	0.35	1.26	1137
Ratio (Subaqueous whole)		0.42	32.5	13.9	56	6.8	14.5
Ratio (Subaqueous confined)		1	7.5	7.7	56	1.0	7.9

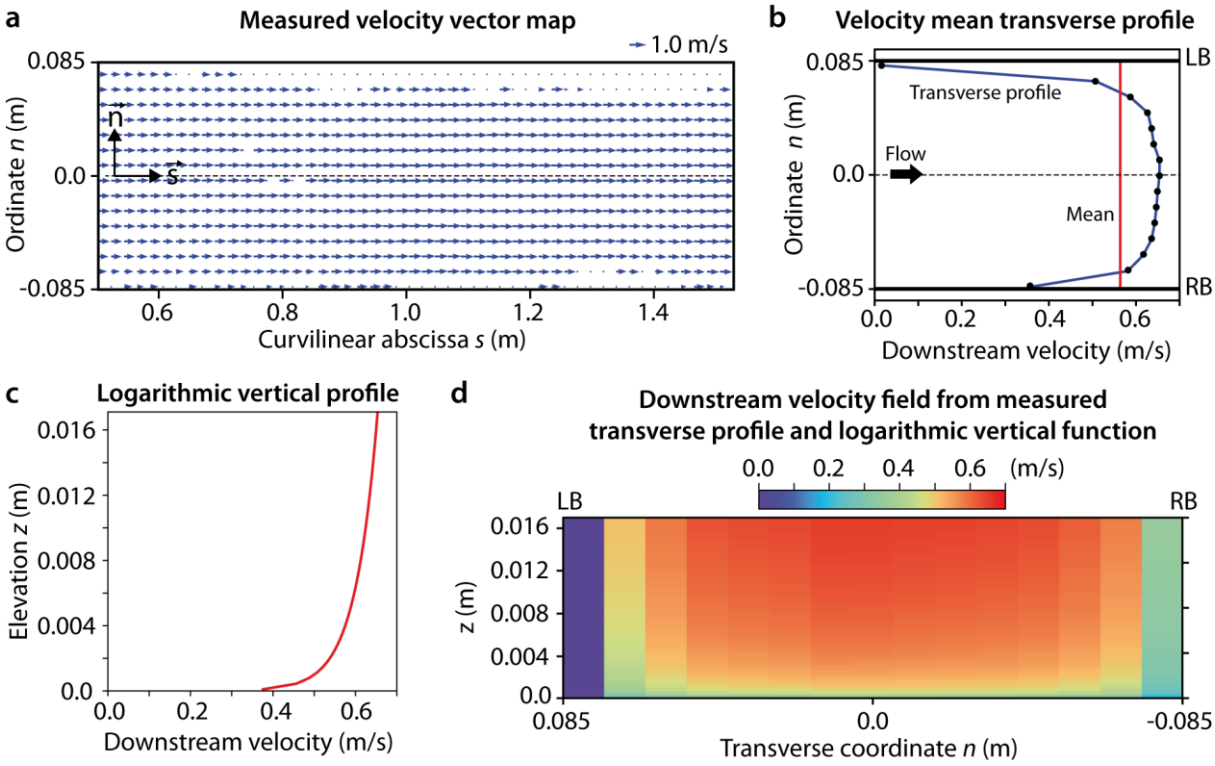

Figure 3.6: Subaerial experiment in the straight channel: (a) PIV derived velocity vector map, (b) transverse velocity profile computed from the vector map combined with the (c) logarithmic vertical profile to derive (d) the subaerial flow stream-wise velocity field in a transverse section. LB: left bank, RB: right bank.

3.3.1.2. Subaqueous flow

Flow velocity in the straight channel was recorded up to 75 mm, but positive velocities are observed until around 40 mm above the channel floor (Figures 3.7a, 3.7b). Hence, the flow was around 2.3 times thicker than the channel. The velocity field displays a decreasing upward trend (Figures 3.7a, 3.7b), with the maximal velocity along the channel floor, and a null velocity around 0.05 m. The fitted vertical profile (equations 3.7 to 3.11) reached a flow height of 64 mm and a mean velocity of 0.029 m/s, with the coefficients: C_f=0.0007, A=3.8, B=2.9, and α=0.5. Moreover, a strong

upward velocity component is also observed directly above the bed (Figure 3.7a), and a right-oriented component on the upper left side of the section that explains the asymmetrical longitudinal velocity profile. The extracted longitudinal velocity section from 5 mm above the channel floor (Figure 3.7c) shows a tight belly-shaped profile with a velocity peak along the centerline and null values along the banks. The mean velocity of this transverse section was 0.05 m/s while the maximum was twice higher (up to 0.09 m/s).

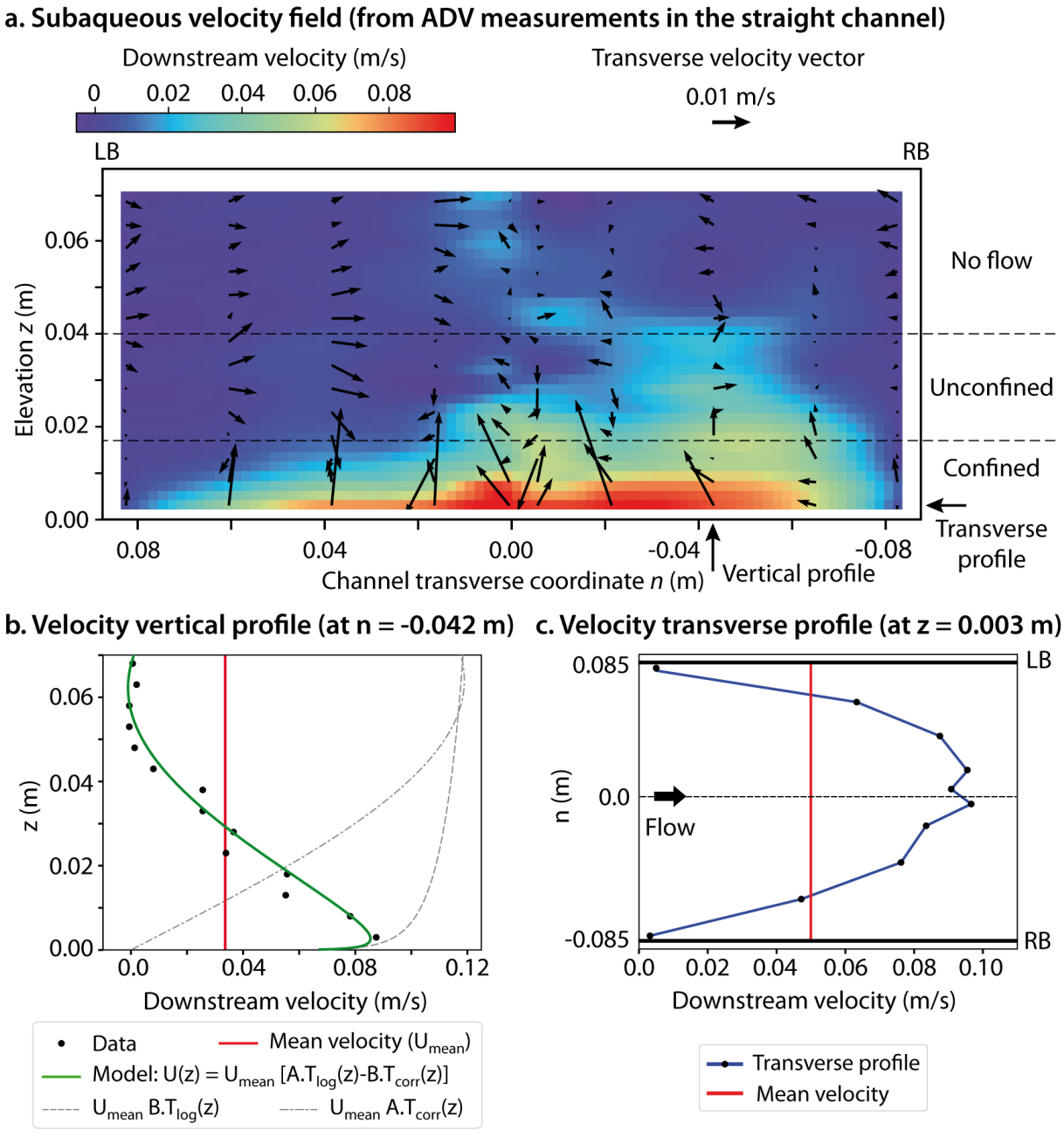

Figure 3.7: Subaqueous flow velocity field in the straight channel (a), and (b) extracted vertical profile at n -0.042 m and (c) transverse profile at z=0.003 m. See equations 3.7 to 3.11 for the expressions of the shape functions T_{log} and T_{corr}.

The mean velocity within the first 4 cm thick layer was 0.016 m/s (Table 3.1). It corresponds to an overall low Froude (0.19) and Reynolds (620) numbers, and is equivalent to a submarine flow 181 m thick, with a velocity of 1.1 m/s and a discharge of 150 m^3/s, within a channel 770 m wide. The mean velocity of the confined flow (i.e. inside the layer corresponding to channel depth – 1.7 cm) was 0.069 m/s which corresponds to a supercritical (Froude number 1.26) and slightly turbulent (Reynolds number >1100) flow (Table 3.1). The confined part would be equivalent to a 77 m thick submarine flow, with a velocity of 4.3 m/s and a discharge of 255 m^3/s.

3.3.2. Velocity field along the sinuous channel

3.3.2.1. Subaerial flow

During the subaerial experiment in the sinuous channel, the water filled up the channel and flowed downstream following the sinuous path. The mean longitudinal velocity was 0.26 m/s and flow depth is 1.7 cm (Table 3.2). This corresponds to a subcritical (i.e. Froude number of 0.64) and turbulent (i.e. Reynolds number >4400) flow. Compared to the straight channel (Table 3.1), the velocity and associated Froude and Reynolds numbers were twice lower. The equivalent upscaled flow yielded a velocity of 4.5 m/s and a discharge of 411 m^3/s.

Table 3.2: Flow parameter comparison of subaerial and subaqueous experiments in the sinuous channel

		H (m)	U_{mean} (m/s)	Q_{comp} (L/s)	f_{drive} (N/m)	Fr	Re
Subaerial		0.017	0.26	0.75	17.2	0.64	4420
Subaqueous*		0.017	0.033	0.095	0.31	0.60	543
Ratio	Confined flow	1	7.9	7.9	55	1.07	8.1

* Assuming that the measured velocity is the mean velocity of the confined flow.

Due to channel morphology, the velocity field became asymmetrical with the highest velocities observed along the inner bank and the lowest ones along the outer banks particularly in the bends (Figure 3.8a). The Figure 3.8b shows the velocity deviations and the normalized cross-stream velocity along the left and right banks of the channel from bend 2 to 4. Velocity deviations were positive (purple area in Figures 3.8 b1, b2) along the inner bank (in green) and negative along the outer bank (in white). The maxima of the velocity deviations in absolute values were around bend apexes, and they were null around inflexion points.

Cross-stream velocities were positive between the apexes of bends 2 and 3 and negative between the apexes of bends 3 and 4 along each channel bank (Figures 3.8 b3, b4). The extreme values were around inflexion points and they are null around apexes. Positive (negative) cross-stream

velocities along the left (right) bank mean that the water flows against the bank and correspond to the purple area in Figures 3.8 b3, b4.

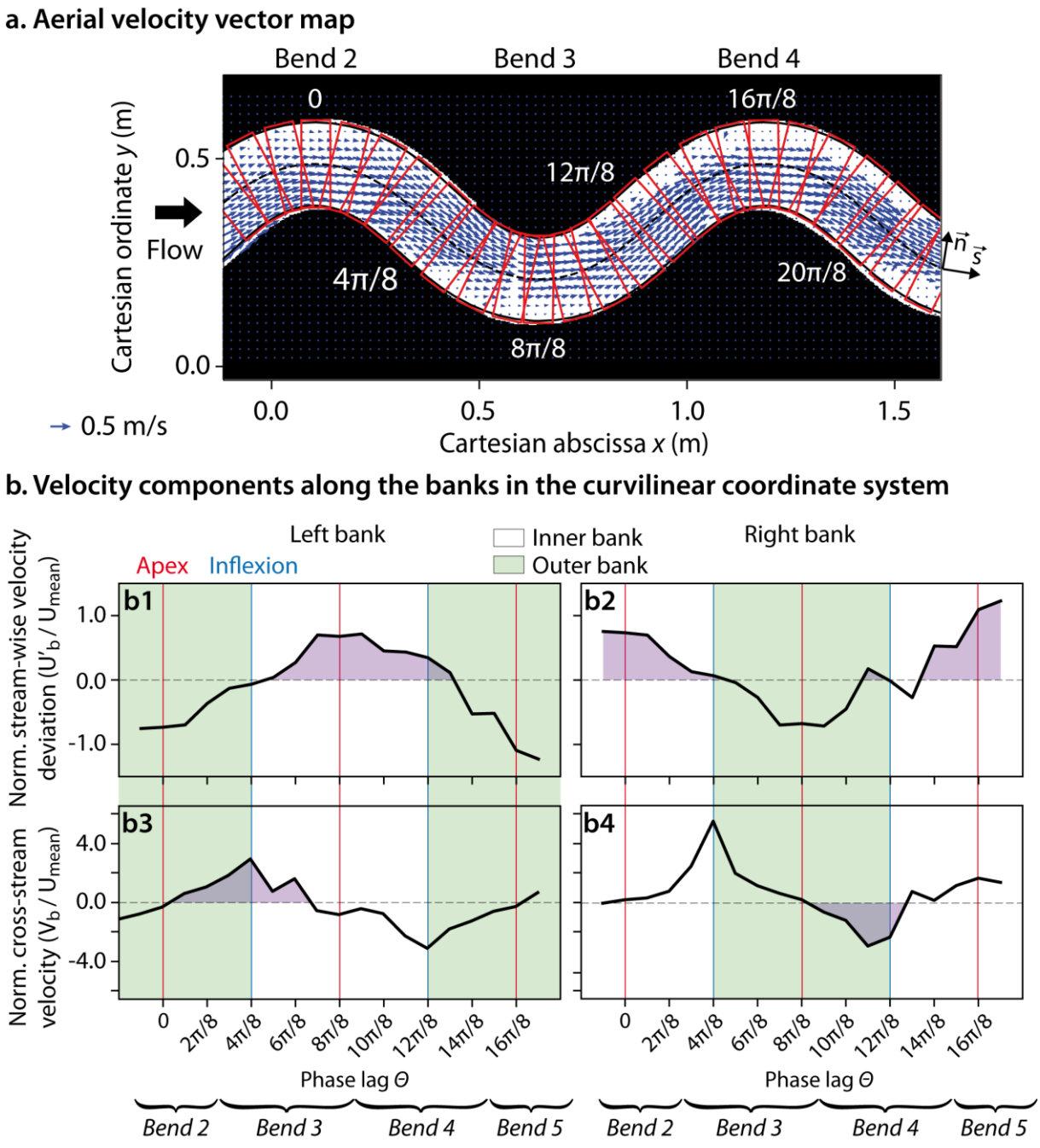

Figure 3.8: Subaerial flow velocity vector map derived from PIV measurements in the sinuous channel (a), and extracted normalized velocity deviations U'_b (b1, b2) and normalized cross-stream velocity V_b (b3, b4) along the left and right channel banks.

3.3.2.2. Subaqueous flow

During the experiments, we observed that the subaqueous flow follows the channel morphology even though over spilling is observed particularly right downstream the two first bend apexes. However, the particles used for PIV measurements never left the channel which suggests that they were confined by the channel.

The flow was asymmetrical due to channel morphology (Figure 3.9a). The mean measured velocity was 0.033 m/s (Table 3.2) but it reached 0.073 m/s along the inner bank. Assuming a flow depth of 17 mm, the flow was thus subcritical (Froude number 0.6) and laminar (Reynolds number 543). Compared to the confined part of the subaqueous flow in the straight channel (Table 3.1), the velocity and associated Froude and Reynolds numbers were twice lower. The equivalent of the confined flow in the sinuous channel yielded a velocity of 2.2 m/s and a discharge of 255 m^3/s.

The figures 3.9 b1, b2 shows that stream-wise velocity deviations reached extreme values right upstream of bend apexes (red lines), between the apex and the upstream inflexion point (blue lines). They were positive (in purple) at the outer to inner (from white to green areas) bank transition, and negative at the inner to outer transition.

Cross-stream velocity variations display lags (Figures 3.9 b3, b4) due to absence of video recording during the experiments (Figure 3.9a). However, available data are consistent with the velocity deviations, with extreme values around inflexion points. Cross-stream velocity was positive – i.e. which means that the current flows against the bank – at outer to inner transition (in purple), and negative at inner to outer transition.

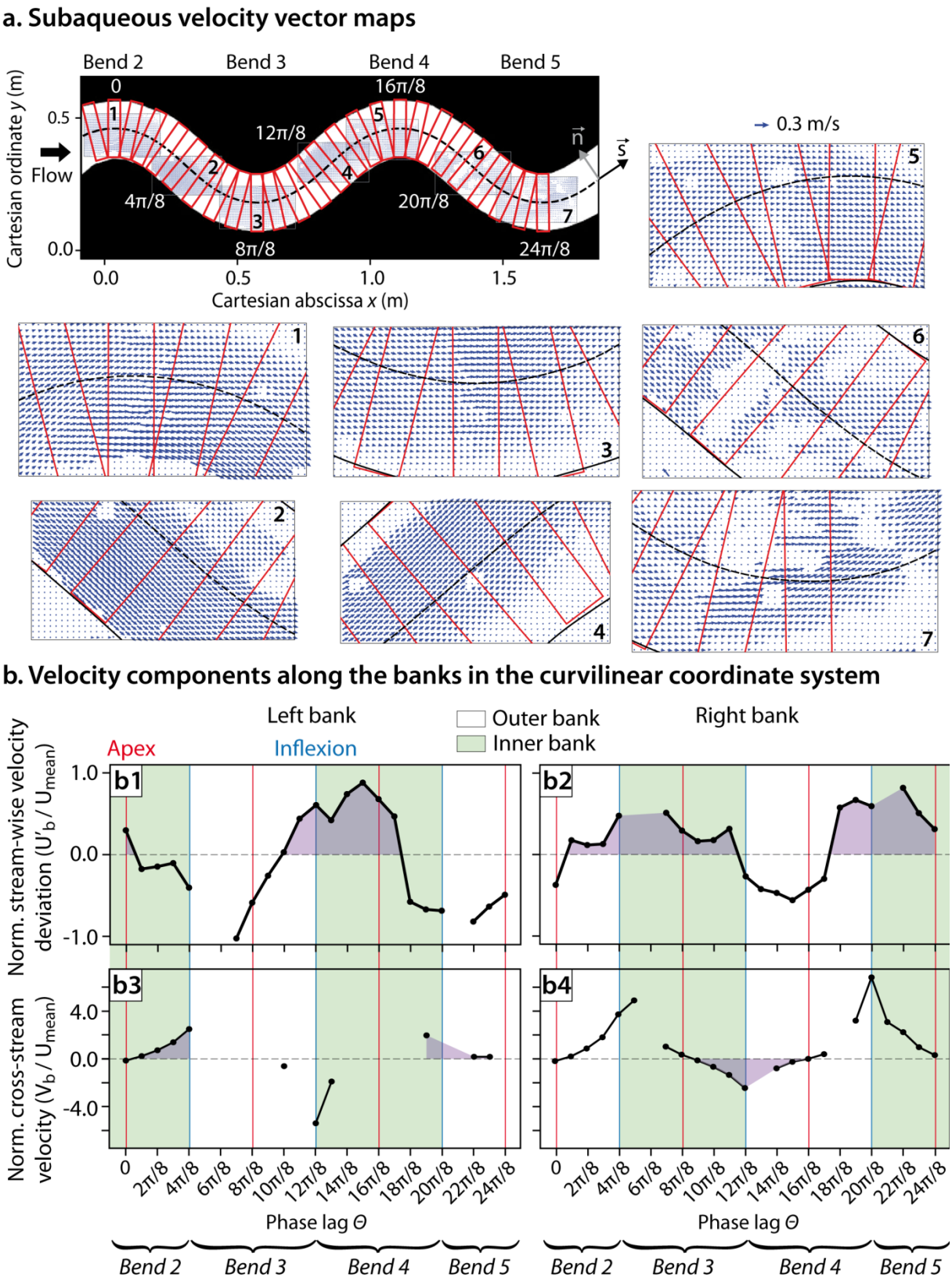

Figure 3.9: Subaqueous velocity vector map from PIV measurements in the sinuous channel (a), and extracted normalized velocity deviations U'_b (b1, b2) and normalized cross-stream velocity V_b (b3, b4) along the left and right banks.

3.4. Discussion

This study compares subaerial and subaqueous flow velocity fields using the same channel morphology, and based on PIV measurements that capture flow velocity field all along the channel. This technique was applied for the first time to subaqueous flows and recorded the velocity of the flow basal layer. The results show that the subaqueous flow velocity field adjusts faster to the channel morphology compared to subaerial flows. These results are discussed in terms of existing migration theories, mainly based on the flow stream-wise velocity deviations (Figure 3.1).

3.4.1. Comparison of subaerial and subaqueous flows

In this study we propose a new stream-wise velocity vertical function for subaqueous flows based on the weighted sum of the fluvial vertical logarithmic profile and a cosine-based function (equation 3.10). This function fits the commonly described belly-shape (Garcia, 1990; Hosseini et al., 2006; Islam and Imran, 2010; Sequeiros et al., 2010), where maximal flow velocities are near the bed and then decreases toward the top of the flow. By adjusting the fitting variables, the proposed function reproduces a large spectrum of velocity vertical profiles (Figures 3.4 and 3.6) corresponding to variable flow conditions (i.e. subcritical to supercritical) with varying degree of flow stratification. Flow stratification partly depends on the Froude number of the flow (Sequeiros et al., 2010; Cortés et al., 2014; Peakall and Sumner, 2015). Interestingly, the parameter α of the vertical velocity function proposed here is related to the Froude number, such as a threshold of 0.5 may correspond to the transition from supercritical (Fr>1, α<0.5) to subcritical (Fr<1, α>0.5) flows. Hence, a refined function that directly depends on the Froude number instead of the parameter α may be derived. Yet, contrarily to previously proposed vertical velocity profiles (Kneller et al., 1999; Hosseini et al., 2006; Bolla Pittaluga and Imran, 2014), the function developed here can be directly integrated and is thus of use to numerical modelers of submarine gravity flows that would need to derive a simplified velocity vertical profile knowing its mean value. Finally, for numerical models that simulate both fluvial and submarine flows, the same function also accounts for fluvial flow by setting the weighting constant of the fluvial profile to one, and the one of the corrective profile to zero.

Velocity profile analysis suggests that the basal layer of subaqueous flows is better suited than the whole flow for comparison with subaerial flows. Indeed, when considering the confinement depth, fluvial and subaqueous flow experienced the same variations of velocity (divided by 2) between the straight and the sinuous channels (Tables 3.1 and 3.2). In addition, the subaerial flow displays the same Froude number (1.3 in the straight channel and 0.6 in the sinuous one) as the confined subaqueous flow, even though the Reynolds numbers are 9 times greater. This result is also

supported by natural observations (Paull et al., 2018) and numerical simulations (Luchi et al., 2018), which highlight the division of the flow in a steady basal driving layer overlaid by a driven layer due to flow stratification. The simulations particularly highlighted this phenomenon under conditions of zero net sediment fluxes at the channel bed and limited mixing, which corresponds to the present case: saline flows inside non-erodible channel. Consequently, this basal driving layer most likely corresponds to the channel forming flow according to the fluvial definition of Wolman and Miller (1960).

3.4.2. PIV for subaqueous flows

To our knowledge, this study is the first to use PIV technique applied to subaqueous flows. For subaerial flows, PIV relies on paper dots that float on the free surface of the flow. The measured velocity is thus the maximal flow velocity. Such a free surface does not exist in subaqueous flows (Figure 3.6a) where the transition between density current and ambient fluid is a diffuse mixing layer. Consequently, the main difficulty for subaqueous flows was to find particles with the right density allowing them being transported in suspension in the flow. The use of millet grains, previously soaked with the saline water, are transported above the bed within a layer several millimeter thick, but thinner than channel depth (<17 mm). Hence, PIV technique applied to subaqueous flows captures here the layer of maximal velocity. We acknowledge that some uncertainties exist on absolute velocities, but we emphasize that variations of velocity are still captured using this technique which allows us to compare subaerial and subaqueous velocity fields in response to channel morphology.

In addition, PIV technique is much easier and cheaper to use than UDVP (ultrasonic Doppler velocity profiling). As mentioned by Peakall and Sumner (2015), it may bring valuable results on subaqueous processes, for instance the response of the flow velocity field to changes of parameters such as the excess density and viscosity of the flow that represent variations of overall sediment and mud concentrations respectively, or the channel geometry and slope. Furthermore, if particles are transported at different elevations within the flow and if these elevations can be precisely extracted, PIV technique could be used to study secondary current dynamics.

3.4.3. Channel migration

The experiments presented here show that the velocity field of the subaqueous flow adjusts faster to the channel morphology than that of the subaerial flow (Figures 3.8a, 3.9a). This result is in agreement with the observation of lower wavelength-to-width ratios for submarine bends than

continental ones (Pirmez and Imran, 2003; Chapter 2). Nevertheless, Sahagian et Diplas (2017), recalling the ubiquitous character of meandering process, postulated that meander initiation occurs in response to an adverse pressure gradient to the main direction of the movement. A lower wavelength-to-width ratio would suggest a higher pressure gradient that enhances the flow to divert from its main direction. Such a higher pressure gradient may result from friction at the upper interface of the flow, in addition to friction at the lower one, which does not exist for rivers. This theory may be tested using a more viscous ambient fluid that would enhance friction at the upper interface of the flow. Yet, subaqueous flows show here a 9 times lower Reynolds number than subaerial flows, which accounts for the scaling of the viscous forces compared to the inertial ones. Thus a lower Reynolds number means a higher impact of viscous forces on the flow and thus a relatively higher adverse pressure gradient.

Channel lateral migration theory assumes that the migration rate is proportional to the stream-wise velocity perturbation along the bank (Ikeda et al., 1981; Johannesson and Parker, 1989). Channel migration is related to bank erosion rate, which itself may be influenced by the shear stress created by the flow against the bank (Smith and McLean, 1977; Kean and Smith 2006; Darby et al., 2010). The highest the longitudinal velocity, the highest is the shear stress. The maximal velocity deviation of subaerial flow is located along the inner bank at bend apexes (Figures 3.8 b1, b2). Thus according to the theory, subaerial channel migration would occur preferentially along the inner side of bend apexes, reducing channel sinuosity. Such inner-side migrations were reported in tight fluvial bends (Hickin, 1978; Nanson, 2010) which is coherent with the wavelength-to-width ratio 2.5 times lower in these experiments compared to natural fluvial ratios (Leopold and Wolman, 1960; Williams, 1986). The subaqueous channel would experience a downstream migration with low variations of bend amplitude. Indeed in the subaqueous experiments herein, the velocity deviation of subaqueous flow is located upstream of bend apexes, in the inflexion zone at the outer to inner bank transition (Figures 3.9 b1, b2). The subaqueous transverse profiles extracted from PIV measurements are similar to those observed by Keevil et al. (2007) from UDVP measurements at 7 and 17 mm above the channel floor.

Alternatively to the common velocity perturbation-driven migration model, one may suggest that flow direction in a curved channel is equally important. For instance, a given flow directed against the outer bank must be more erosive than the same flow oriented away from this bank. As a result, the transverse component of the velocity can have a significant impact on the location of preferential erosion by firstly affecting the distribution of the stream-wise velocity, and secondly by changing the incidence angle of the flow against the bank. Mishra et al. (2018) highlighted the role of sediment transport vector direction in the abrasion mechanism for bedrock river bank erosion.

However, little is known about the impact of the transverse (and the vertical) component of the velocity on bank erosion. This behavior is of interest since it may highly improve migration models that do not explicitly simulate sediment erosion and deposition (Ikeda et al., 1981; Sun et al., 1996; Imran et al., 1999; Zollezzi and Seminara, 2001; Lopez et al., 2008; Frascati and Lanzoni, 2010). The experiments presented here show consistent cross-stream velocities along the channel banks in both in subaerial and subaqueous configurations (Figures 3.8 and 3.9 b3, b4). The remaining question is how the velocity cross-stream component affects the shear stress along the banks and thus the locus of preferential erosion?

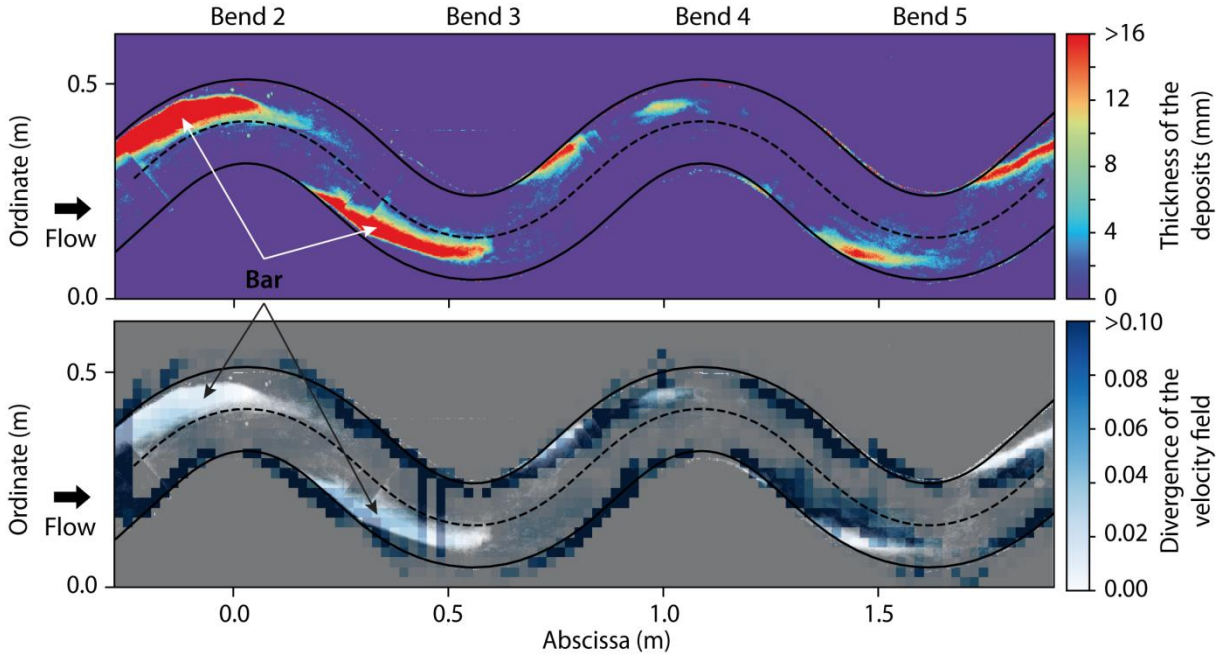

Figure 3.10: Location of the deposits in the sinuous channel under subaerial conditions, and comparison with the divergence of the velocity field.

Finally, channel lateral migration is controlled by both erosion at one side that tends to increase channel width, and deposition at the opposite side that tends to reduce channel width (Eke et al., 2014), although recent work emphasizes the primary role of erosion (van de Lageweg et al., 2014). The subaerial experiments of sediment deposition carried out here lead to the formation of bars right downstream bend apexes, in the inner to outer bank transition zone (Figure 3.10). The location of deposition is related to the locus of maximal divergence of the velocity field (Figure 3.10). Consequently, cross-stream velocity variations also directly impact the location of the deposition. While the erosion should occur around bend apexes (Figure 3.8) according the theory of maximal velocity perturbations, deposition occurs slightly upstream. Hence, differences between erosional and depositional processes are responsible for local changes of channel width (Eke et al., 2014) with

positive feedback and the locus of erosion and deposition, and may thus introduce asymmetrical bank migration, and then cause irregularities during bend development.

3.4.4. Conclusion

In this study, velocity fields of subaerial and subaqueous experiments using similar straight and sinuous channel morphologies were compared. Velocity field measurements in the sinuous channel were achieved using the PIV (Particle Image Velocimetry) technique, which was a first in the case of subaqueous flows. The results support that PIV measurements capture significant behavior of the flow velocity core. We propose a new velocity vertical profile for both fluvial and subaqueous flows based on the weighted sum of a fluvial-like logarithmic profile and a cosine-based function. This function is able to reproduce various submarine velocity vertical profiles corresponding to varying flow conditions more or less stratified, and can thus be used for instance in numerical models.

We find that subaqueous flow velocity field adjusts faster to the channel morphology than the subaerial flow one as shown by the maximal stream-wise velocity deviation along the bank between the inflexion zone and the apex for subaqueous flows, whereas it is located along the inner bank at apexes in the case of subaerial flows. These results explain the smaller submarine bend dimensions compared to river ones relatively to channel width. However, the experiments also reveal cross-stream velocity profiles of subaqueous flows similar to that of subaerial ones. This component of the velocity is never taken into account when calculating the shear stress that controls bank erosion, although it may change migration behavior. Further investigations are needed to better understand how the cross-stream velocity modifies the flow shear stress on the channel floor and along the banks, and then sediment deposition and bank erosion that control channel lateral migration.

Ce chapitre propose une nouvelle fonction permettant de modéliser les profiles verticaux de vitesse des écoulements turbiditiques et fluviatiles par ajustement de ses coefficients. Cette fonction sera ainsi intégrée dans Flumy pour la modélisation de l'écoulement. De plus, ce travail expérimental met en lumière les différences de champ de vitesse des écoulements aériens et sous-aquatiques en réponse à une même morphologie de chenal. Les résultats présentés dans ce chapitre demandent néanmoins à être consolidés par des expériences complémentaires utilisant notamment la technique de PIV développée ici pour les écoulements sous-aquatiques.

Les résultats issus des chapitres 2 et 3, établis par des approches naturaliste et analogique, ont été intégrés pour la transposition de Flumy aux systèmes turbiditiques. Les deux chapitres suivants présentes le modèle turbiditique de Flumy et ses application.

Chapitre 4.

Reproduction of submarine channel-belt architecture and quantification of channel kinematics using a forward model

Abstract

Submarine channel mobility parameters are very poorly constrained due to the cost of acquiring time-related data and the slow evolution of these channels. Previous studies show that, after a phase of bend growth, submarine channel planform morphology tends to stabilize together with increasing channel aggradation creating a concave-up trajectory when observed in cross-sections. A reduced-complexity process-based model was developed to simulate submarine channel evolution including channel migration, aggradation through flow overspill and flow stripping, and avulsions. Channel-belts are simulated over five activity durations from 2000 to 10,000 years such as to respect the dimensions observed by Jobe et al. (2016). Channel kinematics are characterized by both dynamic and stratigraphic mobility numbers, computed from extracted channel centerlines. We find that: 1) channel-belt first-order stratigraphic architecture is accurately reproduced using migration rates (0.05-0.3 m/yr) one order of magnitude smaller than those of fluvial systems and channel aggradation rates of 9-45 m/kyr. 2) The stratigraphic mobility number is not a true equivalent of channel dynamic mobility number, but rather provides a lower limit of it, 3) flow stripping alone does not fully explain submarine channel stabilization, but 4) change of bend growth direction relatively to the cross-section one is partly responsible for observed concave-up trajectory.

4.1. Introduction

Submarine channels act as the main sediment transfer route from the continent to the ocean (Shepard, 1963; Mutti and Normark, 1991; Stow and Mayall, 2000; Deptuck et al., 2007; Wynn et al., 2007). Submarine channels show a high degree of lateral mobility through lateral migration (Abreu et al., 2003; Deptuck et al., 2007; Jobe et al., 2016), avulsions (Kolla, 2007), and vertical mobility through aggradation or incision (Jobe et al., 2016). Very scarce studies tried to quantify channel evolution and kinematics (Talling et al., 2015). The lack of such studies can be explained by the slow evolution of submarine channels and the cost of surveying the modern ones, or the difficulty of acquiring time-related data on fossil systems. However, channel evolution plays a key role on the architecture of channelized turbidite reservoirs (Clark and Pickering, 1996; Mayall et al., 2006). Submarine channel evolution may also be of interest when building long-term offshore infrastructures such as hydrocarbon production or mining units, wind power plants, or when laying communication cables.

Submarine channel lateral and vertical mobility are respectively lower and much higher than that of rivers (Peakall et al., 2000; Wynn et al., 2007; Jobe et al., 2016). It is particularly highlighted by a combined stabilization of the channel planform morphology and an increase in the channel aggradation after a phase of bend growth (Peakall et al., 2000; Jobe et al., 2016). It results in a concave-up channel trajectory on 2D cross-sections transverse to meander bends. Among the few studies quantifying submarine channel evolution, Labourdette and Bez (2010) showed that channel kinematics depend on its degree of confinement by studying 3D displacements of characteristic points extracted from B-spline curve models of successive channel centerlines. Biscara et al. (2013) measured the lateral migration rate around 1.6 to 3.8 m/yr over a period of 50 years in the modern Cap Lopez Canyon. Finally, Jobe et al. (2016) computed from channel-belt architecture the stratigraphic mobility number (ratio of lateral to vertical channel displacements normalized by channel dimensions) that they consider as an equivalent of the fluvial mobility number (ratio of migration to aggradation rates normalized by channel dimensions) (Jerolmack and Mohrig, 2007). They found that both fluvial and submarine channels display concave-up trajectories, but submarine channels show a stratigraphic mobility number ten times lower.

Another approach to study submarine channel evolution relies on small-scale experiments, which produce valuable results on channel initiation (Straub et al., 2008; Rowland et al., 2010; Weill et al., 2014; De Leeuw et al., 2016). Numerical modeling approach constitutes a relevant tool to test hypothesis on submarine channel evolution. Many ruled-based or process-based models of submarine flows (Parker et al., 1986; Imran et al., 1999; Das et al., 2004; Basani et al., 2014; Bolla

Pittaluga et al., 2018; Traer et al., 2018a) and channel evolution (Labourdette, 2008; McHargue et al., 2011; Sylvester et al., 2011; Sylvester and Covault, 2016; Rongier et al., 2017) have been developed with varying degrees of complexity (see section 1.3).

This study aims at evaluating the potential of a reduced-complexity process-based model to reproduce submarine channel kinematics and channel-belt architecture. Even though all the processes that control channel evolution cannot be reproduced with such models, these modeling tools are much simpler to parameterize and computationally faster than more complex models, allowing testing variability. We first present the parameters used to characterize the channel kinematics and channel-belt architecture, then Flumy, the model we developed, and finally the extraction of the channel-belt parameters from the simulations. We quantify submarine channel kinematics from several scenarios and discuss flow stripping as the main driver of channel stabilization. Simulations and field data are compared and we discuss the accuracy of the stratigraphic mobility number and the processes that control channel kinematics.

4.2. Channel-belt characterization

Submarine channel-belts result from the evolution of a submarine leveed-channel from its initiation to the avulsion (Jobe et al., 2016). Submarine channel-belt width varies from 2.4 to 4.1 times the channel width, and their thickness from 1.5 to 7.8 times the channel depth. Channelized sedimentary deposits suggest a concave up channel trajectory, created by a first phase of a high channel lateral migration and a low aggradation, followed by a phase of an increasing aggradation and a decreasing lateral migration until the stabilization of the planform morphology (Figure 4.1; Peakall et al., 2000; Jobe et al., 2016).

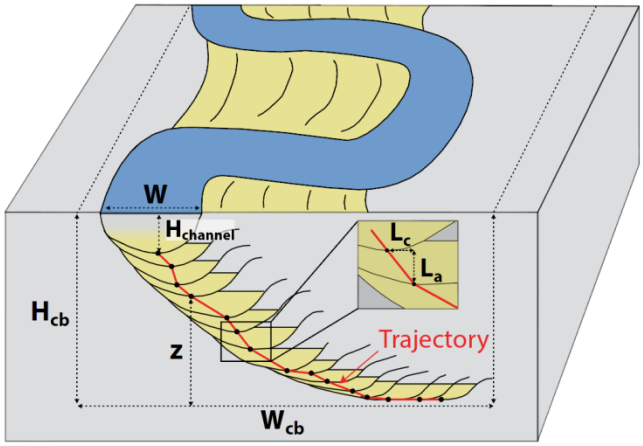

Figure 4.1: Schematic submarine channel-belt defining channel-belt width (Wcb), thickness (Hcb), horizontal and vertical channel local displacements (Lc and La respectively). W: channel width, $H_{channel}$: channel maximal thickness. (modified after Jobe et al., 2016).

However, time-related parameters (i.e. lateral migration rate, aggradation rate, and avulsion frequency) are very poorly constrained because of the limited number of absolute dating on the submarine fans. Development time is estimated to be in the range of 1000 to 10 000 years based on the studies on the Bengal fan (Schwenk et al., 2003), the Congo fan (Mansor, 2009), and the Amazon fan (Manley and Flood, 1988). Jobe et al. (2016) proposed to characterize channel kinematics by defining the stratigraphic mobility number (M_s) either at the scale of the entire channel-belt or at the scale of each migration step. The belt-averaged mobility number M_{sb} corresponds to the ratio of the channel-belt width (W_{cb}) to channel-belt thickness (H_{cb}) normalized by channel width (W) and maximal depth ($H_{channel}$) (equation 4.1; Figure 4.1; Table 4.1). The local stratigraphic mobility number M_{sl} is computed from local channel displacements horizontally (L_c) and vertically (L_a) normalized by channel dimensions (equation 4.2; Figure 4.1; Table 4.1).

$$M_{sb} = \frac{(W_{cb}-W)}{(H_{cb}-H_{channel})}\frac{H_{channel}}{W} \tag{4.1}$$

$$M_{sl} = \frac{L_c}{L_a}\frac{H_{channel}}{W} \tag{4.2}$$

The stratigraphic mobility number is derived from the fluvial mobility number (M_d) that corresponds to the ratio of the migration to the aggradation rates normalized by channel dimensions, and where the subscript *d* here accounts for *dynamic* in contrast with the *stratigraphic* one. Here again, the mobility number is defined at the scale of the whole channel-belt M_{db} (equation 4.3; Table 4.1), computed from the observed mean channel migration ($\overline{Mig}$) and aggradation ($\overline{Aggrad}$) rates, and at the scale of each migration step M_{dl} from the local observed migration (*Mig*) and aggradation (*Aggrad*) rates (equation 4.4; Table 4.1).

$$M_{db} = \frac{\overline{Mig}}{\overline{Aggrad}}\frac{H_{channel}}{W} \tag{4.3}$$

$$M_{dl} = \frac{Mig}{Aggrad}\frac{H_{channel}}{W} \tag{4.4}$$

Table 4.1: Comparison of stratigraphic and dynamic mobility numbers

	Stratigraphic	Dynamic
Belt-averaged	M_{sb}	M_{dl}
Local	M_{db}	M_{dl}

4.3. Model description

Flumy software builds facies 3D blocks at the reservoir scale by simulating processes in play in the submarine realm (Figure 4.2). Flumy has been initially developed to simulate meandering fluvial systems (Lopez et al., 2008; see Chapter 1) and we took advantage of the similarities between

both environments (Flood and Damuth, 1987; Leeder, 1999; Wynn et al 2007; Chapter 2) to implement a turbidite mode taking into account the specificities of submarine systems. Flumy simulates the evolution of a sinuous submarine leveed-channel through time (see Chapter 2). We assume that submarine meandering path results from continuous bend growth associated to channel migration as observed by Biscara et al. (2013) and suggested by the observation of lateral accretion deposits (Abreu et al., 2003; Arnott et al., 2007; Dykstra et Kneller, 2009; Hansen et al., 2017), and bend cutoffs (Lonsdale and Hollister, 1987; Babonneau et al., 2004; Deptuck et al., 2007; Jobe et al., 2016; Wiles et al., 2017).

Following Konsoer et al. (2013), we consider that average flow properties can be inferred from observed channel geometry. This hypothesis is similar to that used for the fluvial concepts of bankfull hydraulic geometry (Leopold and Maddock, 1953) and channel-forming flow discharge (Wolman and Miller 1960; Copeland et al. 2000; Blom et al., 2017). Experiments (Imran et al., 1998; Kane et al., 2008; Straub et al., 2008; Janocko et al., 2013) and numerical models (Traer et al., 2018b) support this hypothesis as they showed that channel morphology and flow properties reach an equilibrium state. Following the definition for fluvial systems, the submarine channel-forming discharge corresponds to the steady discharge that provides the same channel geometry as the succession of intermittent and varied submarine flows. Consequently, Flumy simulates a flow compatible with the input channel geometry to compute channel migration and aggradation rates through time.

The simulation domain consists in a regular pillar grid that is used to store the deposits resulting from the different simulated processes (Figure 4.2). Mesh dimensions are at least twice smaller than channel width (W). The channel is represented by its discretized centerline (centerline points spacing $< 3/4\ W$, independent from the mesh) and a parabolic shape is used when computing channelized deposit geometry. Channel geometry is parameterized by its maximal depth ($H_{channel}$), width (W), and average wavelength (λ) at the final stage of channel-belt development, before an avulsion (Jobe et al., 2016). While the channel width is kept constant, channel depth and wavelength evolve during channel-belt development due to changes of channel length, i.e. bend development and cutoffs, and slope.

The simulation starts tossing a channel centerline in the down slope direction, or importing a given one. Flumy successively computes channel migration, then channel aggradation and levee construction through flow overspills (Peakall et al., 2000; Jobe et al., 2016), flow stripping (Piper and Normark, 1983; Straub et al., 2008), and pelagic sedimentation. These processes are simulated until an avulsion occurs according to a user-defined periodic or poisson probability distribution (mean

avulsion period (T_{av}). A new channel path is then tossed following the steepest slope random walk from the avulsion node (inside or upstream the simulation domain), resulting in the building of a new channel-belt. In order to save computation time, aggradation is periodically computed using a mean aggradation rate (inferred from the desired sand proportion in the 3D block), split into a channel aggradation height (i_{ob}) and an aggradation period (T_{ob},) which can be used with a Poisson probability distribution to reproduce the variability of natural events. In the following, we consider that an iteration during a simulation equals a year in natural systems.

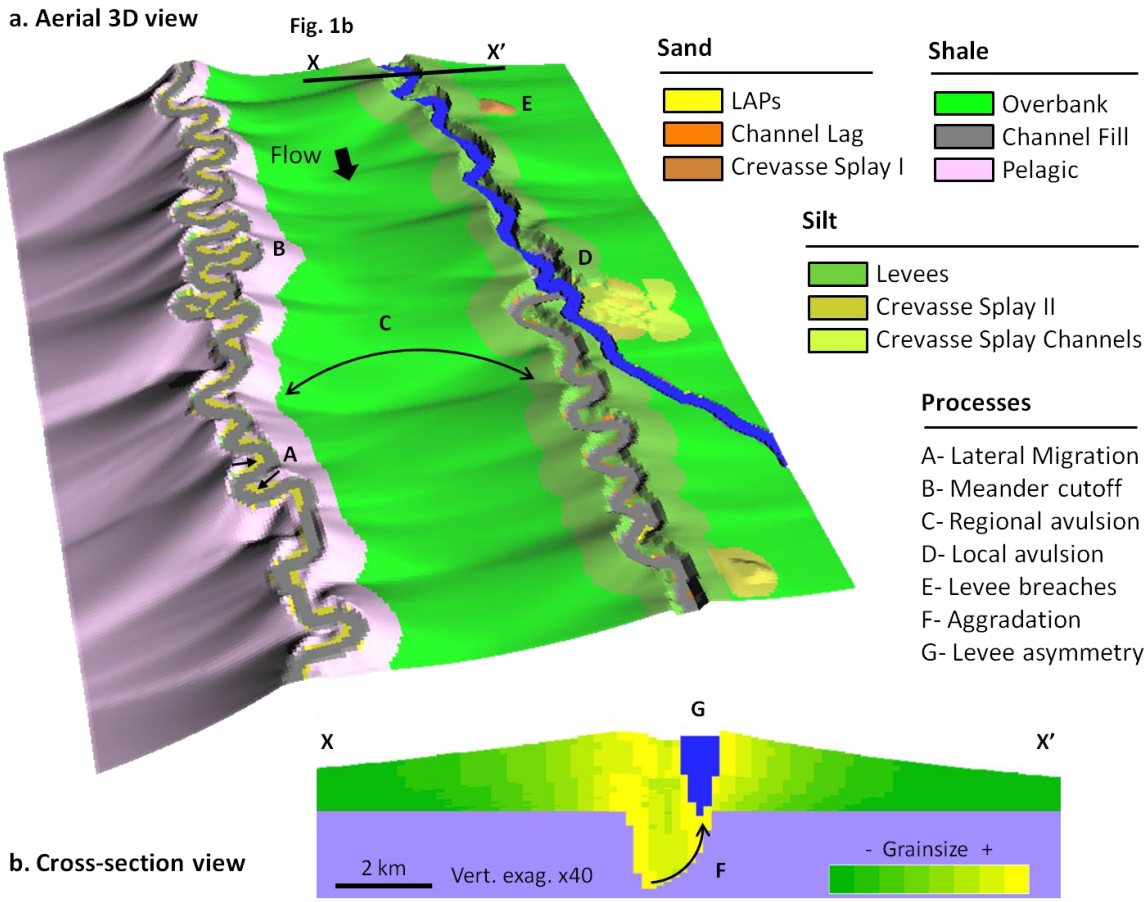

Figure 4.2: Illustration of a Flumy simulation showing the main processes and related deposits in terms of (a) facies arrangement from an aerial 3D view and (b) grain size from a cross-section.

4.3.1. Channel migration algorithm

The migration algorithm computes the channel lateral displacements. It is based on Imran et al (1999) linear model assuming that the migration vectors ($\overrightarrow{Mig_{th}}$) are proportional to the velocity perturbations along the bank (U'_b) in the transverse direction to the centerline ($\vec{n}$) (equation 4.5 – Figure 4.3a). Velocity perturbation is the difference between the longitudinal velocity of the flow and the cross-sectional averaged velocity (U_{mean}). This model of centerline migration is the direct transposition to submarine channels of the fluvial Ikeda et al. (1981) model.

$$\overrightarrow{Mig_{th}} = E.U'_b.\vec{n} \quad (5)$$

The coefficient of proportion (*E*) is called erodibility. For this study this coefficient is constant over the entire domain and during the whole simulation. Velocity perturbations are computed thanks to Saint-Venant equations that correspond to a depth-averaged flow model, combined with a linear transverse velocity profile (Figure 4.3a). This model assumes a steady, turbulent and gradually varied flow, and a flow width much greater than its thickness. These conditions are valid for subcritical dilute turbidity currents that flow on gentle slope during hours or days, and with low variations of sediment budget (Imran et al., 1999). Such channelized currents are most likely to be found downstream the Canyon, in deep-sea basins (Pirmez and Imran, 2003; Traer et al., 2018a). As suggested by Konsoer et al. (2013), we assume in the following that the mean flow height in a straight channel is equal to the maximal channel depth, and corresponds to the driving basal layer described by Luchi et al. (2018). At each channel point, these equations provide us with cross-sectional averaged flow height (H_{mean}) (equation 4.6) and velocity (equation 4.7), plus velocity perturbations (equation 4.8) and flow asymmetry on the bank (dH_{flow}, equation 4.9) which is the difference between the flow elevation and the mean flow height.

$$H_{mean} = H_{mean,0}.sinuo^{1/3} \quad (4.6)$$

$$U_{mean} = U_{mean,0}.sinuo^{-1/3} \quad (4.7)$$

$$\frac{\partial U'_b}{\partial s} + 2.\frac{Cf}{H_{mean}}.U'_b = \frac{1}{2}W.U.\left(\frac{\partial k}{\partial s} - k\frac{C_f}{H_{mean}}.(F^2 + A - 1)\right) \quad (4.8)$$

$$dH_{flow} = \frac{U_{mean}^2 W}{2.g.R.C}.k \quad (4.9)$$

In equations 6 and 7, $H_{mean,0}$ and $U_{mean,0} = \sqrt{\frac{g.R.C.H_{mean,0}.I_0}{C_f}}$ are flow mean height and flow velocity along a straight channel with a slope (I_0) equal to the input global slope, and where R (=1.65) is the sediment reduced density, C the sediment concentration, and g the gravity.

These equations account for the change of channel longitudinal slope with sinuosity (*sinuo*) and assuming a constant flow discharge. For each channel point, sinuosity is computed along an interval of one wavelength centered on the channel point.

In equation 4.8, k denotes the centerline curvature, s the curvilinear coordinate, $F^2 = \frac{U_{mean}^2}{g.R.C.H_{mean}}$ the squared Froude number, $A = A_{aff} + A_{sec}$ with A_{aff} (= 4), the scour factor of Exner equation and A_{sec} (= 3), the secondary flow coefficient (Johannesson and Parker, 1989), and C_f the

coefficient of friction. Since the channel migrates laterally, we compute the coefficient of friction such as the channel instability is maximized according to $C_f = \frac{2.\pi.H_{mean}}{4.\lambda.\left(\sqrt{1+0.5(A+F^2)-1}\right)}$ (Ikeda et al, 1981).

Jobe et al. (2016) suggested that the decreasing lateral migration rate observed from 2D cross-sections, results from flow stripping at the outer bank, which increases outer levee height and then decreases lateral erosion rate. Flumy does not explicitly simulate bank erosion, but the migration rate is slowed down by multiplication of the initial computed value (equation 4.5) by the ratio of the channel depth ($H_{channel}$) to the bank height (H_{bank}) to be eroded (equation 4.10). Bank height is defined as the distance between channel floor and the top of the bank.

$$\overrightarrow{Mig} = \overrightarrow{Mig_{th}}.\frac{H_{channel}}{H_{bank}} \tag{4.10}$$

The migration algorithm solves the set of equations (4.5) to (4.9) at each channel point along the centerline using a backward finite difference scheme. Channel migration tends to increase the length of the centerline and accordingly the distance between channel points. Conversely, in rare cases such as after bend cutoffs, the distance may also decrease. In order to ensure computation stability (Crosato, 2007; Schwenk et al., 2015) and consistent channel morphology, thresholds are applied to keep the channel point distance in the range of 0.25 to 0.75 times the channel width (W). When the distance between two points P_i and P_{i+1} becomes too large, a new point (P_{new}) is added according to equation 4.11 (Figure 4.3a), and new channel point properties are obtained by a linear interpolation of those of the upstream and downstream channel points.

$$\overrightarrow{P_iP_{new}} = \frac{1}{2}\left(\frac{0.5W}{\|\overrightarrow{P_iP_{i+1}}\|}\overrightarrow{P_iP_{i+1}} + \frac{0.5W}{\|\overrightarrow{P_iP_{i-1}}\|}\overrightarrow{P_iP_{i-1}}\right) \tag{4.11}$$

Other migration models find the location of new points using a cubic spline interpolation (Sun et al., 1996; Schwenk et al., 2015), even though such methods are more accurate they are also slower to compute.

Curvature computation highly impacts velocity perturbation and flow asymmetry calculations (equations 4.4 and 4.5). Three methods of curvature computation are usually employed in numerical models (Schwenk et al., 2015) and we implemented the most stable one which relies on the definition of the curvature $k = \frac{1}{Radius}$ where the radius of curvature *Radius* equals (equation 4.12):

$$Radius = \frac{\sqrt{\overrightarrow{P_{i-3}P_i}^2.\overrightarrow{P_iP_{i+3}}^2.\overrightarrow{P_{i-3}P_{i+3}}^2}}{2.det\left(\overrightarrow{P_{i-3}P_i}\ ,\ \overrightarrow{P_{i-3}P_{i+3}}\right)} \tag{4.12}$$

with P_i the channel point where the curvature is computed, P_{i-3} and P_{i+3} the third upstream and downstream points, respectively. This method smoothes the curvature, avoiding the occurrence of extreme values, in particular after the addition of a point during the discretization procedure (Figure 4.3a).

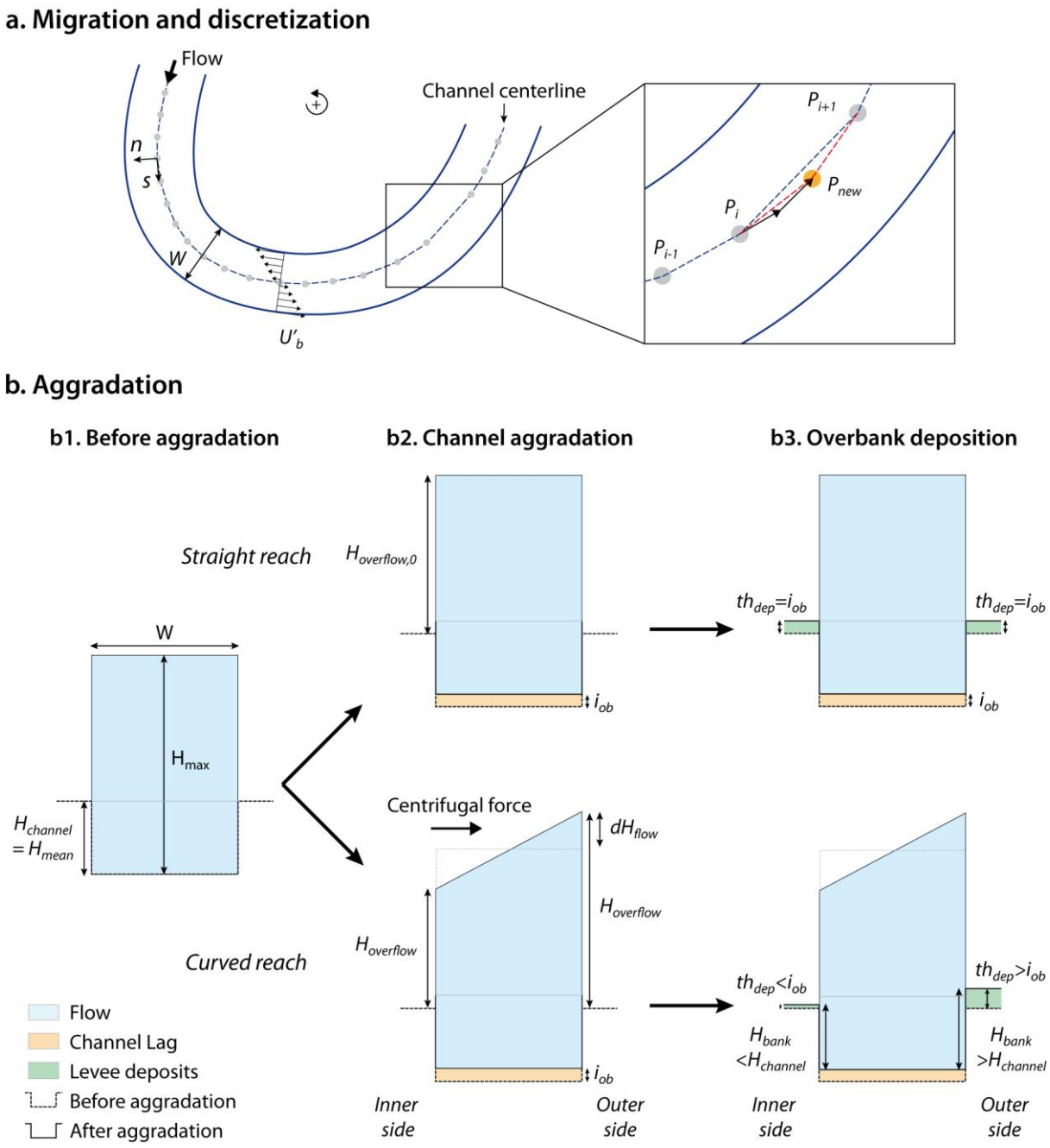

Figure 4.3: Sketch showing (a) curvilinear coordinate system, velocity perturbations (U'_b) in a bend, and discretization procedure, (b) flow model in straight and curved reaches, and differential aggradation of inner and outer levee crests due to centrifugal force.

4.3.2. Aggradation algorithm

In Flumy, aggradation is first computed for the channel, then for levee and overbank deposits. Channel aggradation occurs periodically (period: T_{ob}) with a given height (i_{ob}) (Figure 4.3b). To compute the levee and overbank thickness, the algorithm first computes the diffusion of the overflow through an exponential decay function, and then converts the overflow height into a deposit thickness. Initial overflow height is the difference of elevation between the top of the channelized flow and the top of the bank (Figure 4.3b). We assume that maximal flow height (H_{max}) is equal to three times the mean flow height (H_{mean}) based on experimental studies (Kane et al., 2008; Janocko et al., 2013; Chapter 3). In straight symmetrical channels, where the curvature is null, flow height is constant along transverse sections (equation 4.9). Thus, overflow height ($H_{overflow}$) is the same on both channel banks (by definition $H_{overflow} = H_{overflow,\,0}$ – Figure 4.3b). In curved reaches, the flow becomes asymmetrical and overflow is thicker at outer bend and thinner at inner bend than $H_{overflow,\,0}$ (equation 4.9 – Figure 4.3). The deposit thickness (th_{dep}) is computed by multiplying the overflow height by the depositional factor (f_{dep} – equation 4.13):

$$th_{dep} = H_{overflow} \cdot f_{dep} \tag{4.13}$$

where $f_{dep} = \frac{i_{ob}}{H_{overflow,0}}$.

This model reproduces asymmetrical levees in relation with channel curvature as observed on modern systems (Straub et al., 2008), and these levees follow an exponential decay profile. Several levee thickness decreasing functions (i.e. linear, power, exponential, logarithmic) away from the channel were proposed based on observations in natural submarine systems (Skene et al, 2002; Nakajima and Kneller, 2013; Ezz et al., 2014; Malgesini et al., 2015) and experiments (Bonnecaze et al., 1993; Gladstone et al., 1998; De Rooij and Dalziel, 2009; Kane et al., 2010; Dykstra et al., 2012). Birman et al. (2009) showed that the exponential trend is particularly valid under the condition of negligible water entrainment such as what happens with subcritical flows (Imran et al., 1999) modeled herein.

In conclusion, channel kinematics in Flumy depends on input channel geometry ($H_{channel}$, W, I_0) and erodibility coefficient (E) that controls channel lateral migration, and the input channel aggradation rate split into the couple overbank period (T_{ob}) and channel aggradation height (i_{ob}). Finally, the channel-belt geometry (W_{cb}, H_{cb}) depends on channel kinematic parameters and the avulsion period (T_{av}).

4.4. Methodology

4.4.1. Simulation parameters

Simulation parameters are chosen to match those observed on natural systems. We ran simulations with (Table 4.2): 1) a 600 m wide and 40 m deep channel corresponding to the median geometry observed by Jobe et al (2016); 2) a final wavelength of 3000 m and a regional slope of 0.005 in agreement with the observed median values in submarine systems (Pirmez and Imran, 2003; Chapter 2), 3) a simulation domain of 37.5x30 km² (250x200 cells) that allows over 30 meander loops to develop during simulations.

To reproduce the variability in the avulsion periods (Manley and Flood, 1988; Schwenk et al., 2003; Mansor, 2009), we perform five sets of simulations (Table 4.2) with a development time (T) that ranges from 2000 to 10,000 iterations, and by adjusting the erodibility and aggradation height (T_{ob}=25 iterations in all sets) such as the channel-belt geometry to respect the observations of Jobe et al. (2016).

Table 4.2: Simulation parameters

Constant geometric parameters					
Channel depth $H_{channel}$ (m)	40				
Channel width W (m)	600				
Final wavelength λ (m)	3000				
Regional slope I_0	0.005				
Variable kinematic parameters depending on avulsion period					
Development time T (iteration)	2000	4000	6000	8000	10,000
Erodibility E (x10^{-8})	1.7	0.8	0.55	0.4	0.3
Channel aggradation height i_{ob} (m)	1.1	0.55	0.35	0.27	0.23

Ten channel-belts are simulated for each set of simulations, and for each one 30 channel centerlines including the first and the last ones are periodically exported. Hence, channel-belt geometry and channel kinematics are computed over 279 bends on average for each set of simulation (Figure 4.5). Cross-sections were extracted from the exported centerlines, and were used to compute the belt-averaged (M_{sb}), and the local (M_{sl}) stratigraphic mobility number at consecutive channel locations. In addition, channel displacements, simulation-averaged dynamic mobility number (M_{db}), and local dynamic mobility number (M_{dl}) at the same locations as M_{sl} were computed for comparison. To this end, two tools were developed in Python.

4.4.2. Extraction of channel-belt geometry and channel kinematics

The first tool allows tracking through time the location of meanders defined by their apex and inflexion points (Figure 4.4a). The second one automatically extracts consecutive channel locations along cross-sections transverse to meander bend at their apex.

4.4.2.1. Apex and inflexion point identification

Inflexion points correspond to points along the centerline with a null curvature and where the sign of the curvature changes. Due to the discretization of the centerline, points with a null curvature are rare, and thus, the algorithm keeps the points with the smallest absolute curvature. Moreover, to avoid misidentifications due to local change of curvature sign, distance between two consecutive inflexion points must be larger than a channel width.

The second step is to find the apex between each pair of consecutive inflexion points while taking into account the complex geometry of meander bends (Figure 4.4a). Firstly, the algorithm looks for the three points with the highest bend amplitude. Bend amplitude is taken as the distance between the apex and either the middle of the segment that links inflexion points (A_1) or perpendicularly to this segment (A_2). Both definitions are close in the case of symmetrical bends, but the former one provides with greater values and is better suited than the latter in the case of asymmetrical bends (Figure 4.4a). But in the case of low amplitude bends, where A_1 equals half the distance between inflexion points ($L_{1/2}$), A_2 becomes more relevant to define possible apexes (Figure 4.4a). Finally, the apex corresponds to the point with the highest curvature among the three points previously found. A threshold equal to 1% of the distance between inflexion points is applied on bend amplitude to discard bends too flat.

a. Bend apex definition

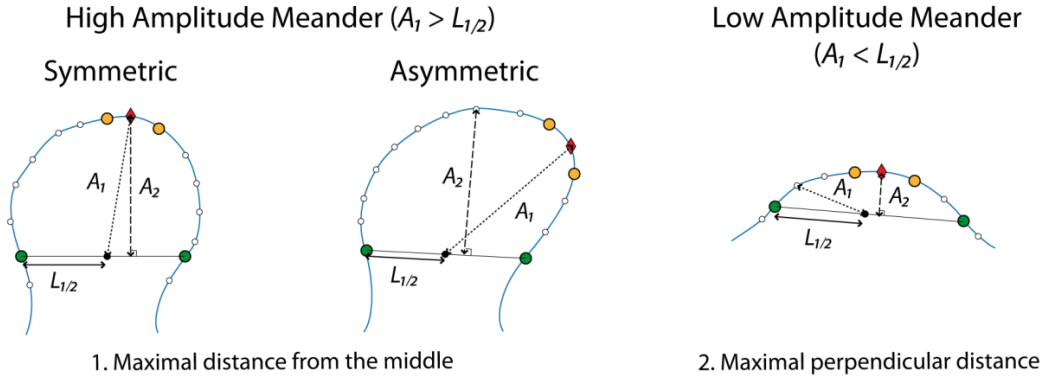

b. Channel centerline evolution during 3000 iterations

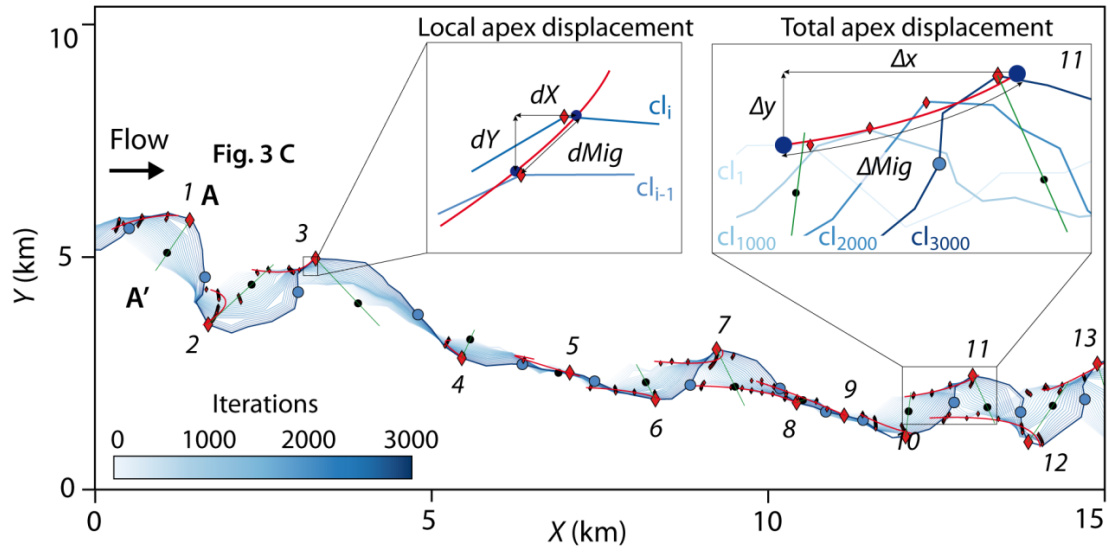

c. Cross-section across bend 1

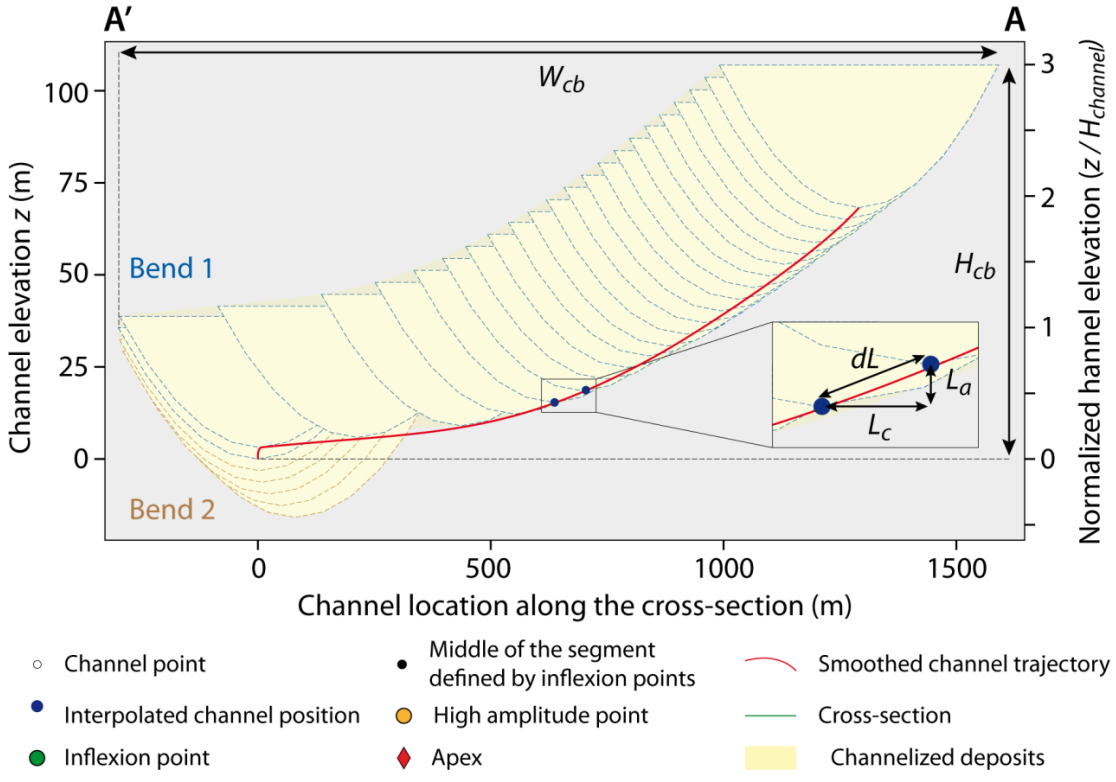

Figure 4.4: Channel kinematic parameter extraction from the simulations: (a) apex definition, (b) Flumy simulation and apex tracking tool (dX, dY, dMig account for the local apex displacements, and ΔX, ΔY, ΔMig for the total displacements in the downstream, cross-stream, and migration directions respectively), (c) simulated cross-section across bend 1 (W_{cb}: channel-belt width, H_{cb}: channel-belt thickness) and showing the apparent local channel displacements laterally (L_c) and vertical (L_a).

4.4.2.2. Bend tracking tool

The successive positions of apex or inflexion points of the same bends through time are used to compute the channel kinematic parameters. The bend tracking algorithm starts from the last iteration of channel-belt development, when bends are the most developed, and tracks the bends backwards in time. The closest apexes at iterations *n* and *n*-1 are attributed to the same bend if they are less than five times the average migration rate apart. When bends at iteration *n*-1 are not linked to previously identified bends, they are added to the list of bends and tracked at preceding iterations. Similarly, a bend at iteration n that does not correspond to a bend at iteration *n*-1, is no longer tracked.

Due to the approximations in the location of the apexes inherent to the channel centerline discretization, 3D trajectories of each apex are smoothed using quadratic parametric curves. These smoothed apex trajectories are then used to extract apex displacements defined at each migration step by four parameters: downstream displacement *dX*, transverse displacement *dY*, vertical displacement *dZ*, and migration distance *dMig* (Figure 4.4b). The total displacements of an apex between the first and the last iterations of activity of a given bend (*ΔX*, *ΔY*, *ΔZ*, *ΔMig*), are similarly characterized along the *X*, *Y*, *Z* directions and along the direction of migration from the first and last smoothed apex locations (Figure 4.4b).

4.4.2.3. Cross-section extraction tool

Cross-sections are drawn across bends defined from the centerline of the last iteration they were active. They lie from the apex and through the midpoint of the segment defined by inflexion points, and extend up to 1.5 times the distance between the apex and the midpoint in order to capture all migration sets (Figure 4.4b). The (*X*, *Y*) location of all channel centerlines that intersect a given cross-section are recorded and the corresponding channel elevation *Z* is linearly interpolated between the two channel points on both sides of the intersection point (Figure 4.4c).

From the extracted cross-sections (Figure 4.4c), channel-belt width (W_{cb}) and thickness (H_{cb}), and channel apparent displacements are computed similarly to Jobe et al. (2016). Channel displacements recorded in cross-sections are apparent since they are proportional to the scalar product of the migration vector ($\overrightarrow{Mig}$) and the section orientation vector ($\overrightarrow{Section}$). Due to channel

downstream migration observed in natural systems and reproduced in Flumy, in nearly all cross-sections, the first migration steps correspond to that of the downstream bend (Figure 4.4b, 4.4c). We choose to compute the parameters W_{cb} and H_{cb} from the two farthest channels, resulting in a maximization of W_{cb} (Figure 4.4c).

4.5. Results

4.5.1. Submarine channel-belt architectures

Figure 4.5 presents channel-belt dimensions, both observed on natural systems and simulated using different development times and corresponding channel kinematic parameters (i.e. erodibility and aggradation height). All the simulations show very close median normalized channel-belt widths (W_{cb}/W) around 2.1 within a range from 1.4 to 2.8 (Figure 4.5a), and median normalized channel-belt thicknesses ($H_{cb}/H_{channel}$) around 2.9 (from 2.1 to 3.2 – Figure 4.5b). Simulated channel-belt aspect ratios vary from 8.4 to 15.6 with median values that range from 11 to 11.9. Simulated normalized channel-belt dimensions – i.e. W_{cb}/W and $H_{cb}/H_{channel}$ – fall within the range of observed values (1.4-4.2 and 1.5-7.7 respectively) and the median values are equal. Simulated channel-belt aspect ratio (W_{cb}/H_{cb}) is very close to the natural one (10.9).

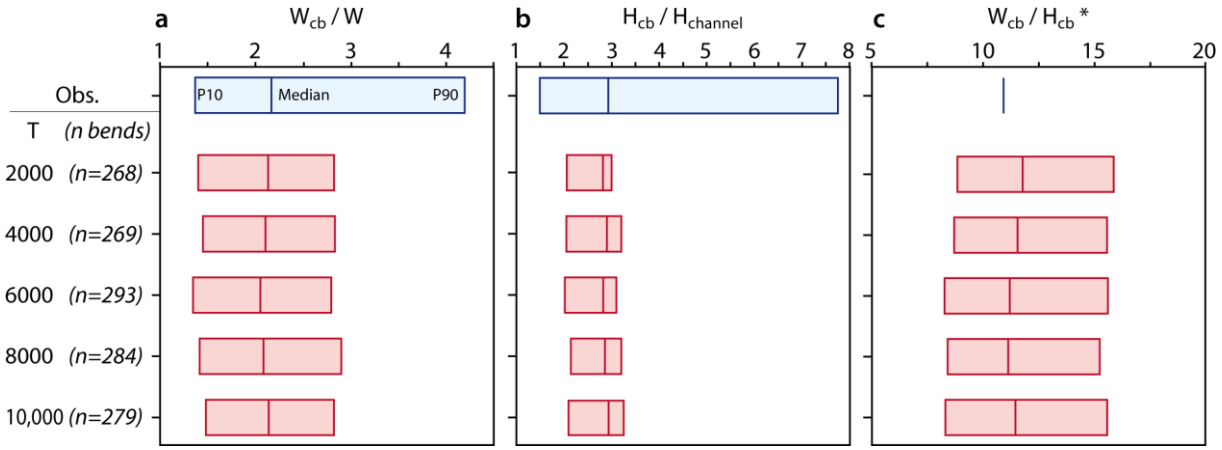

Figure 4.5: Channel-belt normalized width (W_{cb}/W) (a), thickness ($H_{cb}/H_{channel}$) (b) and aspect ratio (W_{cb}/H_{cb}) (c) observed (from Jobe et al., 2016) and simulated for different development times (T). n: number of meanders, P10 tenth percentile, P90: ninetieth percentile. $*\left(\frac{W_{cb}}{H_{cb}}\right)_{obs} = \left[\left(\frac{W_{cb}}{W}\right)_{obs,med} W\right] \Big/ \left[\left(\frac{H_{cb}}{H_{channel}}\right)_{obs,med} H_{channel}\right]$. *W and $H_{channel}$ are channel width and maximal thickness respectively.*

As expected, Flumy simulations are able to reproduce channel-belt geometry by adjusting the parameters controlling channel kinematics. In the following, we compare dynamic mobility numbers (M_{db} and M_{dl}) from resulting migration and aggradation rates, and the stratigraphic ones

(M_{sb} and M_{sl}) from extracted cross-sections. As we do not observe any relationship between the channel-belts geometry and the avulsion period, statistics on channel kinematics are computed using all data together (Figures 4.6 and 4.7).

4.5.2. Channel kinematics

4.5.2.1. Stratigraphic mobility numbers

Median M_{sb} of both observed and simulated channel-belts are equal to 0.6 (Figure 4.6a). Observed M_{sl} displays a global decreasing trend (median values from 1.6 to <0.5) from the younger (lower) to the older (upper) channels (Figure 4.6b). In the simulations, M_{sl} first increases from an elevation of 0.5 (M_{sl}=0.5) to 1 (M_{sl}=0.7) time the channel depth, and then decreases to 0.5 until the final stage of the channel-belt development (Figure 4.6b). The distribution of M_{sl} and the maximal channel-belt thickness are much smaller in the simulations than in natural systems since only the median channel-belt geometry was simulated.

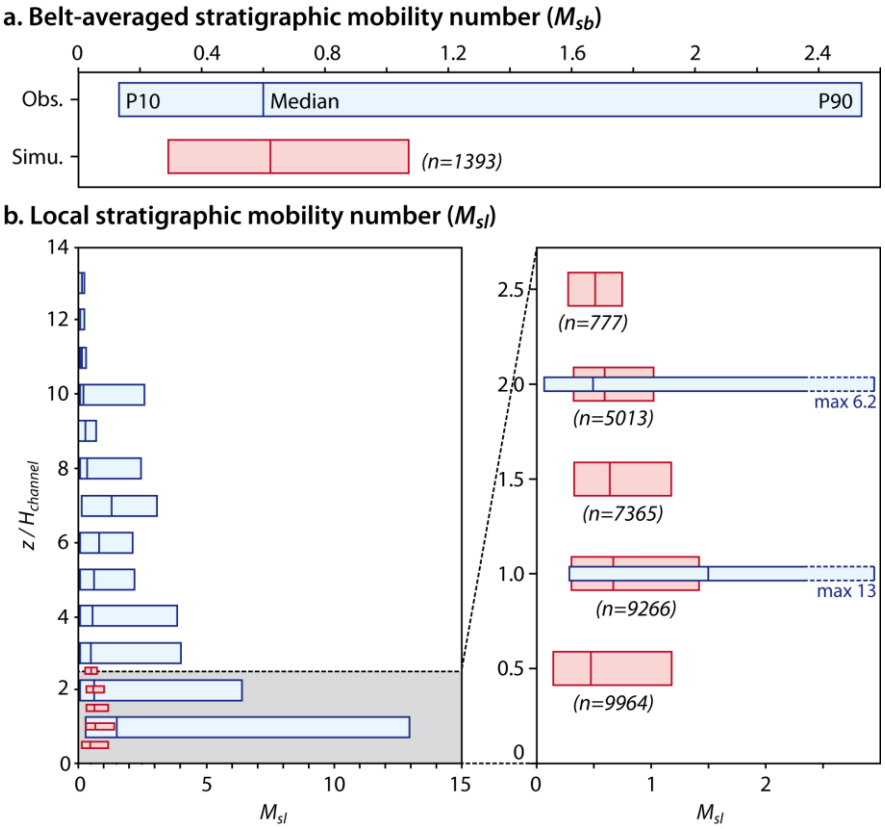

Figure 4.6: Channel apparent kinematics: (a) belt-averaged mobility number (M_{sb}) and (b) local stratigraphic mobility number (M_{sl}) versus normalized channel elevation.

4.5.2.2. Dynamic mobility numbers

Flumy simulations are run with kinematic parameters (i.e. erodibility and aggradation height) chosen to reproduce channel-belts corresponding natural ones. Channel average migration and aggradation rates calculated from the five sets of simulations result respectively from 0.27 to 0.05 m/yr and 44 to 8.8 m/kyr (Figure 4.7a). Consequently, all the scenarii results in a M_{db} equal to 0.4 (equation 4.3).

Figure 4.7b shows that M_{dl}, computed at the same locations as M_{sl}, increases through time from 1.2 to 2.1. Thus, M_{dl} records here an increasing migration rate through time since the aggradation rate is constant all along the simulations. The observed M_{dl} capture the bend migration while M_{db} capture the whole channel kinematics even where the channel poorly migrates, which explains why M_{dl} is much higher than the median M_{db}.

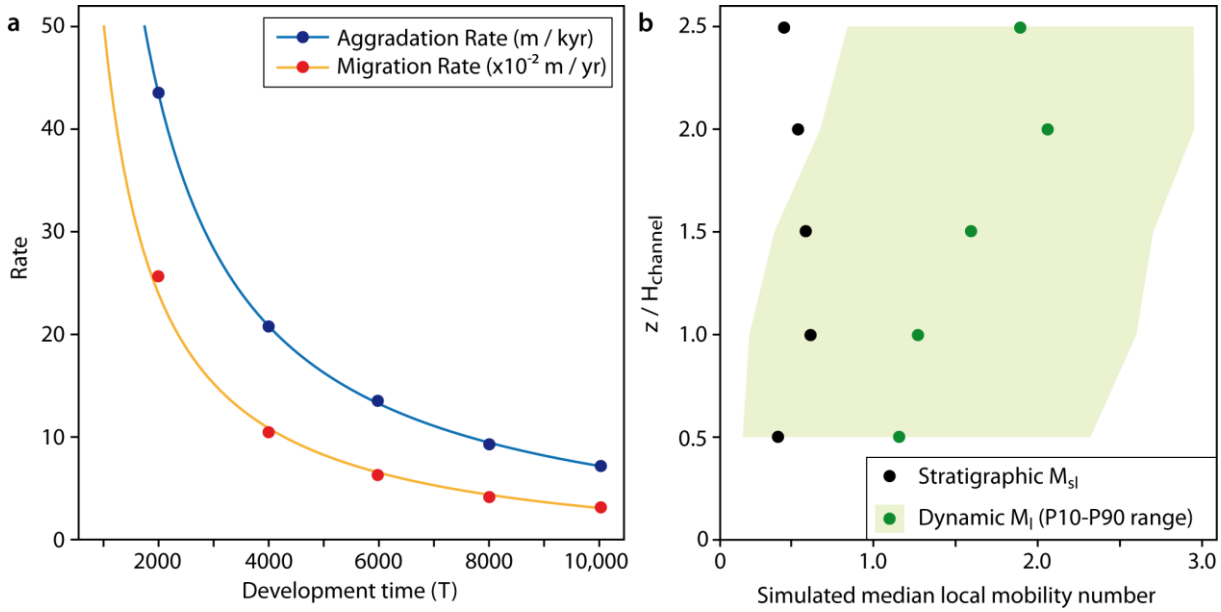

Figure 4.7: Channel actual kinematics for all the simulations: (a) aggradation and migration rates versus the avulsion period (T_{av}), (b) local mobility numbers (stratigraphic and dynamic) versus normalized channel elevation.

Overall, this analysis highlights the differences between apparent channel kinematics characterized by the stratigraphic mobility numbers and the real channel kinematics characterized by the dynamic mobility numbers. In the following, we analyze channel migration to explain these differences.

4.5.3. Channel migration analysis

4.5.3.1. Downstream and cross-stream migrations

Concomitantly with bend growth through time, all simulations display channel downstream migration as shown by apex displacements in the *X* direction (downstream apex migration in Figure 4.4b, Figure 4.8). Apex downstream migration (*dX*) is nearly constant all along the simulation, around 6% of the channel width (Figure 4.8). Cross-stream migration (*dY*) is more complex. After a stable phase around 1.8% of channel width during nearly 40% of the simulation, it then increases up to 3%. This results after the stable phase in a slight increase of apex overall displacements (*dMig*) from 6.3% to 7.4% of the channel width, and in a decrease of the ratio between downstream and cross-stream displacements (*dX/dY*) from 3.7 to 1.8 (Figure 4.8).

Apex total downstream (*ΔX*) and cross-stream migration (*ΔY*) equal 1.3 and 0.4 of the channel width respectively, resulted in a ratio (*ΔX/ΔY*) of 2.7.

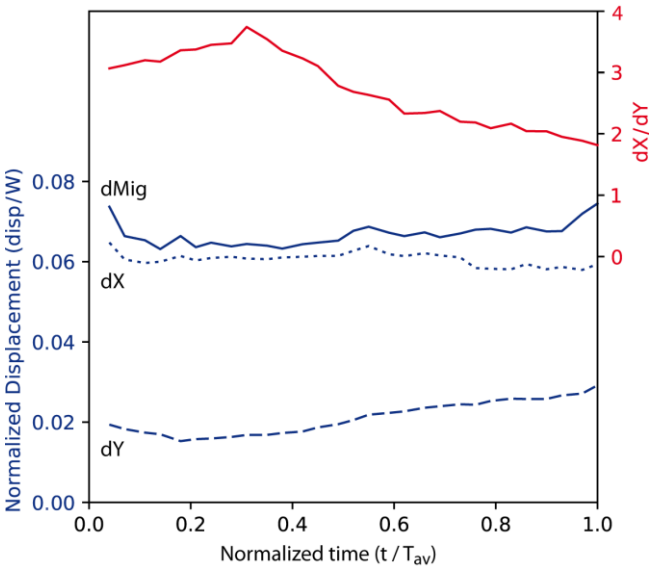

Figure 4.8: Apex mean displacements versus normalized time (T_{av}: avulsion period corresponding to the duration of the simulation).

4.5.3.2. Apparent channel lateral migration

Figure 4.9a displays a typical cross-section (across bend 1 in Figure 4.4b) where, after a first phase of initial channel aggradation, M_{sl} decreases through time due to the decrease of the channel apparent displacements (Figure 4.9 b1). This figure also displays the corresponding channel migration rates. The negative rate during the first phase (left side migration) corresponds to the migration of the downstream bend (bend 2 in Figure 4.4b), concomitantly with the initial aggradation. It is

followed by a positive and nearly constant migration rate (right-side migration) corresponding to the migration of Bend 1 (Figure 4.9 b2). The apparent rate of migration (projection of the true migration rate on the section) shows a decreasing rate of the channel lateral displacements that cannot be attributed to a change in its real migration rate as seen on Figure 4.9 b2. This behavior is explained by changes in the orientation of the migration vector ($\overrightarrow{Mig}$) relatively to that of the cross-section ($\overrightarrow{Section}$, Figure 4.9 b3). Therefore, the more parallel the migration vector and section orientation (small angle close to 0), the higher is the channel apparent lateral displacement for a given real migration rate. In the cross-section, the angle increases from 8° to 80° (Figure 4.9 b3) resulting in a decreasing apparent channel lateral displacement (Figure 4.9 b1).

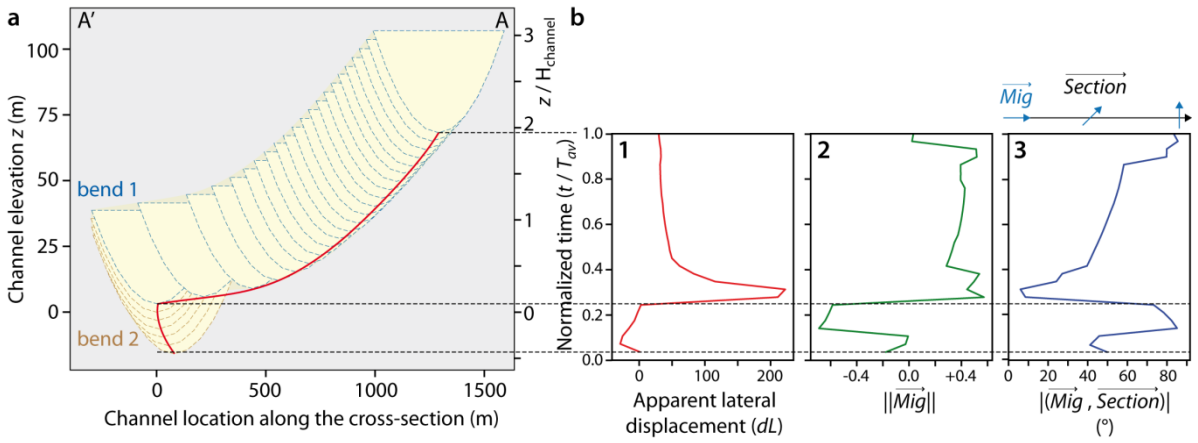

Figure 4.9: Example of a cross-section (a) illustrating the relationship between (b1) channel apparent lateral displacement (dL) and the norm of the migration vector ($\overrightarrow{Mig}$) (b2) and its orientation relatively to the cross-section (b3) at each time step. Same cross-section as Figure 4.4c.

4.6. Discussion

4.6.1. Channel kinematics

In this study, we assume that submarine channel-belts are built over 1000 to 10,000 years based on estimated avulsion periods from modern submarine fans (Manley and Flood, 1988; Schwenk et al., 2003; Mansor, 2009). Channel-belts of geometries similar to the natural ones are obtained with simulated channel lateral migration rates ranging from 0.27 to 0.05 m/yr (Figure 4.7a). These rates are much lower than those measured on Cap Lopez Canyon (2-14 m/yr, Biscara et al., 2013), and even one order of magnitude lower than observed fluvial migration rates (0.7-9.4 m/yr Hickin and Nanson, 1984).

The average channel aggradation rates (Figure 4.7a), are two to ten times higher than reported values from turbidite systems (Damuth and Flood, 1983; Kohl et al., 1985; Curray et al.,

2003; Dennielou et al., 2006; Bourget et al., 2010; Jorry et al., 2011; Lombo Tombo et al., 2015; Jobe et al., 2015). According to the size of the domain and the geometry of the levees, the average aggradation rates in the whole simulated domain are twice lower than that of the channel. The parameters extracted from the simulations correspond to mean aggradational values that show the best fit with marine data for systems with long avulsion periods (several thousand years).

4.6.2. Channel mobility

Flumy and all submarine channel migration models derived from fluvial ones (e.g. Sylvester et al., 2011; Sylvester and Covault, 2016) reproduce realistic submarine channel planform morphologies. The main reason is that fluvial and submarine meander geometries are very similar (Pirmez and Imran, 2003; Chapter 2) and because meander dimensions in Flumy not only depend on channel size and flow properties, but also on input wavelength. In other hand, the results presented here show that Flumy reproduces first-order stratigraphic architecture as shown by the normalized channel-belt dimensions and M_{sb} which agree with observations (Figure 4.5). These results show that linear migration models not only reproduce realistic submarine channel morphologies but also channel-belt first order architecture when coupled with relevant channel aggradation.

Conversely to the hypothesis of Jobe et al. (2016) who postulated that the stratigraphic mobility numbers (equations 4.1 and 4.2) are equivalent to the fluvial mobility numbers (equations 4.3 and 4.4), the stratigraphic mobility number is equivalent to the ratio of the component of migration rate in the direction of the cross-section (and not the whole migration rate) to the aggradation rate. Indeed, the results presented here show that neither belt-averaged nor local stratigraphic mobility numbers (M_{sb} and M_{sl} respectively) are equivalent to dynamic mobility numbers (M_{db} and M_{dl} respectively). The simulations result in a M_{sb} 1.5 times higher than M_{db} (0.6 against 0.4), and while M_{sl} slightly decreases from 0.7 to 0.5 for normalized elevation above 1, M_{dl} keeps rising up to 2 (Figure 4.7b). Stratigraphic mobility numbers are still a useful tool that provides with normalized channel-belt dimensions and the ratio of minimal migration rate to aggradation rate.

4.6.3. Channel stabilization: what causes?

Simulated M_{sl} shows a decreasing trend (above a normalized elevation of 1) as observed on natural channels, even though it remains too high by the end of the development of channel-belts. Decreasing M_{sl} is classically explained by a decreasing apparent lateral migration rate and/or increasing aggradation rate (Jobe et al., 2016), recording the stabilization of channel morphology after a phase of bend growth as described by Peakall et al. (2000). Several processes controlling

migration and/or aggradation rates are invoked, including autogenic processes such as flow stripping on outer banks (Jobe et al., 2016; Piper and Normark, 1983; Straub et al., 2008), reversed secondary currents (Peakall et al., 2000; Corney et al., 2006; Azpiroz-Zabala et al., 2017b), clay hysteresis (Peakall et al., 2000), sediment transport rates in bends (Dorrell et al., 2018), and allogenic ones such as climate variations (Peakall et al., 2000), change of equilibrium profile (Kneller, 2003; Samuel et al., 2003; Hodgson et al., 2011) and flow and sediment discharges (Jobe et al., 2015).

Flumy includes flow stripping that aims at reducing channel lateral migration (equation 4.6). But the results presented here (Figures 4.7 and 4.8) show that simulated migration rate continuously increases because of the increasing channel curvature that dominates the decreasing effect due to flow stripping. Therefore, we deduce that flow stripping alone does not fully explain observed channel stabilization. It would be highly interesting to implement in Flumy a more complex migration model that take into account secondary currents (e.g. non-linear model from Imran et al., 1999) and/or sediment transport to test if the reversal of secondary currents due to increasing channel sinuosity (Azpiroz-Zabala et al., 2017b) and its impact on sediment fluxes (Dorrell et al., 2018) would explain channel stabilization.

Finally, concave-up channel trajectory observed in the simulated 2D cross-sections, is actually mainly created by 3D effect through changes of migration vector directions relatively to the orientation of the cross-sections. Consequently, the results suggest that in addition to previously mentioned processes, the observed concave-up channel trajectory can result from the difference between cross-section and bend growth directions. More generally, this result suggests to keep in mind the whole complexity of submarine systems when interpreting incomplete – especially two-dimensional – data.

4.7. Conclusion

We develop a reduced-complexity process-based model, Flumy, which simulates the main processes at play in channelized submarine systems. These processes include channel lateral migration, aggradation through flow overspill and stripping, and avulsions. We show that:

- Channel-belt first-order stratigraphic architecture is accurately reproduced over 10,000 years under migration rates (0.05 m/yr) one order of magnitude lower than those observed in fluvial systems, and channel aggradation rates of 9 m/kyr;
- Belt-averaged and local stratigraphic mobility numbers are not a true equivalent of belt-averaged and local dynamic mobility numbers, but rather provide lower limits of them;

- Flow stripping alone does not fully explain submarine channel stabilization;
- Changes of bend growth direction relatively to the one of the cross-section are partly responsible of observed concave-up trajectory.

Ce chapitre expose le modèle turbiditique de Flumy. Par rapport au modèle fluviatile présenté en Chapitre 1, plusieurs modifications ont été apportées :

- Le modèle de migration du chenal a d'une part été modifié de telle sorte d'intégrer le modèle d'Imran et al (1999), et afin de prendre en compte la pente locale du chenal permettant d'obtenir des conditions d'écoulement variable en fonction de cette dernière.
- Le calcul des courbures du chenal a été modifié en prenant les troisièmes points amont et aval au point considéré afin de lisser les courbures et d'obtenir davantage de continuité dans les vecteur de migration du chenal, mais surtout en raison de l'influence des courbures dans le calcul de l'asymétrie de l'écoulement (équation 4.9).
- La modélisation de l'écoulement est maintenant découplée de celle du chenal, permettant par exemple à la hauteur de l'écoulement et la profondeur du chenal de varier de façon indépendante.
- L'algorithme d'aggradation ne diffuse non plus l'épaisseur finale des dépôts de levées et d'*overbank* mais l'écoulement turbiditque débordant du chenal, dont sont issus les dépôts. Cette modification permet notamment de simuler les *overspill* à l'extérieur des méandres et de déposer des sédiments y compris sur des points hauts topographiques (cf. Chapitre 5).
- Un profil vertical de distribution des sédiments a également été implémenté permettant de faire varier la granularité des dépôts dans les LAPs et les levées (cf. Chapitre 5).

Ce chapitre montre ainsi que Flumy est capable de reproduire l'architecture stratigraphique au premier ordre des bandes actives de chenaux turbiditiques déconfinés, et propose une quantification des paramètres cinématiques des chenaux. Cette étude apporte également des informations pour la calibration du Nexus de Flumy. De plus, ce chapitre met en garde contre la déduction de paramètres cinématique des chenaux à partir de sections 2D en raison de mécanismes qui se produisent en 3D, permettant par exemple de reproduire des géométries concaves sans variation des taux d'aggradation ou de migration du chenal. Finalement, le chapitre suivant expose un cas d'étude d'application de Flumy au cas de réservoirs turbiditiques confinés.

Chapitre 5.

Process-based model applied to channelized turbidite systems: a case study of the Benin-major valley

Abstract

Channelized turbidite systems are associated with extensive hydrocarbon reservoirs. Yet building realistic turbidite reservoir models is still a challenge. The process-based model Flumy has been firstly developed to simulate the long-term evolution of aggrading fluvial meandering systems in order to build 3D reservoir facies blocks. We take advantage of some similarities between the two environments to transpose Flumy to channelized turbidite systems by simulating the main processes at play in the submarine realm: channel lateral migration, avulsions, aggradation or flow stripping. Input parameters of Flumy mainly include the geometric characteristics of the observed deposits. Flumy builds a flow compatible with the channel geometry. This flow is then used for the simulation of the processes that result in the deposition of the observed sedimentary bodies. Here the transposed Flumy is applied to the case study of the Benin-major valley (Deptuck et al., 2003; 2007). Flumy reproduces the geometry of the incised valley by a smaller-scale channel, including both terraced meanders and early deposited outer levees. The model simulates a complex filling including laterally then vertically amalgamated channelized deposits in the lower and upper parts respectively. However, sand bodies are laterally extended but isolated in the lower part and vertically connected on the top. Flumy also reproduces inner levees that rise onto outer levees at the end of the filling phase. This study shows that Flumy reproduces realistic stratigraphic architecture and can be used to simulate channelized turbidite reservoirs.

5.1. Introduction

Turbidite systems are the end-member of the "sediment-routing system" (Allen, 2008). They accumulate huge amount of deposits that creates among the biggest hydrocarbon reservoirs (Weimer and Slatt, 2004). Most of deep-offshore plays consist of channelized systems. Reservoirs are found in channelized sedimentary bodies, lateral accretion deposits, and levees (Clemenceau et al., 2000; Abreu et al., 2003; Posamentier, 2003; Mayall et al., 2006). The geometry and the architecture of such reservoirs depend on the evolution of the formative channels through time. Thus, these reservoirs are highly complex due to internal baffles and barriers created by shaly deposits (Abreu et al., 2003; Dennielou et al, 2006; Arnott et al., 2007; Cross et al. ,2009; Eschard et al., 2014; Covault et al., 2016).

Hydrocarbon exploration and production rely on 3D geological models that aim at providing potential configurations consistent with scarce data. These models are then used to appraise development risks and to optimize hydrocarbon recovery. Among the first steps of reservoir modeling workflows is the population of reservoir grid with facies (see Introduction). This step often relies on pixel-based methods (Strebelle, 2002; Mariethoz et al., 2014). These methods provide data conditioning, uncertainty estimation through multiple realizations, and high computation speed but they lack realism when simulating complex reservoirs such as the ones derived from channelized systems. To overcome this limitation, they can be coupled with object-based methods that first simulate the geometry of sedimentary bodies like channels (Deutsch and Tran 2002; Labourdette, 2008; Parquer et al. 2017; Rongier et al., 2017). Using these methods, the simulated geometries are more realistic but they highly depend on the input parameters, and reproduce only crudely complex geometries or interwoven sedimentary bodies such as channels and levees. Consequently, these methods are limited in terms of realism and predictivity of the geometry and the internal architecture of channelized reservoirs (Peter et al., 2017). More recently, rule-based methods that aim at mimicking physical and sedimentary processes have come out (Lopez et al., 2008; Pyrcz et al., 2015; McHargue et al 2011; Sylvester et al., 2011; Teles et al., 2016). Depending on the degree of complexity, these methods may need for high computational resources, but are able to reproduce more realistic sedimentary body geometries and facies associations. Among the most complex rule-based methods are the process-based ones that rely on flow and sediment transport modeling in the case of channelized systems (Pyrcz et al., 2015). Nonetheless, the more complex the method, the more complicated is data conditioning.

We take advantage of the similarities between meandering fluvial and submarine leveed-channels (Lonsdale and Hollister, 1979; Flood and Damuth, 1987; Clark and Pickering, 1996; Leeder,

1999; Wynn et al 2007) to transpose to turbidite systems a model (Flumy) that aims at building 3D facies blocks at the reservoir-scale originally dedicated to meandering fluvial sytems. Flumy is at the interface between rule-based and process-based models since some processes are simulated using a process-based approach and others rely on a rule-based one. Flumy is fast computing, includes stochasticity, and the simulations can be conditioned to data. In this study, we present Flumy applied to turbidite systems, and we simulate the incision and the filling of the Benin-major valley.

5.2. Model description

Flumy builds facies 3D blocks at the reservoir scale by simulating processes at play in the submarine realm. Flumy simulates one-threaded sinuous submarine leveed-channels (Chapter 2). The originality of Flumy is that its parameterization relies on the geometry of observed sedimentary bodies. Flumy builds a turbiditic flow compatible with the input geometry (Janocko et al., 2013; Konsoer et al., 2013), and simulates the main processes responsible for the architecture of the reservoir.

5.2.1. Flumy overview

5.2.1.1. Channel migration and aggradation

Migration rate vectors ($\overrightarrow{Mig}$) are assumed to be proportional to the velocity perturbation on the bank (U'_b) and directed in the direction of the normal of the channel ($\vec{n}$) according to equation (5.1) (Imran et al., 1999). Velocity perturbations are the difference between the longitudinal velocity of the flow and the transverse-averaged longitudinal velocity (U_{mean}) (Figure 5.1a). The coefficient of proportion is called the erodibility coefficient (E). In Flumy, this theoretical migration rate vector ($\overrightarrow{Mig_{th}}$) is corrected by the height of the bank (from the channel floor to the top) to erode (H_{bank}) according to equation 5.2 such as the higher the bank, the lower the migration rate. In this equation, $H_{channel}$ is the maximal channel depth.

$$\overrightarrow{Mig_{th}} = E.U'_b.\vec{n} \tag{5.1}$$

$$\overrightarrow{Mig} = \overrightarrow{Mig_{th}}.\frac{H_{channel}}{H_{bank}} \tag{5.2}$$

Aggradation occurs periodically with the aggradation of both channel and levee crests roughly the same in agreement with both experimental work (Straub et al., 2008) and studies on natural systems (Jobe et al., 2016). In curved reaches, flow stripping is simulated depending on the flow and the outer levee heights (Figure 5.1c). Pelagic sedimentation is also simulated by adding a constant thickness of deposits in the whole domain. Finally, channel-belt dimensions are controlled by avulsion frequency relatively to migration and aggradation rates (Chapter 4). Avulsions occur

upstream the domain of simulation and where channel curvature is among the highest. Then, the new channel follows the lowest points of the topography.

Several processes include stochasticity such as channel dimensions, location of the first channel if it is not defined by the user, period of occurrence of aggradation and avulsion, or thickness of the resulting deposits. Consequently, depending on the initial seed, different simulations are obtained with the same set of input parameters.

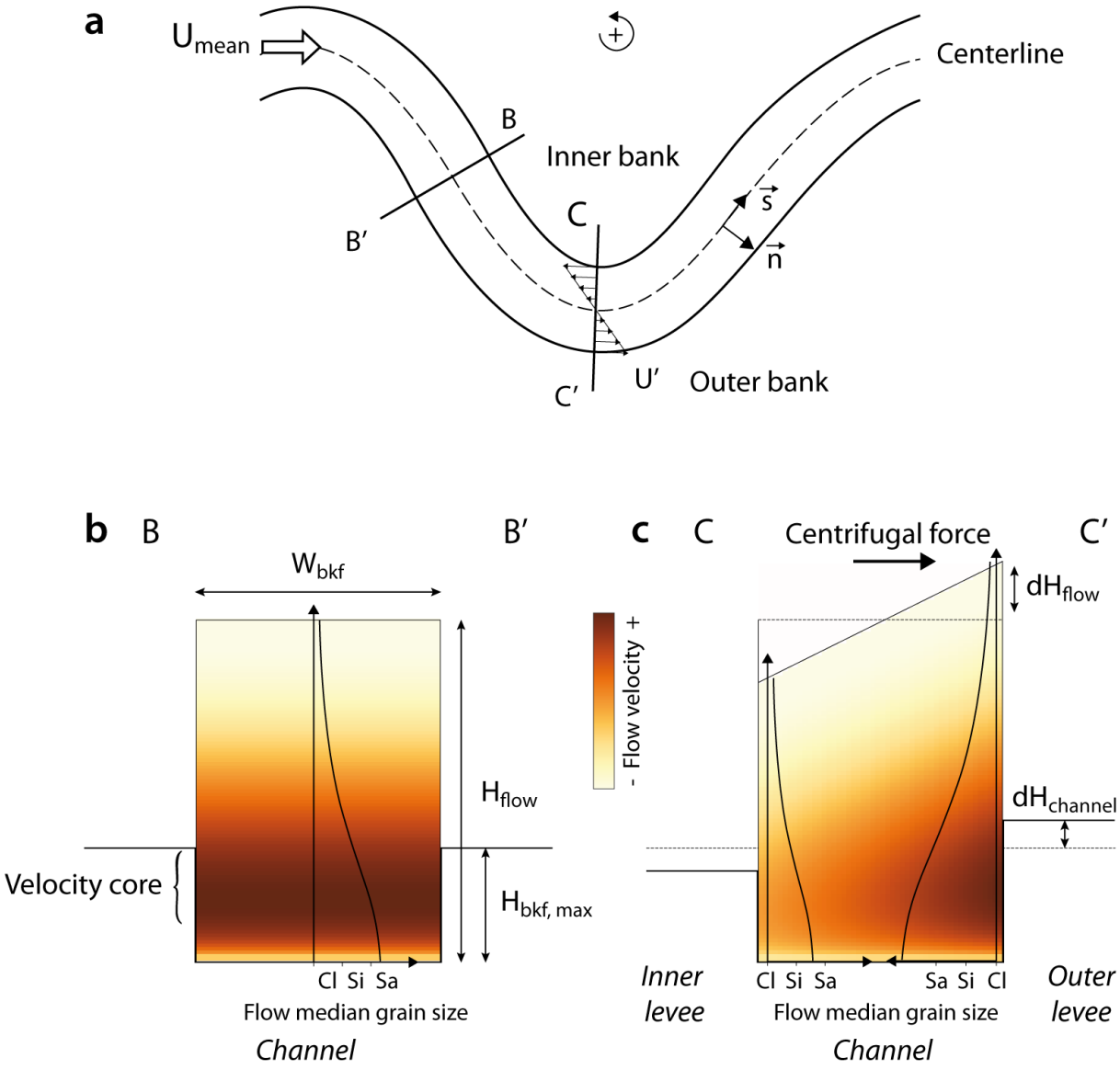

Figure 5.1: Flow modeling in Flumy in plan view (a), in cross-section in a straight reach (b) and in a curved reach (c).

5.2.1.2. Deposit management

The deposits in Flumy are characterized by both a facies and a grain size. Facies correspond to sedimentary bodies such as lateral accretion deposits (LADs), channel lag, levees, overbank deposits, crevasse splays, or channel fill deposits. Sediment grain sizes are discretized in sixteen classes, from clay to cobbles. Deposit characteristics which include their thickness, facies, grain size, and age are stored in a Cartesian pillar grid. Channel lateral migration creates LADs while channel aggradation contributes to channel lag deposits. Levees are built from flow overspill and stripping at the outer bends. Both levee geometry and median grain size follow an exponential decrease away from the channel. The grain size of channelized deposits and the initial grain size of levees depend on the vertical profile of sediment distribution in the flow (Figure 5.1). Abandoned channel left downstream of avulsions or bend cutoffs are filled with fine-sand deposits at the junction with the active channel, and muddy deposits farther. Associated with avulsion, sandy crevasse splays develop at the avulsion point before the stable avulsed channel.

5.2.1.3. Conditioning module

Flumy also includes a conditioning module split into two parts. The Non-Expert-User-calculator (Nexus) is a tool that helps the user to parameterize the simulations from three key parameters: the sand proportion, maximal thickness of the channel, and extension of LADs (Cojan et al., 2011). They can directly be inferred by Flumy from well data, or set by the user. From these three key parameters, the Nexus infers all the parameters needed to give a scenario coherent with input data using a set of channel morphological relationships (Chapter 2) and heuristic formulae (Chapter 1). The second part is the dynamic conditioning module which allows the simulations to fit well data (Rivoirard et al., 2007). It relies on (1) a channel attraction or repulsion from the wells depending on the wanted facies and (2) an external forcing factor map (Emap). The Emap forces channel occupation in one area of the simulation domain by increasing both the erodibility and the probability of occupation after an avulsion.

5.2.2. Flow description

The turbiditic flow is simulated along the channel using a 2D depth-averaged model following Imran et al. (1999). The flow is discretized using a finite difference scheme and the distance between two consecutive computation points ranges between 0.25 and 0.75 times the channel width (W_{bkf}). We assume here a rectangular channel, with a constant width in the whole domain of simulation (Figure 5.1). At each points of the flow pathway, the model provides us with the section-averaged flow discharge, maximal height, and velocity.

The model initializes the flow in a straight channel in the direction of the regional slope (I_0). Channel slope (I_r) is then equal to regional slope. Considering an in-equilibrium flow with the channel (Janocko et al., 2013; Konsoer et al. 2013), the main part of the flow (velocity core) is confined by the channel (Figure 5.1b). Thus, we assume that the flow effective (mean) height ($\overline{H_{flow}}$) is equal to the channel depth (Konsoer et al., 2013; Chapter 3). We also consider that the flow maximal height (H_{flow}) is equal to three times its mean height (Straub et al., 2008; Janocko et al., 2013; Chapter 3). Thus, we compute the flow mean velocity (U_{mean}) according to equation 5.3 then the flow discharge (Q) such as $Q = W_{bkf}.\overline{H_{flow}}.U_{mean}$.

$$U_{mean}^2 = \frac{g.R.C.\overline{H_{flow}}.I_r}{Cf} \quad (5.3)$$

with R (=1.65): the sediment reduced density; g: the gravity; C: the sediment concentration in the flow; C_f the coefficient of friction. Since the channel migrates laterally, we compute C_f such as the channel instability is maximized according to the formula of Ikeda et al. (1981) (equation 5.4):

$$C_f = \frac{2.\pi.\overline{H_{flow}}}{4.\lambda.\left(\sqrt{1+0.5(A+F^2)}-1\right)} \quad (5.4)$$

where λ: the meander wavelength; $A = A_{aff} + A_{sec}$ with A_{off} (=4) the deepening coefficient of Exner equation and A_{sec} (=3) the secondary flow coefficient; $F^2 = \frac{U_{mean}^2}{g.R.C.\overline{H_{flow}}}$ the squared Froude number.

In straight reaches (Figure 5.b), the flow is laterally symmetrical since the depth-averaged longitudinal velocity is constant along the transverse section. Vertically, we assume that the longitudinal velocity follows a bellied shape with an increasing velocity from the channel floor to around 20% of the flow maximal height, then a decreasing until the top of the flow (Stacey and Bowen, 1988; Peakall et al., 2000; Pirmez and Imran, 2003; Kane et al., 2010; Azpiroz-Zabala et al., 2017; Leeuw et al., 2018; Chapter 3). Flumy includes a description of the vertical distribution of sediments in the flow that relies on the Rouse profile (Rouse, 1937) similarly to previous models (Straub et al., 2008; Teles et al., 2016). Depending on the flow velocity, coarse sediments are transported close to the channel floor while the distribution of finer sediments is more homogenous. It results in an upward decreasing median grain size and laterally uniform (Figure 5.1b).

Considering now a sinuous channel, the channel slope decreases while its sinuosity (*Sinuo*) increases according to $I_r = I_0/Sinuo$. The sinuosity is calculated locally using an interval of one wavelength around each point. Thus the new section-averaged velocity is computed using equation (5.3) with the new channel slope, and flow mean and maximal heights are deduced considering a constant flow discharge. In curved reaches, we assume that the flow longitudinal velocity follows a

linear profile (Figure 5.1a) and then the transverse perturbations of velocity (U'_b) and flow height (dH_{flow}) on the bank are calculated according to equations (5.5) and (5.6) respectively:

$$\frac{\partial U'_b}{\partial s} + 2.\frac{C_f}{H_{flow}}.U'_b = \frac{1}{2}W_{bkf}.U_{mean}.\left(\frac{\partial k}{\partial s} - k\frac{C_f}{H_{flow}}.(F^2 + A - 1)\right) \quad (5.5)$$

$$dH_{flow} = \frac{U_{mean}^2.W_{bkf}}{2.g.R.C}.k \quad (5.6)$$

where k is the centerline curvature.

This results in a zone of maximum velocity that drifts toward the outer side and upward. Consequently, the capacity of transport of coarse sediments increases along the outer bank in curved reaches (Figure 5.1c).

5.2.3. LADs and levee deposition

5.2.3.1. Geometry

LADs are deposited over the area where channel was at iteration n-1 and is no longer at iteration n. The geometry of the LADs follows a parabolic shape vertically and the horizontal thickness depends on the distance of migration of the channel.

Levees are built by the flow that spills over the channel. Thus, at constant channel geometry, the higher the levee, the lower is the thickness of the overflow (see section 4.3.2). This thickness is diffused away from the channel according to an exponential decrease function since it fits the shape of natural levees (Skene et al, 1998; Birman et al., 2009; Nakajima et al., 2013). The decreasing parameter is corrected depending on the flow velocity perturbation such as outer levees are wider than inner levees. The height of the overflow is then converted into a thickness of deposits using a depositional factor (see section 4.3.2). This factor is the ratio of the mean flow height in a straight channel to the input aggradation rate. Consequently, along the outer bend where the flow is higher than the mean flow height, the deposited height is greater than in straight reaches. Conversely, levee height is lower on the inner bank.

5.2.3.2. Grain size

The grain size of LADs and levees depends on the vertical profile of median grain size in the flow. Since the median grain size decreases upward, grain size in LADs and at levee crest decreases as well (Hiscott et al., 1997; Leeuw et al., 2018). Laterally in curved reaches, since coarse grains are transported higher in the flow, outer levee initial grain size is coarser than the inner levee one. In levees, grain size exponentially decreases away from the channel. The limit between coarse levee facies and fine overbank facies is set using a grain size threshold of 7.8 µm.

5.3. Case study: the Benin major valley

5.3.1. Context

The Benin-major valley developed off Niger Delta and has been active in the Pleistocene (Deptuck et al., 2003). This system has been widely studied (Deptuck et al., 2003; 2007 and references therein) providing us with a precise description of its geometry and evolution. The valley was built in four phases (Figure 5.2): a first phase of incision of the valley, followed by three phases of filling (see Figure 9 in Deptuck et al., 2003). This system is used as a case study of many deep-offshore reservoirs (Mayall and O'Byrne, 2002; Samuel et al., 2003; Babonneau et al., 2004; Cross et al., 2009).

The erosional fairway is about 100-300 m deep and 2.7-5.1 km wide (Figures 5.2, 5.4b and 5.5a). According to Deptuck et al. (2003, 2007), it was created by incising sinuous channels as shown by meander loops terraced above the floor of the pathway, and the presence of sinuous channels at the base.

Above the erosional surface, phase 1 of the valley filling (Figure 5.2c) is around 20 m thick. In this part, no single channel is observable but instead a zone of chaotic reflectors, interpreted as mass transport deposits, and D-C HARs (Figures 5.4b and 5.5a). These reflectors are interpreted as amalgamated coarse-grained channelized deposits resulting from channel migration with limited vertical aggradation (Figure 5.2c).

Phase 2 was characterized by the construction of inner levees that flank aggrading channels (Figures 5.2d, 5.4b and 5.5a). The channels are mapped over the entire valley and display a sinuous morphology with numerous tight bends. Channel migration was progressive but occasionally the channel abruptly straightened as well. The observable channel width is 300-500 m and the filling thickness is 15 m. The total thickness of phase 2 is around 60 m.

The transition from phase 2 to phase 3 is sharp and marked by a reduction of the sinuosity of the channel and an acceleration of the lateral migration. The aggradation rate in phase 3 was greater than in phase 1 and 2 and meanders became larger (Figures 5.2e, 5.4b and 5.5a). The overall sinuosity increased from phase 2 to the end of phase 3. Since inner levees grew faster than outer levees during phase 2 and phase 3, the valley was progressively filled up. The total thickness of phase 3 reaches 150 m at most. During this phase, channels were 400-600 m wide and even 1000-1500 m at the end before its abandonment. Their thickness was 20 to 30 m by the end.

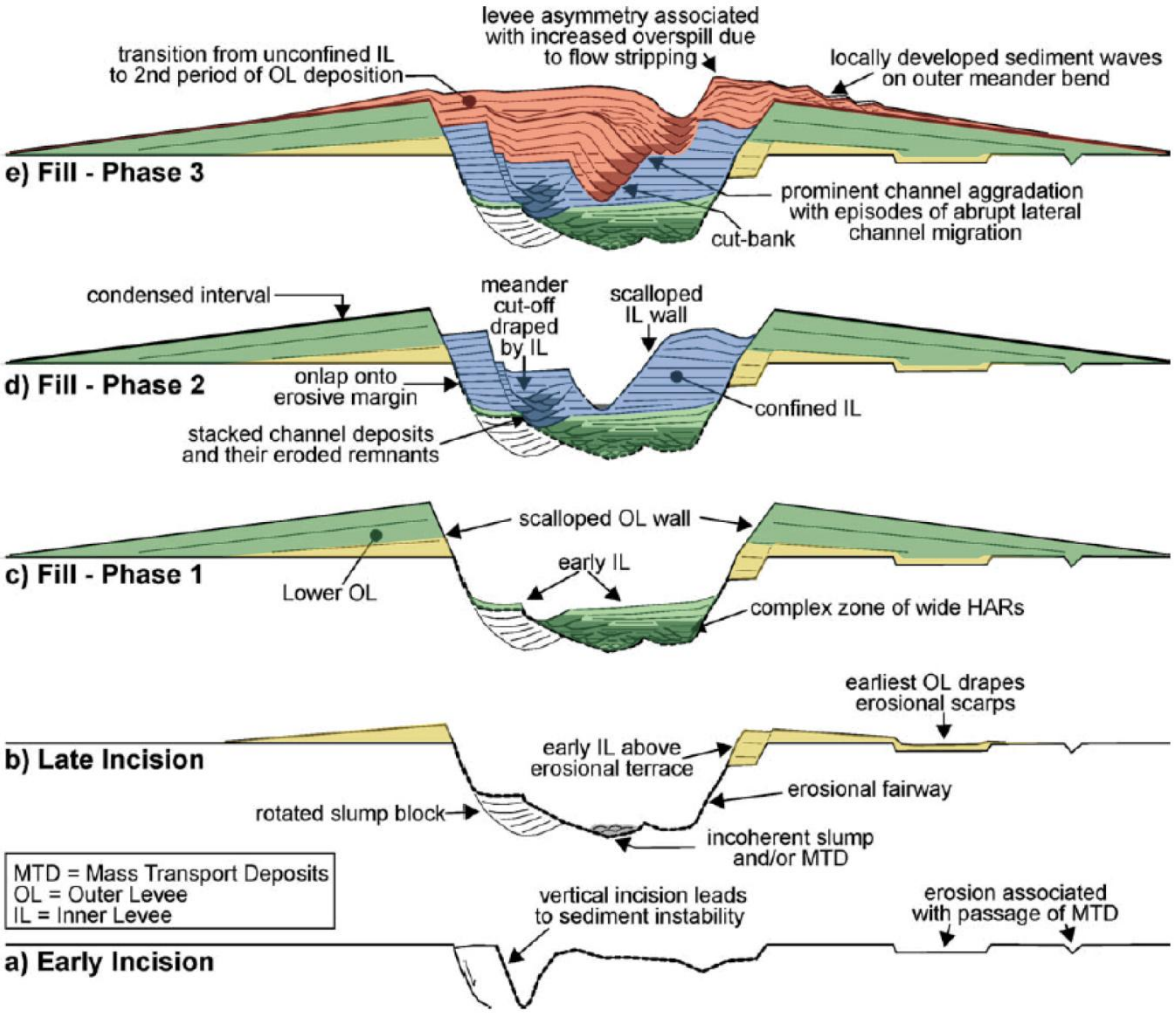

Figure 5.2: Successive phases of Benin-major incision and filling. (Modified after Deptuck et al., 2003)

5.3.2. Parameterization of Flumy

The simulation was run on a 40.4x26.5 km² regular grid with 167 m wide cells (i.e. 243x160 cells) derived from the Figure 2 of Deptuck et al. (2007) (Figure 5.3). The flow was oriented toward the south west. Since we have no information on the paleo-slope, we chose the current valley slope which is about 1%.

In order to build the valley, we created an erodibility map with a zone of high erodibility in the central part of the valley, and a zone of very low erodibility outside the envelope of the valley (Figure 5.3). Since we have no information on the geometry of the incising channel, we chose a channel with the same geometry as aggrading channels. Then, the channel was 400 m wide and 15 m deep. The input wavelength was equal to five times the channel width (Chapter 2) and we chose an avulsion period of 1800 iterations (iter). The initial lateral migration rate was about 0.16 m/iter, corresponding to a median erodibility coefficient of $1.3.10^{-8}$. The simulation started with a relatively low incision rate (0.5 m/10^3 iter) during 1000 iterations allowing the channel to develop meanders

and to build levees. Then migration rate went up to 6 m/10^3 iter until iteration 30,000 (Table 5.1). We assume that an iteration in the model corresponds to about a year.

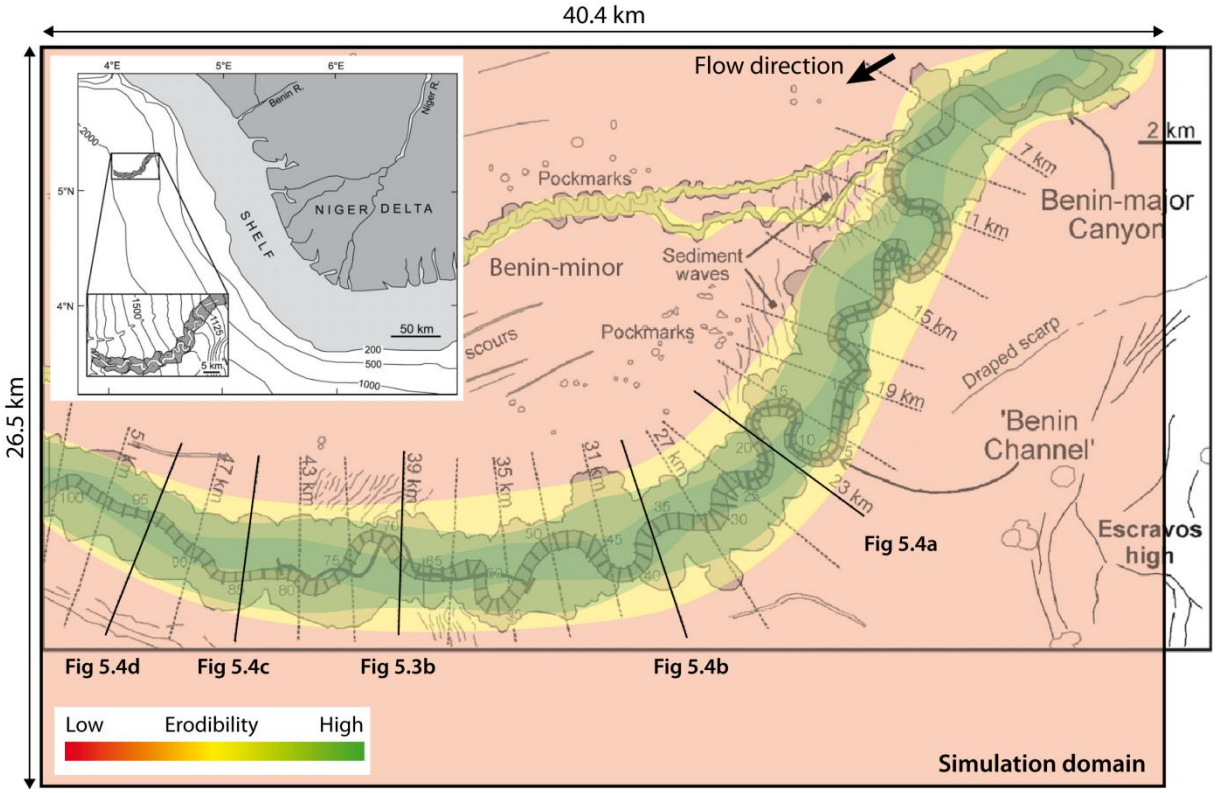

Figure 5.3: Map of the Benin-major valley (modified from Deptuck et al., 2007) and on upper left location off Niger delta (from Deptuck et al., 2003). The simulation domain is delimited by the erodibility map used for the simulation: a zone of high erodibility in green (following the location of the phase 1 of the filling after the Figure 12 in Deptuck et al., 2003), that progressively decreases to a zone of very low erodibility in red.

For the first phase of filling, we kept the same channel geometry and migration rate, and we set the aggradation rate at 4 m/10^3 iter during 2500 iterations (Table 5.1). During phase 2, aggradation rate increased to 6 m/10^3 iter for the next 2500 iterations. Phase 3 was split into two sequences to make a gradual evolution of the geometry of the channel. During the first sequence the channel was 600 m wide, 25 m deep and the wavelength was 3000 m. The aggradation rate was the same as the phase 2 but the migration rate increased due to the change of geometry (same erodibility coefficient). During the second sequence, the channel was 750 m wide and 30 m deep and channel wavelength was 3500 m. Here again we kept the same erodibility but we set the aggradation rate to 30 m/10^3 iter.

Table 5.1: Main parameters of the Flumy simulation

	W_{bkf} (m)	$H_{bkf, max}$ (m)	Wavelength (m)	Aggrad. rate ($m/10^3$ iter)	Obs. Mig rate (m/iter)	Duration (iterations)
Incision	400	15	2000	-0.5	0.16 ($E=1.3e^{-8}$)	1000
				-6		29,000
Filling phase 1	400	15s	2000	+4	0.16 ($E=1.3e^{-8}$)	2500
Filling phase 2	400	15	2000	+6	0.16 ($E=1.3e^{-8}$)	2500
Filling phase 3	600	25	3000	+6	0.22 ($E=1.3e^{-8}$)	2000
	750	30	3500	+30	0.25 ($E=1.3e^{-8}$)	3000

5.4. Results

5.4.1. Valley incision

The global shape of the simulated valley is very similar to the Benin-major valley (Figure 5.4). The simulated valley is about 4 km wide on the top and the incision is 150 m on average. The walls of the valley in the simulation are most often very steep. The simulated valley is also flanked by 15 m high outer levees that developed at the beginning of the incision phase when the flow was still able to spill over outside the valley.

Many terraces at different elevations above the valley floor (either on the banks of the valley, or in the central part) remain after the channel passes through. All terraces are covered either by LADs, channel-fill, or inner levee (levee or overbank facies) deposits. Finally, the valley floor topography is well simulated as well – i.e. from flat to sloped floor and showing at some places topographic highs (Figures 5.4 and 5.5).

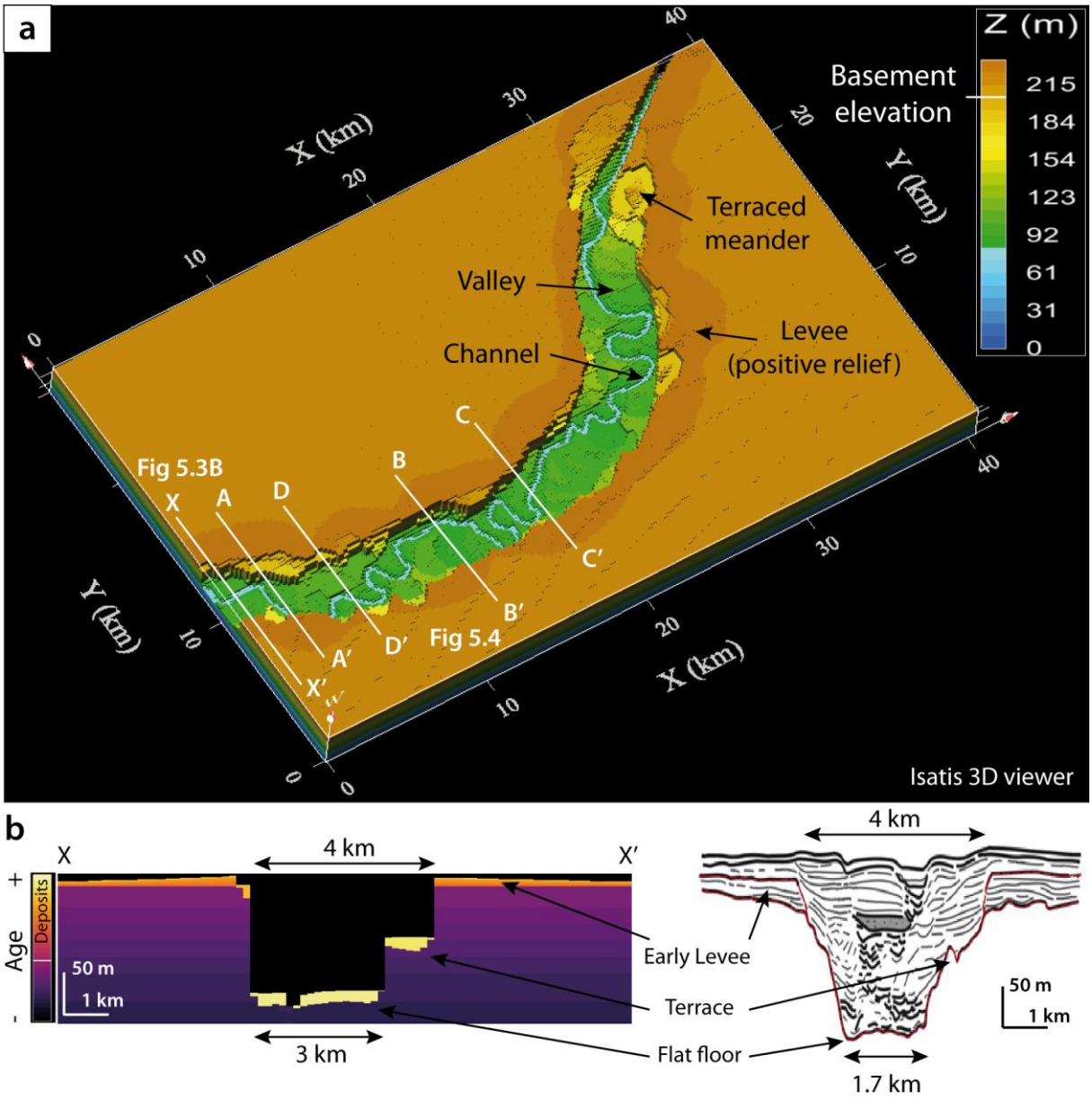

Figure 5.4: Topography after incision in 3D view (a) and in a cross-section (b) to compare with the section at 39 km from Deptuck et al. (2007).For the age, -: old, +: young.

5.4.2. Valley filling

The different styles of filling architecture observed in the Benin-major valley are well reproduced in the simulation (Figure 5.5). All the cross-sections show a first phase with laterally amalgamated channelized deposits, mostly LADs and some channel fill (sand and mud plug) due to meander cutoffs and avulsions. In sections A and B the second phase with a higher aggradation rate (Table 5.1) results in oblique channel trajectory similarly to the filling architecture of the Benin-major valley (Figure 5.5). Channelized deposits are vertically amalgamated by the end of the filling of the valley in section B. Sections C and D display however variations in the filling architecture of the Benin-major valley (Figure 5.5) that are also reproduced with Flumy from the same simulation: after

the first phase channelized deposits are vertically stacked in section C, or show a repetition of lateral then vertical amalgamation in section D. Finally, on the top of the filling, the simulated channel is flanked by asymmetrical inner levees, and younger deposits overlay early outer levees.

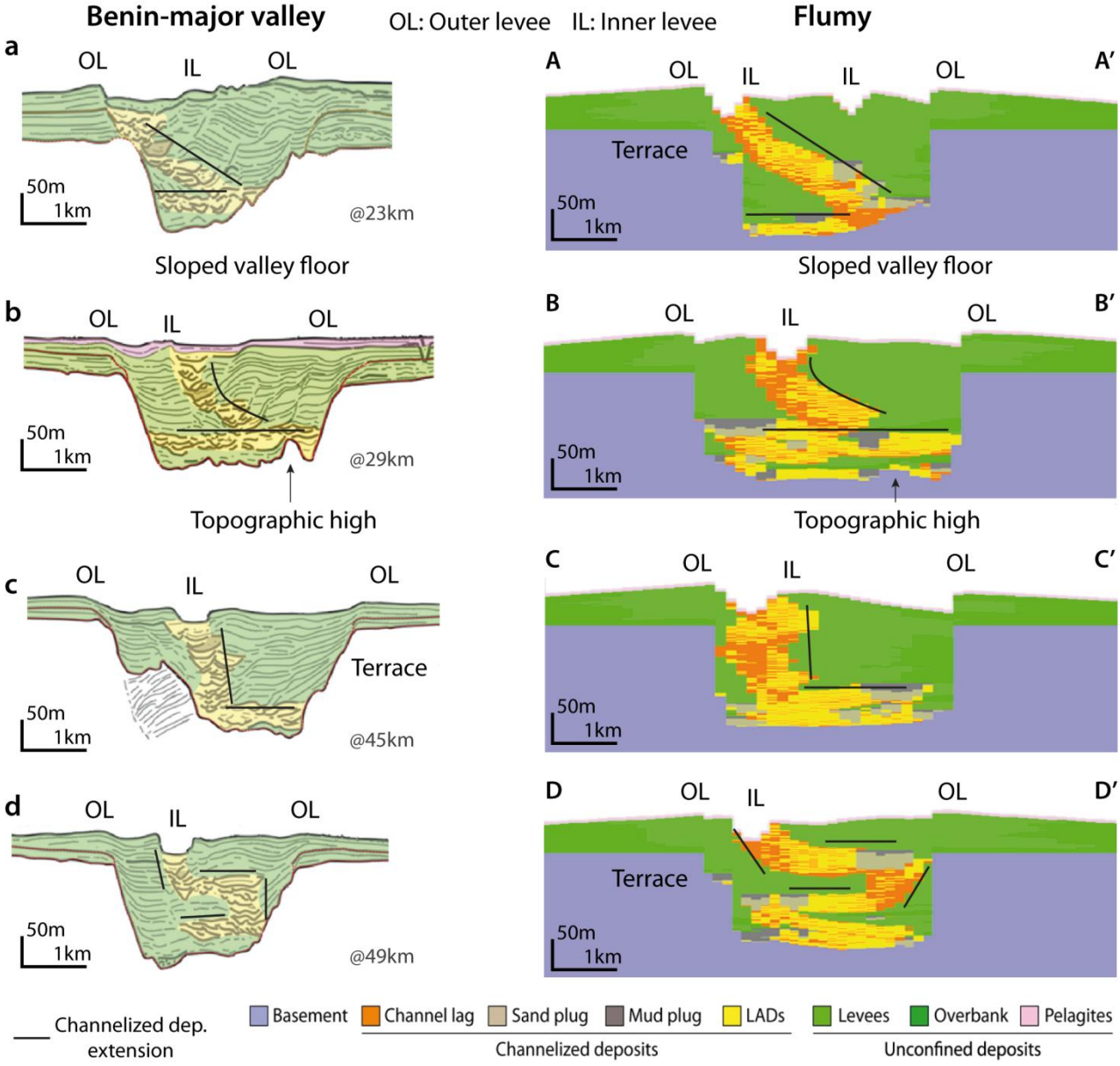

Figure 5.5: Valley filling architecture illustrated by four sections from Deptuck et al. (2007), and four cross-sections displaying the facies of the deposits from the Flumy simulation. Location of cross-sections in Figures 5.3 and 5.4.

The simulation shows a highly variable grain size in the valley filling as shown by Figure 5.6. Connected sand bodies of phase 1 and 2 are wide and relatively thin. They are isolated by wide shaly deposits. Sand bodies of phase 3 are vertically connected.

Sand is not only restricted to channelized deposits but is also part of proximal inner levees (Figures 5.6). LADs are either sandy or silty depending on the flow characteristics. Inner levees of

phase 3 (vertically amalgamated deposits on the top) are siltier than those of phase 1 and 2. This is due to the change of the channel geometry which also results in a higher flow velocity and then a better capacity of transport of coarser sediments. Outer levees display a global coarsening upward pattern. This is because the channel is catching up with the top of the outer levees which results in overflows with coarser sediments. Within this general trend, both inner and outer levees consist of beds of variable thickness and grain size (Figure 5.6).

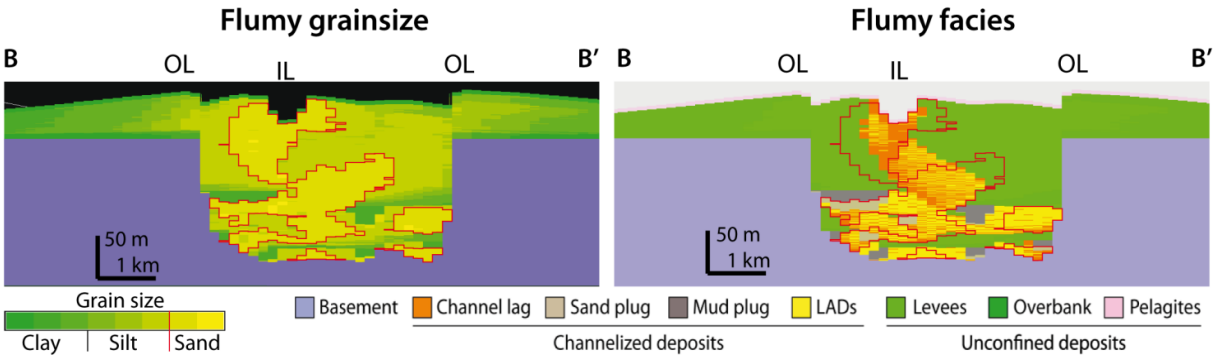

Figure 5.6: Relationship between facies and grain size of the deposits from the Flumy simulation. Location of cross-sections in Figure 5.4.

5.5. Discussion

5.5.1. Filling architecture and reservoir characteristics

The incision and filling patterns of the simulated valley are very similar to that of the Benin-major valley (Figures 5.4 and 5.5). The overall filling consists of (1) laterally amalgamated channelized deposits at the base and (2) vertically amalgamated channelized deposits on the top. However, we find that channelized deposits on terraces and at the base of the valley originate from both the incisional phase and the phase of filling, and not only from the phase of filling as described by Deptuck et al. (2003). Consequently, early deposits that are not subsequently eroded during the filling are older than deposits below the terrace. Moreover, during the filling phase, channels erode the valley walls and then the final geometry of the valley is different from the erosional fairway. This phenomenon was precisely described by Strong and Paola (2008) from experiments in the fluvial context. In terms of reservoir properties, flow barriers may exist at the interface between early and late sand bodies even though they are amalgamated.

In another hand, the LADs at the base of the valley are silty and then the sand bodies are isolated in fine grained deposits. Moreover, the connectivity between sand bodies in the lower and upper parts is not ensured along the whole valley. Flow baffles are also created by the deposition of fine-grained layers on sand bodies due to flow overpills.

5.5.2. Future developments

By the end of the incisional phase, the valley walls are steeper than those of the Benin-major valley. This observation is explained by first the discretization of the simulation grid where the cells are 167 m wide, and by the use of an Emap with sharp boundaries. Simulated valley walls would be smoothed using a refined grid, and/or using a smoother 2D Emap or even a 3D Emap. This would also enhance the accuracy of the simulated geometry with the Benin-major valley. Nonetheless, bank slumping are often described as a cause of valley formation (Kenyon et al., 1995; Carter & Carter 1996; Deptuck et al., 2003). The implementation of this process in Flumy would enhance the simulation of the incisional phase.

The seismic sections in Deptuck et al. (2003; 2007) clearly show the development of sediment waves particularly near outer bend of meander loops. Sediment waves are also widely described in other turbiditic fans (Wynn and Stow, 2002 and references therein). The formation of sediment waves is not simulated in Flumy. However, by modifying the topography, sediment waves might play a role in the location of new channels for instance after an avulsion.

5.5.3. Conditioning

A current limitation of the Flumy simulation is that the simulated channel trajectory is not conditioned by the observed channel paths. Since Flumy is a forward model, that would mean to be able to retrieve the channel morphology at the beginning of the filling and to reproduce the same trajectory. Since channelized deposits are laterally amalgamated, the erosion of previous deposits is responsible for the loss of information. Nonetheless, when a sinuous path is known, a solution may be first to run a backward model (Parquer et al., 2017; Rongier et al., 2017) and then to use the resulting channel location to initialize a Flumy simulation.

5.6. Conclusion

Flumy is a process-based model that simulates channelized turbidite reservoirs. Flumy successfully reproduces the processes at play in the submarine environment such as channel lateral migration, avulsions, aggradation and flow stripping. Its parameterization relies on the observable geometries of the deposits. Flumy builds a flow compatible with the input geometrical parameters to simulate the processes.

The application of Flumy to the Benin-major valley shows that the model is able to reproduce a morphology similar to the natural erosional fairway in terms of dimensions and features such as terraced meander loops, and early deposited outer levees. The simulated stratigraphic architecture resembles the filling of the Benin-major valley. Channelized deposits are laterally amalgamated at the base of the valley and vertically amalgamated on the top. Sand deposits are part of channel lag at the

base of the channel and LADs, but also in proximal levees. Sand bodies are laterally extended and isolated at the base and vertically connected in the upper part. Moreover, while the channel reaches the top of the incisional fairway, inner levees rise onto early outer levees.

Finally, several features and processes observed in the Benin-major valley such as slumps or sediment waves are not reproduced in Flumy. In the future, implementation of such processes would improve again the realism of the Flumy simulations.

Chapitre 6.

Conclusions et perspectives

Ce travail de thèse vise à développer un modèle de **simulation de faciès** pour les **réservoirs** associés aux **systèmes turbiditiques chenalisés**, via la transposition de Flumy initialement développé pour les réservoirs créés par les systèmes fluviatiles méandriformes. Une première partie de ce travail porte sur la **comparaison des systèmes méandriformes fluviatiles et sous-marins**, en combinant les **approches naturaliste**, via une étude géomorphologique de ces systèmes (Chapitre 2), et **analogique**, via la réalisation d'expériences d'écoulements aériens et sous-aquatiques (Chapitre 3). Les résultats de cette première partie sont intégrés lors de la modélisation **numérique** conduisant à l'élaboration du modèle turbiditique de Flumy (Chapitres 4 et 5).

6.1. Flumy : un modèle de simulation des systèmes chenaux-levées turbiditiques

Flumy vise à simuler l'évolution de **systèmes chenaux-levées** tels que définis dans cette étude (Chapitre 2), particulièrement développés de façon **confinés au sein des éventails supérieurs**, ou **libre dans les éventails moyens et inférieurs**, de **systèmes turbiditiques argileux à mixtes** à l'embouchure des grands fleuves (e.g. Amazon, Mississippi, Bengale, Indus, Nile).

En effet, ce travail montre à partir de la **base de données mondiale des conduits d'écoulements sous-marins** établie ici (Chapitre 2), regroupant plus de 48 **systèmes actuels et fossiles** dans diverses contextes géologiques, et où sont appliquées d'une part une **nouvelle classification géomorphologique** de ces conduits basée sur trois critères (présence/absence de levées, nature unitaire ou composite du conduit d'écoulement, caractère confiné ou libre du conduit), et d'autre part de leurs **mesures géomorphologiques** par transposition des méthodes appliquées aux systèmes fluviatiles, que les systèmes chenaux-levées sous-marins forment un groupe homogène de conduits d'écoulement de plus faibles dimensions (10 fois moins larges et profonds que les autres conduits) et de plus forte mobilité latérale (ratios longueur d'onde et amplitude sur largeur du conduit trois fois plus grands que les conduits composites). Ces résultats suggèrent que les **systèmes chenaux-levées sous-marins** sont les conduits d'écoulement les plus **analogues aux systèmes fluviatiles alluviaux méandriformes** initialement simulés dans Flumy.

Les **dimensions médianes** des systèmes chenaux-levées sous-marins et les nouvelles **relations géomorphologiques** établies dans ce travail (Chapitre 2) ont servi de base à **l'établissement du scénario turbiditique par défaut** et au **calcul de l'ensemble des paramètres** de Flumy via son **Nexus** (*Non Expert User calculator*) :

- Un **chenal turbiditique médian** fait environ **800 m de large** et **40 m de profondeur maximale**, ce qui est plus d'un **ordre de grandeur plus grand que le chenal fluviatile médian** reproduit par Flumy (i.e. 30 m de large et 3 m de profondeur maximale).

- Le **rapport d'aspect** (i.e. largeur sur profondeur moyenne) des chenaux sous-marins est également **trois fois plus grand que celui des chenaux fluviatiles méandriformes**.
- Bien que le **rapport longueur d'onde sur amplitude** soit **identique** à celle des **cours d'eau alluviaux méandriformes**, les systèmes chenaux-levées présentent des **méandres trois plus petits pour une largeur donnée de chenal** (i.e. rapports longueurs d'onde sur largeur et amplitude sur largeur). Ces rapports plus faibles s'expliquent à partir des expériences réalisées au cours de ce travail (Chapitre 3), par une adaptation plus rapide à la morphologie du chenal des écoulements sous-aquatiques en comparaison aux aériens, probablement liée aux frictions à l'interface supérieur des écoulements sous-aquatiques, en plus de celles à la base également présentes pour les écoulements aériens.

Finalement, la **paramétrisation de Flumy** pour la modélisation des écoulements turbiditiques à partir des morphologies des chenaux observées s'appuie sur le **concept fluviatile de « *channel forming discharge* »** (Wolman and Miller, 1960 ; Copeland et al., 2000). Or les relations entre la largeur (et l'aire) et la pente des chenaux sous-marins observées dans cette étude (Chapitre 2), ainsi que les résultats de simulations d'écoulements turbiditiques issus de la littérature (Luchi et al., 2018 ; Traer et al., 2018a, b) montrant la division de l'écoulement en une couche basale motrice de forte vitesse et à l'équilibre, surmontée d'une couche diluée et tractée – qui plus est supportés par quelques observations de systèmes naturels (Paull et al., 2018) – appuient la validité de la transposition de ce concept. En outre, la **technique de PIV** (*Particle Image Velocimetry*) permettant la mesure du champ de vitesse, et ici **appliquée pour la première fois aux expériences d'écoulements sous-aquatiques** (Chapitre 3), semble adaptée à l'étude des **variations de vitesse de cette partie basale des écoulements** et leur comparaison aux expériences en milieu aérien.

6.2. Processus simulés par Flumy en contexte sous-marin et perspectives

Le **principal apport** de ce travail à Flumy quant aux processus reproduits est la **simulation, de façon indépendante du chenal, de l'écoulement fluviatile ou turbiditique**, via l'implémentation d'un nouveau module gérant sa modélisation en 3D (Figure 6.1). En effet, contrairement aux écoulements fluviatiles de plein bord, les écoulements turbiditiques sont généralement plus épais que la profondeur du chenal, ce qui a des répercutions sur l'ensemble des processus en milieu sous-marin et notamment l'aggradation des systèmes. Ainsi, la **nouvelle approche** adoptée consiste à faire **dépendre l'ensemble des processus** simulés, et non plus seulement la migration latérale du chenal, **de l'écoulement modélisé en 3D** (hauteur, champ de vitesse, distribution des sédiments), bien que de façon simplifiée pour optimiser le temps de calcul. Par conséquent, la **géométrie des corps**

sédimentaires et la granularité des dépôts s'adaptent aux spécificités des écoulements fluviatiles ou turbiditiques.

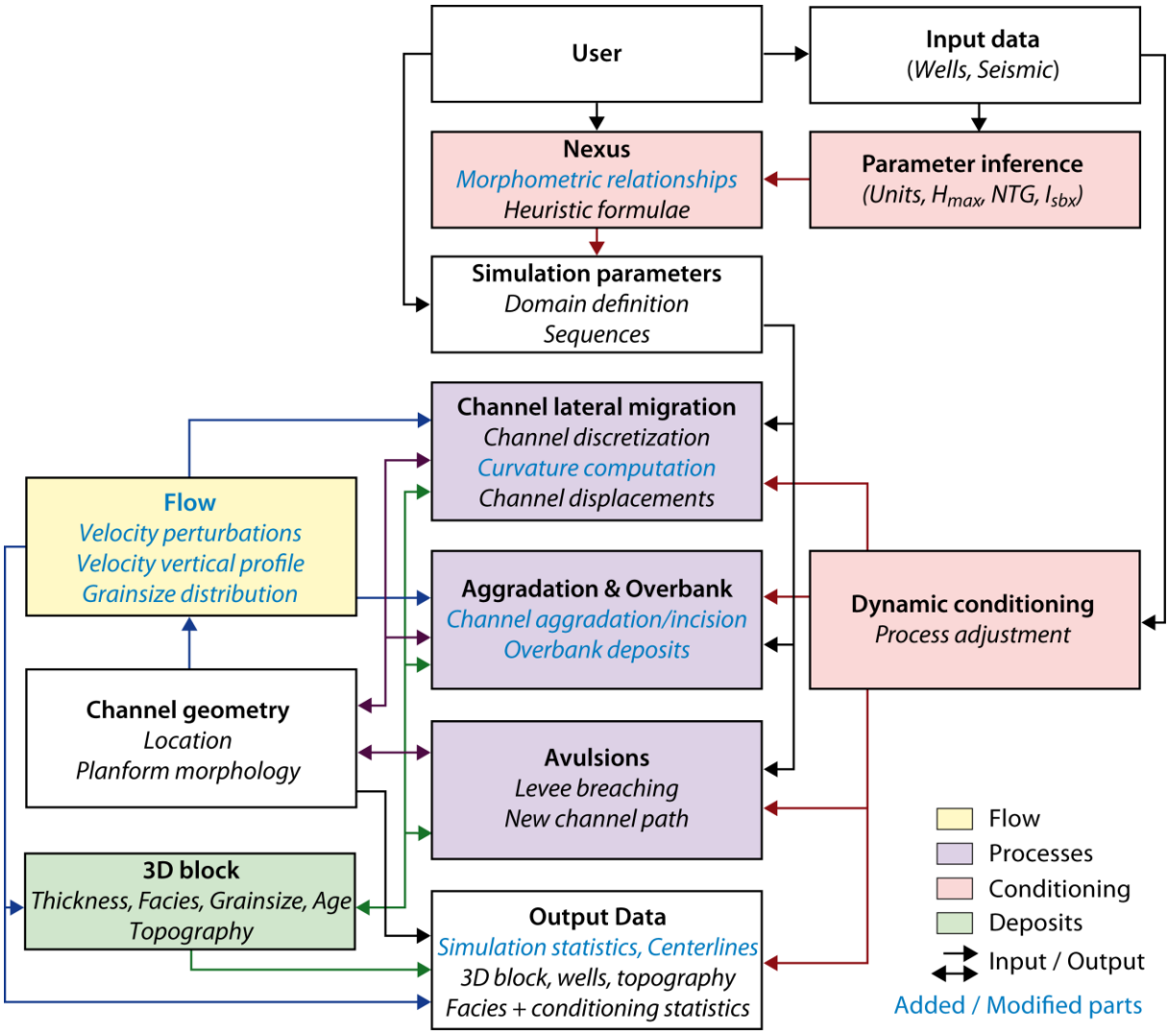

Figure 6.1 : Nouveau schéma de l'organisation modulaire de Flumy et des interactions entre chaque module. Nexus : Non-Expert User calculator, Hmax : profondeur maximale du chenal, NTG : Net-to-Gross, Isbx: indice d'extension des corps sableux. En bleu les modules ajoutés au cours de ce travail de thèse par rapport au schéma initial (Figure 1-3).

Le **modèle de migration du chenal** adapté aux cas des écoulements **sous-marins** permet d'en **reproduire les principales tendances** et ainsi de simuler des **morphologies de chenaux et des architectures stratigraphiques réalistes** (Chapitres 4, 5). Ainsi, que ce soit pour les scénarii fluviatiles ou turbiditiques, la **hauteur et la vitesse moyenne de l'écoulement** en un point donné du chenal **dépendent maintenant de la pente locale du chenal** au sein d'un intervalle d'une longueur d'onde autour de ce point.

De plus, le **profil vertical de vitesse de l'écoulement** s'appuie sur la **nouvelle fonction développée** dans le chapitre 3, correspondant à la somme pondérée du profil vertical de vitesse

d'écoulement fluviatile d'Engelund (1974), et d'un terme correctif basé sur une fonction cosinus (Chapitre 3, équation 3.11). La fonction définie ici est donc employée à la fois dans les scénarii fluviatiles (A=1, B=0 dans l'équation 3.10) et turbiditiques en ajustant les paramètres de pondération.

Dans le cas des écoulements turbiditiques, cette fonction permet de modéliser une grande variété de profils verticaux de vitesse via notamment l'ajustement du paramètre α qui semble dépendre du nombre de Froude. Une **perspective d'évolution** est de faire **dépendre le profil vertical de vitesse** des écoulements turbiditiques directement **de ce nombre de Froude**, permettant ainsi au profil de s'adapter à des variations locales des écoulements. Par exemple, une augmentation locale de la pente conduisant à une augmentation de la vitesse moyenne de l'écoulement et donc du nombre de Froude (Chapitre 3, équation 3.4), résulterait en un écoulement davantage stratifié comme observé dans des simulations numériques (Sequeiros et al., 2010; Cortés et al., 2014; Peakall and Sumner, 2015). En outre, **l'intégration** dans le modèle des **cellules d'écoulements secondaires**, suspectées d'être responsables de la stabilisation de la morphologie planaire du chenal via l'inversion de leur sens de circulation lorsque la sinuosité augmente (Sumner et al., 2014; Azpiroz-Zabala et al., 2017; Dorrell et al., 2018), **permettrait** vraisemblablement **d'améliorer le réalisme des trajectoires** de chenaux simulées.

En outre, le **modèle d'écoulement** développé ici a permis **d'introduire de la variabilité granulométrique** dans les **dépôts chenalisés** (i.e. *CL* et LADs) et les dépôts de **levées**, puisque cette dernière dépend directement de la distribution des sédiments dans l'écoulement via le profil de Rouse (1937). Avec ce profil, les sédiments les plus grossiers sont transportés à proximité du fond du chenal tandis que les plus fins sont transportés de façon plus homogène, ce qui conduit à construire des LADs avec une granularité décroissante vers le haut, et des dépôts de levées plus fins lorsqu'ils se situent davantage en hauteur. De plus, les levées à l'extérieur des méandres présentent également une granularité plus importante que celles à l'intérieur, en raison de l'asymétrie de l'écoulement créée par la courbure du chenal (Chapitre 5). Néanmoins, l**'intégration du module d'écoulement** et en particulier l'implémentation de la **granularité variable des dépôts**, notamment au sein des LADs et *point bars* (*PB*) selon le scénario turbiditique ou fluviatile, a conduit à **ralentir Flumy en moyenne par un facteur 20**. Le temps de calcul étant un des principaux critères pour une utilisation opérationnelle du modèle, une **optimisation des algorithmes développés est donc nécessaire**.

A condition de conserver un temps de calcul raisonnable, le **modèle de dépôt**, voire même d'érosion, implémenté ici **pourrait être raffiné** via la **simulation de ces processus** basée par exemple sur des lois empiriques couramment utilisées (Bagnold, 1962 ; Parker et al., 1986 ; Hiscott, 1994). Ces lois concernent essentiellement le transport en suspension. Or les barres de méandres fluviatiles se

forment principalement par transport de la charge de fond (Church, 2006). Ainsi, **l'implémentation d'un module complet** incluant les **bilans de masse** entre **érosion, transport, et dépôt** des sédiments, éventuellement couplé à l'écoulement (Johannesson et Parker, 1989 ; Zolezzi et Seminara, 2001), permettrait d'améliorer encore la description de la granularité des dépôts et donc l'architecture interne des réservoirs.

De plus, **l'aggradation du système et la construction des levées** sont maintenant **couplées aux écoulements** via le débordement plus ou moins important de ces derniers. Ainsi, le **module d'aggradation** a été modifié de sorte à **simuler** le débordement des écoulements de façon continue le long du chenal (***overspill***), et accentuée à l'apex des méandres (***flow stripping***). L'algorithme commence par le calcul de l'épaisseur initiale de l'écoulement débordant qui dépend fortement des courbures du chenal (Chapitre 4, équation 4.9). Or **l'algorithme de calcul de ces** courbures a également été a**mélioré** (Chapitre 1 et 4) afin de pallier aux éventuelles très fortes valeurs de courbures locales dues à la discrétisation de la ligne centrale. Ensuite, l'écoulement débordant se diffuse en s'éloignant du chenal selon une loi exponentielle décroissante, permettant d'en déduire l'épaisseur et la granularité des dépôts (Chapitres 4 et 5). Ainsi, des dépôts de débordements peuvent être déposés sur des points hauts topographiques si la hauteur de l'écoulement débordant est suffisante. **Ce processus permet** donc la **construction de levées internes** au sein de vallées **et externes** par débordement des écoulements par delà la vallée (Chapitre 5).

Le couplage entre l'aggradation et l'écoulement permet **d'envisager l'approfondissement du chenal par la construction progressive de ses levées** suite à la création de ce dernier lors de l'initialisation d'une simulation ou après une avulsion. En effet, le tracé du chenal est actuellement plaqué sur la topographie existante et le chenal est « creusé » en dessous. Ceci revient à construire le chenal entièrement par incision de ce dernier (Fildani et al., 2013; Maier et al., 2013 ; Weill et al., 2014), or les chenaux fluviatiles et turbiditiques se construisent également par construction de leurs levées (Straub and Mohrig, 2008 ; Rowland et al., 2010 ; de Leeuw et al., 2016). Grâce à l'implémentation du module d'écoulement, un chenal peu profond (par exemple la moitié de sa profondeur calculée) pourrait être créé comme actuellement, puis les débordements abondants de l'écoulement en raison de cette faible profondeur viendraient construire les levées de part et d'autre et ainsi approfondir le chenal.

Les **simulations Flumy gagneraient** également à intégrer des **conditions d'écoulement variables** autour de la moyenne correspondant au débit de formation du chenal. Ces variations stochastiques conduiraient à des distances de migration et des dépôts de levées d'épaisseur variable, ainsi que des alternances de dépôts grossiers et fins en fonction des conditions des écoulements. De

plus, via le **couplage du processus d'avulsion et de l'écoulement**, des écoulements énergétiques favoriseraient le développement de larges ruptures de levée, et donc le développement de lobes de crevasse de plus grande extension et de granularité plus grossière, et augmenteraient la probabilité qu'une avulsion réussisse (Pirmez and Flood, 1995 ; Manley et al., 1997).

Finalement, bien que non présenté dans ce manuscrit, le **modèle fluviatile de Flumy** a également **profité de l'implémentation du module d'écoulement et des améliorations de certains algorithmes** (par exemple le calcul des courbures – Chapitre 4).

6.3. Flumy : un modèle opérationnel de réservoirs turbiditiques chenalisés

Le cas d'étude de la vallée incisée du Bénin-major, représentatif d'un grand nombre de systèmes turbiditiques confinés, a permis de montrer les **capacités de Flumy** quant à **reproduire l'incision puis le remplissage de la vallée** par un chenal de plus petite dimension (Chapitre 5). En effet, la morphologie de la vallée ainsi que les différents éléments géomorphologiques observés tels les levées externes à la vallée, les méandres perchés sur les terrasses, ou encore les reliefs du fond de la vallée, sont très bien reproduits par la simulation. De plus, les différentes architectures de remplissage simulées, issues des trajectoires variables des chenaux et comprenant notamment des corps sédimentaires chenalisés amalgamés latéralement et verticalement, affichent de fortes similitudes avec celles observées dans la vallée du Bénin-major. Néanmoins, la **simulation dans Flumy de l'effondrement des parois de la vallée** lorsque ces dernières deviennent trop raides **améliorerait le processus de formation et la morphologie des vallées incisées**, ainsi que permettrait le dépôt de *slumps* à la base de cette dernière en accord avec les interprétations. Un tel processus peut être simulé via l'ajout d'un critère de stabilité de pente dépendant notamment de la hauteur et de la composition des flancs de la vallée.

De plus, des **lobes distaux** également propices à la formation de réservoirs (Bell et al., 2018), se **développent à l'embouchure des chenaux** notamment au sein de bassins profonds (Dennielou et al., 2017 ; Doughty-Jones et al., 2017). Leur **simulation dans Flumy**, soit par une approche *process-based* (Kane et al., 2016), ou bien *object-based* paramétrée par le chenal (Pettinga et al., 2018), **permettrait de reproduire l'ensemble des éléments constitutifs des réservoirs turbiditiques**.

Outre son utilisation en temps que modèle de réservoir, **Flumy** est un très bon **outil pour étudier les relations entre les processus dynamiques et l'architecture stratigraphique résultante**. Ainsi, la simulation de systèmes chenaux-levées sous-marins avec **Flumy a permis de quantifier les taux moyens de migration** (i.e. 0.05-0.3 m/an) **et d'aggradation** (i.e. 9-44 m/10^3 an) du chenal **et les périodes d'avulsion** (i.e. 2000-10000 ans), connaissant l'architecture stratigraphique finale (Chapitre

4). Bien que le phénomène de stabilisation de la morphologie planaire du chenal ne soit pour le moment pas parfaitement reproduite, cette étude a également **mis en évidence la création de la trajectoire concave vers le haut** couramment observée sur des coupes transverses aux méandres (et responsable de la stabilisation de la morphologie planaire), **par des effets de changement de direction de la migration du méandre par rapport à la direction de la coupe transverse**.

En outre, une étude précise de **l'évolution de la géométrie des méandres** (fluviatiles ou turbiditiques) et du déplacement des apex et points d'inflexion – s'appuyant notamment sur les outils développés dans le cadre de ce travail (Chapitre 4) – **en fonction des paramètres du modèle**, **pourrait permettre de mieux comprendre les relations entre paramètres cinématiques des chenaux et morphologies observées**.

Finalement, bien que Flumy soit présenté comme un modèle *process-based* et donc difficile à conditionner (Figure 1b, Pyrcz et al., 2015), le module de conditionnement dynamique de Flumy permet de respecter en moyenne 90% des informations de faciès aux puits. Le conditionnement aux données ne faisait certes pas partie de ce travail, cependant ce dernier ouvre de **nouvelles perspectives quant au conditionnement**. En effet, l'étude de l'évolution de la trajectoire des points caractéristiques des chenaux (i.e. apex et points d'inflexion) mentionnés précédemment, permet **d'envisager le conditionnement des simulations sur des portions de chenaux visibles,** par exemple à partir de données sismiques. L'élaboration d'un modèle inverse de cette trajectoire dans le temps permettrait par exemple de déterminer une (des) position(s) possible(s) des points caractéristiques du chenal à rebours à partir du dernier tracé observé. De plus, l'introduction de la granularité variable au sein des corps sédimentaires conduit à repenser le **conditionnement** non plus seulement vis-à-vis des faciès, mais également vis-à-vis **de cette granularité**. Enfin, de nouvelles techniques de conditionnement des modèles *process-based* s'appuyant notamment sur les méthodes séquentielles de Monte Carlo (par exemple Skauvold et Eidsvik, 2018), et qui font l'objet d'une nouvelle thèse pour Flumy, suggèrent que le conditionnement aux données ne sera plus un frein à l'utilisation opérationnelle de ces modèles.

Bibliographie

Abbey, E. (1968). Desert solitaire. Éditions Gallmeister, 2016, 344 pp. ISBN 978-2-35178-038-1.

Abad, J. D., Sequeiros, O. E., Spinewine, B., Pirmez, C., Garcia, M. H., & Parker, G. (2011). Secondary current of saline underflow in a highly meandering channel: experiments and theory. Journal of Sedimentary Research, 81(11), 787-813. https://doi.org/10.2110/jsr.2011.61.

Abd El-Gawad, S., Cantelli, A., Pirmez, C., Minisini, D., Sylvester, Z., & Imran, J. (2012). Three-dimensional numerical simulation of turbidity currents in a submarine channel on the seafloor of the Niger Delta slope. Journal of Geophysical Research: Oceans, 117(C5). https://doi.org/10.1029/2011JC007538.

Abreu, V., Sullivan, M., Mohrig, D., Pirmez, C., (2003). Architectural analysis of sinuous, erosionally confined channels: the under-appreciated deepwater channel type. Marine and Petroleum Geology 20, 631–648. https://doi.org/10.1016/j.marpetgeo.2003.08.003.

Albertão, G. A., Eschard, R., Mulder, T., Teles, V., Chauveau, B., & Joseph, P. (2015). Modeling the deposition of turbidite systems with Cellular Automata numerical simulations: A case study in the Brazilian offshore. Marine and Petroleum Geology, 59, 166-186. https://doi.org/10.1016/j.marpetgeo.2014.07.010.

Allen, J.R.L., (1984), Developments in Sedimentology, 663 pp., Elsiever Sci., New York.

Allen, P. A. (2008). From landscapes into geological history. *Nature*, *451*(7176), 274. https://doi.org/10.1038/nature06586.

Allen, P. A. (2017). Sediment routing systems: The fate of sediment from source to sink. Cambridge University Press.

Amos, K. J., Peakall, J., Bradbury, P. W., Roberts, M., Keevil, G., & Gupta, S. (2010). The influence of bend amplitude and planform morphology on flow and sedimentation in submarine channels. Marine and Petroleum Geology, 27(7), 1431-1447. https://doi.org/10.1016/j.marpetgeo.2010.05.004.

Arnott, R. W. C. (2007). Stratal architecture and origin of lateral accretion deposits (LADs) and conterminuous inner-bank levee deposits in a base-of-slope sinuous channel, lower Isaac Formation (Neoproterozoic), East-Central British Columbia, Canada. Marine and Petroleum Geology, 24(6-9), 515-528. https://doi.org/10.1016/j.marpetgeo.2007.01.006.

Azpiroz-Zabala, M., Cartigny, M. J., Talling, P. J., Parsons, D. R., Sumner, E. J., Clare, M. A., et al. (2017a). Newly recognized turbidity current structure can explain prolonged flushing of submarine canyons. Science advances, 3(10), e1700200. https://doi.org/10.1126/sciadv.1700200.

Azpiroz-Zabala, M., Cartigny, M. J., Sumner, E. J., Clare, M. A., Talling, P. J., Parsons, D. R., & Cooper, C. (2017b). A general model for the helical structure of geophysical flows in channel bends. Geophysical research letters, 44(23). https://doi.org/10.1002/2017GL075721.

Baddeley, A. (2018). A Statistical Commentary on Mineral Prospectivity Analysis. In Handbook of Mathematical Geosciences (pp. 25-65). Springer, Cham.

Babonneau, N., Savoye, B., Cremer, M., Bez, M., (2004). Mutliple terraces within the deep incised Zaire Valley (ZaiAngo Project): are they confined levees? In: Lomas, S.A., Joseph, P. (Eds.), Geological Society Special Publications, vol. 222, pp. 91–114. https://doi.org/10.1144/GSL.SP.2004.222.01.06.

Bagnold, R. A. (1962). Auto-suspension of transported sediment; turbidity currents. Proc. R. Soc. Lond. A, 265(1322), 315-319. https://doi.org/10.1098/rspa.1962.0012

Bain, H. A., & Hubbard, S. M. (2016). Stratigraphic evolution of a long-lived submarine channel system in the Late Cretaceous Nanaimo Group, British Columbia, Canada. Sedimentary Geology, 337, 113-132. https://doi.org/10.1016/j.sedgeo.2016.03.010.

Baker, E.; Gaill, F., Karageorgis, A., Lamarche, G., Narayanaswamy, B., Parr, J., et al. (2016). Offshore Mining Industries. In The First Global Integrated Marine Assessment; World Ocean Assessment I; United Nations (UN): New York, NY, USA.

Basani, R., Janocko, M., Cartigny, M. J., Hansen, W. M., & Eggenhuisen, J. T. (2014). MassFLOW-3D TM as a simulation tool for turbidity currents?: some preliminary results. IAS Speical Publ, 46, 587-608.

Bell, D., Kane, I. A., Pontén, A. S., Flint, S. S., Hodgson, D. M., & Barrett, B. J. (2018). Spatial variability in depositional reservoir quality of deep-water channel-fill and lobe deposits. Marine and Petroleum Geology, 98, 97-115. https://doi.org/10.1016/j.marpetgeo.2018.07.023.

Billi, P., Demissie, B., Nyssen, J., Moges, G., & Fazzini, M. (2018). Meander hydromorphology of ephemeral streams: Similarities and differences with perennial rivers. Geomorphology, 319, 35-46. https://doi.org/10.1016/j.geomorph.2018.07.003.

Birman, V. K., Meiburg, E., & Kneller, B. (2009). The shape of submarine levees: exponential or power law?. Journal of Fluid Mechanics, 619, 367-376. https://doi.org/10.1017/S0022112008004862.

Biscara, L., Mulder, T., Hanquiez, V., Marieu, V., Crespin, J. P., Braccini, E., & Garlan, T. (2013). Morphological evolution of Cap Lopez Canyon (Gabon): illustration of lateral migration processes of a submarine canyon. Marine Geology, 340, 49-56. https://doi.org/10.1016/j.margeo.2013.04.014.

Blom, A., Arkesteijn, L., Chavarrías, V., & Viparelli, E. (2017). The equilibrium alluvial river under variable flow and its channel-forming discharge. Journal of Geophysical Research: Earth Surface, 122(10), 1924-1948. https://doi.org/10.1002/2017JF004213.

Bolla Pittaluga, M., & Imran, J. (2014). A simple model for vertical profiles of velocity and suspended sediment concentration in straight and curved submarine channels. Journal of Geophysical Research: Earth Surface, 119(3), 483-503. https://doi.org/10.1002/2013JF002812.

Bolla Pittaluga, M., Frascati, A., & Falivene, O. (2018). A gradually varied approach to model turbidity currents in submarine channels. Journal of Geophysical Research: Earth Surface, 123(1), 80-96. https://doi.org/10.1002/2017JF004331.

Bonnecaze, R. T., Huppert, H. E., & Lister, J. R. (1993). Particle-driven gravity currents. Journal of Fluid Mechanics, 250, 339-369. https://doi.org/10.1017/S002211209300148X.

Bouma, A. H. (1962). Sedimentology of Some Flysch Deposits: A Graphical Approach to Facies Classification. Amsterdam: Elsevier, 169 pp.

Bourget, J., Zaragosi, S., Ellouz-Zimmermann, S., Ducassou, E., Prins, M. A., Garlan, T., ... & Giraudeau, J. (2010). Highstand vs. lowstand turbidite system growth in the Makran active margin: Imprints of high-frequency external controls on sediment delivery mechanisms to deep water systems. Marine Geology, 274(1-4), 187-208. https://doi.org/10.1016/j.margeo.2010.04.005.

Bridge, J. S. (2003). Rivers and Floodplains, 491 pp. Blackwell, Oxford, UK.

Bridge, J. S., & Mackey, S. D. (1993). A theoretical study of fluvial sandstone body dimensions, in Flint, S.S., and Bryant, I.D., eds., The Geological Modelling of Hydrocarbon Reservoirs and Outcrop Analogues: International Association of Sedimentologists, Special Publication 15, p. 213–236.

Bubnova, A., Conditionnement des modèles génétiques de réservoirs chenalisés méandriformes aux données d'exploration. (Doctoral dissertation, Ecole Nationale Supérieure des Mines de Paris). Retrieved from these.fr (http://www.theses.fr/s157204).

Bubnova, A., Ors, F., Rivoirard, J., Cojan, I. (accepted). Automatic Determination of Sedimentary Units from Well Data. Mathematical Geosciences.

Caers, J. (2005). Petroleum geostatistics (p. 104). Richardson: Society of Petroleum Engineers.

Camporeale, C., Perona, P., Porporato, A., & Ridolfi, L. (2007). Hierarchy of models for meandering rivers and related morphodynamic processes. Reviews of Geophysics, 45(1). https://doi.org/10.1029/2005RG000185.

Cantero, M. I., Balachandar, S., Cantelli, A., Pirmez, C., & Parker, G. (2009). Turbidity current with a roof: Direct numerical simulation of self-stratified turbulent channel flow driven by suspended sediment. Journal of Geophysical Research: Oceans, 114(C3). https://doi.org/10.1029/2008JC004978.

Carter, R. M., & Carter, L. (1996). The abyssal Bounty Fan and lower Bounty Channel: evolution of a rifted-margin sedimentary system. Marine Geology, 130(3-4), 181-202. https://doi.org/10.1016/0025-3227(95)00139-5.

Castelino, J. A., Reichert, C., & Jokat, W. (2017). Response of Cenozoic turbidite system to tectonic activity and sea-level change off the Zambezi Delta. Marine Geophysical Research, 38(3), 209-226. https://doi.org/10.1007/s11001-017-9305-8.

Church, M. (2006). Bed material transport and the morphology of alluvial river channels. Annu. Rev. Earth Planet. Sci., 34, 325-354. https://doi.org/10.1146/annurev.earth.33.092203.122721.

Clark, J. D., & Pickering, K. T. (1996). Architectural elements and growth patterns of submarine channels: application to hydrocarbon exploration. AAPG bulletin, 80(2), 194-220.

Clemenceau, G. R., Colbert, J., & Edens, D. (2000). Production results from levee-overbank turbidite sands at Ram/Powell field, deepwater Gulf of Mexico. In Deep-Water Reservoirs of the World, GCSSEPM Foundation 20th Annual Research Conference (pp. 241-251).

Cojan, I., Rivoirard, J., Ors, F., & Renard, D. (2011, May). New Method for an Easy Use of Stochastic Process-Based Models Such as Flumy to Reproduce a Fluvial Meandering Reservoir. In 73rd EAGE Conference and Exhibition-Workshops 2011.

Copeland, R. R., Biedenharn, D. S., and Fischenich, J. C. (2000) Channel-Forming Discharge. Vicksburg, MS: U.S. Army Corps of Engineers, Coastal and Hydraulics RESPONSE TO URBANIZATION IN COASTAL PLAIN 551 Laboratory, U.S. Army Engineer Research and Development Center (ERDC), Report ERDC/CHL CHETN-VIII-5. http://www.dtic.mil/dtic/tr/fulltext/u2/a604706.pdf.

Corney, R. K., Peakall, J., Parsons, D. R., Elliott, L., Amos, K. J., Best, J. L., ... & Ingham, D. B. (2006). The orientation of helical flow in curved channels. Sedimentology, 53(2), 249-257. https://doi.org/10.1111/j.1365-3091.2006.00771.x.

Cortés, A., Rueda, F. J., & Wells, M. G. (2014). Experimental observations of the splitting of a gravity current at a density step in a stratified water body. Journal of Geophysical Research: Oceans, 119(2), 1038-1053. https://doi.org/10.1002/2013JC009304.

Covault, J. A., Sylvester, Z., Hubbard, S. M., Jobe, Z. R., & Sech, R. P. (2016). The stratigraphic record of submarine-channel evolution. The Sedimentary Record, 14(3), 4-11. http://doi.org/10.2110/sedred.2016.3.

Crosato, A. (2007). Effects of smoothing and regridding in numerical meander migration models. Water Resources Research, 43(1). https://doi.org/10.1029/2006WR005087.

Cross, N. E., Cunningham, A., Cook, R. J., Taha, A., Esmaie, E., & El Swidan, N. (2009). Three-dimensional seismic geomorphology of a deep-water slope-channel system: The Sequoia field, offshore west Nile Delta, Egypt. AAPG bulletin, 93(8), 1063-1086. https://doi.org/10.1306/05040908101.

Curray, J. R., Emmel, F. J., & Moore, D. G. (2003). The Bengal Fan: morphology, geometry, stratigraphy, history and processes. Marine and Petroleum Geology, 19(10), 1191-1223. https://doi.org/10.1016/S0264-8172(03)00035-7.

Damuth, J. E., & Flood, R. D. (1983). Morphology, sedimentation processes, and growth pattern of the Amazon deep-sea fan. Geo-Marine Letters, 3(2-4), 109-117. https://doi.org/10.1007/BF02462455.

Darby, S. E., Trieu, H. Q., Carling, P. A., Sarkkula, J., Koponen, J., Kummu, M., ... & Leyland, J. (2010). A physically based model to predict hydraulic erosion of fine-grained riverbanks: The role of form roughness in limiting erosion. Journal of Geophysical Research: Earth Surface, 115(F4). https://doi.org/10.1029/2010JF001708.

Das, H. S., Imran, J., Pirmez, C., & Mohrig, D. (2004). Numerical modeling of flow and bed evolution in meandering submarine channels. Journal of Geophysical Research: Oceans, 109(C10). https://doi.org/10.1029/2002JC001518.

De Leeuw, J., Eggenhuisen, J. T., & Cartigny, M. J. (2016). Morphodynamics of submarine channel inception revealed by new experimental approach. Nature communications, 7, 10886. https://doi.org/10.1038/ncomms10886.

De Leeuw, J., Eggenhuisen, J. T., & Cartigny, M. J. (2018). Linking submarine channel–levee facies and architecture to flow structure of turbidity currents: insights from flume tank experiments. Sedimentology, 65(3), 931-951. https://doi.org/10.1111/sed.12411.

De Rooij, F., & Dalziel, S. (2009). Time-and space-resolved measurements of deposition under turbidity currents. In *Particulate Gravity Currents*, Wiley, New York, 207-215.

Dennielou, B., Huchon, A., Beaudouin, C., & Berné, S. (2006). Vertical grain-size variability within a turbidite levee: Autocyclicity or allocyclicity? A case study from the Rhône neofan, Gulf of Lions, Western Mediterranean. Marine Geology, 234(1-4), 191-213. https://doi.org/10.1016/j.margeo.2006.09.019.

Dennielou, B., Droz, L., Babonneau, N., Jacq, C., Bonnel, C., Picot, M., ... & Olu, K. (2017). Morphology, structure, composition and build-up processes of the active channel-mouth lobe complex of the Congo deep-sea fan with inputs from remotely operated underwater vehicle (ROV) multibeam and video surveys. Deep Sea Research Part II: Topical Studies in Oceanography, 142, 25-49. https://doi.org/10.1016/j.dsr2.2017.03.010.

Deptuck, M.E., Steffens, G.S., Barton, M., Pirmez, C. (2003). Architecture and evolution of upper fan channel-belts on the Niger Delta slope and in the Arabian Sea. Marine and Petroleum Geology 20, 649–676. https://doi.org/10.1016/j.marpetgeo.2003.01.004.

Deptuck, M. E., Sylvester, Z., Pirmez, C., & O'Byrne, C. (2007). Migration–aggradation history and 3-D seismic geomorphology of submarine channels in the Pleistocene Benin-major Canyon, western Niger Delta slope. Marine and Petroleum Geology, 24(6-9), 406-433. https://doi.org/10.1016/j.marpetgeo.2007.01.005.

Deutsch, C. V., & Tran, T. T. (2002). FLUVSIM: a program for object-based stochastic modeling of fluvial depositional systems. Computers & Geosciences, 28(4), 525-535. https://doi.org/10.1016/S0098-3004(01)00075-9.

Dorrell, R. M., Darby, S. E., Peakall, J., Sumner, E. J., Parsons, D. R., & Wynn, R. B. (2014). The critical role of stratification in submarine channels: Implications for channelization and long runout of flows. Journal of Geophysical Research: Oceans, 119(4), 2620-2641. https://doi.org/10.1002/2014JC009807.

Dorrell, R. M., Peakall, J., Burns, C., & Keevil, G. M. (2018). A novel mixing mechanism in sinuous seafloor channels: Implications for submarine channel evolution. Geomorphology, 303, 1-12. https://doi.org/10.1016/j.geomorph.2017.11.008.

Doughty-Jones, G., Mayall, M., & Lonergan, L. (2017). Stratigraphy, facies, and evolution of deep-water lobe complexes within a salt-controlled intraslope minibasin. AAPG Bulletin, 101(11), 1879-1904. https://doi.org/10.1306/01111716046.

Dury, G. H. (1976). Discharge prediction, present and former, from channel dimensions. Journal of Hydrology, 30(3), 219-245. https://doi.org/10.1016/0022-1694(76)90102-5.

Duvbiama, O., & Ikomi, J. (2017, July). 3D Static Modelling of An Offshore Field in the Niger-Delta. In Nigeria Annual International Conference and Exhibition. Society of Petroleum Engineers. https://doi.org/10.2118/189161-MS.

Dykstra, M., & Kneller, B. (2009). Lateral accretion in a deep-marine channel complex: implications for channellized flow processes in turbidity currents. Sedimentology, 56(5), 1411-1432. https://doi.org/10.1111/j.1365-3091.2008.01040.x.

Dykstra, M., Kneller, B., & MILANA, J. P. (2012). Bed-thickness and grain-size trends in a small-scale proglacial channel–levée system; the Carboniferous Jejenes Formation, Western Argentina: implications for turbidity current flow processes. Sedimentology, 59(2), 605-622. https://doi.org/10.1111/j.1365-3091.2011.01268.x.

Eke, E., Parker, G., & Shimizu, Y. (2014). Numerical modeling of erosional and depositional bank processes in migrating river bends with self-formed width: Morphodynamics of bar push and bank pull. Journal of Geophysical Research: Earth Surface, 119(7), 1455-1483. https://doi.org/10.1002/2013JF003020.

Ellison, T. H., & Turner, J. S. (1959). Turbulent entrainment in stratified flows. Journal of Fluid Mechanics, 6(3), 423-448. https://doi.org/10.1017/S0022112059000738.

Engelund, F. (1974). Flow and bed topography in channel bends. Journal of the Hydraulics Division, 100(Proc. Paper 10963).

Eschard, R., Deschamps, R., Doligez, B., Lerat, O., Langlais, V., & Euzen, T. (2013). Connectivity estimation between turbiditic channels and overbank deposits from the modelling of an outcrop analogue (Pab Formation, Maastrichtian, Pakistan). Geological Society, London, Special Publications, 387, SP387-7. https://doi.org/10.1144/SP387.7.

Ezz, H., Cantelli, A., & Imran, J. (2014). A Polynomial Model for Lateral Thickness Decay of Submarine Channel–Levees. Journal of Sedimentary Research, 84(1), 51-57. https://doi.org/10.2110/jsr.2014.7.

Ezz, H., & Imran, J. (2014). Curvature-induced secondary flow in submarine channels. Environmental Fluid Mechanics, 14(2), 343-370. http://doi.org/10.1007/s10652-014-9345-4.

Farhadi, A., Sindelar, C., Tritthart, M., Glas, M., Blanckaert, K., & Habersack, H. (2018). An investigation on the outer bank cell of secondary flow in channel bends. Journal of Hydro-Environment Research, 18, 1-11. https://doi.org/10.1016/j.jher.2017.10.004.

Ferguson, R. I. (1987). Hydraulic and sedimentary controls of channel pattern, in River Channels: Environment and Process, Inst. of Br. Geogr. Spec. Publ. 18, edited by K. Richards, pp. 129–158, Blackwell, Oxford, U. K.

Fildani, A., Hubbard, S. M., Covault, J. A., Maier, K. L., Romans, B. W., Traer, M., & Rowland, J. C. (2013). Erosion at inception of deep-sea channels. Marine and Petroleum Geology, 41, 48-61. https://doi.org/10.1016/j.marpetgeo.2012.03.006.

Flood, R. D., & Damuth, J. E. (1987). Quantitative characteristics of sinuous distributary channels on the Amazon deep-sea fan. Geological Society of America Bulletin, 98(6), 728-738. https://doi.org/10.1130/0016-7606(1987)98<728:QCOSDC>2.0.CO;2.

Foreman, B. Z., Lai, S. Y., Komatsu, Y., & Paola, C. (2015). Braiding of submarine channels controlled by aspect ratio similar to rivers. Nature Geoscience, 8(9), 700. https://doi.org/10.1038/ngeo2505.

Frascati, A., Lanzoni, S., (2009). Morphodynamic regime and long term evolution of meandering rivers. J. Geophys. Res.: Earth Surf. 114(F2), http://doi.org/10.1029/2008JF001101.

Friedkin, J.F., (1945). A Laboratory Study of the Meandering of Alluvial Rivers. U.S. Army Corps Eng., Waterways Exp. Stn., Vicksburg, 40 pp.

Gainski, M., MacGregor, A. G., Freeman, P. J., & Nieuwland, H. F. (2010). Turbidite reservoir compartmentalization and well targeting with 4D seismic and production data: Schiehallion Field, UK. Geological Society, London, Special Publications, 347(1), 89-102. https://doi.org/10.1144/SP347.7.

Gennesseaux, M., Mauffret, A., & Pautot, G. (1980). Les glissements sous-marins de la pente continentale niçoise et la rupture de câbles en mer Ligure (Méditerranée occidentale). Comptes Rendus de l'Académie des Sciences de Paris, 290(14), 959-962.

Ghinassi, M., Nemec, W., Aldinucci, M., Nehyba, S., Özaksoy, V., Fidolini, F. & Mountney, N. (2014), Plan-form evolution of ancient meandering rivers reconstructed from longitudinal outcrop sections. Sedimentology, 61: 952-977. https://doi.org/10.1111/sed.12081.

Giorgio Serchi, F., Peakall, J., Ingham, D. B., & Burns, A. D. (2011). A unifying computational fluid dynamics investigation on the river-like to river-reversed secondary circulation in submarine channel bends. Journal of Geophysical Research: Oceans, 116(C6). https://doi.org/10.1029/2010JC006361.

Gladstone, C., Phillips, J. C., & Sparks, R. S. J. (1998). Experiments on bidisperse, constant-volume gravity currents: propagation and sediment deposition. Sedimentology, 45(5), 833-843.

Gleason, C. J. (2015). Hydraulic geometry of natural rivers: A review and future directions. Progress in Physical Geography, 39(3), 337-360. https://doi.org/10.1177/0309133314567584.

Grappe, B. (2014). Modèles d'écoulement à surface libre pour la simulation à long terme de la migration des systèmes méandriformes (Doctoral dissertation, Ecole Nationale Supérieure des Mines de Paris). Retrieved from thesis.fr (http://www.theses.fr/2014ENMP0008).

Harishidayat, D., Omosanya, K. O., Johansen, S. E., Eruteya, O. E., & Niyazi, Y. (2018) Morphometric analysis of sediment conduits on a bathymetric high: Implications for palaeoenvironment and hydrocarbon prospectivity. Basin Res. 30:1015–1041. https://doi.org/10.1111/bre.12291.

Hassanpour, M. M., Pyrcz, M. J., & Deutsch, C. V. (2013). Improved geostatistical models of inclined heterolithic strata for McMurray Formation, Alberta, Canada. AAPG bulletin, 97(7), 1209-1224. http://doi.org/10.1306/01021312054.

Hansen, L., Janocko, M., Kane, I., & Kneller, B. (2017). Submarine channel evolution, terrace development, and preservation of intra-channel thin-bedded turbidites: Mahin and Avon channels, offshore Nigeria. Marine Geology, 383, 146-167. https://doi.org/10.1016/j.margeo.2016.11.011.

Heezen, B. C., & Ewing, M. (1952). Turbidity currents and submarine slumps, and the 1929 Grand Banks earthquake. American journal of Science, 250(12), 849-873.

Held, A.-E. (2011). Apport de la paléohydrologie dans la quantification des rôles respectifs du climat et de la tectonique des systèmes fluviatiles méandriformes fossiles. Application à des systèmes oligomiocènes d'Europe occidentale. (Doctoral dissertation, Ecole nationale supérieure des mines de Paris). Retrieved from theses.fr (https://www.theses.fr/2011ENMP0008).

Heller, P. L., & Paola, C. (1996). Downstream changes in alluvial architecture; an exploration of controls on channel-stacking patterns. Journal of Sedimentary Research, 66(2), 297-306. https://doi.org/10.1306/D4268333-2B26-11D7-8648000102C1865D.

Hesse, R., Klaucke, I., Khodabakhsh, S., Piper, D. J., Ryan, W. B., & NAMOC Study Group. (2001). Sandy submarine braid plains: potential deep-water reservoirs. AAPG bulletin, 85(8), 1499-1521.

Hickin, E. J., & Nanson, G. C. (1984). Lateral migration rates of river bends. Journal of Hydraulic Engineering, 110(11), 1557-1567. https://doi.org/10.1061/(ASCE)0733-9429(1984)110:11(1557).

Hickin, E. J. (1978). Mean flow structure in meanders of the Squamish River, British Columbia. Canadian Journal of Earth Sciences, 15(11), 1833-1849. https://doi.org/10.1139/e78-191.

Hiscott, R. N. (1994). Loss of capacity, not competence, as the fundamental process governing deposition from turbidity currents. Journal of Sedimentary Research, 64(2a), 209-214. https://doi.org/10.2110/jsr.64.209.

Hiscott, R. N., Hall, R. R., & Pirmez, C. (1997). Turbidity-current overspill from the Amazon Channel: texture of the silt/sand load, paleoflow from anisotropy of magnetic susceptibility, and implications for flow processes. In R. D. Flood, D. J. W. Piper, A. Klaus, & L. C. Peterson (Eds.), (Vol. 155) (pp. 53–78). 1997 Proceedings of the Ocean Drilling Program, Scientific Results.

Hodgson, D. M., Di Celma, C. N., Brunt, R. L., & Flint, S. S. (2011). Submarine slope degradation and aggradation and the stratigraphic evolution of channel–levee systems. Journal of the Geological Society, 168(3), 625-628. https://doi.org/10.1144/0016-76492010-177.

Hooke, R. L. B. (1975). Distribution of sediment transport and shear stress in a meander bend. The Journal of geology, 83(5), 543-565. https://doi.org/10.1086/628140.

Hosseini, S. A., Shamsai, A., & Ataie-Ashtiani, B. (2006). Synchronous measurements of the velocity and concentration in low density turbidity currents using an Acoustic Doppler Velocimeter. Flow Measurement and Instrumentation, 17(1), 59-68. https://doi.org/10.1016/j.flowmeasinst.2005.05.002.

Howard, A. D., & Knutson, T. R. (1984). Sufficient conditions for river meandering: A simulation approach. Water Resources Research, 20(11), 1659-1667. https://doi.org/10.1029/WR020i011p01659.

Howard, A. (1996), Modelling channel migration and floodplain development in meandering streams, Lowland Floodplain Rivers: Geomorphological Perspectives, edited by P. A. Carling and G. E. Petts, pp. 2–41, John Wiley, New York.

Huang, H., Imran, J., & Pirmez, C. (2005). Numerical model of turbidity currents with a deforming bottom boundary. Journal of Hydraulic Engineering, 131(4), 283-293. https://doi.org/10.1061/(ASCE)0733-9429(2005)131:4(283).

Huang, Y. (2018). Sedimentary characteristics of turbidite fan and its implication for hydrocarbon exploration in Lower Congo Basin. Petroleum Research, 3(2), 189-196. https://doi.org/10.1016/j.ptlrs.2018.02.001.

Ikeda, S., Parker, G., & Sawai, K. (1981). Bend theory of river meanders. Part 1. Linear development. Journal of Fluid Mechanics, 112, 363-377. https://doi.org/10.1017/S0022112081000451.

Imran, J., Parker, G., & Katopodes, N. (1998). A numerical model of channel inception on submarine fans. Journal of Geophysical Research: Oceans, 103(C1), 1219-1238. https://doi.org/10.1029/97JC01721.

Imran, J., Parker, G., & Pirmez, C. (1999). A nonlinear model of flow in meandering submarine and subaerial channels. Journal of Fluid Mechanics, 400, 295-331. https://doi.org/10.1017/S0022112099006515.

Imran, J., Khan, S. M., Pirmez, C., & Parker, G. (2017). Froude scaling limitations in modeling of turbidity currents. Environmental Fluid Mechanics, 17(1), 159-186. http://doi.org/10.1007/s10652-016-9488-6.

Islam, M. A., & Imran, J. (2010). Vertical structure of continuous release saline and turbidity currents. Journal of Geophysical Research: Oceans, 115(C8). https://doi.org/10.1029/2009JC005365.

Issautier, B., Viseur, S., Audigane, P., Chiaberge, C., & Le Nindre, Y. M. (2016). A new approach for evaluating the impact of fluvial type heterogeneity in CO2 storage reservoir modeling. Comptes Rendus Geoscience, 348(7), 531-539. https://doi.org/10.1016/j.crte.2015.06.006.

Janocko, M., Cartigny, M. B. J., Nemec, W., & Hansen, E. W. M. (2013). Turbidity current hydraulics and sediment deposition in erodible sinuous channels: laboratory experiments and numerical simulations. Marine and Petroleum Geology, 41, 222-249. https://doi.org/10.1016/j.marpetgeo.2012.08.012.

Jefferson, M. (1902). Limiting width of meander belts. National Geographic Society.

Jerolmack, D. J., & Mohrig, D. (2007). Conditions for branching in depositional rivers. Geology, 35(5), 463-466. https://doi.org/10.1130/G23308A.1.

Jobe, Z. R., Howes, N. C., & Auchter, N. C. (2016). Comparing submarine and fluvial channel kinematics: Implications for stratigraphic architecture. Geology, 44(11), 931-934. https://doi.org/10.1130/G38158.1.

Jobe, Z. R., Sylvester, Z., Parker, A. O., Howes, N., Slowey, N., & Pirmez, C. (2015). Rapid Adjustment of Submarine Channel Architecture To Changes In Sediment Supply ADJUSTMENT OF SUBMARINE CHANNEL ARCHITECTURE TO CHANGES IN SEDIMENT SUPPLY. Journal of Sedimentary Research, 85(6), 729-753. https://doi.org/10.2110/jsr.2015.30.

Jobe, Z., Sylvester, Z., Pittaluga, M. B., Frascati, A., Pirmez, C., Minisini, D., et al. 2017). Facies architecture of submarine channel deposits on the western Niger Delta slope: Implications for grain-size and density stratification in turbidity currents. Journal of Geophysical Research: Earth Surface, 122(2), 473-491. https://doi.org/10.1002/2016JF003903.

Johannesson, H., & Parker, G. (1989). Linear theory of river meanders. River meandering, 12, 181-213. https://doi.org/10.1029/WM012p0181.

Johnson, P. A., & Fecko, B. J. (2008). Regional channel geometry equations: a statistical comparison for physiographic provinces in the eastern US. River Research and Applications, 24(6), 823-834. https://doi.org/10.1002/rra.1080.

Jorry, S. J., Jégou, I., Emmanuel, L., Jacinto, R. S., & Savoye, B. (2011). Turbiditic levee deposition in response to climate changes: the Var Sedimentary Ridge (Ligurian Sea). Marine Geology, 279(1-4), 148-161. https://doi.org/10.1016/j.margeo.2010.10.021.

Kane, I. A., McCaffrey, W. D., & Peakall, J. (2008). Controls on sinuosity evolution within submarine channels. Geology, 36(4), 287-290. https://doi.org/10.1130/G24588A.1.

Kane, I. A., McCaffrey, W. D., Peakall, J., & Kneller, B. C. (2010). Submarine channel levee shape and sediment waves from physical experiments. Sedimentary Geology, 223(1-2), 75-85. https://doi.org/10.1016/j.sedgeo.2009.11.001.

Kane, I. A., Pontén, A. S., Vangdal, B., Eggenhuisen, J. T., Hodgson, D. M., & Spychala, Y. T. (2017). The stratigraphic record and processes of turbidity current transformation across deep-marine lobes. Sedimentology, 64(5), 1236-1273. https://doi.org/10.1111/sed.12346.

Karlstrom, L., Gajjar, P., & Manga, M. (2013). Meander formation in supraglacial streams. Journal of Geophysical Research: Earth Surface, 118(3), 1897-1907. https://doi.org/10.1002/jgrf.20135.

Kassem, A., & Imran, J. (2004). Three-dimensional modeling of density current. II. Flow in sinuous confined and uncontined channels. Journal of Hydraulic Research, 42(6), 591-602. https://doi.org/10.1080/00221686.2004.9628313.

Kean, J. W., & Smith, J. D. (2006). Form drag in rivers due to small-scale natural topographic features: 1. Regular sequences. Journal of Geophysical Research: Earth Surface, 111(F4). https://doi.org/10.1029/2006JF000467.

Keevil, G. M., Peakall, J., Best, J. L., & Amos, K. J. (2006). Flow structure in sinuous submarine channels: velocity and turbulence structure of an experimental submarine channel. Marine Geology, 229(3-4), 241-257. https://doi.org/10.1016/j.margeo.2006.03.010.

Kenyon, N. H., Amir, A., & Cramp, A. (1995). Geometry of the younger sediment bodies of the Indus Fan. In Atlas of Deep Water Environments (pp. 89-93). Springer, Dordrecht.

Khan, Z. A., & Arnott, R. W. C. (2011). Stratal attributes and evolution of asymmetric inner-and outer-bend levee deposits associated with an ancient deep-water channel-levee complex within the Isaac Formation, southern Canada. Marine and Petroleum Geology, 28(3), 824-842. https://doi.org/10.1016/j.marpetgeo.2010.07.009.

Khripounoff, A., Vangriesheim, A., Babonneau, N., Crassous, P., Dennielou, B., & Savoye, B. (2003). Direct observation of intense turbidity current activity in the Zaire submarine valley at 4000 m water depth. Marine Geology, 194(3-4), 151-158. https://doi.org/10.1016/S0025-3227(02)00677-1.

Kneller, B. C., Bennett, S. J., & McCaffrey, W. D. (1999). Velocity structure, turbulence and fluid stresses in experimental gravity currents. Journal of Geophysical Research: Oceans, 104(C3), 5381-5391. https://doi.org/10.1029/1998JC900077.

Kneller, B. (2003). The influence of flow parameters on turbidite slope channel architecture. Marine and Petroleum Geology, 20(6-8), 901-910. https://doi.org/10.1016/j.marpetgeo.2003.03.001.

Kohl, B., Leg, D. S. D. P., & Scientists, S. (1985). Biostratigraphy and sedimentation rates of the Mississippi Fan. In Submarine fans and related turbidite systems (pp. 267-273). Springer, New York, NY.

Kolla, V. (2007). A review of sinuous channel avulsion patterns in some major deep-sea fans and factors controlling them. Marine and Petroleum Geology, 24(6-9), 450-469. https://doi.org/10.1016/j.marpetgeo.2007.01.004.

Komar, P. D. (1973). Continuity of turbidity current flow and systematic variations in deep-sea channel morphology. Geological Society of America Bulletin, 84(10), 3329-3338. https://doi.org/10.1130/0016-7606(1973)84%3C3329:COTCFA%3E2.0.CO;2.

Kondolf, G. M. (2016). Tools in fluvial geomorphology. John Wiley & Sons.

Koneshloo, M., Aryana, S. A., Grana, D., & Pierre, J. W. (2017). A workflow for static reservoir modeling guided by seismic data in a fluvial system. Mathematical Geosciences, 49(8), 995-1020. http://doi.org/10.1007/s11004-017-9696-8.

Konsoer, K., Zinger, J., & Parker, G. (2013). Bankfull hydraulic geometry of submarine channels created by turbidity currents: relations between bankfull channel characteristics and formative flow discharge. Journal of Geophysical Research: Earth Surface, 118(1), 216-228. https://doi.org/10.1029/2012JF002422.

Labourdette, R. (2008). 'LOSCS'Lateral Offset Stacked Channel Simulations: Towards geometrical modelling of turbidite elementary channels. Basin Research, 20(3), 431-444.

Labourdette, R., & Bez, M. (2010). Element migration in turbidite systems: Random or systematic depositional processes?. AAPG bulletin, 94(3), 345-368. http://doi.org/ 10.1306/09010909035.

Leopold, L. B., & Langbein, W. B. (1966). River meanders. Scientific American, 214(6), 60-73.

Leeder, M., (1999). Sedimentology and Sedimentary Basins: From Turbulence to Tectonics. Blackwell, Oxford (592 pp.).

Leigh, D. S., & Feeney, T. P. (1995). Paleochannels indicating wet climate and lack of response to lower sea level, southeast Georgia. Geology, 23(8), 687-690. https://doi.org/10.1130/0091-7613(1995)023<0687:PIWCAL>2.3.CO;2.

Lemay, M., Cojan, I., Grimaud, J. L., Rivoirard, J., Ors, F. (submitted). Geomorphic variability of submarine flow pathways along continental margins: comparison with fluvial meandering channels. Marine and Petroleum Geology.

Leopold, L. B., & Maddock, T. (1953). The hydraulic geometry of stream channels and some physiographic implications (Vol. 252). US Government Printing Office.

Leopold, L. B., & Wolman, M. G. (1957). River channel patterns: braided, meandering, and straight. US Government Printing Office.

Leopold, L. B., & Wolman, M. G. (1960). River meanders. Geological Society of America Bulletin, 71(6), 769-793. https://doi.org/10.1130/0016-7606(1960)71[769:RM]2.0.CO;2.

Limaye, A. B., Grimaud, J. L., Lai, S. Y., Foreman, B. Z., Komatsu, Y., & Paola, C. (2018). Geometry and dynamics of braided channels and bars under experimental density currents. Sedimentology, 65: 1947-1972. https://doi.org/10.1111/sed.12453.

Lombo Tombo, S., Dennielou, B., Berné, S., Bassetti, M. A., Toucanne, S., Jorry, S. J., ... & Fontanier, C. (2015). Sea-level control on turbidite activity in the Rhone canyon and the upper fan during the Last Glacial Maximum and Early deglacial. Sedimentary Geology, 323, 148-166. https://doi.org/10.1016/j.sedgeo.2015.04.009.

Lonsdale, P., & Hollister, C. D. (1979). Cut-offs at an abyssal meander south of Iceland. Geology, 7(12), 597-601. https://doi.org/10.1130/0091-7613(1979)7<597:CAAAMS>2.0.CO;2.

Lopez, S (2003) Modélisation de réservoirs chenalisés méandriformes: approche génétique et stochastique. (doctoral dissertation, Ecole des Mines de Paris). Retrieved from theses.fr (http://www.theses.fr/2003ENMP1260).

Lopez, S., Cojan, I., Rivoirard, J., & Galli, A. (2008). Process-based stochastic modelling: meandering channelized reservoirs. Analogue and Numerical Modelling of Sedimentary Systems: From Understanding to Prediction, Wiley, Oxford, UK, 139-144.

Luchi, R., Balachandar, S., Seminara, G., & Parker, G. (2018). Turbidity currents with equilibrium basal driving layers: A mechanism for long runout. Geophysical Research Letters, 45, 1518–1526. https://doi.org/10.1002/2017GL075608

Maier, K. L., Fildani, A., McHargue, T., Paull, C. K., Graham, S. A., & Caress, D. W. (2013). Punctuated Deep-Water Channel Migration: High-Resolution Subsurface Data From the Lucia Chica Channel System, Offshore California, USA—Reply. Journal of Sedimentary Research, 83(1), 93-95. https://doi.org/10.2110/jsr.2013.6.

Malgesini, G., Talling, P. J., Hogg, A. J., Armitage, D., Goater, A., & Felletti, F. (2015). Quantitative analysis of submarine-flow deposit shape in the Marnoso-Arenacea Formation: what is the signature of hindered settling from dense near-bed layers?. Journal of Sedimentary Research, 85(2), 170-191. https://doi.org/10.2110/jsr.2015.15.

Manley, P. L., & Flood, R. D. (1988). Cyclic sediment deposition within Amazon deep-sea fan. Aapg Bulletin, 72(8), 912-925.

Manley, P. L., Pirmez, C., Busch, W., & Cramp, A. (1997). Grain-size characterization of Amazon Fan deposits and comparison to seismic facies units. In PROCEEDINGS-OCEAN DRILLING PROGRAM SCIENTIFIC RESULTS (pp. 35-52). NATIONAL SCIENCE FOUNDATION.

Mansor, S. (2009). Le processus d'avulsion: enregistrement stratigraphique et sédimentologique: application aux éventails turbiditiques de l'Amazone et du Zaïre. (Doctoral dissertation, Université de Brest). Retrieved from theses.fr (https://www.theses.fr/2009BRES2049).

Mariethoz, G., & Caers, J. (2014). Multiple-point geostatistics: stochastic modeling with training images. John Wiley & Sons.

Matheron, G. (1963). Principles of geostatistics. Economic geology, 58(8), 1246-1266.

Mayall, M., Jones, E., & Casey, M. (2006). Turbidite channel reservoirs—Key elements in facies prediction and effective development. Marine and Petroleum Geology, 23(8), 821-841. https://doi.org/10.1016/j.marpetgeo.2006.08.001.

Mayall, M., & O'Byrne, C. (2002, January). Reservoir prediction and development challenges in turbidite slope channels. In Offshore Technology Conference. Offshore Technology Conference.

McHargue, T., Pyrcz, M. J., Sullivan, M. D., Clark, J. D., Fildani, A., Romans, B., W., et al. (2011). Architecture of turbidite channel systems on the continental slope: patterns and predictions. Marine and Petroleum Geology, 28(3), 728-743. https://doi.org/10.1016/j.marpetgeo.2010.07.008.

Meiburg, E., & Kneller, B. (2010). Turbidity currents and their deposits. Annual Review of Fluid Mechanics, 42, 135-156. http://doi.org/10.1146/annurev-fluid-121108-145618.

Meiburg, E., & Nasr-Azadani, M. M. (2018). Gravity and Turbidity Currents: Numerical Simulations and Theoretical Models. In Mixing and Dispersion in Flows Dominated by Rotation and Buoyancy (pp. 129-180). Springer, Cham.

Menard Jr, H. W. (1955). Deep-sea channels, topography, and sedimentation. AAPG Bulletin, 39(2), 236-255.

Métivier, F., Lajeunesse, E., & Devauchelle, O. (2017). Laboratory rivers: Lacey's law, threshold theory, and channel stability. Earth Surface Dynamics, 5(1), 187-198. https://doi.org/10.5194/esurf-5-187-2017.

Miall, A. D. (1989). Architectural elements and bounding surfaces in channelized clastic deposits: Notes on comparisons between fluvial and turbidite systems. Sedimentary Facies in the Active Plate Margin. Edited by A. Taira and F. Masuda. TERRAPUB, Tokyo, 3-15.

Miall, A. (2014). The facies and architecture of fluvial systems. In Fluvial Depositional Systems (pp. 9-68). Springer, Cham.

Migeon, S., Mulder, T., Savoye, B., & Sage, F. (2012). Hydrodynamic processes, velocity structure and stratification in natural turbidity currents: results inferred from field data in the Var Turbidite System. Sedimentary Geology, 245, 48-62. https://doi.org/10.1016/j.sedgeo.2011.12.007.

Mishra, J., Inoue, T., Shimizu, Y., Sumner, T., & Nelson, J. M. (2018). Consequences of Abrading Bed Load on Vertical and Lateral Bedrock Erosion in a Curved Experimental Channel. Journal of Geophysical Research: Earth Surface. https://doi.org/10.1029/2017JF004387.

Montgomery, D. R., Abbe, T. B., Buffington, J. M., Peterson, N. P., Schmidt, K. M., & Stock, J. D. (1996). Distribution of bedrock and alluvial channels in forested mountain drainage basins. Nature, 381(6583), 587. https://doi.org/10.1038/381587a0.

Mulder, T., & Alexander, J. (2001). The physical character of subaqueous sedimentary density flows and their deposits. Sedimentology, 48(2), 269-299. https://doi.org/10.1046/j.1365-3091.2001.00360.x.

Mutti, E., & Normark, W. R. (1991). An integrated approach to the study of turbidite systems. In Seismic facies and sedimentary processes of submarine fans and turbidite systems (pp. 75-106). Springer, New York, NY.

Nakajima, T., & Kneller, B. C. (2013). Quantitative analysis of the geometry of submarine external levees. Sedimentology, 60(4), 877-910. https://doi.org/10.1111/j.1365-3091.2012.01366.x.

Nanson, R. A. (2010). Flow fields in tightly curving meander bends of low width-depth ratio. Earth Surface Processes and Landforms: The Journal of the British Geomorphological Research Group, 35(2), 119-135. https://doi.org/10.1002/esp.1878.

Normark, W. R. (1970). Growth patterns of deep-sea fans. AAPG bulletin, 54(11), 2170-2195.

O'Cofaigh, C., Dowdeswell, J. A., & Kenyon, N. H. (2006). Geophysical investigations of a high-latitude submarine channel system and associated channel-mouth lobe in the Lofoten Basin, Polar North Atlantic. Marine Geology, 226(1-2), 41-50. https://doi.org/10.1016/j.margeo.2005.09.014.

Ono, K., & Plink-Björklund, P. (2018). Froude supercritical flow bedforms in deepwater slope channels? Field examples in conglomerates, sandstones and fine-grained deposits. Sedimentology, 65(3), 639-669. https://doi.org/10.1111/sed.12396.

Parker, G., Fukushima, Y., & Pantin, H. M. (1986). Self-accelerating turbidity currents. Journal of Fluid Mechanics, 171, 145-181. https://doi.org/10.1017/S0022112086001404.

Parquer, M. (2018). Reverse-time modeling of channelized meandering systems from geological observations (Doctoral dissertation, Université de Lorraine). Retrieved from theses.fr (http://www.theses.fr/2018LORR0081).

Parquer, M., Collon, P., Caumon, G., 2017 Reconstruction of Channelized Systems Through a Conditioned Reverse Migration Method. Mathematical Geosciences 49, 1–30. http://doi.org/0.1007/s11004-017-9700-3.

Paull, C. K., Talling, P. J., Maier, K. L., Parsons, D., Xu, J., Caress, D. W., ... & Chaffey, M. (2018). Powerful turbidity currents driven by dense basal layers. Nature Communications, 9(1), 4114. https://doi.org/10.1038/s41467-018-06254-6.

Peakall, J., McCaffrey, B., & Kneller, B. (2000). A process model for the evolution, morphology, and architecture of sinuous submarine channels. Journal of Sedimentary Research, 70(3), 434-448. https://doi.org/10.1306/2DC4091C-0E47-11D7-8643000102C1865D.

Peakall, J., Amos, K. J., Keevil, G. M., Bradbury, P. W., & Gupta, S. (2007). Flow processes and sedimentation in submarine channel bends. Marine and Petroleum Geology, 24(6-9), 470-486. https://doi.org/10.1016/j.marpetgeo.2007.01.008.

Peakall, J., & Sumner, E. J. (2015). Submarine channel flow processes and deposits: A process-product perspective. Geomorphology, 244, 95-120. https://doi.org/10.1016/j.geomorph.2015.03.005.

Perucca, E., C. Camporeale, and L. Ridolfi (2006), Influence of river meandering dynamics on riparian vegetation pattern formation, J. Geophys. Res., 111, G01001, https://doi.org/10.1029/2005JG000073.

Peter, C., Sacchi, Q., Serazio, C., & Verga, F. (2017). Capturing channelized reservoir connectivity uncertainty with amalgamation curves. Marine and Petroleum Geology, 88, 329-342. https://doi.org/10.1016/j.marpetgeo.2017.07.017.

Pettinga, L., Jobe, Z., Shumaker, L., & Howes, N. (2018). Morphometric scaling relationships in submarine channel–lobe systems. Geology. https://doi.org/10.1130/G45142.1.

Piper, D. J., & Normark, W. R. (1983). Turbidite depositional patterns and flow characteristics, Navy submarine fan, California Borderland. Sedimentology, 30(5), 681-694. https://doi.org/10.1111/j.1365-3091.1983.tb00702.x.

Pirmez, C., & Flood, R. D. (1995). Morphology and structure of Amazon Channel. In Proceedings of the Ocean Drilling Program. Initial Reports (Vol. 155, pp. 23-45). Ocean Drilling Program.

Pirmez, C., Beaubouef, R. T., Friedmann, S. J., & Mohrig, D. C. (2000). Equilibrium profile and baselevel in submarine channels: examples from Late Pleistocene systems and implications for the architecture of deepwater reservoirs. In Global deep-water reservoirs: Gulf Coast Section SEPM Foundation 20th Annual Bob F. Perkins Research Conference (pp. 782-805). https://doi.org/10.5724/gcs.00.15.0782.

Pirmez, C., & Imran, J. (2003). Reconstruction of turbidity currents in Amazon Channel. Marine and petroleum geology, 20(6-8), 823-849. https://doi.org/10.1016/j.marpetgeo.2003.03.005

Posamentier, H., (2003). Depositional elements associated with a basin floor channel–levee system: case study from the Gulf of Mexico. Marine and Petroleum Geology 20, 677–690. https://doi.org/10.1016/j.marpetgeo.2003.01.002.

Postma, G., & Kleverlaan, K. (2018). Supercritical flows and their control on the architecture and facies of small-radius sand-rich fan lobes. Sedimentary Geology, 364, 53-70.

Pyrcz, M. J., Boisvert, J. B., & Deutsch, C. V. (2009). ALLUVSIM: A program for event-based stochastic modeling of fluvial depositional systems. Computers & Geosciences, 35(8), 1671-1685. https://doi.org/10.1016/j.cageo.2008.09.012.

Pyrcz, M. J., Sech, R. P., Covault, J. A., Willis, B. J., Sylvester, Z., & Sun, T. (2015). Stratigraphic rule-based reservoir modeling. Bulletin of Canadian Petroleum Geology, 63(4), 287-303. https://doi.org/10.2113/gscpgbull.63.4.287.

Raffel, M., Willert, C. E., Scarano, F., Kähler, C. J., Wereley, S. T., & Kompenhans, J. (2018). Particle image velocimetry: a practical guide. Springer.

Rivoirard, J., Cojan, I., & Geffroy, F. (2007, September). Controling the location of deposits in meandering channelized reservoir models. In EAGE Conference on Petroleum Geostatistics.

Rongier, G., Collon, P., & Renard, P. (2017). A geostatistical approach to the simulation of stacked channels. Marine and Petroleum Geology, 82, 318-335. https://doi.org/10.1016/j.marpetgeo.2017.01.027.

Rongier, G. (2016). Connectivity of channelized sedimentary bodies: analysis and simulation strategies in subsurface modeling (Doctoral dissertation, Université de Lorraine). Retrieved from theses.fr (http://www.theses.fr/2016LORR0026).

Rouse, H., 1937. Modern conceptions of the mechanics of fluid turbulence. Trans. ASCE 102, 463–543

Rotnicki, K. (1991). Retrodiction of palaeodischarges of meandering and sinuous alluvial rivers and its palaeohydroclimatic implications. Temperate palaeohydrology, 431-471.

Rowland, J. C., Hilley, G. E., & Fildani, A. (2010). A test of initiation of submarine leveed channels by deposition alone. Journal of Sedimentary Research, 80(8), 710-727. https://doi.org/10.2110/jsr.2010.067.

Sahagian, D. L., & Diplas, P. (2017, December). On the Fundamental Cause of River Meanders. In AGU Fall Meeting Abstracts.

Salles, T., Lopez, S., Cacas, M. C., & Mulder, T. (2007). Cellular automata model of density currents. Geomorphology, 88(1-2), 1-20. https://doi.org/10.1016/j.geomorph.2006.10.016.

Samuel, A., Kneller, B., Raslan, S., Sharp, A., & Parsons, C. (2003). Prolific deep-marine slope channels of the Nile Delta, Egypt. AAPG bulletin, 87(4), 541-560.

Sauer, V. B., & Turnipseed, D. P. (2010). Stage measurement at gaging stations (p. 45). US Department of the Interior, US Geological Survey.

Schwenk, J., Lanzoni, S., & Foufoula-Georgiou, E. (2015). The life of a meander bend: Connecting shape and dynamics via analysis of a numerical model. Journal of Geophysical Research: Earth Surface, 120(4), 690-710. https://doi.org/10.1002/2014JF003252.

Schwenk, T., Spieß, V., Hübscher, C., & Breitzke, M. (2003). Frequent channel avulsions within the active channel–levee system of the middle Bengal Fan—an exceptional channel–levee development derived from Parasound and Hydrosweep data. Deep Sea Research Part II: Topical Studies in Oceanography, 50(5), 1023-1045. https://doi.org/10.1016/S0967-0645(02)00618-5.

Sebacher, B., Hanea, R. G., & Ek, T. (2015, September). Quantifying the Uncertainty in the Facies Probability Cubes Using an Ensemble Kalman Filter Methodology. In Petroleum Geostatistics 2015. http://doi.org/10.3997/2214-4609.201413630.

Sequeiros, O. E., Spinewine, B., Beaubouef, R. T., Sun, T., García, M. H., & Parker, G. (2010). Characteristics of velocity and excess density profiles of saline underflows and turbidity currents flowing over a mobile bed. Journal of Hydraulic Engineering, 136(7), 412-433. https://doi.org/10.1061/(ASCE)HY.1943-7900.0000200.

Shepard, F. P. (1963). Importance of submarine valleys in funneling sediments to the deep sea. Progress in oceanography, 3, 321-332. https://doi.org/10.1016/0079-6611(65)90028-5.

Shepard, F. P. (1965). Types of submarine valleys. AAPG Bulletin, 49(3), 304-310.

Shepherd, M. (2009). Oil Field Production Geology: AAPG Memoir 91 (Vol. 91). AAPG.

Shumaker, L., E., Jobe, Z., Johnstone, S., A., Pettinga, L., A., Cai, D., Moody, J., D. (2018). Controls on submarine channel-modifying processes identified through morphometric scaling relationships. Geosphere. https://doi.org/10.1130/GES01674.1.

Sidorchuk, A., Borisova, O., & Panin, A. (2001). Fluvial response to the Late Valdai/Holocene environmental change on the East European Plain. Global and Planetary Change, 28(1-4), 303-318. https://doi.org/10.1016/S0921-8181(00)00081-3.

Skauvold, J., & Eidsvik, J. (2018). Data assimilation for a geological process model using the ensemble Kalman filter. Basin Research, 30(4), 730-745. https://doi.org/10.1111/bre.12273.

Skene, K. I (1998). Architecture of submarine channel levees. Unpublished PhD Thesis, Dalhousie University, Halifax, Nova Scotia, 362 pp

Skene, K. I., Piper, D. J., & Hill, P. S. (2002). Quantitative analysis of variations in depositional sequence thickness from submarine channel levees. Sedimentology, 49(6), 1411-1430. https://doi.org/10.1046/j.1365-3091.2002.00506.x.

Smith, J. D., & McLean, S. R. (1977). Boundary layer adjustments to bottom topography and suspended sediment. In Elsevier Oceanography Series (Vol. 19, pp. 123-151). Elsevier. https://doi.org/10.1016/S0422-9894(08)70839-0.

Stacey, M. W., & Bowen, A. J. (1988). The vertical structure of density and turbidity currents: theory and observations. Journal of Geophysical Research: Oceans, 93(C4), 3528-3542. https://doi.org/10.1029/JC093iC04p03528.

Stow, D. A., & Mayall, M. (2000). Deep-water sedimentary systems: new models for the 21st century. Marine and Petroleum Geology, 17(2), 125-135. https://doi.org/10.1016/S0264-8172(99)00064-1.

Straub, K. M., & Mohrig, D. (2008). Quantifying the morphology and growth of levees in aggrading submarine channels. Journal of Geophysical Research: Earth Surface, 113(F3). https://doi.org/10.1029/2007JF000896.

Straub, K. M., Mohrig, D., McElroy, B., Buttles, J., & Pirmez, C. (2008). Interactions between turbidity currents and topography in aggrading sinuous submarine channels: A laboratory study. GSA Bulletin, 120(3-4), 368-385. https://doi.org/10.1029/2007JF000896.

Strebelle, S. (2002). Conditional simulation of complex geological structures using multiple-point statistics. Mathematical geology, 34(1), 1-21. http://doi.org/10.1023/A:1014009426274.

Strebelle, S. B., & Journel, A. G. (2001, January). Reservoir modeling using multiple-point statistics. In SPE Annual Technical Conference and Exhibition. Society of Petroleum Engineers. https://doi.org/10.2118/71324-MS.

Strong, N., & Paola, C. (2008). Valleys that never were: time surfaces versus stratigraphic surfaces. Journal of Sedimentary Research, 78(8), 579-593. https://doi.org/10.2110/jsr.2008.059.

Sumner, E. J., Peakall, J., Dorrell, R. M., Parsons, D. R., Darby, S. E., Wynn, R. B., ... & White, D. (2014). Driven around the bend: Spatial evolution and controls on the orientation of helical bend flow in a natural submarine gravity current. Journal of Geophysical Research: Oceans, 119(2), 898-913. https://doi.org/10.1002/2013JC009008.

Sun, T., Meakin, P., Jøssang, T., & Schwarz, K. (1996). A simulation model for meandering rivers. Water resources research, 32(9), 2937-2954. https://doi.org/10.1029/96WR00998.

Sweet, W. V., & Geratz, J. W. (2003). Bankfull hydraulic geometry relationships and recurrence intervals for North Carolina's coastal plain. Journal of the American Water Resources Association, 39(4), 861-871. https://doi.org/10.1111/j.1752-1688.2003.tb04411.x.

Sylvester, Z., Pirmez, C., & Cantelli, A. (2011). A model of submarine channel-levee evolution based on channel trajectories: Implications for stratigraphic architecture. Marine and Petroleum Geology, 28(3), 716-727. https://doi.org/10.1016/j.marpetgeo.2010.05.012.

Sylvester, Z., & Covault, J. A. (2016). Development of cutoff-related knickpoints during early evolution of submarine channels. Geology, 44(10), 835-838. https://doi.org/10.1130/G38397.1.

Tahmasebi, P. (2018). Multiple Point Statistics: A Review. In Handbook of Mathematical Geosciences (pp. 613-643). Springer, Cham.

Tal, M., & Paola, C. (2010). Effects of vegetation on channel morphodynamics: results and insights from laboratory experiments. Earth Surface Processes and Landforms, 35(9), 1014-1028. https://doi.org/10.1002/esp.1908.

Talling, P. J., Allin, J., Armitage, D. A., Arnott, R. W., Cartigny, M. J., Clare, M. A., ... & Hill, P. R. (2015). Key Future Directions For Research On Turbidity Currents and Their Deposits. Journal of Sedimentary Research, 85(2), 153-169. https://doi.org/10.2110/jsr.2015.03.

Teles, V., Chauveau, B., Joseph, P., Weill, P., & Maktouf, F. (2016). CATS–A process-based model for turbulent turbidite systems at the reservoir scale. Comptes Rendus Geoscience, 348(7), 489-498. https://doi.org/10.1016/j.crte.2016.03.002.

Traer, M. M., Fildani, A., Fringer, O., McHargue, T., & Hilley, G. E. (2018a). Turbidity current dynamics: 1. Model formulation and identification of flow equilibrium conditions resulting from flow

stripping and overspill. Journal of Geophysical Research: Earth Surface, 123(3), 501-519. https://doi.org/10.1002/2017JF004200.

Traer, M. M., Fildani, A., Fringer, O., McHargue, T., & Hilley, G. E. (2018b). Turbidity current dynamics: 2. Simulating flow evolution toward equilibrium in idealized channels. Journal of Geophysical Research: Earth Surface, 123(3), 520-534. https://doi.org/10.1306/02090403100.

Tye, R. S. (2004). Geomorphology: An approach to determining subsurface reservoir dimensions. AAPG bulletin, 88(8), 1123-1147. https://doi.org/10.1306/02090403100.

van de Lageweg, W. I., van Dijk, W. M., Baar, A. W., Rutten, J., & Kleinhans, M. G. (2014). Bank pull or bar push: What drives scroll-bar formation in meandering rivers?. Geology, 42(4), 319-322. https://doi.org/10.1130/G35192.1.

Dijk, W. M., Lageweg, W. I., & Kleinhans, M. G. (2012). Experimental meandering river with chute cutoffs. Journal of Geophysical Research: Earth Surface, 117(F3). https://doi.org/10.1029/2011JF002314.

van Oorschot, M., M. G. Kleinhans, G. Geerling, and H. Middelkoop (2016), Distinct patterns of interaction between vegetation and morphodynamics, Earth Surf. Processes Landforms, 41(6), 791–808. https://doi.org/10.1002/esp.3864.

Weill, P., Lajeunesse, E., Devauchelle, O., Métiver, F., Limare, A., Chauveau, B., & Mouazé, D. (2014). Experimental investigation on self-channelized erosive gravity currents. Journal of Sedimentary Research, 84(6), 487-498. https://doi.org/10.2110/jsr.2014.41.

Weimer, P., & Slatt, R. M. (2004). Petroleum systems of deepwater settings. Society of Exploration Geophysicists and European Association of Geoscientists and Engineers.

Wetzel, A. (1993). The transfer of river load to deep-sea fans: a quantitative approach. AAPG Bulletin, 77(10), 1679-1692.

Willems, C. J., Nick, H. M., Donselaar, M. E., Weltje, G. J., & Bruhn, D. F. (2017). On the connectivity anisotropy in fluvial Hot Sedimentary Aquifers and its influence on geothermal doublet performance. Geothermics, 65, 222-233. https://doi.org/10.1016/j.geothermics.2016.10.002.

Williams, G. P. (1978). Bank-full discharge of rivers. Water resources research, 14(6), 1141-1154. https://doi.org/10.1029/WR014i006p01141.

Williams, G. P. (1986). River meanders and channel size. Journal of hydrology, 88(1-2), 147-164. https://doi.org/10.1016/0022-1694(86)90202-7.

Wiles, E., Green, A., Watkeys, M., & Jokat, W. (2017). The Zambezi Channel: A new perspective on submarine channel evolution at low latitudes. Geomorphology, 286, 121-132. https://doi.org/10.1016/j.geomorph.2017.02.014.

Wolman, M. G., & Miller, J. P. (1960). Magnitude and frequency of forces in geomorphic processes. The Journal of Geology, 68(1), 54-74. https://doi.org/10.1086/626637.

Wynn, R. B., Cronin, B. T., & Peakall, J. (2007). Sinuous deep-water channels: Genesis, geometry and architecture. Marine and Petroleum Geology, 24(6-9), 341-387. https://doi.org/10.1016/j.marpetgeo.2007.06.001.

Wynn, R. B., & Stow, D. A. (2002). Classification and characterisation of deep-water sediment waves. Marine Geology, 192(1-3), 7-22. https://doi.org/10.1016/S0025-3227(02)00547-9.

Yan, N., Mountney, N. P., Colombera, L., & Dorrell, R. M. (2017). A 3D forward stratigraphic model of fluvial meander-bend evolution for prediction of point-bar lithofacies architecture. Computers & Geosciences, 105, 65-80. https://doi.org/10.1016/j.cageo.2017.04.012.

Yang, K., Smith, L. C., Chu, V. W., Pitcher, L. H., Gleason, C. J., Rennermalm, A. K., & Li, M. (2016). Fluvial morphometry of supraglacial river networks on the southwest Greenland Ice Sheet. GIScience & Remote Sensing, 53(4), 459-482. https://doi.org/10.1080/15481603.2016.1162345.

Zolezzi, G., & Seminara, G. (2001). Downstream and upstream influence in river meandering. Part 2. Planimetric development. Journal of Fluid Mechanics, 438, 183-211. https://doi.org/10.1017/S002211200100427X.

Annexes

Annexe A. Base de données des systèmes turbiditiques

System	Location	Zone	Data type	N	References
Amazon	N Brazil	Top CS	M	1	Babonneau et al. (2002) Fig 16
Amazon	N Brazil	Toe CS	M	9	Damuth et al (1988) fig 7 Babonneau et al. (2002) Fig 16 Pirmez and Flood (1995) Fig 16, 17 Pirmez and Imran (2003) Fig 10
Amazon	N Brazil	Toe CS	AS	2	Damuth et al. (1988) fig 11
Amazon	N Brazil	Proximal BF	M	3	Babonneau et al. (2002) Fig 16 Pirmez and Flood (1995) Fig 19 Pirmez and Imran (2003) Fig 10
Amazon	N Brazil	Distal BF	M	4	Pirmez and Flood (1995) Fig 13 Pirmez and Imran (2003) Fig 10
Amazon	N Brazil	Distal BF	AS	1	Damuth et al. (1988) fig 19
Bengal	E India	Top CS	M	2	Curray et al. (2003) fig 17
Bengal	E India	Toe CS	M	2	Curray et al. (2003) fig 19
Bengal	E India	Toe CS	AS	1	Curray et al. (2003) fig 19
Bengal	E India	Proximal BF	M	11	Curray et al. (2003) Fig 23 Hubsher et al. (1997) Fig 3 – 5 Schwenk et al. (2005) Fig 4, 5, 8
Bengal	E India	Proximal BF	AS	2	Curray et al. (2003) Fig 29
Bengal	E India	Distal BF	M	8	Curray et al. (2003) fig 7, 9, 11 – 14 Hubsher et al. (1997) Fig 6, 7
Bengal	E India	Distal BF	AS	4	Curray et al. (2003) Fig 25, 26 Hubsher et al. (1997) Fig 6, 7
Benin major	Nigeria	Toe CS	AS	15	Deptuck et al. (2003) Fig 6, 8
Bounty	SE N-Zealand	Proximal BF	M	1	Carter and Carter (1996) fig 7
Bounty	SE N-Zealand	Distal BF	M	8	Carter and Carter (1996) fig 7
Cap Lopez Canyon	Gabon	Top CS	M	2	Biscara et al. (2013) fig 5
Cap Timiris	Mauritania	Top CS	M	4	Antobreh et Krassel (2006) fig 4
Cascadia	USA (WA)	Proximal BF	M	7	Griggs & Kulm (1973) fig 3, 5, 7 – 10
Congo	Angola	Top CS	M	7	Shepard and Emery (1973) fig 3 Babonneau et al. (2002 fig 7
Congo	Angola	Toe CS	M	19	Shepard and Emery (1973) fig 3 Babonneau et al. (2002) fig 7 Babonneau et al. (2004) fig 9
Congo	Angola	Proximal BF	M	5	Shepard and Emery (1973) fig 3 Babonneau et al. (2002) fig 7 Savoie (2001) Fig 4
Congo	Angola	Distal BF	M	9	Babonneau et al. (2002) fig 7 Droz et al. (1996) fig 6 Dennielou et al. (2017) Fig 4, 7 Doughty-Jones et al. (2017) fig 16
Dalia M9 Green Ch	Angola	Toe CS	AS	4	Abreu et al. (2003) fig 2, 9
EAB canyon	Peru	Top CS	M	4	Hagen et al. (1994) fig 7
Foix	S France	Top CS	M	1	O'Connell et al. (1985) fig 3
Golo fan	SE France	Proximal BF	M	3	Gervais (2002) fig IV-8

					Pichevin et al. (2003)
Golo fan	SE France	Distal BF	M	3	Gervais (2002) fig IV-8 Pichevin et al. (2003)
Mississippi	USA (MI)	Proximal BF	AS	2	Kolla et al. (2007) fig 12 Posamentier (2003)
Hecho Ainsi II	*Spain*	Proximal BF	AO	1	Bakke et al. (2008) fig 2
Hereau canyon	S France	Top CS	M	2	Baztan et al. (2009) fig 4
Hueneme fan	USA (CA)	Proximal BF	M	2	Skene et al. (2002) fig 15
Indus	W India	Top CS	M	1	McHargue et Webb (1986) fig 4
Indus	W India	Toe CS	M	2	McHargue et Webb (1986) fig 4
Indus CLS C1	W India	Toe CS	AS	3	Deptuck et al. (2003) fig 2
Indus CLS C2	W India	Toe CS	AS	6	Deptuck et al. (2003) fig 3, 4
Indus CLS C3	W India	Toe CS	AS	6	Deptuck et al. (2003) fig 4
Indus CLS C3	W India	Proximal BF	M	1	Rodrigez et al. (2011) fig 8
Kaoping Canyon	Taiwan	Top CS	M	1	Liu et al. (1993) fig 11
La Jolla	USA (CA)	Distal BF	M	3	Normark (1970) fig 10
Lacaze canyon	S France	Top CS	M	2	Baztan et al. (2009) fig 6
Lofoten	W Norway	Proximal BF	M	1	O'Cofaigh et al. (2006) fig 5
Lucia Chica Chs	USA (CA)	Top CS	M	8	Maier et al. (2013)
Madeira channel	E Morocco	Proximal BF	M	3	Stevenson et al. (2013) fig 6
Magdalena	Columbia	Proximal BF	M	2	Estrada et al. (2005) fig 6
Magdalena	Columbia	Distal BF	M	1	Estrada et al. (2005) fig 6
Mahin Avon	Nigeria	Proximal BF	M	11	Hansen et al. (2017) fig 8
Mahakam	Indonesia (E Borneo)	Proximal BF	AS	3	Kolla et al. (2007) fig 13 Normark et al. (2002) Fig 21
Mahakam	Indonesia (E Borneo)	Distal BF	AS	3	Saller et al. (2008) fig 6, 9
Messenger Fm	*New Zealand*	Distal BF	AO	1	Janocko et al. (2013) fig 10
Monterey	USA (CA)	Toe CS	M	5	Komar (1969) fig 3
NAMOC	E Canada	Proximal BF	M	3	Skene (1998) fig 36
Navy fan	USA (CA)	Toe CS	M	1	Bowen et al. (1984) fig 5
Navy fan	USA (CA)	Proximal BF	M	2	Bowen et al. (1984) fig 5
Navy fan	USA (CA)	Distal BF	M	2	Bowen et al. (1984) fig 5
Niceto valley	Italia (Sicily)	Toe CS	M	1	Gamberi et al. (2013)
Niger fan	Nigeria	Top CS	M	8	Jobe et al. (2015) fig 5, 7, 9, 10
Niger fan	Nigeria	Top CS	AS	5	Jobe et al. (2015) fig 5, 7, 9
Niger fan	Nigeria	Proximal BF	M	1	Jobe et al. (2015) fig 15
Niger fan	Nigeria	Distal BF	M	1	Jobe et al. (2015) fig 16
Nile fan Pliocene	Egypt	Toe CS	AS	5	Samuel et al. (2003) fig 7, 9, 11
Nile fan Pliocene	Egypt	Proximal BF	AS	2	Cross et al. (2009) fig 8, 11
Nile fan Pliocene	Egypt	Distal BF	AS	2	Cross et al. (2009) fig 11
Off N Borneo	Indonesia (N Borneo)	Top CS	M	2	Straub et al. (2008) fig 4
Orinoco System	Venezuela	Proximal BF	AS	3	Wood et al. (2009) fig 14
Red River canyon	S China	Top CS	M	1	Gong et al. (2015) fig 13
Red River canyon	S China	Toe CS	M	2	Gong et al. (2015) fig 13
Rhone	S France	Top CS	M	1	Lombo Tombo et al. (2012)
Rhone	S France	Toe CS	M	9	Torres et al. (1999) fig 4 Lombo Tombo et al. (2012)
Rhone	S France	Proximal BF	M	5	Droz et Bellaiche (1985) fig 10 Torres et al. (1999) fig 4 Lombo Tombo et al. (2012)
Rosario Fm	*Mexico*	Toe CS	AO	2	Janocko et al. (2013) fig 10
Ruppert Inlet	W Canada (BC)	Proximal BF	M	2	Hay et al. (1983) fig 5
Ruppert Inlet	W Canada (BC)	Distal BF	M	3	Hay et al. (1983) fig 5

Schiehallion field	N Scotland	Distal BF	AS	1	Gainski et al. (2013) fig 9
Surveyor Channel	USA (AK)	Proximal BF	M	9	Ness & Kulm (1973) fig 2 A
Tanzania	Tanzania	Proximal BF	M	2	Bourget et al. (2008) fig 3
Toyama	N Japan	Top CS	M	2	Nakajima et al. (1998) fig 4
Toyama	N Japan	Toe CS	M	7	Nakajima et al. (1998) fig 4 Nakajima & Satoh (2001) fig 10
Valencia	E Spain	Top CS	M	1	O'Connell et al. (1985) fig 4c
Vidal	Guiana	Top CS	M	18	Embley et al. (1970) fig 6, 9
Villafranca	Italia (Sicily)	Proximal BF	M	3	Gamberi et Rovere (2011) fig 6 – 8
West africa	West Africa	Proximal BF	AS	2	Mayall et al. (2006) fig 6, 8
West africa	West Africa	Toe CS	AS	3	Janocko et al. (2013) fig 2, 8, 9
West africa	West Africa	Proximal BF	AS	15	Janocko et al. (2013) fig 6, 8 - 10, 13, 14
Zambezi	Mozambique	Proximal BF	M	5	Droz et Mougenot (1987) fig 4 Wiles et al. (2017) Fig 4, 6

CS: Continental Slope, BF: Basin Floor, M: modern, AS: ancient seismic, AO: ancient outcrop, N number of datasets

RÉSUMÉ

Les systèmes turbiditiques chenalisés permettent le transfert de sédiments depuis le plateau continental vers le domaine marin profond de la même façon que les cours d'eau sur les continents. Les dépôts sédimentaires turbiditiques forment parmi les plus grands réservoirs d'hydrocarbures actuellement exploités. MINES ParisTech développe depuis une vingtaine d'années Flumy, un modèle numérique simulant l'évolution d'un système fluviatile méandriforme pour la simulation de réservoirs. L'approche proposée dans ce travail est de transposer Flumy aux systèmes sous-marins profitant de l'analogie entre ces environnements. La géomorphologie des systèmes chenalisés méandriformes fluviatiles et sous-marins est d'abord comparée à partir de données naturelles, et des expériences en laboratoire mettent en évidence les différences dans les écoulements aériens et sous-aquatiques. L'intégration dans Flumy de ces résultats permet de reproduire l'architecture stratigraphique des réservoirs turbiditiques.

MOTS CLÉS

Turbidites, Systèmes méandriformes, Modélisation de réservoir, Flumy, Géomorphologie

ABSTRACT

Channelized turbidite systems act as sediment transfer routes through the submarine realm similarly to rivers on the continents. The turbidite sedimentary deposits create among the biggest hydrocarbon reservoirs currently produced. MINES ParisTech has developed in the last twenty years Flumy, a numerical model that simulates the evolution of a meandering fluvial system to simulate reservoirs. In this work, we propose to transpose Flumy to submarine systems taking advantage of the analogy between these environments. Using natural data, the geomorphology of channelized meandering fluvial and submarine systems is compared, and laboratory experiments highlight the differences in terms of aerial and subaqueous flow behavior. The integration of the results of these studies allows Flumy to accurately simulate the stratigraphic architecture of channelized turbidite reservoirs.

KEYWORDS

Turbidites, Meandering systems, Reservoir modeling, Flumy, Geomorphology